Simulating supernova feedback in galaxy disks

PETER EDWARD CREASEY

Simulating supernova feedback in galaxy disks

Peter Edward Creasey

Abstract

In this thesis I examine supernova feedback in hydrodynamical simulations of galaxy disks. Understanding this process entails the numerical evaluation of cooling in radiative shocks, and we present a set of simulations using two widely used numerical schemes: smoothed particle hydrodynamics and adaptive mesh refinement. We obtain a similarity solution for a shock-tube problem in the presence of radiative cooling, and test how well the solution is reproduced. We interpret our findings in terms of a resolution criterion, and apply it to realistic simulations of cosmological accretion shocks onto galaxy halos, cold accretion and thermal feedback from supernovae or active galactic nuclei. To avoid numerical overcooling of accretion shocks onto halos that should develop a hot corona requires a particle or cell mass resolution of $10^6\,\mathrm{M}_\odot$, which is within reach of current state-of-the-art simulations. At this mass resolution, thermal feedback in the interstellar medium of a galaxy requires temperatures of supernova or AGN driven bubbles to be in excess of 10^7 K at densities of $n_\mathrm{H} = 1.0\,\mathrm{cm}^{-3}$, in order to avoid spurious suppression of the feedback by numerical overcooling.

In order to improve sub-grid models of feedback we perform a series of numerical experiments to investigate how supernova explosions shape the interstellar medium in a disk galaxy and power a galactic wind. We model a simplified ISM, including gravity, hydrodynamics, radiative cooling above 10^4 K, and star formation that reproduces the Kennicutt-Schmidt relation. By simulating a small patch of the ISM in a tall box perpendicular to the disk, we obtain sub-parsec resolution allowing us to resolve individual supernova events.

We run a large grid of simulations in which we vary gas surface density, gas fraction, and star formation rate in order to investigate the dependencies of the mass loading, $\beta \equiv \dot{M}_\mathrm{wind}/\dot{M}_\star$. In the cases with the most effective outflows we observe a β of 4, however in other cases we find $\beta \ll 1$. We find that outflows are more efficient in disks with lower surface densities or gas fractions. A simple model in which the warm clouds are the barriers that limit the expansion of the blast wave reproduces the scaling of outflow properties with disk parameters at high star formation rates. We extend the scaling relations derived from an ISM patch to infer an effective mass loading for a galaxy with an exponential disk, finding that the mass loading depends on circular velocity as $\beta \propto V_\mathrm{d}^{-\alpha}$ with $\alpha \approx 2.5$ for a model which fits the Tully-Fisher relation. Such

a scaling is often assumed in phenomenological models of galactic winds in order to reproduce the flat faint end slope of the mass function. Our normalisation is in approximate agreement with observed estimates of the mass loading for the Milky Way.

Finally, we extend these simulations to follow the ejecta produced by these SNe, allowing us to track the distribution of metals as they are mixed into the different phases of the ISM and swept out into a galactic wind. Such calculations are important both directly in predicting the enrichment of the intergalactic medium, but also with the sister problem of understanding the enrichment of the host galaxies and the mass-metallicity relation, owing to the unique role that supernovae are believed to play both as the sources of galactic winds and the sources of galactic metals. We study the dependence of the amount of metals released per unit of star formation, $\beta_{\rm Z} \equiv \dot{M}_{\rm z}/\dot{M}_{\star}$, and the fraction of metals released, $\beta_{\rm Z}/y$. We include thermal and momentum feedback from massive stars and find these make a less significant contribution to the galactic wind than SNe. We build up a model of galactic chemical evolution and we demonstrate that these models are compatible with the metallicity distributions of faint stars and compare to closed box models of chemical evolution. We infer metal retention fractions from the observed data, although this may be complicated by recycling in the galaxy halos. We compare these rates to the fraction of metals ejected in the simulations and demonstrate approximate agreement, although the simulation data has considerable scatter, primarily due to the stochastic nature of the feedback in the limited volumes of the simulations.

Simulating supernova feedback in galaxy disks

by P. E. Creasey

A thesis submitted to the University of Durham
in accordance with the regulations for
admittance to the Degree of Doctor of Philosophy.

Department of Physics
University of Durham
August 2012

Contents

List of Figures

List of Tables

Declaration

The work described in this thesis was undertaken between 2008 and 2012 while the author was a research student under the supervision of Dr. Tom Theuns, Prof. Richard G. Bower and Dr. Cedric Lacey in the Department of Physics at the University of Durham. This work has not been submitted for any other degree at the University of Durham or any other University.

Parts of this work have appeared in the following papers

- Creasey, P., Theuns, T., Bower, R. G. and Lacey, C. G., "Numerical overcooling in shocks", 2011, MNRAS, 415, 3706-3720 (Chapter 2)
- Creasey, P., Theuns, T. and Bower, R. G. "Understanding how Supernovae drive Galactic Winds", submitted to MNRAS (Chapters 3 and 4)

All figures were produced by the author with the following exceptions:

- Figure 1.1: Wiersma et al. (2009a), reproduced with permission
- Figure 1.2: courtesy of Richard G. Bower (the Eagle project, in prep.)

A number of publicly available codes were used in the creation of this work. FLASH (used in Chapters 2-5) was in part developed by the DOE-supported ASC/Alliance Center for Astrophysical Thermonuclear Flashes at the University of Chicago. GADGET (used in Chapters 2 and 3) was written by Volker Springel, with modifications by Tom Theuns, Joop Schaye, Rob Crain (Leiden Observatory, Netherlands), Claudio Dalla Vecchia (MPE, Germany) and Rob Wiersma. The simulations performed in this thesis were produced on the COSMA computer at the ICC, Durham University, UK. Some additional simulation data was provided by Rob Crain for Chapter 2.

Acknowledgements

My heartfelt thanks go to my supervisors Tom Theuns and Richard Bower, without whom this thesis would not have been possible. Tom's unlimited supply of ideas, combined with a readiness and enthusiasm to make a back-of-the-(large) envelope calculation that may include writing a script to analyse an unexplored dataset during meetings makes him a role model of a modern physicist. Richard Bower's more traditional influence, giving experienced insight and providing encouragement and useful comments at the appropriate times would be any asset to any project, but was particularly helpful for my thesis. I would also like to thank Cedric Lacey, whose considerable knowledge and thoughtful comments were very helpful for both the start of my studies and the work at the start of this thesis.

The work in this thesis was not conceived in a vacuum, and discussions with Peter Thomas, Justin Read, Tom Abel, Daniel Price, Romain Teyssier, Martin Stringer, Crystal Martin, Claudia Lagos and Andrew Pontzen shaped this work and the ideas within. On a more technical level, my collaboration with the machines in Durham has been qualitatively improved by the many interventions of Lydia Heck.

A number of others in Durham have improved this thesis considerably, at various levels of indirection. I am lucky to have the friendship of Ben Lowing, who was always willing to talk about astrophysics and coding with me. Ann-Marie Einhaus has provided me with a friendly ear and numerous cups of tea. My time in Durham was enormously improved by Dora Förhing, who will always be special to me. The working environment of the ICC has also been made stimulating and enjoyable by the many students and staff, too numerous to mention individually, but particularly my office mates and the students of student theory journal club.

Finally, I would like to thank my family, whose endless support has provided me with so many opportunities that I would not otherwise have had, and I certainly would not have been writing this thesis in Durham without their help over the years.

Chapter 1 | *Introduction*

The aim of cosmology is the study of the very largest scale, the Universe itself. As a science, it is the marriage of theory and observation, comprising the theoretical equations for the dynamics of the constituent components; and the observed phenomena such as galaxies and the microwave background. Recent technological advances in the last few decades have exploded the amount of observed data and brought previously small discrepancies into the foreground, forcing scientists to frequently refine their models to keep up the relationship.

The current paradigm is of an observable universe where the seeds were set by a period of inflation, producing a flat universe with deviations about the mean density described almost exactly by a (homogeneous and isotropic) Gaussian random field with a scale invariant power spectrum. A subsequent period of evolution where the baryons were hot enough to be ionized (and thus highly coupled to the electromagnetic field) imprinted the duration of this epoch and the fraction of baryonic matter onto the power spectrum (called baryon acoustic oscillations), which can be observed as a relic both in the cosmic microwave background (CMB) and the clustering of galaxies.

Over the next 13.7 billion years the overdensities in this random field have collapsed under their own gravity to form dense objects. It is here that we make a distinction between the collisionless dark matter particles and the collisional baryons; the former collapse to form a multi-phase medium (i.e. many velocities in a small volume), whereas the latter redistribute energy over a mean free path (forming a single phase, described by the continuum approximation that underpins the subject of fluid dynamics). The result of either mechanism is a series of collapsed structures known as halos, with a mean density of approximately $200\times$ the critical density of the universe.

Despite these differences in phase space, the distinguishing property of baryons in this scenario is usually heralded to be their ability to *cool*, i.e. hot dense baryons at the centres of the collapsed structures are thermally coupled with the cold sparse baryons far away by the transport of electromagnetic waves (photons), allowing thermal energy to move from the former to the latter. By removing the pressure support of the hot baryons, collapse is resumed and even higher density baryonic objects can form.

The collapse is again delayed as the baryons form a set of luminous objects called stars, whose distinguishing qualities are that they are sufficiently hot and dense to undergo nuclear fusion (providing additional thermal pressure support) and are opaque (impeding the escape of that thermal energy). This delay will in most cases last tens of billions of years (dependent almost entirely on the baryonic mass of the object), which appears to be a sufficient time for some of the baryons to condense into cosmologists, who investigate such things.

This skeletal description of the dynamics in the universe leads to some of the most pressing questions in cosmology which underpin this thesis, which are

1. How much luminous material (i.e. stars) is expected to arise in halos of a given total mass.

2. How we can construct computer simulations that capture these dynamics (even at the large scale).

In the remainder of this chapter I will describe the model above in more precise technical detail. Section 1.1 outlines the physical processes governing the collapse of baryonic matter and the key observational features such as galaxies and supernovae which play a central role. Section 1.2 then describes the process of simulating these on a computer, specifically the approximations used for the dynamical equations and the discretisation into a finite set of variables. Finally I summarise the remaining chapters and give the motivation for this thesis in Section 1.3.

1.1 Galaxy formation

In this section I will outline the physics of galaxy formation (see e.g. Peebles, 1993; Peacock, 1999) from a series of small perturbations in the initial density field which grow to form the observed universe we see today. I begin with a discussion of evolution on cosmological scales, followed the Gaussian random field formalism that is used to approximate the collapse of material in the linear regime. I then focus on the baryonic material, and the property of cooling which allows the formation of galaxies within the overdense regions. Finally I discuss supernova-driven outflows from galaxies and relate this to our understanding of star formation and the comparison with the properties and structure of our own galaxy.

1.1.1 ΛCDM and the linear universe

For a spatially homogeneous and isotropic but temporally varying universe, the metric must be of the form $\mathrm{d}s^2 = a(t)^2\mathrm{d}\mathbf{x}^2 - c^2\mathrm{d}t^2$ where t is the regular time but $\mathbf{x}$ represents a co-moving spatial

location, i.e. it only represents the actual distance today, when the scale factor $a(t) = 1$. The evolution of this scale factor is described by the Friedmann equation,

$$\left(\frac{\dot{a}}{a}\right)^2 = \frac{8\pi G}{3}\rho + \frac{c^2}{3}\Lambda \tag{1.1}$$

where ρ is the energy density of matter divided by c^2, there is no curvature ($k = 0$) and Λ is the cosmological constant. This equation is often re-written in the following form

$$H(t)^2 \equiv \left(\frac{\dot{a}}{a}\right)^2 \tag{1.2}$$

$$= H_0^2\left[\Omega_m a^{-3} + \Omega_\gamma a^{-4} + \Omega_\Lambda\right] \tag{1.3}$$

where the energy density of matter has been further separated into the fractions of relativistic matter (Ω_γ which as far as we know is just photons and neutrinos at early times) and non-relativistic matter (Ω_m, baryons and cold dark matter). Ω_Λ is the fraction of 'dark energy' and we have normalised this to the present day such that $\Omega_m + \Omega_\gamma + \Omega_\Lambda = 1$.

The equation of motion of a non-relativistic particle in comoving co-ordinates is

$$\ddot{\mathbf{x}} = -H(t)\dot{\mathbf{x}} \tag{1.4}$$

(Peacock, 1999, an acceleration sometimes known as 'Hubble drag'). The cumulative effects of the expansion of the universe upon the collapse of matter are dramatic, and the density contrast of virialised regions of matter (known as halos) to the critical density is expected to be ~ 200 ($18\pi^2$ for an $\Omega_m = 1$ universe, but is relatively insensitive to Ω_m, see e.g. Eke et al., 1996).

The assumption of virialised halos all of the same density contrast allows us to relate the mass of halos to their circular velocity via the Hubble parameter

$$v_{200}^3 = 10GM_{200}H(z) \tag{1.5}$$

(Mo et al., 1998), and if we know the particle mass this also gives them a characteristic temperature. These quantities will be useful in Chapters 2,3 and 4.

1.1.2 Gaussian Random Fields

The possibility that the initial conditions for the growth of structure can be described by a Gaussian random field that is isotropic and homogeneous allows us to make several statements about the overdensities. Firstly, the isotropy and homogeneity of the covariance function tell us that the Fourier modes $\tilde{F}(\mathbf{k})$ of our random field $f(\mathbf{x})$, related by our choice of definition

$$f(\mathbf{x}) = (2\pi)^{-3/2}\int e^{-i\mathbf{k}\cdot\mathbf{x}}\tilde{F}(\mathbf{k})\mathrm{d}\mathbf{k}\,, \tag{1.6}$$

will be independent Gaussians,

$$\mathbb{E}\left[\tilde{F}(\mathbf{k}_1)\tilde{F}(\mathbf{k}_2)^\dagger\right] = \delta\left(\mathbf{k}_1 - \mathbf{k}_2\right) P(|\mathbf{k}_1|)\,, \tag{1.7}$$

and $P(k)$ is known as the *power spectrum* of f (isotropic and homogeneous but non-Gaussian random fields also have an isotropic power spectrum, however, we will only consider the Gaussian case at this time) . This gives us a method of realising the Gaussian random field from which we can simulate the collapse of structures with N-body simulations (e.g. Efstathiou et al., 1985). Such simulations allow us to probe the properties of collapsed structures of collisionless particles. These properties include the distribution, substructure and many other statistics of dark matter halos, but for the purposes of this section it is sufficient to understand the number density of such structures, which becomes important in Chapter 3.

The number density of halos

The identification of regions that will collapse to form halos is achieved by testing whether a spherical volume of radius R has a mean density above a critical threshold $\delta_c(R)$. This can be approximated as testing the density in a smoothed random field, where the smoothing is a low pass filter with k-space cutoff $k(R)$, i.e. an overdensity

$$\delta(k) = (2\pi)^{-3/2} \int_{|\mathbf{k}|<k} e^{-i\mathbf{k}\cdot\mathbf{x}} \tilde{F}(\mathbf{k}) \mathrm{d}\mathbf{k} \tag{1.8}$$

which, being a linear combination of mean-zero Gaussians (the $\tilde{F}(\mathbf{k})$) is itself mean zero Gaussian with variance

$$\Delta(k)^2 \equiv \mathbb{E}\left[|\delta(k)|^2\right] \tag{1.9}$$

$$= \int_0^k 4\pi k^2 P(k) \mathrm{d}k\,. \tag{1.10}$$

This leads to the result that the probability that a point in the smoothed random field has overdensity $\delta(k) > \delta_c(k)$ as

$$\mathbb{P}\left[\delta(k) > \delta_c(k)\right] = 1 - \Phi\left(\frac{\delta_c(k)}{\Delta(k)}\right)\,, \tag{1.11}$$

where Φ is the cumulative normal distribution function.

The advantage of choosing the sharp cutoff for our filter is the function $\delta(k)$ can then be treated as a Brownian motion in $\Delta(k)$. The reason this is possible is that each of the Fourier modes $\tilde{F}(\mathbf{k})$ are independent, and thus as we increase k we are simply including additional spherical shells (in k-space) which will be independent from the modes already included (i.e. the function $\delta(k)$ has *independent increments*), and so is just a Wiener process with 'time' $t = \Delta(k)$.

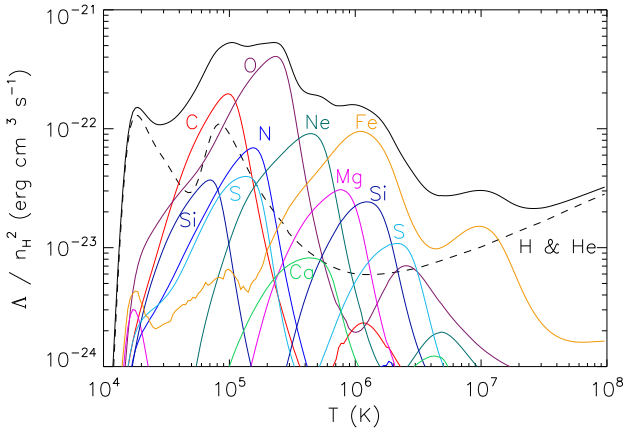

Figure 1.1: Normalised cooling rates as a function of temperature for solar abundances, assuming CIE. Reprinted with permission from Wiersma et al. (2009a).

The advantage of these independent increments is that when the overdensity threshold $\delta_c(k)$ is constant, we can apply a symmetry argument to relate the probability that $\delta(k) > \delta_c$ to the probability that $\delta(s) = \delta_c$ for some $s \in [0, k]$, i.e.

$$\mathbb{P}\left[\exists s \in [0,k] : \ \delta(s) = \delta_c\right] = 2\mathbb{P}\left[\delta(k) > \delta_c\right] \tag{1.12}$$

(e.g. Bond et al., 1991). It is then possible to deduce the number density of these halos in the analytic form (including the troublesome factor 2 of Press and Schechter, 1974) as

$$\frac{\mathrm{d}n}{\mathrm{d}m} = \frac{2\bar{\rho}\delta_c}{m\Delta(k)^2}\frac{\Delta'(k)}{m'(k)}\phi\left(\frac{\delta_c}{\Delta(k)}\right) , \tag{1.13}$$

where $\bar{\rho}$ is the mean density of the Universe, ϕ is the normal distribution function and the relation of the mass of halos to their size in k-space is $m(k) \propto \bar{\rho}k^{-3}$ (see also White, 1994).

It is possible to extend this argument to non-sharp filterings for $\delta(k)$ (breaking the assumption of independent increments), and to non-constant thresholds $\delta_c(k)$ (breaking the symmetry assumption), but in general these are not analytic and must be solved via Monte-Carlo methods.

1.1.3 Cooling of baryons

Let us now turn our attention to the distribution of baryons. In order for baryons to collapse and form the luminous galaxies that are ubiquitous they must lose some of their pressure support via cooling. It is for this reason that we must discuss in some detail the cooling functions used in astrophysics. In Fig. 1.1 we reprint the cooling function used in Wiersma et al. (2009a) for elements with solar abundances and in collisional ionisational equilibrium (CIE), which illustrates the complexity involved in the summation over all the different transitions of each different

species. Nevertheless, for an overall understanding I outline three different regimes in the following paragraphs, $T > 10^6$K, $10^6 > T > 10^4$K and 10^4K $> T$ which broadly trisect the regimes of interest.

$\mathbf{T > 10^6}$K

Above 10^6K, radiative losses are dominated by thermal bremsstrahlung, that is the radiation produced when free electrons are deflected by the positively charged atomic nuclei. The emission per unit volume is

$$\frac{\mathrm{d}E}{\mathrm{d}t} \propto -Z^2 T^{1/2} N N_e \tag{1.14}$$

(Longair, 1996), where Z is the charge of the nucleus and N, N_e are the number densities of nuclei and electrons respectively, i.e. proportional to the square of the density (since it is due to 2-body collisions) and the square-root of the temperature (since the thermal de Broglie wavelength shrinks for high energy electrons). Below 10^8K metal transitions, particularly Fe, start to dominate (see also Fig. 1.1).

$\mathbf{10^6 > T > 10^4}$ K

At intermediate temperatures the strongest lines observed are hydrogen recombination lines, such as Hα and Hβ (the first two lines of the Balmer series), although at solar metallicities a large interval in temperature is dominated by oxygen and carbon transitions.

$\mathbf{T < 10^4}$K

At low temperatures the emission is dominated by the collisional excitations of molecules (e.g. H_2) and metals (e.g C^+). For enriched gas, molecules with a strong electric dipole moment such as CO dominate the emission with their rotational transitions. For primordial gas, the emission is much weaker as it relies on the transitions of H_2.

1.1.4 Galactic winds and Supernovae

The picture of baryons cooling and infalling to form galaxies described in the previous section is complicated by the observation that many of the baryons are not only failing to cool onto galaxies but are actually being ejected (see, e.g. Heckman et al., 1990; Martin, 2005), implying the existence of heat sources inside galaxies that can heat some fraction of the baryons above the specific binding energy of the galaxy. For low mass ($\lesssim 10^{10.5}\ h^{-1}\mathrm{M}_\odot$) galaxies this source is believed to

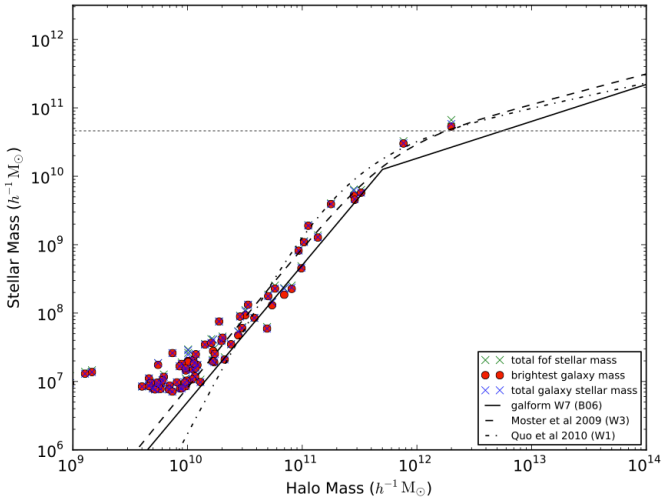

Figure 1.2: Mass in stars vs. halo mass (i.e. baryons and dark matter) from abundance matching, courtesy of Richard G. Bower (the Eagle project, in prep.). The stellar mass drops far below the baryonic fraction of the halo mass, $\Omega_\mathrm{b} M_\mathrm{h}/\Omega_\mathrm{m}$ at both low ($M_\star \lesssim 10^{10.5}\mathrm{M}_\odot$) and high ($M_\star \gtrsim 10^{10.5}\mathrm{M}_\odot$) stellar masses (*dashed grey line*).

be supernovae (SNe, e.g. Larson, 1974) whilst for large galaxies ($\gtrsim 10^{10.5}\ h^{-1}\mathrm{M}_\odot$) the supermassive black holes (known as active galactic nuclei) are believed to be primarily responsible.

Due to the difficulty of simulating baryonic effects and the uncertainties surrounding the processes, a number of phenomenological models such as GALFORM (Cole et al., 2000) have been developed which follow the evolution of a population of galaxies with idealised geometry and for which the parameters of the models can be rapidly validated against observables. Although using the data to infer processes in such a way is challenging, these models have enjoyed significant successes in simultaneously predicting properties of the observed galaxy population.

Our focus in this thesis will be on the SN feedback, and indeed the effects of this are rather dramatic. In Fig. 1.2 we show a sample stellar mass vs. halo mass function, i.e. the amount of stellar material compared to the gravitational mass. If all the gas were turned into stars the stellar mass would be $M_\star = \Omega_\mathrm{b} M_\mathrm{h}/\Omega_\mathrm{m}$, however at low and high stellar masses this appears to be strongly suppressed.

1.1.5 Components of the MW and Solar Neighbourhood

The evolution galaxy disks and the star formation which ultimately results in SNe and the ejection of material is not a fully understood process. There is, however, one galaxy for which we have strong constraints for the properties and structure of the disk, and that is our own Milky Way. In

this section I will describe some of the methods used to probe the Milky Way and other galaxies (albeit at rather lower resolution) and explore their properties and structures. Although it is unrealistic to build a complete theory of galactic disks from a single disk, the observations can be used to disfavour theories in which the MW would be an extremely unlikely object.

The Solar Neighbourhood

The Sun orbits the centre of the MW in a circle of radius $R_\odot = 8.5\ \mathrm{kpc}$ with an orbital period of approximately 240 Myr (Kerr and Lynden-Bell, 1986). As such, the local neighbourhood lies outside the bulge of the galaxy, in a disk stratified by age with the older stars in a thicker (i.e. higher velocity dispersion) disk, and the cold molecular gas and young stars in a thin disk.

The distribution of atomic hydrogen (HI) is estimated from the 21cm line of HI. The magnetic moment of the hydrogen nucleus splits the ground state energies of the hydrogen atom to produce a 'hyperfine' transition of 5.877×10^{-6}eV, producing photons of 21.1 cm. This is a forbidden transition with probability $2.9 \times 10^{-15}\ \mathrm{s}^{-1}$. By measuring the flux at different latitudes and longitudes it is possible to construct a model of the HI distribution of the galaxy in galactocentric radius (R) and height above the disk (z), e.g. Lockman (1984). This has also been applied to measure the HI surface densities of other nearby galaxies, such as the THINGS survey (Walter et al., 2008).

Broadly speaking, the HI in disk galaxies appears in a disk that is somewhat more uniform than the stellar disk which has close to an exponential profile. In addition, the HI disk is much more extended than the stellar disk.

The HI in the MW appears to exist in a layer of FWHM of approximately 365 pc, independent of R, with a surface density at the solar neighbourhood of $\Sigma_{\mathrm{HI}} = 3.6\ \mathrm{M}_\odot\,\mathrm{pc}^{-2}$ (Kulkarni and Heiles, 1987). Bahcall et al. (1992) describes a two component model of atomic hydrogen both with surface densities $\Sigma_{\mathrm{HI}} = 4\ \mathrm{M}_\odot\,\mathrm{pc}^{-2}$ and velocity dispersions of 7 and 9 $\mathrm{km\,s}^{-1}$.

The molecular hydrogen (H_2) of disk galaxies shows a distinct distribution compared to that of the atomic hydrogen. Molecular gas in MW is primarily traced by proxy of the CO molecule. CO has a large dipole moment with a $J = 1 \rightarrow 0$ rotational transition of 2.6mm which is often the brightest emission line of molecular regions. This transition is excited by collisions with molecular hydrogen and decays spontaneously. The relationship between the flux I_{CO} and the H_2 column density (referred to as X_{CO}) is constrained by a number of observations; however, it is still only known to a factor of a few (e.g. Scoville and Sanders, 1987).

The molecular component of the MW is observed to exist in a distribution of Giant Molecular Clouds (GMCs) much less extended than that of the HI. Most of these clouds exist within $R =$

$3-7$ kpc (the so-called 'molecular ring') and 90% of the molecular mass of the MW lies within the solar circle (Scoville and Sanders, 1987). These measurements seem in agreement with other spiral galaxies (e.g. Wong and Blitz, 2002), although those galaxies generally have a 'core' of molecular gas, absent from the bulge of the MW. If one averages over large enough scales (i.e. many molecular clouds) it is possible to define a surface density of molecular gas, in which case the local neighbourhood would have a $\Sigma_{\mathrm{H}_2} \approx 10\ \mathrm{M}_\odot \mathrm{pc}^{-2}$.

The non-gaseous components of the MW disk are in the form of stars and dark matter. Local stars can be identified by parallax (such as the Hipparcos survey), giving estimates of the surface density of a thin and thick disk of stars. The remaining dark component is estimated from the gravitational potential implied by the dynamics of the disk. The model of Flynn et al. (2006) has $\Sigma_{\mathrm{gas}} = 13.2\ \mathrm{M}_\odot\,\mathrm{pc}^{-2}$ and $\Sigma_\star = 35.5\ \mathrm{M}_\odot\,\mathrm{pc}^{-2}$, with a recent paper by Bovy and Tremaine (2012) estimating the local dark matter density to give $\Sigma_{\mathrm{dm}} \approx 20\ \mathrm{M}_\odot\,\mathrm{pc}^{-2}$ within $z = \pm 1$ kpc (the velocity dispersion of the dark matter is of course extremely high, causing it to be distributed in a diffuse halo, and thus any attempt to describe it with a surface density is strongly dependent upon the height taken).

The connection with Star Formation

Since star formation occurs out of cold gas, it might be expected that there would be some observational correlation between the distribution of cold gas and the star formation rate, and indeed there has been considerable progress in this area, both for whole galaxies and more recently for regions within galaxies.

The most commonly used formulation for star formation rate is the power law suggested by Schmidt (1959),

$$\dot{\Sigma}_\star = A \left(\frac{\Sigma_{\mathrm{gas}}}{1\ \mathrm{M}_\odot\,\mathrm{pc}^{-2}} \right)^n \ \mathrm{M}_\odot\,\mathrm{yr}^{-1}\,\mathrm{kpc}^{-2}\,, \tag{1.15}$$

with exponent n in the range $1-2$. The gas referred to in Schmidt's original work was estimated from 21cm measurements (i.e. HI). The rate of star formation can be estimated from a wide variety of sources, but for reference modern estimates usually come from the H-α line (656nm due to recombination of warm ionised gas), the far ultraviolet continuum (due to hot young stars) or from infra-red flux (radiation reprocessed by dust).

In a seminal paper Kennicutt (1998) applied this globally to a number of other galaxies to estimate the parameters as $A = (2.5 \pm 0.7) \times 10^{-4}\ \mathrm{M}_\odot\,\mathrm{yr}^{-1}\,\mathrm{kpc}^{-2}$ and $n = 1.4 \pm 0.15$, with the best fit using Σ_{HI} rather than including molecular gas. Notably, the extension of the HI disks outside the star forming disks suggests there is some critical threshold of $3-10\ \mathrm{M}_\odot\,\mathrm{pc}^{-2}$ below

which star formation does not occur, or occurs at a very low rate (e.g. Kennicutt, 1989; Martin and Kennicutt, 2001; Schaye, 2004).

In order to make the connection to a *local* star formation law (i.e. based upon the volume density, $\rho_{\rm gas}$), it is necessary to make some assumptions about the vertical distribution of matter in a galactic disk. One such condition is given by the Toomre stability criterion (Toomre, 1964), where a differentially rotating disk is stable against large scale self gravitating models only if the parameter

$$Q \equiv \frac{\sigma_{\rm r}\kappa}{3.36G\Sigma} \tag{1.16}$$

$$> 1\,, \tag{1.17}$$

where $\sigma_{\rm r}$ is the radial velocity dispersion, Σ is the self gravitating surface density and κ is the epicyclic frequency,

$$\kappa^2 \equiv \frac{2\omega}{R}\frac{d}{dR}(R^2\omega)\,, \tag{1.18}$$

where for disk with constant rotation velocity $V_{\rm disk}$, we find $\kappa = \sqrt{2}V_{\rm disk}/R$. Notably if the velocity dispersion is isotropic (i.e. $\sigma_{\rm r} = \sigma_{\rm z}$), this is almost equivalent to saying the orbital time ($t_{\rm orb} = \sqrt{8}\pi/\kappa$) has to be less than the vertical oscillation time ($t_{\rm dyn} \approx \sigma_{\rm z}/G\Sigma$, where the exact coefficient depends upon whether we are referring to collisionless particles or a gas with adiabatic index γ).

If we apply this to the solar neighbourhood of the MW, we see that the vertical oscillation time is ≈ 60 Myr, below the 240 Myr required to orbit the galactic centre, suggesting the stellar population with this vertical velocity dispersion is unstable to the formation of large scale modes (i.e. $Q < 1$). For higher values of the velocity dispersion the components will be stable, however.

The proximity of the exponent of Eq. (1.15) to 1.5 is rather suggestive of a local star formation law of the form

$$\dot{\rho}_\star \propto \frac{\rho}{t_{\rm dyn}} \tag{1.19}$$

(Kennicutt, 1998), since the $t_{\rm dyn} \propto (G\rho)^{-1/2}$, giving an overall dependence of the local star formation rate on the density as $\rho^{3/2}$, very similar to the exponent of $n = 1.4$ suggested earlier for $\Sigma_{\rm gas}$. Notably this would require that the correspondence of $\Sigma_{\rm gas}$ to $\rho_{\rm gas}$; i.e. all disks have the same scale height $\sim \Sigma/\rho$ (see Schaye and Dalla Vecchia, 2008 for a thorough discussion of the role of the Jeans length in local and global star formation laws).

More recently, high angular resolution maps of nearby galaxies have allowed a more refined picture of star formation at different regions of the same galaxy. Wong and Blitz (2002) studied the radial distribution of atomic and molecular gas in seven nearby spiral galaxies and found that

star formation was more correlated with total gas surface density $\Sigma_{\rm HI+H_2}$. Bigiel et al. (2008) have extended this to estimate the local star formation law with coefficients (using $\Sigma_{\rm HI+H_2}$ in Eq. (1.15)) of $A = 8.7 \times 10^{-4}\ {\rm M_\odot\,yr^{-1}\,kpc^{-2}}$ and $n = 1.0$, with a significant steepening below $\Sigma_{\rm gas} = 9\ {\rm M_\odot\,pc^{-2}}$.

Coincidentally, it would appear that all the star formation thresholds lie near to the local gas density estimated in the solar neighbourhood. Clearly there is ongoing star formation here, however, as evidenced by the Orion nebula, at only ~ 400 pc distant.

In summary, we have given a brief overview of the physical processes that we wish to capture in our simulations, i.e. that of gravity for all matter, and the baryonic processes of cooling and star formation. In the next section we describe how these processes are translated into hydrodynamical simulations.

1.2 Hydrodynamical simulations

The simulation of hydrodynamical problems can be broadly divided into a four-stage process to produce a numerical answer which constitutes a sufficiently close approximation to the exact solution. There is usually some competition between the desire to include all the relevant processes, the requested accuracy of the solution and the computational resources available to the simulator. In real life these requirements will also include the finite time of the scientist to write simulation and analysis code and the opportunity to re-use existing software, or software with which the scientist is already familiar, but for the purposes of this section we will ignore these and concentrate only on the scientific problem and the methods used to solve it (for a more extensive discussion of the use of computer simulations for scientific experimentation, see the introduction of Hockney and Eastwood, 1988). The four stages are outlined below.

Initial conditions are the description of the problem at a single time, defining the fluid variables at every spatial position at that point in time.

Choose the physical processes. These are the laws of physics we will include in our simulation, defined as a set of governing equations which dictate how the fluid variables interact. The list of possible processes is large but in astrophysics commonly includes gravity, cooling/radiation transport, magnetic fields and nuclear burning.

Choose the discretisation. The simulation volume (in both space and time) will need to be divided up into smaller regions, each described with just a few variables. Such a discretisation is usually adaptive (irregular in time), but may be spatially regular (i.e a grid) or irregular

(e.g. a mesh), which itself may vary in time (see section 1.2.2). The description of the fluid on these regions in the simplest case is uniform, but may also be estimated to vary as some low order polynomial. Once this is decided, the governing equations must also be discretised onto these volumes.

Computation and validation. The final stage of this process is conceptually the easiest but practically the hardest; to implement all these on a computer and perform the simulation. In very simple cases it is possible to fully analyse the errors that the previous steps will introduce, but in practice these errors are often estimated empirically, by iterating through variations of the discretisation and other numerical parameters. Simple cases with known solutions are still very important, however, as they provide a reference against which problems in the implementation can be caught early.

1.2.1 The dynamical equations

The starting point for any fluid scheme are the Navier-Stokes equations, which describe the conservative evolution of mass and momentum in a fluid. The evolution of mass is given by the continuity equation,

$$\frac{\partial}{\partial t}(\rho) + \frac{\partial}{\partial x_i}(\rho v_i) = 0\,, \tag{1.20}$$

where ρ is the fluid density and v_i are the component of the velocity. The Navier-Stokes equations describe the evolution of momentum due to pressure, p, and viscous forces (the two terms on the RHS)

$$\frac{\partial}{\partial t}(\rho v_i) + \frac{\partial}{\partial x_j}(\rho v_i v_j) = -\frac{\partial p}{\partial x_i} + \frac{\partial}{\partial x_j}\sigma_{ij}\,, \tag{1.21}$$

and the continuity equation for the internal energy e is

$$\frac{\partial}{\partial t}(e) + \frac{\partial}{\partial x_j}(e v_j) = -p\frac{\partial v_i}{\partial x_i} + \sigma_{jk}\frac{\partial v_j}{\partial x_k}\,, \tag{1.22}$$

where

$$\sigma_{ij} = \eta\left(\frac{\partial v_i}{\partial x_j} + \frac{\partial v_j}{\partial x_i} - \frac{2}{3}\frac{\partial v_k}{\partial x_k}\delta_{ij}\right) + \zeta\frac{\partial v_k}{\partial x_k}\delta_{ij}\,, \tag{1.23}$$

is the viscous stress tensor and η and ζ are known as the shear and bulk viscosity coefficients respectively. These coefficients can be measured for real fluids, however, in most astrophysical flows they are so small that the viscous term is insignificant outside of shocks (i.e. the flows have high Reynolds number, the ratio of inertial forces to viscous forces on the length scale of the domain).

This system of equations can be closed by describing how the pressure (p) depends upon the local thermal energy, an equation of state. If we assume the fluid is particulate in nature, and the

particles have no extra energy states (such as rotation and vibration) then the pressure is given by

$$p = (\gamma - 1)\rho u \,, \tag{1.24}$$

where $\gamma = \frac{5}{3}$ and $u = e - \frac{1}{2}v^2$ is the specific thermal energy (whose evolution can be deduced from Eq. (1.22)).

A consequence of the insensitivity of the fluid motion outside of shocks to the viscosity is that it becomes possible to substitute an alternative viscous term into the RHS of Eq. (1.21) and, for a large range of discretisations, obtain the same numerical result. As such it is common to introduce an *artificial viscosity* at a much greater level than physical and with a slightly adjusted term (e.g. the prescription of von Neumann and Richtmyer, 1950) for superior numerical properties.

A notable feature of equations (1.20), (1.21) and (1.22) is that they are all, in the mathematical sense, continuity equations, and as such the total quantity of mass, momentum and energy does not evolve with time. If the discretisation proceeds directly from these then it, too, will completely conserve those quantities and as such be known as a *conservative* scheme. In the remainder of this section, however, we are going to add a number of terms (forces) to the RHS of Eq. (1.21) and (1.22), such as self-gravity, which, whilst they are *possible* to write in a conservative form, in general will not be as they are already sufficiently difficult to calculate in a non-conservative form. Consequently, energy and momentum are not usually precisely conserved except in 'pure-hydro' problems.

Gravity and Cooling

The Newtonian approximation for gravity is usually written in potential form

$$\nabla^2\Phi = 4\pi G\rho \,, \tag{1.25}$$

where G is Newton's constant and for simplicity we assume physical co-ordinates and neglect the expansion terms from Section 1.1. The additional force term to add to Eq. (1.21) is

$$\mathbf{f} = -\rho\nabla\Phi \,, \tag{1.26}$$

and introduces an extra term in the energy calculation in the usual way.

In contrast, an interesting property of equations (1.20), (1.21) and (1.22) is that they are all *local*, i.e. the dynamical equations describing the local quantities such as density and velocity, can all be found in terms of combinations of other local quantities (where we do not include spatial derivatives). This is in fact rather fundamental, and it is currently believed that all the laws of physics operate in this fashion.

This has a direct useful consequence for the simulation of the equations of physics, in that the time evolution of a spatial volume depends only upon its neighbouring volumes. If we apply this to the implementation of the simulation on large computers, we see there is a consequence in terms of *parallelisation*, that in principle data communication only needs to occur between computational units that are evaluating the evolution of spatially connected regions.

Eq. (1.25), however, does not have this local property, i.e. the potential is a function of the global density field. If we were to write it in a local form (the weak field limit of the Einstein field equations), then we could calculate the evolution of the potential in a purely local way (re-introducing the gravity waves that were lost by taking the Newtonian approximation in Eq. 1.25). The reason that this is avoided is that the wave speed of these equations (the rate at which the regions interact) is the speed of light, which is extremely restrictive in terms of our time discretisation (see also section 1.2.2), i.e. it would require very many time steps to perform the same simulation. This difficulty is sidestepped by applying Eq. (1.25), which introduces the computational difficulty of performing a non-local calculation. It is worth noting that this substitution of problems yields a successively smaller relative benefit as our usage of parallel computation increases, since the calculation is often limited by communication.

In mathematical terms we have taken a set of hyperbolic equations (for general relativity) and replaced them with a parabolic equation (the boundary value problem of Eq. (1.25)). This is analogous to the anelastic approximation in meteorology (removing acoustic waves) to find a parabolic equation for pressure, and to most radiation transport schemes.

The evaluation of self-gravity is an extensive subject in itself and is linked closely to the form of discretisation one chooses. The most notable choice is to perform the calculation on a *regular grid*, which allows the use of the Fast Fourier Transform (FFT) algorithm with a scaling of $N \log N$ (where N is the number of cells). It is possible to recover this scaling using trees, but in general the proportionality is much higher, making the regular grid a particularly influential choice, so much so, in fact, that particle schemes (N-body) will often use a hybrid scheme where part of the gravitational field is calculated on a grid, the so-called Particle-Particle Particle-Mesh ($\mathrm{P^3M}$) scheme of Hockney et al. (1973).

We now turn our attention to cooling. The removal of thermal energy can be applied to Eq. (1.22) by the insertion of an additional term on the RHS, i.e.

$$\rho \left.\frac{\mathrm{d}u}{\mathrm{d}t}\right|_{\Lambda} = -\Lambda(T, Z, n)n^2 \,, \tag{1.27}$$

where n is the number density of particles, T the temperature and Z the metallicity. The term n^2 has been factored out such that Λ is constant for a process with pure two-body collisions.

It is possible to go further and relax the constraint of ionisation equilibrium, i.e. to track the temperature of each different species; however, this comes at considerable cost due to the large number of species in enriched gas (see also Section 1.1.3).

As a final remark it may be questioned where all the energy that has been removed by cooling has been transported to. The evolution of the radiation field introduces another hyperbolic equation with a wave speed equal to that of light (similar to gravity), with the additional complication that we are interested in following the waves (i.e. the directional transport of energy). Such is the difficulty of solving this in its full generality that it is nearly always heavily approximated by taking an optically thin or thick regime, solving for moments of the radiation field (e.g. Gnedin and Abel, 2001) or even assuming the radiation field exists as a uniform background. Once the radiation field is known, heating terms can be added to Eq. (1.27) by using the absorption cross-sections of each species.

1.2.2 Discretisation and Advection

In this section we describe how the physical equations from the previous section are discretised into a scheme with a finite number of elements whose evolution can be simulated on a computer. In astrophysics the most common methods are a Lagrangian scheme called Smoothed Particle Hydrodynamics (SPH) and a variable-sized mesh scheme called Adaptive Mesh Refinement (AMR). There is also a very recent Lagrangian scheme known as AREPO (Springel, 2010) which has much in common with AMR, which we will also briefly mention. We describe both the spatial and the temporal discretisation of these along with some of the advantages and disadvantages of each.

Time discretisation

The temporal extent, Δt, of the discretisation used is dependent upon the rate at which information traverses a cell. These wave speeds can be calculated exactly at any given point as the eigenvalues of a matrix of coefficients formed from equations (1.20), (1.21) and (1.22) to find a maximum of $c_s + |\mathbf{v}|$, where c_s is the local sound speed. Approximating this over a cell of minimum width Δx gives the Courant-Friedrichs-Lewy condition (Courant et al., 1928)

$$\Delta t < \eta \frac{\Delta x}{c_s + |\mathbf{v}|}\,, \tag{1.28}$$

where $\eta < 1$ is some proportionality constant weakly dependent on the geometry of the cells, the advection scheme and the specific problem. Violation of this will result in a scheme which is inaccurate and usually highly unstable.

A related question is whether a scheme has a *global* time step or a *local* one, i.e. whether all cells end at the same set of times (a global time step) or whether some are allowed to continue over temporal boundaries (local time steps).

The traditional answer to this question is to use global time steps, since by doing this one is guaranteed to be able to form an explicit scheme, i.e. the future states depend upon the past states, but not the other way around. In problems of very large dynamic range, however, this is extremely inconvenient, and it is desirable to produce schemes where systems with a short dynamical time (e.g. supernova remnants) can be probed without performing a similar number of time increments on the rest of the galaxy. (e.g. GADGET-2, Springel, 2005, ENZO, Bryan and Norman, 1997, RAMSES, Teyssier, 2002).

Lagrangian codes

Lagrangian codes discretise the fluid evolution into regions that move with the local velocity field, and as such they are discretising the mass rather than the volume. This is particularly appealing for astrophysics because the regions of interest (such as galaxies or planets) are also regions where the mass is concentrated, naturally giving a reasonable approximation to the dynamic range of interest.

A secondary advantage is that such a scheme retains the property of Galilean invariance that is held by the equations of the previous section. One benefit of this is the loss of spurious heating of high Mach flows in the rest frame (as for the cells in Lagrangian codes, the fluid is always at rest).

The disadvantage of such ideas, however, is usually the difficulty of following the interfaces, which adjust their shape as the mass elements change location. One very popular scheme that avoids this is Smoothed Particle Hydrodynamics (SPH, Gingold and Monaghan, 1977), which essentially ignores the advection terms, except for shocks, and follows the fluid motion assuming each particle evolves adiabatically in the local density field.

The modern formulation (e.g. Springel and Hernquist, 2002) starts with the observation that for adiabatic flow (i.e. only including the pressure term on RHS of Eq. (1.21)), the Lagrangian derivative

$$\frac{D}{Dt}(p\rho^{-\gamma}) = 0\,, \tag{1.29}$$

indicating that the quantity $p_i\rho_i^{-\gamma}$ stays constant for all particles (this is in fact a function of the entropy, and as such is known as the pseudo-entropy). If we apply the further constraint that the

total energy is conserved

$$E = \sum_i m_i \left(\frac{1}{2} |v_i|^2 + \frac{p_i}{(\gamma - 1)\rho_i} \right) , \tag{1.30}$$

then the adiabatic pressure forces between fluid elements can be computed directly from the differential of the Lagrangian for any differentiable density function, giving the net acceleration of the fluid element,

$$\ddot{\mathbf{x}}_i = \sum_j \frac{m_j}{m_i} \frac{p_j}{\rho_j^2} \frac{\partial}{\partial \mathbf{x}_i} \rho_j \, , \tag{1.31}$$

where ρ_j is the density evaluation for particle j as a function of all the particle positions. Notably this is usually written as two terms by symmetrising about the ith particle. The final element in this scheme is the construction of the density estimate, which is formed using a *smoothing kernel* in the following manner,

$$\rho_i = \sum_j m_j W \left(|\mathbf{x}_i - \mathbf{x}_j|, h_i \right) , \tag{1.32}$$

where W is the smoothing kernel and h is the smoothing length. W needs to be differentiable and approximately normalised (such that $\sum_i m_i/\rho_i$ fills the whole volume, otherwise the densities will be systematically offset) and we would prefer it to be compact so that the calculation of ρ_i only requires a summation over a finite number of particles, known as the neighbours. Consequently W is usually chosen to be a radially symmetric cubic approximation to a Gaussian, although some authors (in particular Read et al., 2010) suggest it may be desirable to have a kernel with radially monotonically increasing gradient (which is thus not continuous at the origin) to avoid any 'clumping' instability.

The use of a variable smoothing length h (i.e. an h_i for each particle depending on the local density) requires some careful handling, since Eq. (1.32) becomes an implicit equation. It is tempting to return this to an explicit equation by setting h_i to be the n-th nearest neighbour of particle i, but this complicates the evaluation of the derivatives in Eq. (1.31) (the so-called grad-h terms of SPH) and introduces discontinuous derivatives (as the order of the neighbours changes), so it is preferable to just set $h_i = K\rho_i^{-1/3}$ and iteratively solve for the solution of Eq. (1.32) and have a straightforward evaluation of the derivatives in Eq. (1.31).

There is an additional subtlety with variable smoothing lengths in that the binary relation of being a *neighbour* is now no longer symmetric, i.e. the i-th particle may be the neighbour of the j-th particle, but not vice-versa. In this case whilst the sum in Eq. (1.32) is still only over the neighbours of particle i, the sum in Eq. (1.31) must be performed over all particles of which i is a neighbour.

These equations completely describe a system of particles whose pressure forces evolve adiabatically. The missing piece(s) of such a scheme all relate to the mixing of matter and energy between the different particles. At its most basic, this is a viscosity term to capture shocks, but should also include particle diffusion (e.g. Balsara, 1995; Price and Monaghan, 2005; Agertz et al., 2007; Read et al., 2010 etc.). We will discuss this more in Chapter 2.

We now briefly discuss an alternative Lagrangian scheme to SPH known as Arepo (Springel, 2010) which in many ways bears a much greater resemblance to the Eulerian schemes of the next subsection. The heart of this scheme is the formal division of the volume into convex cells with planar faces (by the construction of a Voronoi tessellation). Although the centres of these cells move with the fluid, the advection through each face can be computed using the flux calculations of the following section, albeit with the added complication that the faces are changing shape with time (the translation of the faces is relatively easy to account for).

Eulerian (Grid) codes

An Eulerian discretisation of the fluid is one where there is a chosen frame of reference upon which the discretisation is fixed, i.e. the cell boundaries do not move with time. This is generally expanded to include discretisations where cells can be merged/divided as the simulation progresses (so-called adaptive mesh refinement, AMR).

When only a small number of fluid variables are tracked in each cell it is attractive to employ a regular grid, since this removes the need to store or calculate the geometry of each cell. In the simplest case the fluid will be assumed to be uniformly distributed across each cell, but can also vary as some low order polynomial (e.g. the piecewise parabolic mesh scheme of Colella and Woodward, 1984) which are generally less diffusive than the uniform approximation.

The problem of calculating the resultant flow profile from two homogeneous regions separated by a planar boundary is known as the Riemann problem, and its solution is not analytic (although it is straightforward to calculate iteratively to any required precision with the aid of a computer). In the general case the fluid forms 5 regions: the undisturbed left and right fluids, the shocked low pressure fluid and a rarefaction zone where the higher pressure fluid decompresses to match the pressure of the other, where it piles up behind a contact discontinuity. At the shock the conditions are calculated using the integral form of equations (1.20-1.22), i.e. the conservation of mass, momentum and energy, which leads to the Rankine-Hugoniot jump conditions. At the interfaces of the rarefaction zone the entropy is constant (the material expands adiabatically), whilst at the contact discontinuity there is the additional constraint of zero flux across the interface. I calculate an example solution to this in Fig. 1.3. If we remove the condition that the initial fluids are at rest,

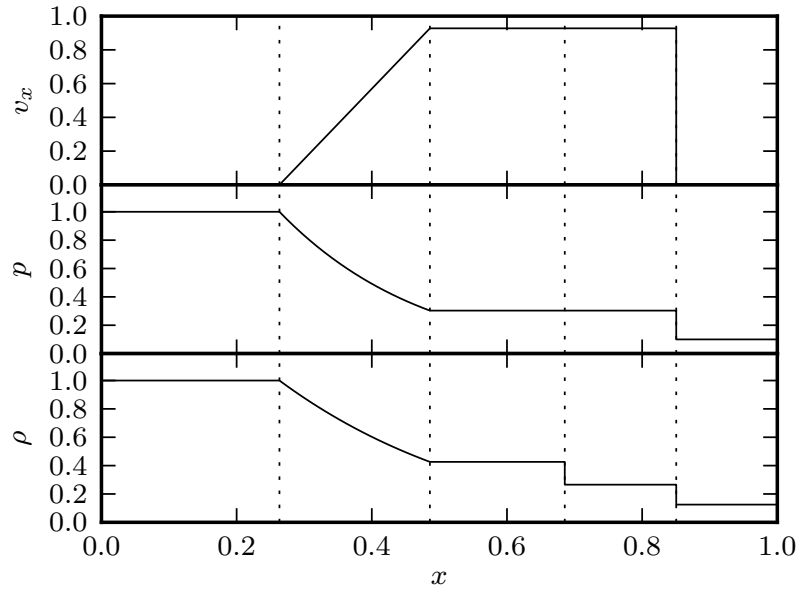

Figure 1.3: Similarity solution for the Sod shock tube test of the Riemann problem. The initial conditions were $\rho = 1.0$,0.125, $p = 1.0$,0.1 on the left and right sides of $x = 0.5$, respectively, with adiabatic index $\gamma = 1.4$. The time shown is $t = 0.2$. The vertical dotted lines indicate the four different interfaces described in the text which are the beginning of the rarefaction, the end of the rarefaction, the contact discontinuity and the shock, from left to right respectively.

as would be done in a hydrodynamics code, there are some additional solutions with a double shock or a double rarefaction zone in the cases where the fluid is converging or diverging.

Due to the non-analytic nature of the Riemann problem, the calculation of the flux between cells is usually estimated with an approximate Riemann solver, such as the Roe solver or variants of the Harten, Lax and van Leer (HLL) solver (Harten et al., 1983, but see also Einfeldt, 1988 and Toro et al., 1994). Since the Riemann problem includes cases which result in a shock wave, these solvers automatically include the treatment of shocks without explicitly including viscosity terms (although in practice many schemes employ a very small amount of viscosity). In the higher order schemes (such as MUSCL, van Leer, 1979 or PPM, Colella and Woodward, 1984) the discontinuity over a shock is problematic in the extrapolation stage, producing characteristic oscillations that must be damped with a slope limiter (sometimes referred to as a flux limiter).

One might also consider whether the use of an Eulerian grid, which by its nature is not Galilean invariant, will manifest a limitation due to this. The equations of motion now have a preferred velocity (the rest frame) and directions (parallel to the axes). In terms of the for-

mer there is a known problem of spurious heating in highly supersonic flows and also the strict timestep limitation implied by Eq. (1.28). In terms of the latter there are a number of issues with the ordering of calculations of fluxes (e.g. x-y-z or z-y-x) and the coupling of these with other forces on the fluid. These are largely resolved with techniques such as Strang splitting (Strang, 1968). However, there is still considerable interest in *unsplit* schemes which have no ordering.

The adaptive mesh variation of Eulerian codes (such as FLASH, Fryxell et al., 2000, RAMSES or ENZO), allow the grid of cells to be recursively subdivided into smaller cells by a factor of two (along each dimension) at each level. Typically, the variation in levels is only allowed to be 1 between adjacent cells, limiting the number of neighbours of a cell to 24 (i.e. 6 faces, each subdivided into 4 cells). FLASH goes a step further, by grouping fixed arrangements of cells into blocks, termed 'block structured AMR'. This hybrid scheme combines some of the advantages of fixed grids such as efficient loops over the regularly ordered cells within a block, with the advantages of adaptive mesh of not having to apply high resolution to all of the simulation domain.

This brings us to the question of the refinement criterion for an AMR scheme. In contrast to the SPH scheme described in the previous section which applies resolution by following mass, in AMR the user has complete freedom to choose a refinement scheme that depends on the local or global properties, constrained by spatial variation of resolution in adjacent volumes described above. The default criterion in FLASH is to let the code estimate the local length scale based on the second derivative of the fluid variables, which is automatically known for each cell for a piecewise parabolic scheme. Notably this will always flag a discontinuity - such as a shock - for refinement, so in practice one has to introduce a maximum refinement level. Alternatively, it is possible to produce a discretisation in approximation to SPH methods by use of a refinement criterion conditioned on mass (i.e. the mass enclosed within a cell).

1.3 Structure of this thesis

In this thesis we explore some of the uses of hydrodynamical codes in astrophysical simulations of galaxies. In Chapter 2 we look at some of the differences between hydrodynamical schemes and construct a test problem for a shock front with cooling. By comparing the analytic solution with the resolution dependent solution found by the codes we are able to estimate an accuracy criterion for astrophysical shocks and cooling functions. We analyse this in a number of cosmologically relevant astrophysical environments such as virial shocks and supernova blast waves to investigate the implications for cosmological simulations of galaxy formation.

In Chapter 3 we turn our investigations to high resolution experiments exploring the genera-

tion of galactic winds in disk galaxies. By simulating very small regions we are able to resolve individual SNe and the subsequent entrainment of gas into a galactic wind. By performing a number of these simulations we are able to investigate the dependence of these outflows upon the disk parameters such as surface density and gas fraction.

In Chapter 4 we extend some of this work by analysing the implications of these fits on galaxy formation models. We consider both analytic formulations of galaxy formation and observed constraints (in particular the luminosity-velocity width relation, Tully and Fisher, 1977) to derive two possible scalings for the strength of feedback upon galaxy rotation velocity. These schemes are interesting both for hydrodynamical simulations (where stellar feedback is imposed in a 'sub-grid' model) and for phenomenological models of hierarchical galaxy growth (so called semi-analytic models) where the outflows are set with a direct prescription.

In Chapter 5 we add an additional ingredient to our simulations by including the metal enrichment by SNe. By tracing the metal ejection from galaxies we are able, along with some analytic arguments, to draw conclusions about the mass-metallicity relationship of galaxies. Each chapter in this thesis is intended to stand alone; however, Chapter 6 makes some concluding points and outlines directions for future research.

Chapter 2

Numerical overcooling in shocks

2.1 Introduction

Radiative cooling and shocks are two important ingredients in galaxy formation theory (White and Rees, 1978b). Whilst most codes used in astrophysics have facilities for handling both of these, the scales at which these operate and interact are challenging. We will start with a short tour of the processes and of the numerical codes we will use to simulate them. We describe a 1-dimensional model problem of a radiatively cooling shock with an analytic solution which we model with two popular codes in astrophysical simulations, FLASH (Fryxell et al., 2000) an adaptive mesh refinement (AMR) code, and GADGET (Springel, 2005), a smoothed particle hydrodynamics code (SPH; Gingold and Monaghan, 1977; Lucy, 1977). The results of our simulations give appropriate criteria with which we can analyse the efficacy of our numerical schemes in a wide variety of astrophysical environments. We also investigate the mitigating factors such as the ratio of the cooling to dynamical times, which may enable a simulation to give approximately correct results when otherwise we would consider there to be insufficient resolution.

There has been considerable discussion of the treatment of discontinuities in SPH (Price, 2008; Read et al., 2010), motivated by problems illustrated by Agertz et al. (2007), but the issues highlighted in here are of a different nature. Those papers focus on spurious forces introduced by the SPH scheme whilst we focus on evaluating the errors introduced as we approach the resolution limit, which are to some extent unavoidable.

2.1.1 Astrophysical shocks

The science of astrophysics is an ideal domain for the investigation of shock fronts on a variety of scales. Stellar winds form shocks as they push in to the interstellar medium. On larger scales SNe form very high Mach number shocks as they plough into the surrounding gas and form remnants. On larger scales still, galactic winds, driven by starbursts and active galactic nuclei (AGN), shock

against the inter galactic medium (IGM). In the context of galaxy formation we can also consider accretion shocks, where gravitationally accelerated infalling gas shocks to form a hot corona in the dark matter potential well.

Of particular interest to us in this chapter are radiatively cooling shocks. To an extent, all the aforementioned shocks have radiative cooling, however the cosmological accretion shocks and SNe are particularly topical. In galaxy formation simulations the SNe at early times form remnants well below the resolution of current simulations and need to be modelled with subgrid physics (see Kay et al., 2002 for a review of feedback methods). The cooling of the hot gas causes a transition from a thermally-driven to a momentum-driven phase, losing a significant fraction of the SNe energy. A similar transition is thought to occur in the thermal to momentum transition of winds powered by an AGN (Booth and Schaye, 2009).

Cooling in accretion shocks may affect the fuelling of star formation in the host galaxy. If the gas is shocked to too high a temperature it will not cool over a Hubble time, preventing star formation (though non-spherical geometries may allow the gas to compress first and thus cool faster, see e.g. Birnboim and Dekel, 2003). In a cosmological simulation, however, the resolution around these cooling regions may be so coarse as to resolve these cooling regions with only a few particles. In this chapter we intend to probe the effect of limited numerical resolution in these cases, and how these may affect the outcome of the simulation.

2.1.2 Physical shock fronts

Before we concentrate on the numerical aspect of cooling in shocks, we begin by briefly considering the processes that occur in a real physical shock front. A shock front is a region where one of the usually conserved fluid properties, entropy, is allowed to change. It is worth considering why such a property is otherwise treated as a constant, and why shocks are a special case.

In the kinetic theory of gases, a gas is described as a large number of particles (e.g. atoms, molecules, ions) in constant random motion. The frequency of collisions defines a timescale, and also a typical length between collisions, the mean free path. If all processes acting on the gas happen on timescales much greater than the time between collisions, then the classical theory of adiabatics tells us that there will be another conserved property which, for an ideal gas, is p/ρ^{γ}. Here, p, ρ and γ are the pressure, density and adiabatic index, respectively. This property is a function of the entropy, and in astrophysics is often used as a proxy.

It is worth recalling that processes which change the fluid entropy (e.g. shocks, radiative absorption, thermal conduction) will occur on timescales on the order of, or shorter than, the period between collisions (or over lengths on the order of the collision length). Mechanisms

which heat the gas on slower time scales will be *adiabatic* processes, and will alter the thermal energy with only very small increases in entropy[1].

Now we come to shock fronts. A canonical example of a shock front would be a 1 dimensional system where the upstream fluid travels supersonically with respect to the down wind fluid (i.e faster than the thermal velocities of the particles), until it reaches the shock, where the majority of its mechanical energy (the bulk motion of the particles) is converted into thermal energy. This happens because the pairs of particles that collide can have very different velocities: particles in the shock front change their energy on a timescale on the order of the collision time between a pair of up and down wind particles, which is much shorter than that between two down wind, or two upwind, particles. From this description we immediately see that physical shocks must occur over length scales on the order of the mean free path, which is usually much smaller than other physical length scales in the problem.

The mean free path (Δx) depends upon the number density of particles (n) and their collisional cross section (σ), as

$$\Delta x = \frac{1}{n\sigma}\,. \tag{2.1}$$

In the case of a partially or fully ionized gas, particles may interact on a shorter length scale (Zel'Dovich and Raizer, 1967), that of the plasma skin depth/plasma oscillation length

$$\Delta x = c\left(\frac{4\pi n_e e^2}{m_e}\right)^{-1/2} \approx 10^6 \left(\frac{n_e}{1\,\mathrm{cm}^{-3}}\right)^{-1/2} \mathrm{cm}\,. \tag{2.2}$$

Since the particles are not interacting via Coulomb collisions this is known as a 'collisionless shock'; the mechanism of interaction is the plasma oscillation (coupling together charged particles). Care must be taken, however, as the post-shock gas may be out of thermal and ionizational equilibrium for the problem in question (something that would not be a concern if the collision length is small), making these cases challenging to simulate.

The trapping of relativistic ions between magnetic fields in the up and down-stream phases and subsequent acceleration is also believed to be the origin of the power law spectrum of high-energy cosmic rays, a Fermi acceleration process.

Finally, we should complete this discussion by mentioning turbulence as a source of entropy. In general the bulk oscillations of fluids will occur on scales much larger than the mean free path and is thus unable to change the entropy. Transfer of spectral energy to shorter wavelengths,

[1] One can of course construct systems in which the time scale of interest is long enough such that viscosity, thermal diffusion, etc. dominate the large scales too. These problems, however, have low Reynolds and Péclet numbers respectively, and are the exception rather than the norm in computational astrophysics

however, implies that eventually bulk oscillations reach the scale of the mean free path and will be dissipated into thermal energy (Kolmogorov, 1941).

2.1.3 Shocks in simulations, artificial viscosity

Now let us consider shocks in simulations. Almost exclusively, the resolution of simulations will be much coarser than a physical shock width. This is not necessarily a problem, however, as the bulk properties of the post-shock gas may be deduced from the conservation of energy and momentum, and the assumption that the shock process does not produce oscillations on scales much larger than the mean free path.

In this chapter we will contrast two schemes for numerical hydrodynamics that are popular in cosmology: SPH and AMR. Smoothed Particle Hydrodynamics (SPH; Gingold and Monaghan (1977); Lucy (1977), see Monaghan (2005) and Springel (2005) for recent reviews) is a (pseudo) Lagrangian scheme in which the fluid is represented by a set of particles that move along with the flow. In this chapter we will illustrate the behaviour of SPH using the GADGET SPH implementation of Springel (2005). Adaptive Mesh Refinement (AMR) follows how fluid flows across a (stationary) computational mesh, whose cell size may be locally 'refined' or 'de-refined' based on some criterion. In this chapter we use the FLASH code, a block-structured AMR implementation by Fryxell et al. (2000).

The physical process of kinetic energy dissipation by particle collisions is represented in the continuum approximation by a viscous term in the Navier-Stokes equations,

$$\frac{\partial}{\partial t}(\rho v_i) + \frac{\partial}{\partial x_j}(\rho v_i v_j) = -\frac{\partial p}{\partial x_i} + \frac{\partial}{\partial x_j}\sigma_{ij}\,, \tag{2.3}$$

where

$$\sigma_{ij} = \eta\left(\frac{\partial v_i}{\partial x_j} + \frac{\partial v_j}{\partial x_i} - \frac{2}{3}\frac{\partial v_k}{\partial x_k}\delta_{ij}\right) + \zeta\frac{\partial v_k}{\partial x_k}\delta_{ij}\,, \tag{2.4}$$

is the viscous stress tensor and η and ζ are known as the shear and bulk viscosity coefficients, respectively. These coefficients can be measured for real fluids, however in most astrophysical flows they are so small that the viscous term is insignificant outside of shocks (i.e. the flows have high Reynolds number).

The variant of SPH used in this chapter handles shocks with a prescription known as artificial viscosity (although Godunov type methods for SPH also exist, see Inutsuka, 1994). Artificial viscosity was originally developed for grid codes (von Neumann and Richtmyer, 1950), and use the bulk viscosity term in Eq. (2.3), however, with the coefficient raised by several orders of magnitude. These larger values prevent the shocks generating large unphysical oscillations due to the coarseness of the sampling (see the numerical stability criterion of Friedrichs and Lax,

1971). In SPH they also fulfil a second role of preventing particle interpenetration (see Bate, 1995 for a thorough discussion). A number of artificial viscosity prescriptions are in use, the most common being that of Monaghan & Balsara (Balsara, 1995), a Lax-Friedrichs style viscosity that is turned on for compressing flows. The implementation in our version of Gadget is based on signal velocities (Monaghan, 1997).

In mesh codes shocks can be treated with artificial viscosity but more commonly a conservative Riemann solver (based upon Godunov's scheme, Godunov and Ryabenki 1964) is used. Riemann solvers (see e.g the HLL solver, Harten et al., 1983) give exact solutions in 1d or planar shock problems with homogeneous pre- and post-shock fluids, but are somewhat diffusive in other cases. They are still the preferred method for grid codes, however, and the default used in FLASH is a directionally split Riemann solver (Colella and Woodward, 1984). Oscillations near the discontinuities are controlled with a monotonicity constraint.

2.1.4 Radiative cooling

Radiative cooling is an essential ingredient in galaxy formation as it is the process which allows the baryons in dark matter halos to dissipate thermal energy and thus collapse to form galaxies. Multiple cooling mechanisms are important in the astrophysical domain, however in this chapter we will primarily be interested in collisional line cooling and at higher temperatures, thermal bremsstrahlung. The evolution of the specific thermal energy, u, due to cooling can be written as

$$\rho \dot{u}|_{\Lambda} = -\Lambda(T; Z) n^2 \,, \tag{2.5}$$

where ρ is the density, T the temperature, Z the metallicity and n the particle number density (for brevity we will subsequently refer to the radiative component of the specific cooling rate $\dot{u}|_{\Lambda}$ as $\dot{u}_{\Lambda}$). When baryon-photon interactions with the CMB and an ionizing background are important we have followed the prescriptions of Wiersma et al. (2009a) (see also Fig. 2.7, below).

The implementation of cooling in our versions of GADGET and FLASH is performed by an adaptive time step integration over each cell/particle. The effects of cooling are included in the hydrodynamic solver by *operator-splitting*, i.e. the separation of the two processes A (radiative cooling), and B (shock heating) into individual steps,

$$\dot{X} = (A + B)\, X \tag{2.6}$$

$$X_{t+\Delta t} - X_t \approx A(\Delta t) B(\Delta t) X \,, \tag{2.7}$$

where the errors on the latter term on the order of the time step Δt depend upon the commutator $[A, B]$. Since the physical process of shock heating should occur over a much shorter time scale

than that of radiative cooling we can justify this being zero. The numerical implementation of shock heating will of course take a longer time scale and thus would interact with the cooling if operator splitting was not introduced, however there is no physical motivation to prefer such a scheme in this case.

2.2 Radiatively Cooling shocks, a model problem

A typical test problem in numerical hydrodynamics is that of the formation of a 1-dimensional shock in a 'test tube'. In one form of this problem a tube is initialised with gas of constant polytropic index γ, the left and right halves converging with opposing velocities v_0 and $-v_0$. For a sufficiently high velocity v_0 a shock will form, creating a downstream region with higher temperature, pressure and density. This problem has a similarity solution for constant γ. In our set-up the gas is allowed to cool radiatively, and the downstream region can then cool to form a dense post-shock region. The initial conditions are thus

$$\rho(x, t_0) = \rho_0 \tag{2.8}$$

$$p(x, t_0) = p_0 \tag{2.9}$$

$$T(x, t_0) = T_0 \tag{2.10}$$

$$v(x, t_0) = \begin{cases} v_0, & x < 0 \\ -v_0, & x > 0 \end{cases} \tag{2.11}$$

We note that the symmetry of this problem makes it equivalent to the wall shock (where there is an immovable boundary at $x = 0$, Monaghan 1997). In order to minimise the amount of modification in our SPH code we chose to set up the symmetric problem rather than implement an immovable boundary.

2.2.1 Similarity solution for a radiative 1D shock

If the temperature dependence of the cooling rate is sufficiently simple, then this 1 dimensional shock problem has a similarity solution even in the presence of cooling. Such is the case for a cooling function which is a piecewise linear function of the temperature, such that the rate of radiative cooling, $\dot{u}|_\Lambda$, of the specific energy u, is given by a 'cooling spike' :

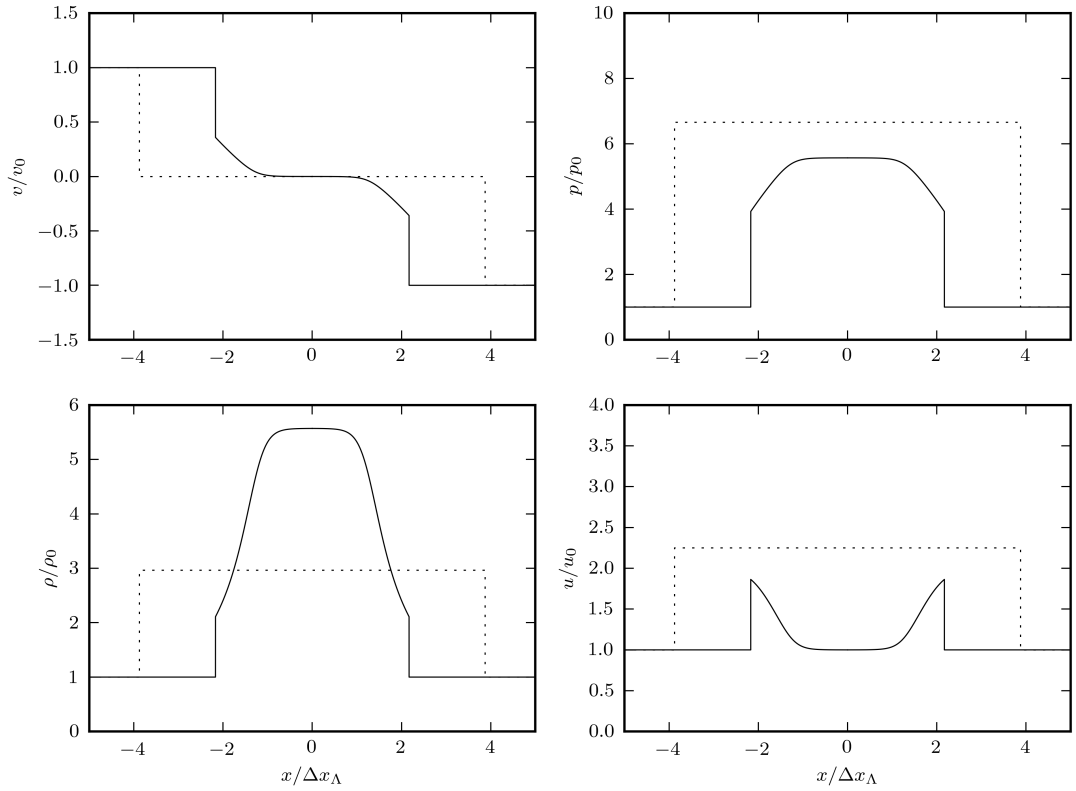

Figure 2.1: *Solid lines* represent the analytic solution for the colliding gas problem discussed in Section 2.2 when cooling is included. Incoming gas from the left and right shocks and then compresses and cools to form a cold dense region in the centre. For the example shown, the Mach number of the upstream gas is 1.5 w.r.t. the cold, central gas and the time is $5.1\,\Delta x_\Lambda/c_0$ (see Eq. (2.17)). For comparison, *dashed lines* show the solution without cooling at the corresponding time. At early times (i.e. $t \lesssim \Delta x_\Lambda/c_0$) the cooling profile is not of given form, as it has not had sufficient time to reach a stationary state (details of the similarity solution for cooling through a shock can be found in appendix A).

$$\rho\dot{u}|_\Lambda = \begin{cases} 0, & T < T_0 \\ -\Lambda n^2 (T - T_0)/T_0, & T_0 \leq T \leq \frac{1}{2}(T_1 + T_0) \\ -\Lambda n^2 (T_1 - T)/T_0, & \frac{1}{2}(T_1 + T_0) \leq T \leq T_1 \\ 0, & T_1 \leq T \end{cases} \tag{2.12}$$

where Λ is a positive constant and cooling is maximum at $T = \frac{1}{2}(T_1 + T_0)$. For simplicity, in all simulations discussed below we initialise the temperature to T_0 (where the cooling vanishes), so the initial gas is not cooling.

The gas is chosen to be pure atomic hydrogen, i.e.

$$\gamma = \frac{5}{3} \tag{2.13}$$

$$\rho = m_p n \tag{2.14}$$

$$p = n k_B T\,. \tag{2.15}$$

For comparison the reader should see the simulations of Hutchings and Thomas (2000) who used a more realistic astrophysical cooling function, at the expense of not having an analytic solution. For the cooling post-shock region we find analytic solutions in a similarity variable $\lambda \equiv \rho/\rho_0$ of the form (see Appendix A for details)

$$\begin{aligned} T/T_0 &= ((a+1)\lambda^{-1} - a\lambda^{-2}) \\ x - x_0 &= \frac{-v_s k_B T_0}{(\gamma - 1)\Lambda n_0} \left[\frac{\gamma - a}{a - 1} \log(1 - \lambda^{-1}) + \right. \\ &\quad \frac{1 - a\gamma}{(a-1)a^2} \log(1 - a\lambda^{-1}) \\ &\quad \left. - \frac{a+1}{a}\lambda^{-1} - \frac{\gamma + 1}{2}\lambda^{-2} \right] \\ a &\equiv \frac{\rho_0 v_s^2}{p_0}. \end{aligned}$$

The value of the shock velocity v_s and the final density in the cold, post-shock region ρ_0 can be found by imposing conservation of mass and momentum (see Appendix A.2). The solution is shown in Figure 2.1.

2.2.2 Shock stability

Chevalier and Imamura (1982) find that positive increasing linear cooling functions produce stable shocks. Applying this to the cooling function in Eq. (2.12) we see that we have stable shocks provided the post shock temperature $T_s < \frac{1}{2}(T_1 + T_0)$ or $T_s > T_1$, which is the case for all the

shocks we study later (we define the shock temperature T_s as the temperature immediately after the shock, which is computed in Appendix A.2). If the gas is shocked to $\frac{1}{2}(T_1 + T_0) < T_s < T_1$ then the shock may be unstable as the cooling function has a negative slope, $\partial_T \left(-\rho \dot{u}_\Lambda\right) < 0$. Intuitively this can be understood in terms of the length of the cooling region: if the length increases the shock velocity will be higher, causing the post shock gas to be hotter, which increases the cooling time, which feeds back into a longer cooling region.

2.2.3 Numerical solution

Initial conditions

The similarity solution is described with two (dimensionless) parameters. The first is the ratio of the upper to the lower temperature in the cooling spike, which we will set to 20, i.e. $T_1 = 20T_0$. This is motivated by the temperature dependence of the radiative cooling function of an astrophysical plasma (see also Fig. 2.7), where individual elements contribute significantly to the cooling over approximately a 1 dex range in temperature.

The second parameter is the Mach number of the shock, which we will quote in the rest frame of the problem (rather than the rest-frame of the post-shock gas, for example),

$$\mathcal{M} \equiv \frac{v_0}{c_0}\,, \tag{2.16}$$

where $c_0 \equiv (\gamma p_0/\rho_0)^{1/2}$ is the upstream sound speed. Our tests are performed at $\mathcal{M} = 4.70$ and $\mathcal{M} = 6.04$. The former has been chosen such that the shock reaches a temperature somewhat below the maximum of the cooling function, $(T_1 + T_0)/2$ (where the shock will be stable) and the latter such that the shock reaches a temperature somewhat above T_1 (where there is no cooling).

We plot positions in units of the cooling length,

$$\Delta x_\Lambda \equiv \frac{k_B T_0 c_0}{\Lambda n_0}\,. \tag{2.17}$$

Similarly we express times in units of $\Delta x_\Lambda / c_0$. As observed in Monaghan (1997), numerical schemes (including both SPH and AMR) usually produce a transient unphysical thermal bump at $t = 0$ when there is no post-shock region. To avoid contamination by this transient we run our simulation for a time $14.2\Delta x_\Lambda/c_0$ and $7.1\Delta x_\Lambda/c_0$ for the $\mathcal{M} = 4.7, 6.04$ shocks respectively (i.e. we simulate for several sound crossing times of the cooling region, to make sure it is in a stationary state).

For our SPH simulations we set up a long box, periodic along all boundaries. The particle mass is chosen to be

$$m_{\rm SPH} = \rho_0 \cdot (0.3\Delta x_\Lambda)^3\,, \tag{2.18}$$

(i.e a mean inter-particle spacing of $0.3\Delta x_\Lambda$). We note that this setup creates a rarefaction wave that propagates inwards from the far edges of the computational volume (due to the discontinuity on this boundary), and thus we need a box long enough such that these rarefactions do not reach our domain of interest in the simulation time. The particles were set up with a 'glass' distribution (White, 1994) to minimise relaxation effects in the pre-shock fluid (the SPH kernel allows a cubic lattice arrangement of particles to slightly reduce its density, and hence release some thermal energy, by relaxing to a glass like state). We also raised the level of the bulk artificial viscosity constant, α, to 3 (from 1, see Springel 2005 for a complete description of the artificial viscosity prescription). We found this to be necessary to prevent ringing and the appearance of large scatter in the entropy of SPH particles in the post-shock region (see also Abel 2011).

For the AMR simulations we again set up a long box with cell spacing $0.3\Delta x_\Lambda$, with periodic boundaries in the y and z directions and inflowing gas along the (long) x axis. No refinement was allowed, effectively making this a uniform Eulerian mesh.

We considered allowing an alternative refinement criterion, however the standard FLASH refinement schemes will refine a shock to the maximum allowed level (since it contains a discontinuity), reducing it to the uniform mesh case. We refer the reader to the dashed lines in Figs. 2.2 & 2.4 to compare resolutions.

We note that the use of inflowing boundary conditions in FLASH allowed us to avoid the rarefaction waves we created in SPH, and thus we could use a much shorter box (by a factor 10). To set the scene we begin by looking at shocks in the absence of cooling.

Test without cooling

The test problems in the absence of cooling are compared in the left panel of Fig. 2.2 and the upper panel of Fig. 2.4 ($\mathcal{M} = 4.7, 6.04$ respectively). Provided we use the higher than usual value of the artificial viscosity ($\alpha = 3$) in GADGET, both the SPH and AMR codes handle this shock well (as expected), with the shock smeared out over a few times the resolution length h in SPH, and a few cells in FLASH. At GADGET's default value for the artificial viscosity ($\alpha = 1$) we find that this is too high a Mach number shock to be handled (we do however return to the original value when we study the lower Mach number shocks in section 2.3). In Fig. 2.3 we tested both altering the value of the artificial viscosity and adjusting the maximum time step (between GADGET's default adaptive scheme and a global minimum Courant step applied to all particles). The higher value of artificial viscosity was found to significantly reduce the scatter in the post shock thermal energies, superior to a reduction in the global time step. We would, however, expect that at very high Mach number shocks a more conservative time step would be required. The small offset of

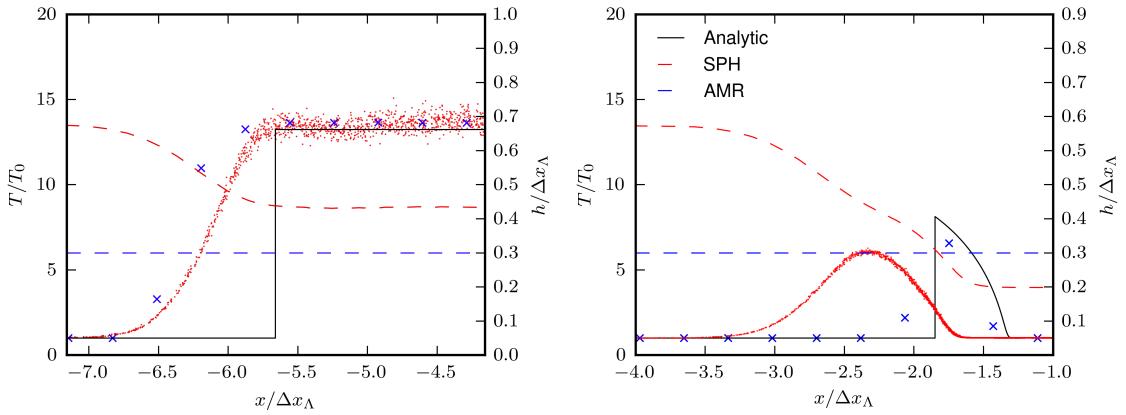

Figure 2.2: *Left panel* plots the temperature in a Mach $\mathcal{M} = 4.7$ shock without cooling. Each *blue cross* represents a column of FLASH cells (the tube is orthogonal to the mesh), each *red point* represents a GADGET particle, the *black line* is the analytic solution. *Red dashes* denote the smoothing lengths of the GADGET particles, *blue dashes* the separation of FLASH cells (right axes). Incoming gas from the left (and right, not shown) collides to form a homogeneous hot, rarefied region in the centre. As expected, both codes reproduce the correct profile relatively well. The shock is seen to be spread over several cells (FLASH) or smoothing lengths (GADGET). *Right panel* as for left panel but including cooling. The analytic solution shows that the gas shocks to a lower temperature (due to the smaller difference between the incoming gas velocity and the shock velocity), followed by a 'cooling tail'in the post-shock region. When simulated using GADGET SPH particles shock in several steps before reaching their maximum temperature. As they do so, particles cool to some extent in the smoothed shock and hence reach a lower maximum temperature than the analytic solution (the SPH shock is also offset to the left of the analytic shock). In the FLASH run gas gets shocked to higher temperatures, closer to the analytic solution. Note that as the gas gets compressed the downstream SPH smoothing length is smaller than the FLASH cell size.

the edge of the shock in both codes is due to a transitory effect at the start of simulation (noted also by Monaghan, 1997)

Test with cooling

First let us consider the case of cooling for the $\mathcal{M} = 4.7$ shock. This should result in a gas temperature of less than $(T_1 + T_0)/2$, i.e. we are on the left side of the cooling spike. The initial

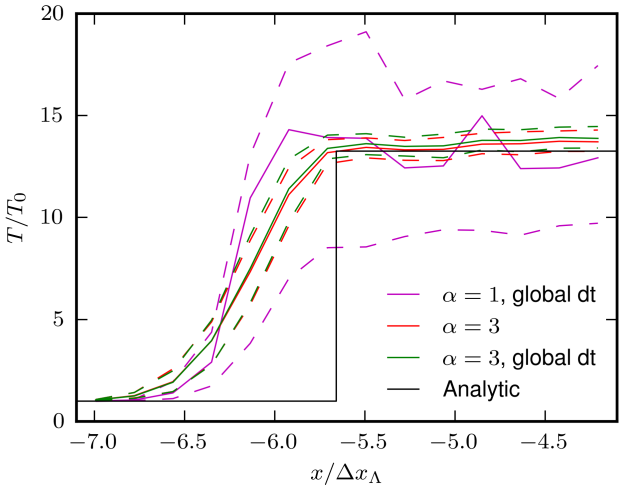

Figure 2.3: Comparison of the effects of altering the viscosity and timestep on the shock from the upper panel of Fig. 2.2. *Red lines* show the higher viscosity ($\alpha = 3$) scheme with adaptive time steps, *green lines* the same viscosity but a global minimum timestep (set to the minimum Courant step of all particles) and *purple lines* the global minimum timestep but with the default viscosity ($\alpha = 1$), *black line* the analytic solution. *Dashed lines* show the 10th and 90th percentiles.

collision of gas can result in higher temperatures and follows an evolution for which we have no analytic solution, before settling down to our stationary case.

In Fig 2.2 (right panel) we see the FLASH and GADGET representations of these shocks. Both codes reach a maximum temperature which is lower than that of the similarity solution. In SPH we attribute this to 'pre-shocking' , i.e particles will shock in several stages and cool as they are being shocked. In FLASH we attribute this to the cooling operation being applied after the hydrodynamics in a time step, such that we do not record the post-shock temperature. Neither GADGET nor FLASH has the resolution to reproduce the cooling tail particularly well here, although the final cold state is achieved in both cases.

For our second cooling test we look at a more extreme case, $\mathcal{M} = 6.04$. This shocks the gas up to a temperature $T > T_1$ from which it cannot cool, hence the analytic solution is the same as for a shock without cooling. In Fig. 2.4 we show the left hand side of the shocked regions. Here the FLASH simulation reproduces the analytic result very well, but the GADGET simulation suffers from much more severe numerical overcooling through the pre-shock region, which prevents the gas from reaching the temperature from which it is unable to cool (due to our choice of $\Lambda(T)$). As a result we see pile-up of high density cold gas around $x = 0$, and the shocked region is left

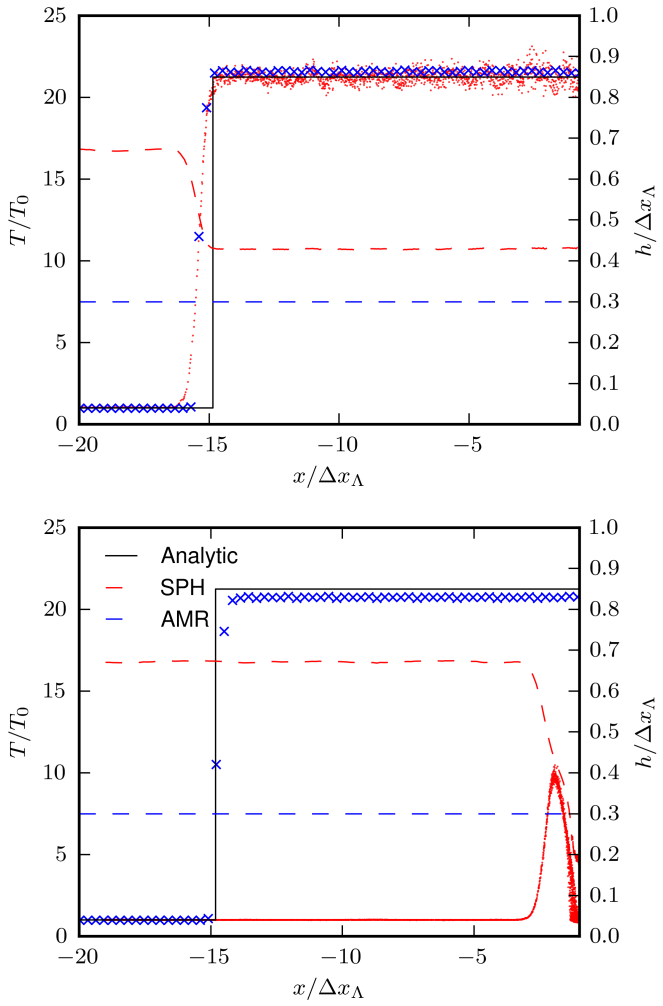

Figure 2.4: As for Fig. 2.2 but for an $\mathcal{M} = 6.04$ shock. *Upper panel* shows the case without cooling, with a higher post-shock temperature than Fig. 2.2. *Lower panel*, the case with cooling. Here the SPH particles shock over several smoothing lengths, allowing them time to cool. Unfortunately, this means they never reach the higher temperature where cooling vanishes and their temperatures decline to the pre-shock value, forming a cold dense region similar that in Fig. 2.2. The shift of the position of the shock front is due to the conservation of mass; cooling allows the post-shock gas to be compressed down to a small region around $x = 0$. We note here that FLASH adequately captures the post-shock temperature even when cooling is included.

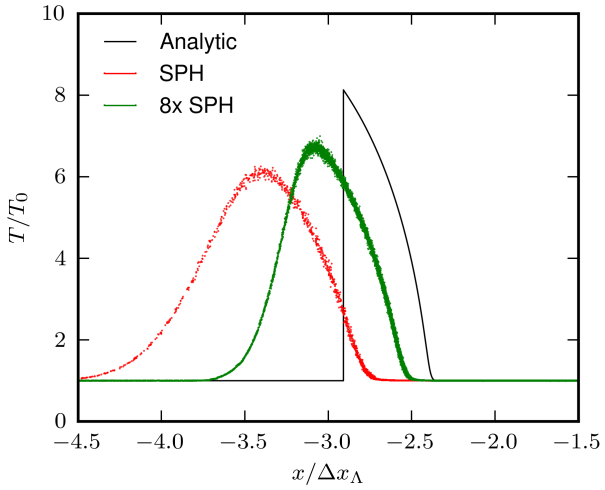

Figure 2.5: As for the lower panel of Fig. 2.2, but for two different SPH particle resolutions:*red points* are the SPH particles as for the lower panel of Fig. 2.2, whereas *green points* are for a $2\times$ better resolution run (i.e. a factor of 8 times more particles). The lower resolution run reproduces the temperature peak to within 25%, for the higher it is around 15%. When the simulation is close to convergence, we would expect $\Delta T \propto \Delta u \propto h$, the smoothing length, i.e to get within 1% of the temperature we would need a factor of $\sim 10^4$ more particles (compared to the lower resolution run). At higher resolutions the offset between the exact and simulated shock fronts is also reduced.

far behind that of the FLASH run[2]. As a result of this overcooling the SPH simulation fails to form any hot gas at all. We note, however, that this is a general problem and not specific to either GADGET or SPH.

2.2.4 Convergence study for GADGET results

As it stands, we can be confident that the results we have just given for SPH are not converged, as they have failed to reach our stable analytic solution. The problem we have attempted to solve involves no elements that an SPH code would not be expected to handle in the limit where the SPH resolution length $h \to 0$, and using a good prescription for artificial viscosity. The outstanding question here is thus only one of how much resolution is required; to this end we

[2]Note that if cooling is prevented, the shock speed will be much higher relative to the rest frame. This is easily understood in terms of conservation of mass, the gas is shocked to a lower density and a much larger region is required to contain it.

re-ran the $\mathcal{M} = 4.7$ simulation with a factor of 8 increase in the particle count[3] (from $\approx 80,000$ to $\approx 660,000$). Let us first, however, make some general remarks about the problem.

Given the maximum temperature, T_s, of the radiating shock we can estimate the error ΔT of the SPH maximum temperature by estimating the radiative cooling over the shock (the physical shock is non-adiabatic and so occurs on timescales many orders of magnitude shorter than that of the cooling, as discussed in the Introduction). Assuming the width of the SPH shock is $\sim h$, the temperature difference will be given, to first order, by

$$\frac{\Delta T}{T_0} \sim \frac{h}{v_0 k_B T_0} \cdot m_p \left|\dot{u}_\Lambda(T_s)\right| \sim \frac{h}{\Delta x_\Lambda}\,, \tag{2.19}$$

where we have assumed that all the mechanical energy has been converted into thermal energy, and that $T_s \gg T_0$. For larger smoothing lengths we expect ΔT to become sub-linear in the smoothing length, since the cooling is weaker at lower temperatures (assuming we are on the left hand side of the 'cooling spike').

If we apply this argument to Figure 2.5 we see that increasing the number of particles by a factor of ~ 8 (i.e. reducing h by a factor of 2) reduces the temperature error by a factor of ~ 1.5, suggesting that we are not quite in the linear regime. To reach a temperature within 1% of the analytic temperature would seem to require increasing the particle count by a factor of $\sim 10^4$. Although this is (barely) possible for this particular case, such resolution is not feasible in cosmological calculations. Most shocks in cosmological simulations will occur at lower resolution than we have used in this test case, therefore it may be necessary to seek an alternative solution involving a switch to prevent cooling during the shock process. We intend to explore such a switch in future work.

2.3 A resolution criterion for radiative shocks

Having established the difficulty of modelling some shock problems with radiative cooling we now wish to obtain a criterion against which we can judge simulations. Such a tool will allow us to identify those simulations where resolution is not a problem and those where more care is required. In the following section we will discuss the effects of resolution in quite a general way before deriving a metric from a simple model problem. We will frame our discussion in terms of SPH, however there will be analogous arguments for mesh codes.

[3] One can, of course, successively reduce the width of the shock tube in a 3d simulation to achieve the same scaling as a 1d one, i.e. $h \propto N_{\rm SPH}^{-1}$. In an astrophysical simulation, however, this option is usually unavailable as the shock will be embedded in an environment which needs to be simulated in full 3d.

Let us take a general case of a numerical simulation of a radiative shock. We assume we have pre-shock gas with velocity, specific internal energy and density v, u, ρ which passes through a shock and comes to rest (v is the velocity of the incoming gas with respect to that of the post-shock gas). First we note that the SPH shock has a width which is some multiple of the smoothing length $h \propto (m_{\rm SPH}/\rho)^{1/3}$ (for a mesh this would be the width of a cell), where the numerical factor will include some dependence on the artificial viscosity prescription. The change in thermal energy will be $\Delta u \propto v^2$ by energy conservation, and thus we can define a rate of 'shock-heating',

$$\dot{u}|_{shock} = \Delta u/\Delta t \tag{2.20}$$

$$= kv^3(\frac{m_{\rm SPH}}{4\pi\rho/3})^{-1/3}\,, \tag{2.21}$$

where k is some constant depending upon the details of the SPH scheme used (e.g neighbour counts). This heating rate is entirely numerical, as can be seen by the presence of the SPH particle mass $m_{\rm SPH}$: in the continuum approximation of the underlying fluid equations the shock heats the gas instantaneously, hence the heating rate is singular. As we reduce the particle mass, h decreases and the numerical rate at which particles are heated over the shock front increases.

By taking the ratio of the physical rate of gas cooling to the numerical rate at which the gas is shock heated (which, ideally, we would wish to be almost infinite) we can analyse the effects of shock resolution. Only if the absolute value of this dimensionless ratio is small do we expect the shock heating to overwhelm the cooling, i.e. we require

$$|\dot{u}_\Lambda|\frac{1}{c^3\,\mathcal{M}^3}\left(\frac{m_{\rm SPH}}{\rho}\right)^{1/3} < \eta_{\rm SPH}\,, \tag{2.22}$$

for the numerical solution to achieve close to the correct post-shock temperature, where η is a dimensionless parameter. Here we have written the velocity of the incoming gas as $v = \mathcal{M}c$ in terms of the Mach number and the upstream sound speed, $c \equiv c_0$. The equivalent for a mesh code can be written with the side length h of a cubic mesh cell written in terms of the mass enclosed, $m_{\rm AMR} = \rho h^3$, to give

$$|\dot{u}_\Lambda|\frac{1}{c^3\,\mathcal{M}^3}\left(\frac{m_{\rm AMR}}{\rho}\right)^{1/3} < \eta_{\rm AMR}\,. \tag{2.23}$$

In the subsequent section we attempt to determine a reasonable value of η which we can use to evaluate other simulations.

2.3.1 Heaviside cooling function

To achieve an extremely simple radiative shock we set up a wall shock (see section 2.2) with a low Mach number $\mathcal{M} = 2$ and the piecewise cooling function

$$\dot{u}_\Lambda = \left(\frac{u_0^{3/2}}{\Delta x_0}\right) \cdot \begin{cases} 0, & u \leq u_0 \\ -\tilde{\Lambda}\left(\frac{\rho}{\rho_0}\right), & u_0 < u \end{cases} \tag{2.24}$$

where $\Delta x_0 \equiv (m_{\rm SPH}/\rho_0)^{1/3}$ is the initial inter-particle spacing, $\tilde{\Lambda} > 0$ a dimensionless cooling parameter, u_0 the initial specific internal energy and as in Section 2.2 we use $\gamma = 5/3$. In the SPH simulation the particles are initially arranged on a cubic lattice of dimensions $1024 \times 8 \times 8$ in units of Δx_0 (1024 referring to the long x direction). The simulations were all performed with periodic boundary conditions. Usually a cooling function would be independent of the inter-particle spacing, however we chose to re-use our initial conditions whilst adjusting the dimensionless constant $\tilde{\Lambda}$, and in this way scale the LHS of Eq. 2.22. This is equivalent to using a fixed cooling function but adjusting the inter-particle spacing.

We now make a couple of observations. Firstly, we note that we can calculate the instantaneous post-shock state using the equations derived in Appendix A, to find $\rho_s/\rho_0 = 2.52$, ; $u_s/u_0 = 2.44$. We note that this ratio is independent of the cooling parameter $\tilde{\Lambda}$. Increasing $\tilde{\Lambda}$ in the simulations, however, we expect the maximum post-shock temperature to fall as thermal energy is radiated away over the numerically broadened shock[4].

In Fig. 2.6 we see the results of these simulations plotted at a time of $t = 141 u_0^{-1/2} \Delta x_0$. We note that the particle distribution in the pre-shock region has also diverged from a lattice arrangement (if it were still a lattice the particles would appear at multiples of Δx_0) into something more glass-like. This is to be expected as the SPH equations of motion favour a large distance to the nearest neighbour for a given density, which can be achieved with a close-packed or glass-like arrangement. The position, velocity and Mach number of the shock at late times are independent of the cooling function, for fixed u_0 (provided the cooling function restores the thermal energy of the gas to u_0) as is shown in Appendix A.

With a low cooling parameter ($\tilde{\Lambda} = 0.11$, black crosses) we see that the post-shock thermal energy reaches near the theoretical value, whilst with a high cooling parameter ($\tilde{\Lambda} = 0.74$, red crosses) we see that the simulation produces almost no hot gas. We take the mid-point of the thermal energies as a minimum value the code should reach to give at least approximately the

[4]One might have expected the post shock thermal energy ratio for a mach 2 shock to be precisely $2\gamma(\gamma-1)+1 = 3.22$ as in the case without cooling, however the immediate post-shock region is still in motion w.r.t the final cold post-shock gas (hence $\tilde{\Lambda} = 0$ is a special case).

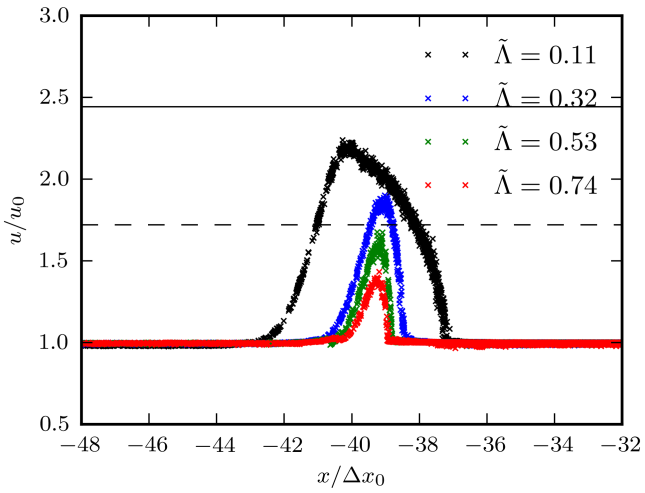

Figure 2.6: Specific thermal energy vs. position for radiative shocks with a Heaviside cooling function, Eq. (2.24). *Black, blue, green, red crosses* are for SPH simulations with dimensionless cooling rates of $\tilde{\Lambda}$=0.11, 0.32, 0.53, 0.74, respectively; positions are quoted in units of the initial (pre-shock) particle spacing Δx_0, thermal energies in units of the initial thermal energy u_0. *Solid line* indicates the analytic instantaneous post shock thermal energy $u_s/u_0 = 2.44$. *Dashed line* indicates mid-point energy between the initial and final thermal energy $\frac{1}{2}(u_s + u_0)/u_0$. When the cooling rate is low ($\Lambda = 0.11$, black crosses), the numerical overcooling is small and the simulation gets close to the right post-shock temperature. Increasing the cooling rate degrades the accuracy of the numerical result. We use this to set a maximum cooling rate that the simulation can tolerate, for example by requiring that the simulated post-shock temperature be larger than half the correct result (horizontal dashed line).

correct answer. From Fig. 2.6 this corresponds to a cooling parameter of $\tilde{\Lambda} \approx 0.4$. Substituting this maximum value into Eq. (2.22) allows us to evaluate the parameter η as

$$\eta = \tilde{\Lambda} u_0^{3/2} \frac{1}{c^3 \mathcal{M}^3} \left(\frac{\rho}{\rho_0} \right)^{2/3} \tag{2.25}$$

$$= \tilde{\Lambda} \left(\gamma \left(\gamma - 1 \right) \right)^{-3/2} \mathcal{M}^{-3} \left(\frac{\rho}{\rho_0} \right)^{2/3} \tag{2.26}$$

$$\approx 0.08 \,, \tag{2.27}$$

(where we have used the post-shock density $\rho = \rho_s = 2.52 \rho_0$), or, using Eq. (2.22),

$$|\dot{u}_\Lambda| \frac{1}{c^3 \mathcal{M}^3} \left(\frac{m_{\rm SPH}}{\rho} \right)^{1/3} < 0.08 \,. \tag{2.28}$$

This is the value of η we will use throughout the remainder of this chapter.

A similar analysis with FLASH yields an only slightly weaker criterion,

$$|\dot{u}_\Lambda| \frac{1}{c^3 \mathcal{M}^3} \left(\frac{m_{\rm AMR}}{\rho} \right)^{1/3} < 0.09 \,, \tag{2.29}$$

where $m_{\rm AMR}$ refers to the mass contained in a mesh cell (since the mass in cells varies we have taken $m_{\rm AMR}$ to be the value in the cell immediately to the right of the shock, for consistency with the evaluation of ρ).

It is worth discussing the differences between a grid and an SPH scheme when the adaptive capabilities are utilised. SPH has a resolution (smoothing) length which refines in areas of high density as $\rho^{-1/3}$. AMR on the other hand can have much more general refinement criteria, for example allowing higher resolution to be applied on features which need not be dense (e.g. shocks). As such AMR has something of an advantage when it comes to shocks, as almost all refinement schemes will refine over discontinuous variables to the maximum level, and hence there is no need to impose the refinement criterion Eq. (2.29). Of course it is possible that a region of space in the simulation is already maximally refined, yet even so fails to satisfy the criterion Eq. (2.29). We can then interpret this as a test of how well the finite resolution of an AMR simulation represents the physics in the problem.

To refine a simulation in a given volume V of a 2 dimensional structure (such as a shock) to scale h in SPH requires $N_{\rm SPH} \propto h^{-3}$ particles, whilst in AMR one would only need $N_{\rm cell} \propto h^{-2}$ cells (we note that limitations on the refinement level between cells does not in general alter this scaling relation).

This can be contrasted with a sheet like structure in a vacuum (e.g. a gravitationally collapsed disk of thickness $\ll h$), which will only require $N_{\rm SPH} \propto h^{-2}$ particles, the same relation as

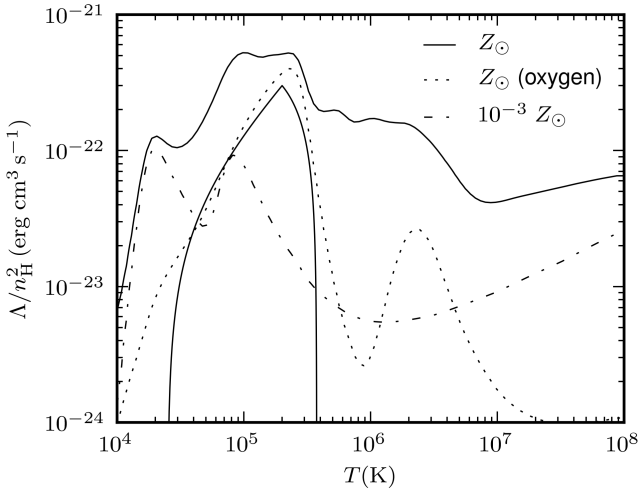

Figure 2.7: Cooling functions used in the GIMIC simulations at redshift 0. *Upper solid* and *dot-dashed lines* represent astrophysical cooling functions for a plasma with metallicity $[Z/Z_\odot] = 0, -3$ (where square brackets denote the base-10 logarithm) respectively in the presence of an ionizing background (Wiersma et al., 2009a). *Lower solid line* shows a cooling spike such as in section 2.2, for comparison, on the same logarithmic scale. *Dotted line* shows cooling due to oxygen only, again assuming a solar abundance.

AMR[5].

Note that we have been concentrating on how well the simulations reproduce *shocks* in the presence of cooling. In practise we would also like the code to correctly reproduce the *cooling tail*, *i.e.* the cooling of the gas once it has passed through the shock (the right-hand side of Fig. 2.6). Clearly here we would like to resolve the cooling length from Eq. (2.17), by requiring that $\Delta x_\Lambda \gtrsim h$ in SPH (or the cell size in mesh codes).

In the subsequent section we will apply the resolution criterion we derived to estimate in which areas of cosmological simulations numerical overcooling could be problematic.

2.4 Effects of resolution on galaxy formation

2.4.1 Galaxy formation simulations

In this section we apply the resolution criterion of Eq. (2.28) to different regions of temperature and density in the the GIMIC SPH simulation of Crain et al. (2009). First we will plot the distribution of gas in temperature-density space and identify some environments of interest. We

[5]As such SPH could be viewed as a refinement scheme optimised for gravitationally collapsed structures.

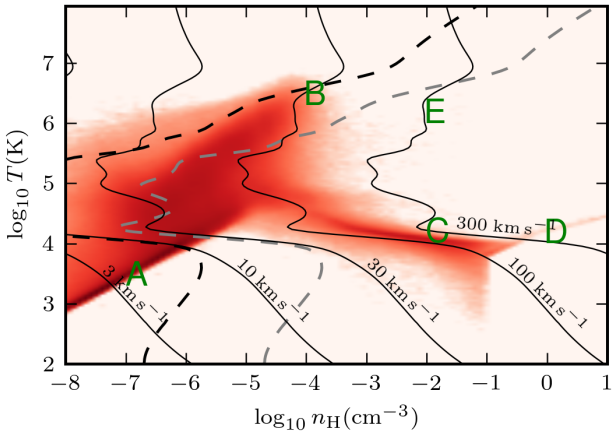

Figure 2.8: Resolution requirements for correctly representing shocks in different regions of a temperature-density diagram. *Solid contours* are labelled with the minimum values of the shock speed, $v = c\,\mathcal{M}$, obtained from Eq. (2.28), that avoids excessive overcooling in the shock precursor, for simulations using an SPH particle mass of $m_{\rm SPH} = 10^6 {\rm M}_\odot$. The radiative cooling rate adopted is that of a plasma with solar abundances of elements, $[Z/Z_\odot] = 0$, as shown in Fig. 2.7. The overlaid *red shaded region* is the phase density in $(T, n_{\rm H})$ space of SPH particles in a cosmological feedback simulation (see text). *Bold letters* refer to example environments described in Table 2.1. *Heavy black* and *grey dashed lines* refer to $t_{cool} = t_{dyn}$ and $t_{cool} = 0.1 t_{dyn}$ respectively. See text for discussion.

will then discuss the radiative shock resolution in this parameter space, but also explore mitigating factors which may allow us to have confidence in simulations even when they fail to accurately resolve the shocks.

The GIMIC simulations are zoomed re-simulations of nearly spherical regions picked from the Millennium simulation (Springel et al., 2005), including gas dynamics. Each sphere has a radius of $18h^{-1}$ Mpc, and the SPH particle mass is $m_{\rm SPH} \approx 10^6 h^{-1} {\rm M}_\odot$. Radiative cooling in the simulation includes line cooling of eleven elements, Compton cooling with the CMB and thermal bremsstrahlung in the presence of a uniform but evolving ionising background, as described in Wiersma et al., 2009a (see Fig. 2.7). The background cosmology, as for the Millennium simulation, is $\Omega_{\rm m} = 0.25$, $\Omega_\Lambda = 0.75$, $\Omega_{\rm b} = 0.045$, $n_s = 1$, $\sigma_8 = 0.9$, $H_0 = 100\ h$ km s^{-1} Mpc^{-1}, $h = 0.73$. The enrichment of gas by nucleosynthesis in stars is described in Wiersma et al. (2009b). Photo-heating, radiative and adiabatic cooling, shocks induced by galactic winds and

due to accretion, result in gas occurring over a wide range of densities and temperatures, illustrated in Fig. 2.8. Five points A-E in this $T - \rho$ space correspond to physical states where we want to investigate to what extent the simulation properly resolves radiative shocks (see also Table 2.1). For a general discussion of these diagrams see Wiersma et al. (2010). The simulation code described here was also used in the OWLS project (Schaye et al., 2010a).

Point A is a typical IGM point outside virialised halos, at low density and temperature. Here we see a very well defined mild upward slope of temperature with ρ of the post reionization gas. This gas is cooling due to adiabatic expansion of the universe and is being photo-heated by the UV-background . For a recombination coefficient $\propto T^{-0.7}$ this will at late times result in a temperature-density relation of $T \sim \rho^{1/1.7}$ (Hui and Gnedin, 1997; Theuns et al., 1998).

Point B corresponds to gas heated in an accretion shock, falling into a galactic halo, or shocked by a galactic wind. Mechanical energy has been converted into thermal energy, and the density will jump by a factor up to ~ 4. When this gas cools, it will form the warm gas of point C which may condense to fuel star formation in a central galaxy (White and Rees, 1978b).

On the far right, $n_{\rm H} > 10^{-1}$ cm^{-3}, is a sharp vertical feature in the distribution of SPH particles. This boundary delineates cold halo gas from gas which undergoes star formation in the model used in GIMIC. The denser gas represents a multi-phase interstellar medium, for which the imposed pressure-density relation in GIMIC is $p \propto n_{\rm H}^{4/3}$, known as an effective equation of state for the ISM. Such a state is intended to mimic the physical pressure response in dense gas undergoing star formation (point D), compressing this gas results in significant star formation with associated feedback (see Schaye and Dalla Vecchia (2008) for motivation and details). The SPH density then represents a volume average density of star-forming gas, whereas the physical ISM lies in approximate pressure equilibrium, but with a hot and cold phase and corresponding variation in densities. In particular the simulation does not allow this gas to cool radiatively. Finally, point E represents the domain of type II SNe that ignite in the hot (10^6K) sparse phase of the ISM, generated by the activity of previous generations of SNe. We note that there is little gas marked in this phase as the cooling time is short.

Now let us consider this simulation in terms of its ability to resolve the radiative shocks that occur in these 5 regions. Equation (2.28) suggests that a radiative shock of velocity v will be resolved if it satisfies

$$v > \left(\frac{|\dot{u}_\Lambda|}{0.08}\right)^{1/3} \left(\frac{m_{\rm SPH}}{\rho}\right)^{1/9}, \tag{2.30}$$

i.e. there is a minimum shock velocity which can be resolved. Shocks below this velocity will tend to artificially radiate away their energy because there will be cooling through the (artificially extended) shock region. Shocks above this velocity will heat up the gas on such a short timescale

	n_H (cm^{-3})	T (K)	Λ (erg cm^3/s)	h (kpc)	v_{min} (km/s)
A. IGM	10^{-7}	2000	10^{-24}	150	5
B. Hot halo	10^{-4}	2×10^6	10^{-22}	15	100
C. Cold halo	10^{-2}	10^4	5×10^{-24}	3	200
D. ISM (AGN)	10^0	10^4	5×10^{-24}	0.7	400
E. ISM (SNe)	10^{-2}	10^6	10^{-22}	3	400

Table 2.1: Astrophysical shock environments identified in Fig. 2.8.

in the simulation that the cooling in the shock region will make little difference to the final result.

In Fig. 2.8 we plot contours of given v, the minimum shock velocity for which there is no significant overcooling in shocks. At each temperature and density a cooling rate is evaluated (using the cooling rate from Wiersma et al., 2009a, shown in Fig. 2.7, evaluated at solar metallicity,

and in the absence of an ionising background), which is combined with a particle mass of $m_{\rm SPH} = 10^6 {\rm M}_\odot$, to derive a minimum shock velocity which can be resolved. Note that Eq. (2.30) is very weakly dependent on particle mass, and thus changing mass resolution is a very ineffective way of shifting the contours. These contours represent the minimum velocity shock which can be resolved at each T, ρ. Any shocks at lower velocities will appear artificially colder due to resolution effects.

A key point, however, is that even if we fail to resolve the radiative shock, the cooling of the gas in many cases may be inevitable anyway. Indeed, there can be situations where other processes are occurring on much longer timescales than the cooling, and for which having an incorrect thermal history of the gas is not a problem as far as the dynamics of the system is concerned[6]. Establishing a general criterion for these is not trivial, here we will simply compare to the locally estimated dynamical time $t_{dyn} \equiv (G\rho)^{-1/2}$ as indicative of the timescales for other processes. We assume that the simulation will cool adequately if $t_{dyn} \gg t_{cool}$ even in the case that radiative shocks are resolved poorly (we define $t_{cool} \equiv |\dot{u_\Lambda}| / u$). The heavy dashed black contour in Fig. 2.8 represents the line where $t_{dyn} = t_{cool}$. All points to the left of this represent $t_{dyn} < t_{cool}$ so certainly we would wish to completely resolve any shocks here. We have also included in dashed grey a line where $0.1 t_{dyn} = t_{cool}$ to demonstrate a somewhat stronger limit. The necessity of resolving the thermal history to the right of this line, is questionable, because

[6]Note that even if dynamics is not affected, there may be other consequences of numerically underestimating the amount of hot gas, for example when calculating the spectrum of cooling radiation.

the gas cooling time is so small in any case. Of course these simulations assume ionisation equilibrium and optically thin gas, so the cooling rates may have been overestimated. In addition if one were to attempt to track the chemistry of the shocked gas, for example the formation and destruction of molecular hydrogen, then having a correct thermal history could still be important (Abel et al., 1997).

Now let us evaluate the resolution criterion of Eq. (2.30) for the five diverse environments of Table 2.1. First we take point A, for radiative shocks in the IGM; here we can see that the low density and cooling rate combine to allow us to resolve all shocks above 5 km s^{-1}, almost certainly much exceeding our requirements.

For point B we have taken a value for gas heated by a virial shock to 2×10^6 K. The higher density and cooling rate here push up the minimum shock velocity we can resolve to around 100 km s^{-1}, comparable to the virial shock velocities v_{200} themselves for halos of mass $\sim 10^{12}\mathrm{M}_\odot$:

$$v_{200} = \left(10GH(z)M_{200}\right)^{1/3}, \tag{2.31}$$

(Mo et al., 1998), where G is the gravitational constant, $H(z)$ the Hubble parameter and M_{200} is the virial mass of the halo. For $z \gtrsim 1$ we can approximate the Hubble parameter as $H(z) \approx H_0\Omega_m^{1/2}(1+z)^{3/2}$ to see

$$\begin{aligned} v_{200} &\approx 201\,\mathrm{km\,s^{-1}} \left(\frac{h}{0.73}\right)^{1/3} \left(\frac{\Omega_m}{0.25}\right)^{1/6} \times \\ &\quad \left(1+\frac{z}{3}\right)^{1/2} \left(\frac{M_{200}}{10^{12}\mathrm{M}_\odot}\right)^{1/3}, \end{aligned} \tag{2.32}$$

$$T_{200} = \frac{1}{3}\frac{\mu m_\mathrm{p}}{k_\mathrm{B}} v_{200}^2 \tag{2.33}$$

$$\begin{aligned} &\approx 1.0 \times 10^6\,\mathrm{K} \left(\frac{h}{0.73}\right)^{2/3} \left(\frac{\Omega_m}{0.25}\right)^{1/3} \times \\ &\quad \left(1+\frac{z}{3}\right) \left(\frac{M_{200}}{10^{12}\mathrm{M}_\odot}\right)^{2/3}, \end{aligned} \tag{2.34}$$

where Ω_m is the matter density in units of the critical density and $h = H_0/100\,\mathrm{km\,s^{-1}\,Mpc^{-1}}$. For lower mass halos the gas actually cools even faster and the shocks are more difficult to resolve, however the cooling may be so short as to save the situation. We explore this situation further in Section 2.4.2.

For point C we consider the warm gas within galactic disks. The minimum shock velocity which can be resolved close to the star formation threshold is higher than for point B, because the cooling rate is higher. However the cooling time is so much smaller than the dynamical time in the disk, so that we suspect that gas cooling will be inevitable in any case. This suggests that,

although numerical overcooling is potentially severe here, it is unlikely to have any important effects on the evolution of the disc.

At a higher temperature than C we have point E, a fiducial point for a (type II) supernova blast wave shocking to hot ($\sim 10^6$K), rarefied ($n_{\rm H} \sim 10^{-2}$ cm^{-3}) ISM (irradiated and inflated by the massive progenitor star). We have a high minimum resolved shock velocity due to the fast cooling of this gas, making its simulation problematic. We expect the gas to form a cold, dense shell (Cox, 1972), and the lack of resolution to manifest itself primarily in an alteration of the onset of this phase. We discuss the implications for SN feedback further in Section 2.4.3.

Finally, for point D we have considered the case of an AGN outflow shocking into a dense ISM of $n_H \sim 1$ cm^{-3}. The minimum resolved velocity is so high here that we can have little confidence in the simulated shock dynamics (excluding the most basic properties such as conservation of momentum). The gas is cooling fast compared to dynamical time scales, yet we have similar concerns to point E about the artificial suppression of feedback.

2.4.2 Virial Shocks

We now consider the effects of the resolution requirement Eq. (2.28) on the discussion of cold accretion and virial shocks around halos. Here we are following the ideas of spherical collapse set out in White and Rees (1978b). The basic question here is what is the fate of gas as it accretes on to a halo, and gets shocked as it converts its mechanical energy into thermal energy. If the cooling time is short, then this hot phase will be a temporary one, however if the cooling time is long, then a hydrostatic hot halo of gas will form within the halo, the scaling relations for which can be found in *e.g.* Mo et al. (1998).

The properties and stability of such spherical shocks have been studied by *e.g.* Birnboim and Dekel (2003), depend on mass and redshift. More massive halos have hotter shocks with longer cooling times. At a given mass lower redshifts imply lower densities and hence slower cooling, and hence easier build-up of a hot halo. It must be recalled, however, that in this situation geometry will also play a role. If the gas accretion can achieve a configuration where it will penetrate farther into the halo (*e.g.* in filaments), it will shock at higher densities and generally have a shorter cooling time (the situation is complicated by the fact that the gas continues to accelerate, and so the shock will generally be hotter).

Here we first consider applying our resolution criteria to the spherical case. Assuming a spherical halo of mean density

$$\bar{\rho}_{200} = 200 \left(\frac{3H^2}{8\pi G} \right) , \tag{2.35}$$

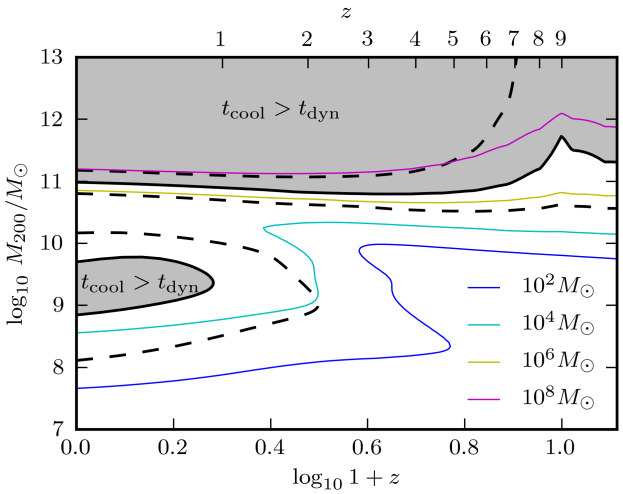

Figure 2.9: Contours of maximum SPH particle mass $m_{\rm SPH}$ required to prevent numerical overcooling at a virial shock, for gas ($[Z/Z_\odot] = -3$) accreting onto halos of different virial masses M_{200} at a given redshift z. Coloured lines corresponding to $m_{\rm SPH} = 10^8, 10^6, 10^4, 10^2 {\rm M}_\odot$ limits are represented by the *thin maroon, yellow, cyan* and *blue lines* respectively. *Black lines* compare cooling time to the dynamical time of the halo: $t_{cool} = t_{dyn}$ (*heavy solid line*), $t_{cool} = 2t_{dyn}$, $t_{cool} = \frac{1}{2}t_{dyn}$ (*heavy dashed lines*). The *shaded grey* region denotes $t_{cool} > t_{dyn}$. Numerical overcooling due to lack of resolution in regions where $t_{cool} \gtrsim t_{dyn}$ will likely affect the dynamics of the accreting gas, hence SPH simulations would appear to need resolutions $\sim 10^6\,{\rm M}_\odot$.

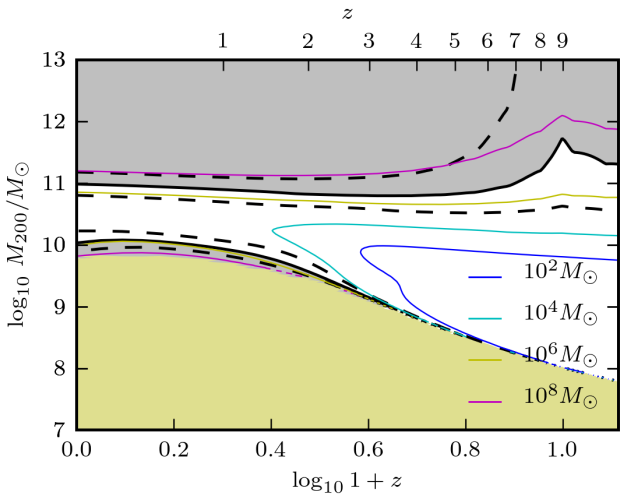

Figure 2.10: As for Figure 2.9, this time including a uniform ionising background, see text for details. In the *gold region* (lower left of the figure), the gas is being heated rather than cooled, so resolution of the shock is of lesser importance.

and virial mass M_{200}, we take the accreting gas to shock to the virial temperature[7] T_{200} and virial velocity v_{200} given in Eqs. (2.31) and (2.33), respectively. For the baryon density at the edge of the halo we use

$$\rho_{\rm b} = \frac{1}{3}\frac{\Omega_{\rm b}}{\Omega_{\rm m}}\rho_{200}, \tag{2.36}$$

where the factor $1/3$ is the ratio of edge to mean densities for an isothermal sphere of profile $\rho = \rho_0(r/r_0)^{-2}$. We can then apply our shock resolution criteria in terms of the maximum mass of SPH particles that do not suffer from numerical overcooling in the shock,

$$m_{\rm SPH,max} = \eta^3 |\dot{u}^{-3}_{\Lambda(T_{200})}|\, v^9_{200}\, \rho_{\rm b}\,, \tag{2.37}$$

where our convergence tests suggest that $\eta \approx 0.08$.

Equation (2.37) defines curves in a plot of virial mass M_{200} versus redshift z, shown in Fig. 2.9 for a cooling rate appropriate for a plasma with solar abundance ratios but mean metallicity of $[Z/Z_\odot] = -3$ (we have chosen the lower metallicity as more representative of accreting gas that has yet to be enriched by several generations of star formation). In Fig. 2.10 we show the case where cooling is partly suppressed by the presence of a uniform ionising background (see Wiersma et al. (2009a) for details). Each thin coloured line represents the limiting particle mass required to prevent numerical overcooling in the corresponding spherical accretion shock. Clearly the resolution requirement is punitatively strict (smallest $m_{\rm SPH}$) for small halos ($M_{200} \sim 10^{8-10}{\rm M}_\odot$), especially at high redshifts ($z \sim 9$). Intuitively this can be understood because these masses correspond to virial temperatures near the peak of the cooling function, and at higher redshifts the mean baryon density (and thus collisional cooling rate) grows. In the presence of an ionising background cooling is suppressed in lower-mass halos that cool mostly through hydrogen lines. At lower masses the ionising radiation has a very large effect, and gas will be *photo-heated* instead of cooling (Okamoto et al., 2008b).

However, even though lack of resolution will lead to overcooling in some halos, the cooling time in these halos may be so short that the gas would cool quickly anyway. The grey area in the figure indicates where the dynamical time in the halo is shorter than the cooling time: in this region we expect that numerical overcooling may prevent the formation of a hot halo. Conversely, in the white region, cooling is so fast that even if a hot halo were to form, it would quickly cool. The demarcation line between these scenarios follows closely the $\sim 10^6{\rm M}_\odot$ limiting SPH mass (yellow line). Simulations run with that resolution or better will be able to form hot spherical halos

[7]The infalling gas has actually twice this energy so if it shocks into the rest frame of the halo the temperature will be increased by a factor of 2, however we will ignore this for now.

in situations where we would expect such a hot halo to form. At lower resolution, simulations may artificially suppress the formation of a hot halo due to numerical overcooling in the accretion shock.

Our considerations apply only at the virial radius. However, nearer the centre of halos we expect this conclusion to remain valid, as the cooling time diminishes faster than the dynamical time. The very high mass halos have $2t_{dyn} < t_{cool}$ (heavy dashed black line) and we expect these to be in near hydrostatic equilibrium. As a result of these analyses we conclude that $10^6 \mathrm{M}_\odot$ is a sensible upper limit for the gas particle mass in cosmological simulations intending to capture the evolution of proto-galactic halos, although lower masses enable more accurate resolution of the thermal history of gas in lower mass halos.

2.4.3 Thermal feedback

Thermal feedback refers to the mechanism whereby injection of thermal energy into the ISM causes adiabatic expansion of the gas and subsequent suppression of star formation due to the diminished density. The simplest model to envisage is perhaps that of a single supernova creating a hot, spherical, rarefied, blast wave. On larger scales, however, we expect to see analogous effects from star forming regions and AGN. In this section we intend to consider our results in terms of thermal feedback in SPH. We will review the basic physics of thermal feedback and its role in galaxy evolution. We will then discuss its implementation in SPH and derive some quantitative criteria for accurately resolving it. Finally, we will relate our observations to the feedback experiments in other work.

We begin by considering the problem of simulating a supernova blast wave. Here we are primarily concerned with the situation where we may artificially radiate away the thermal energy of the blast wave due to a lack of resolution. This would result in the premature transition from a thermally driven to a momentum driven phase.

A concise overview of the evolution of a supernova remnants can be found in Cox (1972). Essentially the blast wave will follow a Sedov-Taylor self-similar solution (Sedov, 1959) until the shock temperature T_s falls to a value where the radiative cooling exceeds the cooling via adiabatic expansion. A full calculation is beyond the scope of the present chapter, however, we can get close just by dimensional considerations

$$k_B T_s = \left(E_0^2 m_{\mathrm{p}}^3 n_{\mathrm{H}}^4 \Lambda^6\right)^{1/11} \tag{2.38}$$

$$\approx k_B \cdot 4 \times 10^6 \mathrm{K}\,, \tag{2.39}$$

where $E_0 = 10^{51}$ erg is the SNe energy, $n_{\mathrm{H}} = 1.0$ cm^{-3}, $\Lambda = 10^{-22}$ erg cm^3/s. The value of

Cox 1972 is a factor 2 smaller, at 2.0×10^6K.

In a simulation we would like to resolve the transition in the supernova shock from being pressure driven to being momentum driven, which typically occurs for shock temperatures $T_s \sim 2.0 \times 10^6$K; numerical overcooling may cause the shock to transition too early, hence underestimating the feedback effect of the explosion on star formation in the surroundings. Using the Sedov similarity solution for a 3 dimensional blast wave in a uniform cold medium of adiabatic index $\gamma = 5/3$ and density ρ_0 (which we will shortly take to be the density of the ISM), we can then write the pressure and temperature just inside the shock wave in terms of the shock velocity v_s, as

$$\rho_s = \frac{\gamma+1}{\gamma-1}\rho_0 \tag{2.40}$$

$$p_s = \frac{2}{\gamma+1}\rho_0 v_s^2 \tag{2.41}$$

$$k_B T_s = \bar{\mu}\frac{p_s}{\rho_s} = 2\frac{\gamma-1}{(\gamma+1)^2}\bar{\mu}v_s^2, \tag{2.42}$$

where $\bar{\mu}$ is the mean particle mass. Combining this with the resolution criterion of Eq. (2.28) we find that (excluding fairly pathological cooling functions) the cooling will be hardest to resolve at the lower temperatures, *i.e.* at $T_s = 2.0 \times 10^6$ K.

Applying fiducial values for the ISM of $\bar{\mu} \approx 0.6\, m_p$ at $T_s = 2.0 \times 10^6$ K yields a shock velocity, density and cooling rate of

$$v_s = 380\ \mathrm{km\,s^{-1}} \tag{2.43}$$

$$\rho_s \approx 9 \times 10^{-24}\ \mathrm{g\,cm^{-3}} \tag{2.44}$$

$$\dot{u}|_\Lambda \approx -180\ \mathrm{cm^2\,s^{-3}}, \tag{2.45}$$

and the corresponding radius of the blast wave

$$r_s = 1.15\left(\frac{E}{\rho_0}\right)^{1/5} t^{2/5} \tag{2.46}$$

$$= 1.15^{5/3}\left(\frac{E}{\rho_0}\right)^{1/3}\left(\frac{2}{5}\right)^{2/3} v_s^{-2/3} \tag{2.47}$$

$$\approx 15\ \mathrm{pc}, \tag{2.48}$$

where $E \sim 10^{51}\mathrm{erg}$ is the thermal energy injected by the explosion. The corresponding limiting SPH particle mass that avoids numerical overcooling, evaluated from Eq. (2.28), is

$$m_{\mathrm{SPH}} = 70\mathrm{M}_\odot\left(\frac{\rho_s}{9\times10^{-24}\mathrm{g\,cm^{-3}}}\right) \times \left(\frac{v_s}{380\ \mathrm{km\,s^{-1}}}\right)^9\left(\frac{|\dot{u_\Lambda}|}{180\ \mathrm{cm^2\,s^{-3}}}\right)^{-3}. \tag{2.49}$$

The small values of both the radius and the required minimal mass resolution imply that most cosmological simulations of galaxy formation are far from resolving individual SN explosions, however detailed simulations of high-z dwarf galaxies do indeed already reach such extreme resolutions (*e.g.* Wise and Abel (2008)). For a state of the art mass resolution for a cosmological simulation of say $10^5\,\mathrm{M}_\odot$, a star particle really represents very many stars and hence also many SNe. Simply scaling-up E_0 to represent the many SNe that go off does not really help much, as for example the blast radius only scales $\propto E^{1/3}$. In reality different SNe will go off in different places, and once the density of the ISM is decreased due to one explosion, another explosion in the lower density gas will have a much larger effect, eventually resulting in a percolating hot phase.

However these small scales cannot yet be resolved in current cosmological simulations, hence they fail to follow the transition from pressure to momentum-driven SN shells. One can try to model the expected effects by simply heating a small number of neighbouring SPH particles. In this case our resolution study indicates that the reheating temperature must be sufficiently high for numerical overcooling not to affect the dynamics. We can thus generalise the above calculation to find the minimum temperature for resolved thermal feedback for a given SPH particle mass. To perform this calculation we will need to associate a shock velocity with a single particle, which we will take to be the Sedov shock velocity for a blast wave of the same mass as the SPH particle

$$v_s = 1.15^{5/2}\sqrt{\frac{\pi}{3\gamma(\gamma-1)}}\cdot\frac{4}{5}c_s \tag{2.50}$$

$$= 1.1c_s\,. \tag{2.51}$$

Combined with Eq. (2.30) we find

$$u_{\mathrm{fb}} \gtrsim \frac{\eta^{-2/3}}{1.1^2\cdot\gamma(\gamma-1)}\left(\frac{m_{\mathrm{SPH}}}{\rho}\right)^{\frac{2}{9}}(|\dot{u}_\Lambda|)^{2/3} \tag{2.52}$$

$$= 4\left(\frac{m_{\mathrm{SPH}}}{\rho}\right)^{\frac{2}{9}}(|\dot{u}_\Lambda|)^{2/3}\,, \tag{2.53}$$

the minimum thermal energy required to avoid numerical overcooling.

Dalla Vecchia and Schaye (2008) argue that for thermal feedback to be effective requires that the sound crossing time across an SPH particle, $t_s = h/c_s$, be smaller than the cooling time, $\tau_c = u/|\dot{u}_\Lambda|$. Using $\rho\,h^3 \sim m_{\mathrm{SPH}}$, $t_s < \tau_c$ requires that

$$u_{\mathrm{fb}} \gtrsim \left(\frac{m_{\mathrm{SPH}}}{\rho}\right)^{2/9}(|\dot{u}_\Lambda|)^{2/3}\,, \tag{2.54}$$

which is identical apart from a numerical factor to Eq. (2.53). Our criterion is stronger as it takes

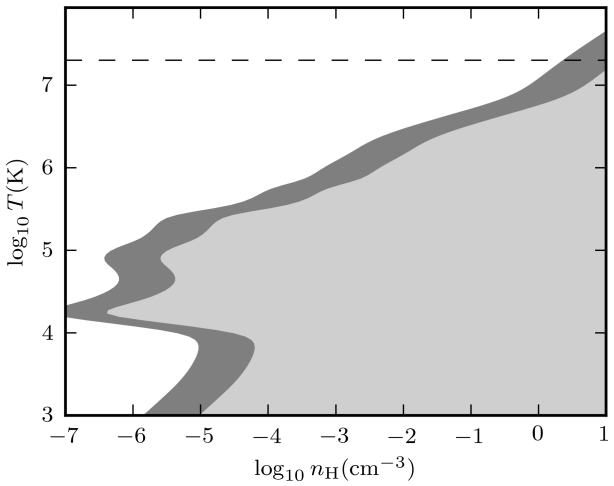

Figure 2.11: Minimum re-heating temperature T required to avoid numerical overcooling as a function of hydrogen number density n_{H}, assuming an SPH resolution of $m_{\mathrm{SPH}} = 10^6 \mathrm{M}_\odot$ and solar metallicities. Cooling is so rapid in the *shaded* regions that the transition from thermally driven to momentum driven expansion phases of supernova bubbles is so fast that much of the injected energy will be lost to radiation. The *light grey shaded region* corresponds to Eq. (2.54), the *dark grey shaded* is the more demanding Eq. (2.53). The *white region* is where the reheating temperature is sufficient to force thermal feedback despite resolution concerns. *Dashed line* is an estimate of the specific energy of SNe from Kay et al. (2002).

into account that the code will in practise overestimate the cooling of the gas in shocks; the lower value simply requires there to be a shock.

In Fig. 2.11 we explore the parameter space for modelling thermal feedback in an SPH simulation with $10^6 \mathrm{M}_\odot$ particles. At each density, there is a minimum temperature required to drive an adiabatic blast wave phase. The light grey region is defined by the sound crossing time argument of Eq. (2.54) and the dark grey is from Eq. (2.53). In the white region we expect effective thermal feedback; in the dark grey region it will be suppressed by overcooling in shocks, and finally in the light grey the code will be unable to produce a shock at all.

It is helpful to introduce some numbers. For gas with hydrogen number density $n_{\mathrm{H}} = 1$ cm^{-3}, a $m_{\mathrm{SPH}} = 10^6 \mathrm{M}_\odot$ particle would need to be heated to a temperature of $T_s \approx 5 \times 10^6 \mathrm{K}$ to be in the pressure driven phase, according to Eq. (2.54). However our resolution study suggests that we need a higher temperature of $\approx 10^7 \mathrm{K}$ to prevent excessive overcooling through the shock, implying that at this resolution the simulation cannot properly represent the effects of

thermal feedback. Note also from Eq. (2.53), that this improves only very slowly with improved resolution, $\propto m_{\rm SPH}^{2/9}$. Relating back to models of feedback, this is somewhat problematic as the specific energy of supernovae [8] is estimated to only be around 2×10^7K (dashed line in Fig. 2.11) which can still be too low for the simulation code to properly follow the thermal evolution of the explosion.

Clearly this has important consequences for prescriptions for supernova-driven thermal feedback. In densities above $n_{\rm H} = 1\,{\rm cm}^{-3}$ the thermal feedback starts to reduce its effectiveness, even if we ignite all our SNe in a single timestep, yet this is one of the key environments where feedback is required.

One way to drive feedback at this resolution, whilst still maintaining a globally consistent initial mass function, is to stochastically inject the energy of SNe due to star formation. Since the mean thermal energy of a single particle can then be greater than 2×10^7K we can remain in the effective region of Fig. 2.11. To balance the IMF other star forming particles will need to receive less or no SNe energy. The alternative is to increase the resolution, but again the low exponent of $m_{\rm SPH}$ in Eq. (2.53) makes this quite prohibitive.

The issue is further complicated by the existence of a multi-phase ISM not resolved by the simulation. This is the motivation for many of the prescriptions for feedback, such as applying a fraction of the supernovae energy as kinetic energy (Navarro and White, 1993), disabling the cooling of thermal bubbles (Gerritsen, 1997) or releasing the energy of many accumulated supernovae in one step. A more thorough discussion of all these methods can be found in Kay et al. (2002). Another approach is to model the net feedback effects by a subgrid model (for example an imposed equation of state without cooling as in Schaye et al., 2010a), or to model the hot and cold phases separately by representing clouds in the cold phase as collisionless particles (Booth et al., 2007).

At lower densities it becomes easier to thermally drive a blast wave due to the reduced cooling rate, reinforcing the importance of simulating a multiphase ISM. For their star formation threshold of $n_{\rm H} = 10^{-1}$ cm^{-3}, the high-resolution OWLS simulations of Schaye et al. (2010a) can represent thermally driven SNe at the edges of discs, but not in more central regions. Indeed, at higher densities the required temperatures rapidly reach extreme values. Booth and Schaye (2009) note that in their simulations, AGN feedback requires reheating temperatures $T_s > 10^8$K, as at lower temperature the energy is simply radiated away. We believe that this problem is not a physical one but one of resolution. At lower temperatures the density is higher, the cooling faster,

[8] The specific energy of supernovae is the energy released by supernovae per unit mass of star-forming gas (Kay et al., 2002), i.e. if all supernovae were to ignite simultaneously we would reach this mean temperature.

and the cooling region behind the shock cannot be resolved, as is clear from Fig. 2.11.

2.4.4 Shocks at the sound speed

As an interesting aside it is worth considering that there will usually be an upper limit to the resolution required. If we assume that the weakest shock has a velocity on the order of the sound speed, $c_s = (\gamma(\gamma-1)u)^{1/2}$, then the minimum requirement for the particle mass for a given problem will be

$$m_{\rm SPH} = (0.08)^3 \left(\gamma(\gamma-1)\right)^{9/2} \min_{x\in \rm V}\left\{|\dot{u}_\Lambda|^{-3} u^{9/2}\rho\right\} . \tag{2.55}$$

Unfortunately such a limit will usually be very small indeed, at least for cosmological simulations, because of the low sound speed of cold, dense gas present in galactic discs. However if one chooses to go down this path, then one can examine the following criteria. If we have a conventional collisional cooling function then $\dot{u}_\Lambda/\rho$ is independent of density, and we can make the additional assumptions that $\dot{u}_\Lambda \rightarrow 0$ as $u \rightarrow 0$, and for large u

$$\frac{|\dot{u}_\Lambda|}{\rho} \sim u^{1/2} \tag{2.56}$$

(thermal bremsstrahlung), giving

$$m_{\rm SPH} \propto \min_{x\in \rm V}\left\{\rho^{-2}\right\} , \tag{2.57}$$

i.e. the smallest particle mass is determined by the highest density in the problem. This analysis is of course not valid with Compton cooling via the CMB, or the presence of a UV background, as neither process is collisional.

2.5 Conclusions

In this chapter we have examined the role of radiative cooling in shocks. We have found a general analytic solution for 1d piecewise linear collisional cooling functions and compared it to numerical simulations of the same shock, performed with an SPH code (GADGET) and an AMR code (FLASH). These codes smear out the shock over several particles or cells, and such an artificial 'pre-shock' results in numerical overcooling which may prevent the formation of a hot post-shock region. We have estimated a general resolution criterion to avoid such overcooling, and applied it to the problems of virial shocks and the production of hot gaseous halos. We have found that to avoid numerical overcooling of accretion shocks onto halos that should develop a hot corona requires a particle or cell mass resolution of $10^6 {\rm M}_\odot$ (Fig. 2.10), which is within reach of current state-of-the-art simulations.

Similarly, we have applied our estimates to thermal feedback from AGN or supernovae blast waves, in the presence of radiative cooling. We have seen that the energy required to drive thermal feedback at a given mass scale, for current numerical results, is an order of magnitude higher than one would expect just from physical considerations. For cosmological simulations ($10^6 \mathrm{M}_\odot$ gas particles) of an $n_\mathrm{H} = 1.0\,\mathrm{cm}^{-3}$ interstellar medium we see (Fig. 2.11) that temperatures in excess of 10^7 K are required to effectively drive thermal feedback by avoiding spurious suppression of the feedback by numerical overcooling.

Although all of these issues can be rectified by increasing the resolution, the minimum thermal energy of injected feedback required to avoid artificial cooling scales weakly with decreasing particle mass, $\propto m_\mathrm{SPH}^{2/9}$, see Eq. (2.53). Consequentially, a potentially fertile region of study may be that of cooling switches, *i.e.* a criterion for disabling cooling through a shock. Such a switch would allow a simulation to resolve temperatures much closer to the physical temperatures of radiative shocks without requiring extreme resolutions. Unfortunately it is not a straightforward problem to have a criterion that will consistently suppress cooling in the presence of shocks yet does not affect cooling in regions where there are no shocks. Since we can never hope to completely remove resolution effects it seems sensible to have a more limited aim, perhaps to capture the temperatures of shocks up to some maximum cooling rate. As such one might wish to suppress cooling, when the cooling time is greater than some fraction of the shock heating time. We intend to explore this avenue in future work.

Further work could include the effects of shock-induced non-collisional ionizational equilibrium (CIE) or non-thermalised gas. Since the resolution can make such a significant modification to the thermal history of a gas, we expect a criterion due to non-CIE may be quite strict.

Chapter 3

How supernovae power galactic winds

3.1 Introduction

Feedback is an essential ingredient of galaxy formation models. It is invoked to suppress the formation of large numbers of small galaxies (Rees and Ostriker, 1977; White and Rees, 1978a; White and Frenk, 1991). While photo heating can suppress star formation in the smallest halos, it cannot explain the low efficiency of SF in halos more massive than $10^9\,\mathrm{M}_\odot$ (Efstathiou, 1992; Okamoto et al., 2008a). Feedback is also invoked to explain why such a small fraction of the baryons are in stars today (Fukugita et al., 1998; Balogh et al., 2001). An efficient feedback implementation also appears essential for simulations to produce realistic looking disk galaxies (Scannapieco et al., 2011). Observations of galactic winds at low (Heckman et al., 1990, 2000) and high $z \sim 3$ redshift (Pettini et al., 2001) do show gas with a range of temperature and densities moving with large velocities of 100s of km s^{-1} with respect to the galaxy's stars, although the interpretation in terms of mass loss is complicated by the multi-phase nature of the wind (see e.g. Veilleux et al., 2005 for a recent review). Complimentary evidence for outflows comes from the high metal abundance detected in the IGM (Cowie et al., 1995), even at low densities (Schaye et al., 2003; Aguirre et al., 2004). Numerical simulations make it plausible that galactic winds are responsible for this metal enrichment (Cen and Ostriker, 1999; Aguirre et al., 2001; Theuns et al., 2002; Aguirre et al., 2005; Oppenheimer and Davé, 2006; Tescari et al., 2011), with low-mass galaxies dominating the enrichment of the bulk of the IGM (Booth et al., 2012).

The sheer amount of energy released by supernovae (SNe) make the injection of energy into the interstellar medium (ISM) by SN explosions a prime candidate for driving galactic winds (Dekel and Silk, 1986). However it is challenging to understand in detail how SNe regulate the transfer of mass and energy between the different phases of the ISM, as envisaged in the model of McKee and Ostriker (1977), and how and when this leads to the emergence of a galactic wind. Efstathiou (2000) and Silk (2001) extend the McKee and Ostriker (1977) model to examine how

such interactions lead to self-regulation of star formation. They show that the properties of the galactic wind can be broadly understood once a temperature and density for the hot phase is found. This requires a model of evaporation of cold and warm clouds, yet without a more detailed understanding of the geometry and turbulence, we can go little further than steady spherically symmetric conduction models, which go back to Cowie and McKee (1977). Even if feedback is indeed due to SNe, it is not yet clear whether this is a consequence of their injection of hot gas, of turbulence (Mac Low and Klessen, 2004; Scannapieco and Brüggen, 2010), of cosmic rays (Jubelgas et al., 2008), of the combined effects of magnetic fields, cosmic rays, and the galaxy's differential rotation (Kulpa-Dybeł et al., 2011), or all of the above.

Full hydrodynamic modelling of the interplay between the various components of the ISM in a Milky Way-like galaxy in a proper cosmological context is not yet currently possible due to the large range of scales involved, with density ranging from 4×10^{-31} g cm^{-3} outside of halos to $\sim 10^{-20}$ g cm^{-3} in cold clouds, temperatures from a few Kelvin inside star forming regions to $\sim 10^{8}$K inside SN remnants, and time scales from a few thousand year for the propagation of a SN blast wave inside the ISM to $\sim 10^{10}$ years for the age of the Galaxy. Excitingly, such full hydro-dynamical modelling begins to be possible for higher redshift dwarfs (e.g Wise and Abel, 2008), but for the moment models of larger galaxies at $z \sim 0$ are limited to simulating a patch of galactic disk. In addition, we would also like to identify and understand the physics that is important in driving material from the galactic disk, and so it is desirable to have a series of numerical experiments. This is the approach we will follow in this chapter.

We begin by discussing constraints on galactic winds derived from current theoretical models of galaxy formation, and place our work in the context of comparable approaches. In section 3.3 we introduce the set-up of our own simulations. Briefly, we use a very simple model of the ISM which neglects the cold phase, and which is stirred by hot gas injected by SN explosions. Next we demonstrate that our sub-pc simulations have sufficient resolution to resolve individual explosions, and illustrate the behaviour of both the ISM and of the wind for a reference model with properties chosen to be similar to that of the solar neighbourhood. In Section 3.5 we vary the properties of the simulated ISM (total and gas surface densities, star formation rate, cooling rate), and investigate if and when a wind is launched, and how its properties depend on that of the ISM. We obtain scaling relations of the wind to the ISM and apply them in Section 4.2 to predict wind properties for a full galactic disk, and investigate how the wind properties depend on the galaxy properties. We summarise in Section 4.3.

3.2 Constraints on galactic winds

3.2.1 Model requirements and observations

We will assume that the baryon fraction in Milky-Way-sized halos, and halos of lower mass, falls significantly below the cosmological value, $f_b = \Omega_b/\Omega_M$ due to the action of a galactic wind. Let the gaseous mass outflow rate from this wind be $\dot{M}_{\rm wind}$, and the star formation rate $\dot{M}_\star$. A simple way to parameterise the efficiency of the SN-driven wind in removing baryons from the halo, is its *mass loading*, i.e. the ratio

$$\hat{\beta} \equiv \frac{\dot{M}_{\rm wind}}{\dot{M}_\star}\,, \tag{3.1}$$

where our $\hat{\beta}$ is equivalent to the β of Stringer et al. (2011). We introduce the hat in order to distinguish the average mass loading for a galaxy, $\hat{\beta}$, from a local mass loading β at some point on the disk. If a galaxy exhausts its gas supply in star formation (and does not recycle wind material) then we will be left with a gas poor galaxy with baryon fraction reduced by a factor $1/(1+\hat{\beta})$.

In order to infer the fraction of baryons ejected from galaxies we can use the statistics of galaxies and dark matter halos. The number density of halos as a function of their mass can be approximated for masses below the exponential cut-off scale as a power law (Press and Schechter, 1974; Reed et al., 2007),

$$\frac{{\rm d}n}{{\rm d}\log M} \propto M^{-0.9}\,. \tag{3.2}$$

Contrast this with the slope of the galaxy stellar mass function at low masses,

$$\frac{{\rm d}n}{{\rm d}\log M_\star} \propto M_\star^{1+\alpha}\,, \tag{3.3}$$

where observationally α is found to be in the range $[-1.5, -1]$, see e.g. (Blanton et al., 2003, 2005; Baldry et al., 2005, 2012; Li and White, 2009). Naively identifying each dark matter halo with a galaxy of a given stellar mass (e.g. Guo et al., 2010) yields a galaxy mass to halo mass relation of $M_\star \propto M^{-0.9/(\alpha+1)}$. Identifying the stars as the main baryonic component implies a mass loading that scales with halo mass relatively steeply as (see also Stringer et al., 2011)

$$1+\hat{\beta} = f_{\rm b}\,\frac{M}{M_\star} \propto M^{(1.9+\alpha)/(1+\alpha)} \propto M^{-0.8}\,, \tag{3.4}$$

where we substituted a faint end slope of $\alpha = -1.5$ to derive the last exponent. Notably, this exponent $\to \infty$ as $\alpha \to -1$ and falls to zero as $\alpha \to -1.9$, as such it is rather poorly constrained even by a well measured slope of the galaxy stellar mass function at low masses. One can infer not only that at low masses the mass loading $\hat{\beta} \gg 1$ but also that it is strongly increasing towards lower-mass galaxies.

Assume star formation results in the explosion of ε_{100} supernovae per $100\,\mathrm{M}_\odot$ of stars formed, each with energy E_{SN}, and that a fraction η_T gets converted into kinetic energy of an outflow. Neglecting other sources of energy then implies that

$$\hat{\beta}\, v_{\mathrm{wind}}^2 = 2(710\,\mathrm{kms}^{-1})^2\, \eta_T\, \varepsilon_{100}\, \frac{E_{\mathrm{SN}}}{10^{51}\,\mathrm{erg}}\,, \tag{3.5}$$

where v_{wind} is the wind speed. If ε_{100}, the thermalisation factor η_T and E_{SN} are all constants, then the product $\hat{\beta}v_{\mathrm{wind}}^2$ is also a constant. In this case large values of $\hat{\beta}$ imply lower wind speeds, and vice versa. If the mass-loading $\hat{\beta}$ indeed increases with decreasing halo mass, then of course eventually $\hat{\beta}$ may become so large that the wind can no longer escape from the galaxy's potential well. Such small halos may be subject to other destructive mechanisms, such as evaporation by re-ionization or obliteration by the explosions of the first stars. For massive halos, in order for the wind to escape it requires high wind speeds, implying low mass loading. The semi-analytical model of galaxy formation presented recently by Bower et al. (2011) imposes similar constraints on galactic winds to obtain fits to the faint-end of the galaxy mass function as inferred from our naive expectations: galactic winds need to have values of the mass loading $\hat{\beta} \sim 1$ for Milky Way-like galaxies, with an indication that $\hat{\beta}$ increases even further towards lower masses. The best fitting models have $\hat{\beta} \sim 10$ giving $v_{\mathrm{wind}} \sim 300\ \mathrm{km\,s}^{-1}$.

Numerical simulations of galaxy formation also try to implement galactic winds with similar properties. Cosmological simulations such as Oppenheimer and Davé (2008); Dubois and Teyssier (2008) and Shen et al. (2010) include simple star formation prescriptions in combination with efficient feedback in an effort to produce a reasonable galaxy population, although they struggle to produce significant winds to remove enough baryons from Milky Way-sized galaxies. These simulation implement the increase in mass-loading to smaller galaxies by hand. The OWLS simulations (Schaye et al., 2010b) examined a variety of feedback prescriptions and models with efficient feedback in terms of a strong galactic winds fit a variety of properties of the galaxy population, including the Tully-Fisher relation (McCarthy et al., 2012). However, in such models the properties of the winds are still part of the sub-grid modelling, i.e. the wind's properties are not computed but rather are simply imposed. This is required since the mass of gas entrained by a single supernova is a tiny fraction of the mass resolution element of the simulation (Creasey et al., 2011).

There are compelling theoretical reasons to expect a high mass loading in galaxy winds, but are such winds seen in practise? The observational evidence for galactic outflows, at least in *starburst galaxies*, is extremely strong (Heckman et al., 1990, 2000; Pettini et al., 2001; Martin, 2005; Martin et al., 2002; Strickland and Heckman, 2009). Unfortunately it is notoriously difficult

to constrain the wind properties from the data directly, partly because of uncertain metallicity and ionisation corrections needed to translate between the observed ion outflow and inferred total wind values, and partly because observing the wind in the spectrum of its galaxy does not provide spatial information of where the absorbing gas is located (Bouche et al., 2011, but see Wilman et al., 2005; Swinbank et al., 2009 for a few cases of resolved studies of winds). The outflowing gas is likely multi-phase in nature, complicating further the interpretation of the data. The picture for non starburst galaxies is even more complex, with Strickland and Heckman (2009) noting the lack of evidence for superwinds in such galaxies. As Chen et al. (2010) point out, however, the evidence for the high velocity outflows come from blueshifted absorbers such as Na D are tracing cooler material which is a fraction of the wind (or MgII, for example Weiner et al., 2009 in the Deep2 galaxies). As far as it can be measured, the velocity of the outflow seems to be only weakly dependent on the SFR (Rupke et al., 2005). Probing the circum-galactic medium around galaxies with a sight line to a background quasar allowed Bouche et al. (2011) to infer values of $\hat{\beta} = 2 - 3$ and wind speeds $v_{\rm wind} = 150 - 300$ km s^{-1} for a set of L$_\star$ galaxies at redshift $z \sim 0.1$. They claim these wind speeds are in fact below the escape speed, and hence we may be observing a galactic fountain rather than a proper outflow.

The picture of SNe as the driver of galactic winds also has consequences in terms of the metallicity of the galaxy. As SNe inject both metals and energy we expect and find a corresponding metallicity deficit for low mass galaxies (Tremonti et al., 2004), interest in which goes back to Larson (1974). Both simple models (Peeples and Shankar, 2011; Dayal et al., 2012) and simulations (Finlator and Davé, 2008) show that galactic winds are an essential ingredient to obtain the observed mass-metallicity relation in galaxies.

Summarising, observations provide strong evidence for the presence of galactic winds in star forming galaxies, but the parameters of such winds are currently not tightly constrained. Models that make recourse to such winds to quench star formation require relatively high values of the wind's mass loading, $\hat{\beta} \sim 1$ for MW-like galaxies, with $\hat{\beta}$ increasing for lower mass galaxies. But do SNe-driven winds indeed meet these requirements, and if they do, why?

3.2.2 Galactic winds in simulations

In order to directly simulate the *generation* of galactic winds requires a much higher resolution than cosmological simulations, as the sites of energy injection must be resolved (discussed further in section 3.3). As such there are a range of simulations attempting either to simulate galaxies at high redshift where the total volume is smaller, simulating galaxies at low redshift but with some sub-grid approximation to the physics (e.g. the multi-phase method of Springel and Hernquist,

2003) or actually resolving the individual SNe but not for a full galaxy.

Mac Low and Ferrara (1999) attempted to study the blow-out produced by a dwarf galaxy using azimuthal symmetry and a grid resolution of 25 pc. Individual supernovae were not resolved in these simulations, instead there is a continuous injection of energy in the mid-plane. Measured mass-loss fractions were extremely small, only a few percent for galaxies over $10^6 \mathrm{M}_\odot$.

Mori et al. (2002) looked at high-z dwarf galaxies where SNe could lift material out of the halo to pollute the IGM with metals. Wise and Abel (2008) managed to drive 95% of the baryons from low mass halos at high redshift using the extremely energetic explosions from population III stars.

Fujita et al. (2004) performed a 2d axisymmetric simulation of a dwarf galaxy at redshift 9, going down to a $2.6\ \mathrm{pc}$ cell size in the centre of the simulation. They managed to eject metals in to the IGM, but unless the star formation was increased considerably were unable to eject significant amounts of the ISM. Strickland and Stevens (2000) similarly performed 2d axisymmetric simulation of a starburst to compare with the nearby starburst galaxy, M82, allowing them to reach 15 pc resolution. The focus was primarily on the X-ray properties of these winds, yet those winds are quite comparable to the winds we show. We note that their wind is mass-loaded by hand, using the prescription of Suchkov et al. (1996). A full 3d version of this type of galaxy was tried by Cooper et al. (2008), but only with reference to the X-ray properties.

Powell et al. (2011) performed an AMR simulation for a redshift 9 dwarf galaxy, where the highest density regions in the simulation reach similar resolutions to our own, with $1\ \mathrm{pc}$ resolution, and again find the efficiency of ejection of gas from the galaxy is less than the mass accretion rate.

It is possible to study massive objects at lower redshift if one is prepared to use some sub-grid scheme for the multi-phase ISM to decrease the resolution requirement. Simulations of winds in more massive galaxies include Dubois and Teyssier (2008); Hopkins et al. (2012a), though both struggle to capture mass loadings above unity with pure SN feedback, however Hopkins et al. (2012a) sees a significant improvement by including the winds from high mass stars.

Concentrating on a column of ISM of a galaxy allows one to reach very high resolution, and such simulations were performed by Joung and Mac Low (2006), who concentrate mainly on the turbulent structure of the ISM where they found the largest kinetic modes occurred on scales of $\sim 200\ \mathrm{pc}$. This work was extended in Joung et al. (2009) to parameterise sub-grid models in terms of turbulent pressure. These authors allow the gas to cool to the cold phase, then include a diffusive heating term to prevent the high density gas becoming thermally unstable. More recently, Hill et al. (2012) investigated the effects of magnetic fields.

While preparing this chapter for publication, Gent et al. (2012) have studied a supernova regulated three-phase ISM, where the focus is on the resultant properties of the ISM w.r.t. different cooling functions, but also show outflows which are comparable in velocity and mass loss to ours.

3.2.3 Self consistent simulations

Ideally one would wish to probe the efficiency with which star formation can drive winds with simulations that self consistently included all the relevant physics, i.e. a full galaxy containing a star forming ISM, those stars subsequently redistributing their energy as type II SNe explosions, including outflows and cosmological infall. Unfortunately the range of scales involved in this problem makes such an approach currently computationally infeasible. To progress we must either truncate our resolution at some scale before we have fully resolved the physics, or to truncate our physics such that the available resolution becomes sufficient. The former route is one where we assume that we understand the physical processes to a certain degree and make our best effort at the calculation, forcing us to go deeply in to convergence studies. The latter is that of the numerical experiment where it is assumed that a certain amount of numerical calculation is possible and we make our best effort to include the processes, requiring us to make full comparison with the real Universe to test these assumptions (many simulations, are, of course, a mixture of these approaches). Our focus will be on the latter case, that of the numerical experiment. We will also restrict ourselves to looking at the *launch* region of the galactic wind, where gas is expelled from the galaxy but not necessarily from the halo. This is consistent with what is needed to improve subgrid models in semi-analytic models and hydro simulations.

The motivation for our choice of scale relates to the need to resolve individual SN blast waves as they sweep the ISM (as for example described by Cox, 1972). Briefly, such explosions involve three distinct stages (e.g. Truelove and McKee, 1999), beginning with the very early stage during which SNe ejecta expand almost freely into the ISM. As the ejecta sweep-up ISM preceded by a shock, eventually a reverse shock will run back into the ejecta, heating them to very high temperatures, signalling the start of the Sedov-Taylor stage (Sedov, 1959; Taylor, 1950). In both stages radiative cooling is negligible and consequently they can be described by similarity solutions, but the transition between them cannot. Finally at late times, the hot interior of shocked ejecta cools radiatively, and the swept-up shell of ISM and ejecta continue to 'snow-plough' further into the ISM, conserving momentum. Thornton et al. (1998) examine these last two states using a set of 1 dimensional simulations of the evolution of explosions in a uniform ISM, examining in detail the transition from the ST-phase to the snow-plough phase. They claim that radiative cooling is so efficient that typically only 10 per cent of the initial blast energy is transferred to the ISM.

We would in principle like to resolve the earliest phase of the explosions when ejecta dominate, but in this chapter we restrict ourselves to initiate our SNe in the Sedov-Taylor phase. The transition between ejecta-dominated and ST-phase occurs approximately when the shock has swept-up an amount of of ISM mass that is comparable to that originally ejected. In low density regions the size of the bubble where the transition happens may then be relatively large, and it would be worthwhile investigating whether this matters; we intend to do so in future work. Given this limitation, and for the typical ISM densities near the centre of the disk in our simulations, it then suffices to resolve scales of order of a few parsecs to fully capture the cooling of the swept-up shell of ISM (e.g. Cox, 1972), and such a simulation will be able to resolve both the cooling and some part of the adiabatic phase of the remnant.

As such the dependence of our question upon sub-parsec phenomena can be seen only in two key areas, raising the following questions

1. Star formation occurs on these scales, and thus controls the distribution (in time and space) of supernovae. Does this affect the properties of the galactic wind, for example because supernovae explode in high density environments and/or near to other supernovae?

2. The medium that the SNe drive into contains structures on sub-parsec scales, for example cores of molecular clouds. Does this departure from a classical fluid affect the large scale wind?

We will argue that the answers to both the above the questions may indeed be negative, motivating a set of simulations of a highly simplified ISM. Such a simulation would also improve our physical understanding of the role of the individual processes.

On the first question we note that the progenitor of type II core collapse SNe are massive stars (Smartt, 2009) with lifetimes $\sim 1 - 30$ Myrs (Portinari et al., 1998), therefore the majority of SN energy associated with an instantaneous burst of stars with for example a Chabrier (2003) initial mass function will be released after ~ 30 Myrs. It is thought the birth cloud of such stars is likely destroyed before by the combined effects of stellar winds, proto-stellar jets and radiation (e.g. Matzner, 2002), and there is observational evidence for this (e.g. Lopez et al., 2011). Some clouds may form by turbulent compression when overrun by a spiral arm, and may disperse by the same flows that created them in the first place on a short time-scale (Dobbs, 2008, see also Tasker and Tan, 2009).

In any case, when the SNe explodes it will in general not do so inside its natal cloud. For this reason we assume that the SNe explode in typical environments in the disk plane of galaxies. Note however that the SNe may still be clustered rather than Poisson, a complication that we

neglect. Typical giant molecular clouds have a velocity dispersion of ~ 4 km s^{-1} (Scoville and Sanders, 1987; McCray and Kafatos, 1987), which over 10 Myr results in a dispersion of around 40 pc, which is a significant fraction of our box size and the typical distance between molecular clouds.

The second question is delicate, and worthy of significant discussion. We first note that we follow the nomenclature of Wolfire et al. (1995), where the $T \sim 100$K phase of the ISM is called the cold neutral medium (hereafter CNM), the $T \sim 10^4$K phase as the warm neutral medium (hereafter WNM) and the $T \gtrsim 10^6$K phase as the hot ionised medium (HIM). The CNM exists in the form of dense clouds, occupying a very small fraction of the total volume but with a significant fraction of the total mass. These clouds are believed to be in pressure equilibrium (Spitzer, 1956), with the WNM and HIM, thus making their energy budget (pressure $\times$ volume) also a small fraction of the ISM thermal energy. Their pressure support is probably composed of a combination of magnetic, thermal and cosmic ray components. The proportions of energy in thermal, bulk and turbulent motions of the HIM and WNM are still not entirely known though there is consensus that much of the turbulence is supersonic (Elmegreen and Scalo, 2004). A supersonic nature of turbulence in the ISM requires that the energy budget is dominated by inertial terms of the turbulent motions over the thermal and magnetic terms in the WNM and HIM.

Despite their small fraction of the energy budget, however, the cold phase can perform the role of a heat sink. Thermal energy from the warm and hot phases can be transported in to the cold phase via thermal conduction which can be dissipated via the molecular transitions of this cold gas (particularly CO, H_2), metal lines (in particular CI*), and dust. The excited states of the molecules, however, are rather long lived and whilst they are certainly important for star formation they may not significantly cool the WNM phase of the ISM due to its sparse nature (de Jong et al., 1980; Martin et al., 1996). The molecules also play an important role as an absorber of photo-ionizing radiation, however we will ignore radiative driving here. The simulations described in this chapter simply neglect the cold phase, by truncating the cooling function below a value of $T_0 = 10^4$ K. If we were to include cooling below T_0 we would have to include significantly more physics (magnetic fields, heat conduction, diffuse heating): here we want to investigate and understand the simpler yet still complex case of a two-phase medium.

We have also intentionally left out the physics of cosmic rays (see, e.g. Pfrommer et al., 2007) and magnetic fields (e.g. Breitschwerdt and de Avillez, 2007) which may be important in providing support against collapse, particularly in the CNM. Our goal is to understand the resultant ISM without these complications, before discussing the implications of their addition. We would also like to stress that although we have included gravity, we have not included *self-*

gravity (i.e our gravity is time-independent and only self-consistent for the initial set-up) which would be a poor approximation if we had included the dense, cold material of the CNM. Without the CNM gravity does not influence material on scales below the Jeans length of the WNM, equivalent to the scale height of the warm disk.

3.3 Simulations

In the following section we will describe the simulations we have performed of supernova driven outflows from an idealised ISM. Our simulations model the ISM and halo of a disk galaxy in a tall column, with long (z) axis perpendicular to the galactic disk, and co-rotating with the disk material. We use outflow conditions at the top and bottom of the column, and periodic boundary conditions in x and y. We describe the initial conditions of the gas and the physical processes (gravity, cooling and supernova feedback) we have included, and detail their numerical implementation. Finally we describe some tests we have performed on the code and the parameters we chose to explore in our simulation set.

The simulations use a modified version of the FLASH 3 code (Fryxell et al., 2000). FLASH 3 is a parallel, block structured, uniform time-step, adaptive mesh refinement (AMR) code. Its second order (in space and time) scheme uses a piecewise-parabolic reconstruction in cells. Due to the extremely turbulent nature of the ISM in our simulations, we find that FLASH attempts to refine (i.e. to use the highest resolution allowed) almost everywhere within our simulation volume. Therefore we disable the AMR capability of FLASH and run it at a constant refinement level (albeit varied for our resolution studies). To mitigate the overhead of the guard-cell calculations we increase our block size to 32^3 cells per block.

For the gas physics we have assumed a monatomic ideal gas equation of state,

$$p = (\gamma - 1)\rho u \,, \tag{3.6}$$

where u is the specific thermal energy and $\gamma = 5/3$ is the adiabatic index. This deviates slightly from the physical equation of state which should include the transition in mean particle mass that occurs as the atomic hydrogen becomes ionised, but the impact of this simplification is small compared to the other uncertainties in this kind of simulation.

It is worth contrasting this with some other simulations of the ISM. Dobbs (2008) investigates the CNM with self-gravity and magnetic fields in disks but assumes no feedback or cooling. In a series of simulation de Avillez and Breitschwerdt (2004, 2005a,b) uses a set up similar to ours, with imposed gravity, cooling, SNe turbulence and magnetic fields in columns through disks of

$1 \times 1 \times 10$ kpc, although the focus is not on the mass loading. More recently the ERIS simulations (Powell et al., 2011) simulated the ISM in a single high redshift dwarf galaxy. Cooper et al. (2008) perform a simulation of the central region of an M82-like starburst galaxy with gravity, cooling and energy injection due to supernovae (although this energy injection is continuous within a central volume, rather than stochastic as in our simulations).

3.3.1 Physical processes

The simplified ISM discussed in Section 3.2.3 is shaped by three fundamental processes: gravity, cooling and energy injection from supernovae, which dominate when we are only considering the WNM and HIM. We stress that our aim is to simplify the problem as much as possible so that we can extract the physical principles. In future works we will experiment with making some assumptions more realistic. Below we discuss the effects and implementation of all these processes.

Gravity

The gas in our simulations is initially in (vertical) hydrostatic equilibrium. In a disk galaxy the gravitational acceleration is induced by the gas and stars in the disk, baryons in the bulge and dark matter (in the halo and possibly the disk, see e.g. Read et al. 2008). Despite these complications, when one moves to the (non-inertial) frame moving locally with the disk, the dominant effective potential lies in the vertical direction, with a scale height of a few hundreds of parsecs. Since the shape of this profile is approximately in accordance with the gaseous one, we model the total gravity of all components (gas, stars, dark matter) as being in proportion to the gaseous component, with a multiplier of the inverse of the gas fraction, $\frac{1}{f_{\rm g}}$, to account for the stellar and dark matter components, i.e. the gravitational potential depends on the gas density through Poisson's equation as

$$f_{\rm g} \nabla^2 \phi = 4\pi G \rho \; . \tag{3.7}$$

We also make a second assumption, namely that the gravitational profile of the disk is fixed in time, $\phi = \phi[\rho_0]$. This is assumed because the minimum temperature of our cooling function (discussed in Section 3.3.1 below) sets the Jeans length on the order of the scale of the disk height, so we do not expect smaller self-gravitating clouds to appear in our simulations. In contrast, in the ISM of the Milky Way small self-gravitating clouds can form, because the ISM does cool to lower temperatures, however the physics of star formation is not the process we wish to address in this chapter.

Other terms we have neglected include those introduced by the Coriolis force across our simulation volume, due to our non-inertial choice of frame,

$$\dot{\mathbf{v}}_{\rm cor} = -2\mathbf{\Omega} \wedge \mathbf{v}\,, \tag{3.8}$$

where Ω is the angular velocity of the galaxy. Our simulations, however, will typically be of such short time scales and volumes that the Rossby number (the ratio of inertial to Coriolis terms) is large. Nevertheless, more complete simulations would include this, along with the time dependent gravitational changes introduced by spiral density waves. Note that our simulations also neglect the velocity shear that is present in a differentially rotating disc.

Radiative cooling

The cooling function $\Lambda(T)$ of $T \sim 10^4 - 10^7$K gas with solar abundances is primarily due to bound-bound and bound-free transitions of ions, whereas above $T = 10^7$K it is largely dominated by bremsstrahlung (Sutherland and Dopita, 1993). Below $T \sim 8000$K there is a sharp decrease by several orders of magnitude, causing a build up of gas in the WNM. Cooling below 8000K is due to dust, metal transition lines such as CI*, and at very low temperatures, molecules.

Whilst the imprint of small features in the cooling function should be observable in the ISM, it is really the cut-off at $T \sim 8000$ K that controls the WNM, and as such we approximate the cooling function with a Heaviside function with a step at $T_0 = 10^4$ K,

$$\rho\dot{u} = \begin{cases} -\Lambda n^2, & T \geq T_0 \\ 0, & T < T_0\,, \end{cases} \tag{3.9}$$

where we in addition assume pure hydrogen gas so that the number density $n = \rho/m_p$, and $\Lambda = 10^{-22}\,\mathrm{erg\,cm^3\,s^{-1}}$ (although this value is varied in a few of the simulations). We implement this very simple functional form so that we can explicitly check the effect of the normalisation of the cooling function, and to make sure that any characteristic temperature of the gas is not due to features in Λ.

The cooling function of Eq. (3.9) results in a cooling time for gas with $T \geq T_0$ of

$$\begin{aligned} t_{\rm cool} &\equiv \frac{m_p u}{\Lambda n} \\ &\approx 660\,\mathrm{yr}\left(\frac{T}{T_0}\right)\left(\frac{n}{1\ \mathrm{cm^{-3}}}\right)^{-1} \times \\ &\quad \left(\frac{\Lambda}{10^{-22}\,\mathrm{erg\,cm^3\,s^{-1}}}\right)^{-1}. \end{aligned} \tag{3.10}$$

Since we have chosen a discontinuous function for our cooling, we implement a scheme in our code which prevents cooling below T_0 (although the hydrodynamic forces can still achieve lower

temperatures adiabatically). This largely prevents the overshoot errors resulting from an explicit solver in this kind of problem.

To test the importance of the choice of cooling function, we also implemented the cooling function appropriate for cosmic gas with solar abundance pattern from Sutherland and Dopita (1993),

$$\Lambda_{\rm SD}(T) = 5.3 \times 10^{-24} \left(T_8^{1/2} + 0.5 f_m T_8^{-1/2} \right) \, \mathrm{erg\,cm^3\,s^{-1}} \,, \tag{3.11}$$

where $T_8 \equiv T/10^8$ K, with $f_m = 0.03$ for low metallicity gas, and $\Lambda = 0$ for $T < 10^4\,\mathrm{K}$. All runs where this cooling function is used are marked 'SD' (see table 3.1). The minimum of this cooling function is at $5 \times 10^7 f_m$ K, where the cooling rate

$$\Lambda_{\rm SD,min} = 1.30 \times 10^{-24} \, \mathrm{erg\,cm^3\,s^{-1}} \,, \tag{3.12}$$

(ignoring the cut-off below 10^4 K). We show in section B that the behaviour of the ISM in our simulations is surprisingly independent on the exact shape of the cooling function $\Lambda(T)$, although it depends on the minimum value at high temperatures $\gg 10^4$ K.

Energy injection by supernovae

The Kennicutt-Schmidt (KS) relation connects observed surface density of star formation in a disk galaxy, $\dot{\Sigma}_\star$, to its gas surface density $\Sigma_{\rm g}$,

$$\dot{\Sigma}_\star \approx 2.5 \times 10^{-4} \Sigma_{\rm g1}^{1.4} \, \mathrm{M_\odot\,yr^{-1}\,kpc^{-2}} \,, \tag{3.13}$$

(Kennicutt, 1998), where $\Sigma_{\rm g1} \equiv \Sigma_{\rm g}/1\,\mathrm{M_\odot pc^{-2}}$. We will use this to set the SFR in our simulations, but we also perform some simulations with an alternative formulation using a higher star formation rate, discussed in Appendix B. Our idealised model of a supernova explosion is the injection of 10^{51} ergs (Cox, 1972) of thermal energy in a small volume, implicitly assuming instantaneous thermalisation of the SN ejecta. The distribution in time of these is taken to be a Poisson process (the Poisson process has the Markov property and so our SNe are independent) with a time independent rate computed from the initial parameters of the disk. For the local spatial distribution of SNe we assume the star formation rate to be proportional to the initial density, i.e.

$$\mathbb{E}[\dot{\rho}_\star \, \mathrm{dV\,dt}] = \dot{\Sigma}_\star \frac{\rho(t=0)}{\Sigma_{\rm g}} \, \mathrm{dV\,dt} \,. \tag{3.14}$$

A consequence of this choice is that if the scale height of the gas profile evolves significantly the distribution of SNe will become inconsistent with the instantaneous mass profile. We discuss this further later.

Given the star formation rate, the associated core-collapse SN rate is computed assuming the stellar initial mass function yields ε_{100} SNe per $100\,\mathrm{M}_\odot$ of star formation. For reference, for a Chabrier (2003) initial mass function with stars with masses $\in [0.1, 100]\ \mathrm{M}_\odot$, of which those with mass in the range $[6, 100]\ \mathrm{M}_\odot$ undergo core collapse, $\varepsilon_{100} = 1.8$.

The final element of the SN prescription is the distribution of the injected energy over the computational grid. The choice of volume over which to spread the thermal energy of the supernovae is influenced by two considerations. If the volume is too large the remnant will evade the adiabatic expansion phase and immediately proceed to the radiative phase (Cox, 1972; Creasey et al., 2011). If the volume is very small the code will require many extra time steps evaluating the initial stages of a Sedov-Taylor blast wave and will perform unnecessary computation[1]. Following Cox (1972), the radius at which the blast wave cools and forms a dense shell is

$$R_s = 15.6 \left(\frac{E_{\mathrm{SN}}}{10^{51}\,\mathrm{erg}}\right)^{3/11} \left(\frac{\Lambda}{10^{-22}\,\mathrm{erg\,cm^3\,s^{-1}}}\right)^{-2/11} \times \left(\frac{n}{1\,\mathrm{cm^{-3}}}\right)^{-5/11} \mathrm{pc}\,, \tag{3.15}$$

however to account for higher densities and the numerical spreading of shocks it is wise to resolve a fraction of this (Creasey et al., 2011).

Taking the above into consideration, for our simulations we spread the thermal energy of each SN over several cells given by the multivariate (3D) normal distribution of standard deviation 2 pc, consistent with being smaller than the cooling radius of Eq. (3.15) for densities $n < 77\,\mathrm{cm^{-3}}$ ($\rho < 1.3 \times 10^{-22}$ g cm^{-3}).

Time-stepping

In addition to the numerical considerations described above, we also needed to make some adjustments to the time step calculation in FLASH. The default time-stepping scheme in FLASH uses a Strang-split method (Strang, 1968, an operator splitting method where the hydrodynamic update occurs in two half steps, with the order in which the Riemann-solver operates reversed from xyz to zyx between the first and the second half step). Source terms such as the injection of SN energy, are evaluated at the end of each half step, after the Riemann solver has been applied. This makes the implementation of the supernova energy injection problematic, as the thermal energy in a cell can increase by many orders magnitude followed by a hydrodynamic step before a new time step is calculated. The latter hydrodynamic step then almost inevitably violates the CFL

[1] To get some idea of the computational requirement of this, we recall that the velocity of a 3 dimensional Sedov blast wave evolves as $v \sim t^{-3/5}$. Substituting this into the Courant-Friedrichs-Lewy (CFL) condition we see that the number of time steps required to reach a given radius is proportional to that radius.

condition and the Riemann solver fails to converge. We avoid this by making the timestep limiter for the supernova source terms *predictive*, i.e. we utilise the foreknowledge of the pre-computed SNe times to recognise when a supernova will occur before the end of the timestep given by the CFL condition and return a timestep of either up to just before the supernova, or of the predicted CFL timestep after the supernova has occurred, whichever is smaller.

Code tests

A set up as complex as this requires some testing to confirm that the physical processes have been correctly implemented. As such we ran a number of simpler problems as well as the convergence tests in Appendix B.

In order to test our hydrostatic set up we simulated the disk without supernovae for several dynamical times. Some sub-percent evolution in the gas occurred, almost certainly due to our evaluation of the analytic solution for the gravitational potential and density at the centres of cells producing some discretisation error. The implementation of the cooling function was tested largely in Creasey et al. (2011). We follow a similar approach where we made the cooling rate for each cell an output of our code which was compared with the instantaneous rate predicted from the temperature and density of each cell (again there were small differences due to the comparison of an instantaneous rate with the average from an implicit scheme).

The implementation of the individual SN in our set-up is largely similar to that of the Sedov-Taylor blast wave solution implemented in FLASH as a standard test, and compared to the similarity solution. We calculate the location and times of SNe explosions ahead of the simulation, and verify that the code indeed injects them correctly.

We initially also performed these calculations using the GADGET simulation code (Springel, 2005) that has been successfully applied to many cosmological simulations. Unfortunately the adaptive time-stepping algorithm proved problematic for correctly following the blast waves, and we noticed similar problems as recently highlighted by Durier and Dalla Vecchia (2012): particles may be on long time-steps in the cold ISM, and largely fail to properly account for being shocked by the blast wave from a nearby particle. Durier and Dalla Vecchia (2012) addressed this problem with a time step propagation algorithm, however we did not have this nor the algorithm of Saitoh and Makino (2009) available and the alternative of a global timestep would have been far too computationally expensive due to the large dynamic range in time steps required in the evolution of the blasts. As such we used the global adaptive time stepping algorithm of FLASH.

3.3.2 Initial conditions

Our initial setup is a tall box poking vertically through an idealised disk profile. We choose the long axis in the z-direction in order to capture a multiple of the gravitational scale height of the disk. The profile is a 1-dimensional gravitationally bound isothermal one with gas surface density $\Sigma_{\rm g}$. As discussed in section 3.3.1 we have excluded the effects of shear (due to the Coriolis force in the disk) and large scale motions which may drive some turbulence down to the small scales. The gas density is

$$\rho(z; t = 0) = \frac{\Sigma_{\rm g}}{2b} \mathrm{sech}^2 \left(\frac{z}{b}\right) , \tag{3.16}$$

and the corresponding gravitational acceleration follows from Eq. (3.7),

$$\nabla\Phi = 2\pi G \Sigma_{\rm g} f_{\rm g}^{-1} \tanh \left(\frac{z}{b}\right) . \tag{3.17}$$

Setting the gas temperature to T_0 (which is also the base of the imposed cooling function) and assuming the gas to be initially in hydrostatic equilibrium, the scale height is

$$\begin{aligned} b &= \frac{f_{\rm g} k_{\rm B} T_0}{{\rm m_p} \pi G \Sigma_{\rm g}} && (3.18) \\ &\approx 61 \left(\frac{f_{\rm g}}{0.1}\right) \left(\frac{\Sigma_{\rm g}}{10\,{\rm M_\odot\,pc^{-2}}}\right)^{-1} {\rm pc}\,, && (3.19) \\ & && (3.20) \end{aligned}$$

where numerically

$$\rho(z; t = 0) \approx 3.4 \left(\frac{\Sigma_{\rm g}}{10\,{\rm M_\odot\,pc^{-2}}}\right)^2 \left(\frac{f_{\rm g}}{0.1}\right)^{-1} \mathrm{sech}^2 \left(\frac{z}{b}\right) {\rm m_p\,cm^{-3}}\,. \tag{3.21}$$

The (vertical) dynamical time of the disk is

$$\begin{aligned} t_{\rm dyn} &= \sqrt{\frac{b f_{\rm g}}{G \Sigma_{\rm g}}} \\ &\approx 12 \times 10^6 \left(\frac{f_{\rm g}}{0.1}\right) \left(\frac{\Sigma_{\rm g}}{10\,{\rm M_\odot\,pc^{-2}}}\right)^{-1} {\rm yr}\,, && (3.22) \end{aligned}$$

and the ratio of the dynamical time to the cooling time

$$\begin{aligned} \zeta &\equiv \frac{t_{\rm dyn}}{t_{\rm cool}} \\ &\approx 1.7 \times 10^5 \left(\frac{\Lambda}{10^{-22}\,{\rm erg\,cm^3\,s^{-1}}}\right) \left(\frac{\Sigma_{\rm g}}{10\,{\rm M_\odot\,pc^{-2}}}\right) . && (3.23) \end{aligned}$$

The exact gravitational potential is given by

$$\Phi(z) = 2\pi G b \Sigma_{\rm g} f_{\rm g}^{-1} \log\cosh \left(\frac{z}{b}\right) , \tag{3.24}$$

	Range of values explored	Fiducial value
$\Sigma_{\rm g}\,({\rm M}_\odot\,{\rm pc}^{-2})$	2.5, 3.23, 4.17, 5.39, 6.96, 8.99, 11.61, 15, 30, 50, 150, 500	11.61
$f_{\rm g}$	0.01, 0.015, 0.022, 0.033, 0.050, 0.1, 0.2, 0.5, 1.0	0.1
$\dot{\Sigma}_\star$	Eq. (3.13), (B.1)	Eq. (3.13)
$\Lambda\,({\rm erg\,cm^3 s^{-1}})$	1, 2, 4, 8, 16×10^{-22}, SD	10^{-22}
Resolution (pc)	0.78, 1.56, 3.12, 6.25	-

Table 3.1: Parameter variations in our simulation. Each simulation is initialised with an isothermal profile with a surface density of $\Sigma_{\rm g}$ in cold gas and gas fraction of $f_{\rm g}$ (i.e. a total mass density of $\Sigma = \Sigma_{\rm g}/f_{\rm g}$). Star formation proceeds either in a pure Kennicutt-Schmidt prescription, or the dynamical time variation in Eq. (B.1). Cooling above 10^4 K proceeds at a rate Λ and we study the simulations at several resolutions to test for convergence.

and the pressures and temperatures for hydrostatic equilibrium is

$$p = \pi G \Sigma_{\rm g} f_{\rm g}^{-1} b \rho(z) \tag{3.25}$$

$$\approx 3.3\times10^4 \left(\frac{\Sigma_{\rm g}}{10\,{\rm M}_\odot\,{\rm pc}^{-2}}\right)^2 \times \tag{3.26}$$

$$\left(\frac{f_{\rm g}}{0.1}\right)^{-1} {\rm sech}^2\left(\frac{z}{b}\right)\,{\rm K\,cm^{-3}}\,. \tag{3.27}$$

Finally, the hydrostatic temperature for all our disks is chosen to be

$$T_0 = 10^4\,{\rm K}\,. \tag{3.28}$$

3.3.3 Numerical parameters and boundary conditions

To produce simulations of a realistic ISM we make the following choices of parameters. In terms of resolution we must have cell sizes fine enough to capture the cooling of supernova remnants (Eq. 3.15) yet the simulation volume needs to be large enough to capture several scale heights of the star forming disk. In terms of gas fractions and gas surface densities we choose values approximating those in the solar neighbourhood and some variations. In practise we chose fiducial values for the disk parameters ($\Sigma_{\rm g} = 11.61\,{\rm M}_\odot\,{\rm pc}^{-2}$, $f_{\rm g} = 0.1$) and examine this reference model in detail. For reference, the gas surface density of the solar neighbourhood of the Milky

Way has been estimated at $\Sigma_{\rm g} = 13.2\ {\rm M}_\odot\,{\rm pc}^{-2}$, with a dynamical density of $\Sigma_\star = 74\ {\rm M}_\odot\,{\rm pc}^{-2}$ (Flynn et al., 2006).

In order to test the dependence of winds on the disk properties we perform a slice of the parameter space varying $\Sigma_{\rm g}$ and $f_{\rm g}$ (see Table 3.1). Not all parameter combinations are explored, as we cut out the simulations with very small scale heights (due to resolution constraints) and large scale heights (due to the finite box size). The dependence of the results on cooling, resolution, box size and star formation rate can be seen in Appendix B.

All our simulations were conducted in box sizes of $200 \times 200 \times 1000$ pc with constant cell sizes. All cells were cubic, and in the vertical direction the number of cells for our default resolution is 640, with corresponding cell size of 1.6 pc. We vary the numerical resolution using 160,320,640,1280 cells in z, with corresponding cell sizes ranging from $6.25 - 0.78$ pc. These simulations are denoted L2, L3, L4, L5 respectively. We also test the effect of adjusting our box size with simulations of $2\times$ and $4\times$ the width (see Appendix B).

The gas surface density $\Sigma_{\rm g}$ is varied from $2.5{\rm M}_\odot\,{\rm pc}^{-2}$ to $15{\rm M}_\odot\,{\rm pc}^{-2}$ in 8 logarithmically spaced steps followed by three additional steps of 30, 50 and 500 ${\rm M}_\odot\,{\rm pc}^{-2}$. Notably some of these are below the minimum surface density threshold for star formation of Schaye (2004) of $3 - 10\ {\rm M}_\odot\,{\rm pc}^{-2}$ (although there is evidence that star formation proceeds below this level, e.g. Bigiel et al., 2008). The gas fraction $f_{\rm g}$ was varied from 0.01-0.05 in 5 logarithmic steps followed by additional steps of 0.1, 0.2, 0.5 and 1.0. The cooling function Λ was varied from 3.9×10^{-25} to $1.6 \times 10^{-21}\ {\rm erg\,cm^3\,s^{-2}}$, and we ran additional models with the Sutherland and Dopita (1993) cooling function as parameterised in Eq. (3.11). Each of our experiments is evolved over 20 Myr (typically thousands of cooling times) in order to simulate many SNe.

3.4 Results

In this section we discuss the results of the simulations described in the previous section. We begin with a discussion of a single snapshot, allowing us to investigate the instantaneous properties of the idealised ISM and outflow. We then move to looking at the evolution of a simulation and the statistics we can measure before finally investigating the effects of all the parameters discussed in the previous section.

3.4.1 Fiducial run

The impact of SNe depends strongly on whether they explode in the dense gas or in the more rarefied HIM. The supernovae in the disk blast bubbles in the ISM and compress the warm gas

into thin sheets. When supernovae explode in the rarefied regions, either at the edge of the disk or inside previously evacuated bubbles, the heated gas pushes out of the central region and then rapidly escapes from the simulation volume in a rarefaction zone above and below the disk. Such a rarefaction zone is the ISM portion of the galactic wind (i.e. the gas whose thermal energy far exceeds the potential barrier to escaping the disk). Some warm clouds are dragged along with this wind. A movie of this simulation is available online along with time dependent versions of some of the other figures [2]

In Figure 3.1 we show an $x - z$ slice of the fiducial run, at a time of 12 Myr. We can see that the combined action of multiple SNe has disrupted the disk considerably, with the warm gas squeezed into dense sheets and globules entrained in outflowing gas, and around half the volume now occupied by a hot tenuous phase. The gas appears to be in well defined phases, an HIM (greens and yellows) and a WNM (dark blue) with little gas at intermediate temperatures (see also Fig. 3.2). Notably there is more temperature variation in the hot phase (a few orders of magnitude) than in the WNM (which is all close to 10^4 K). The density plot also appears to show two distinct phases, a high and low density medium, where the high densities show up in the temperature plots as WNM. In the velocity plot we can see a bulk vertical outflow from the disk, with velocity correlating with height. The pressure plot shows a dramatically lower dynamic range than either the temperature or density plots, but has some distinctive shells due to individual SN remnants. The impression of a volume in quasi pressure equilibrium is reinforced by the profile plot where the temperature and density fluctuations appear to anti-correlate, resulting in comparatively small pressure variations.

Above the plane of the disk the outflow is also very inhomogeneous, containing significant turbulence as well as some warm clouds or globules with cometary shapes. The corresponding locations in the density and pressure panels reveal that these clouds are also overdense and slightly under-pressured. In velocity the clouds appear to be receding from the disk at a lower velocity than the HIM, that is rushing past them at around 100 km s^{-1}. The hot wind appears to be stripping the edges of these warm clouds, as evidenced by their tails.

After only 12 Myr the original disk has undergone considerable disruption but is still observed as a connected feature in this slice (and the majority of the mass of the simulation remains in the central region). The disk has also been disrupted asymmetrically, with more mass pushed into the lower half space by the stochastic locations of the SNe. The externally imposed gravity will ultimately return this mass to the base of the potential, yet the combined action of the supernovae has been enough to displace it.

[2] See `http://astro.dur.ac.uk/~rmdq85`.

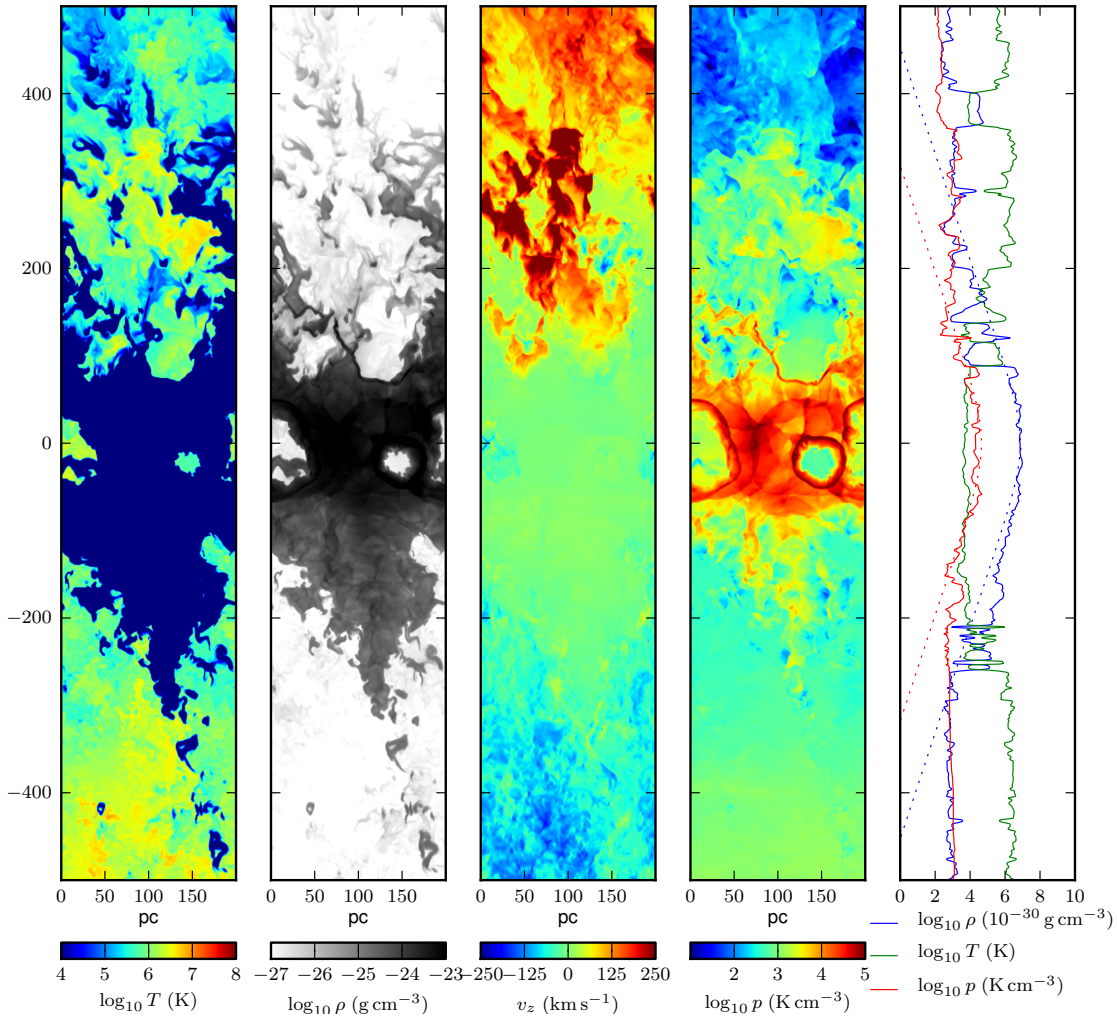

Figure 3.1: Left to right, temperature, density, vertical velocity and pressure plots through a slice of the simulation, at time 5 Myr. Temperature is coloured between $10^4 - 10^8$ K, density between $20^{-27} - 10^{-23}$ g cm^{-3}, v_z from -250 to 250 km s^{-1} and pressure from $10 - 10^5$ K cm^{-3}. On the far right is the profile of density, temperature and pressure along a vertical line through the centre of the slice. In *dotted blue* and *red* we show the hydrostatic density and pressure profiles at $t = 0$. Around $z = 0$ we can see the disrupted disk in the temperature and density plots, with the warm gas squeezed into sheets and globules, and a significant fraction of the volume now consumed by a hot ($\sim 10^{6.5}$ K) sparse phase. In the velocity plot we can see a bulk vertical outflow from the disk. The outflow is inhomogeneous, entraining significant turbulence as well as some warm gas, swept away from the disk.

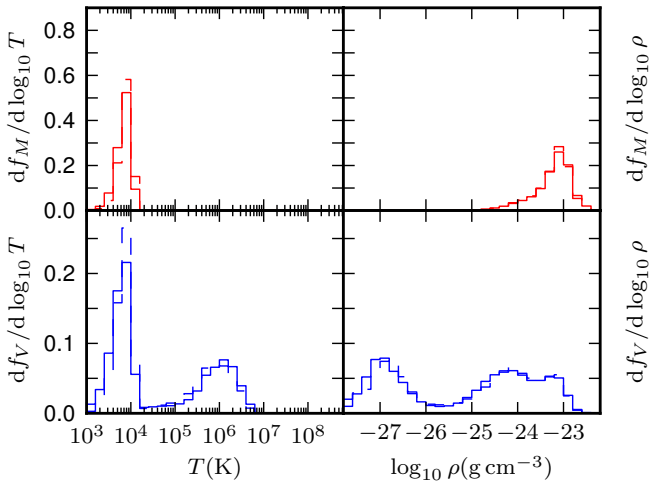

Figure 3.2: Density and temperature probability distributions for the fiducial run (the simulation of Fig. 3.1) at 10 Myr, *solid, dashed* and *dotted* lines denote the L4, L3, L2 resolution runs, respectively, and are almost indistinguishable for many of the bins. *Upper panels* show the mass fractions in temperature and density, *lower panels* show the corresponding volume fractions. We see a clear bimodality between the WNM (at low temperature and high density) and the HIM (at high temperature and low density). Almost all of the mass is in the WNM phase, but a significant fraction of the volume in the HIM.

Whilst we have run these simulations at different resolutions, it is important to note that the turbulent and chaotic nature of these simulations results in specific features such as individual clouds being at different locations or indeed absent between the different runs. Global properties, however, such as the outflow mass and temperature will be less stochastic, and we devote Appendix B to the convergence study of these properties. In general these simulations are numerically well converged. In the following figures we also include a few convergence comparisons where space allows.

The value of the ISM pressures in our simulations are around $10^3\,\mathrm{K\,cm^{-3}}$, comparable to the pressure in simulations such as Joung and Mac Low (2006) and Joung et al. (2009). Estimates of the pressure of a star forming ISM vary, Bowyer et al. (1995) find a pressure of around $2 \times 10^4\,\mathrm{K\,cm^{-3}}$ in the local bubble, although in the centre of the highly star forming region of 30 Doradus, Lopez et al. (2011) estimate a pressure of $\sim 7{\times}10^6\,\mathrm{K\,cm^{-3}}$ from IR dust measurements.

Figure 3.1 suggests that the hot and warm phases are quite distinct, and we test this by inspecting the volume fractions in Fig. 3.2. The warm phase is very tightly distributed below 10^4K, as we might expect since the only mechanism for cooling here is by adiabatic expansion. The lack of

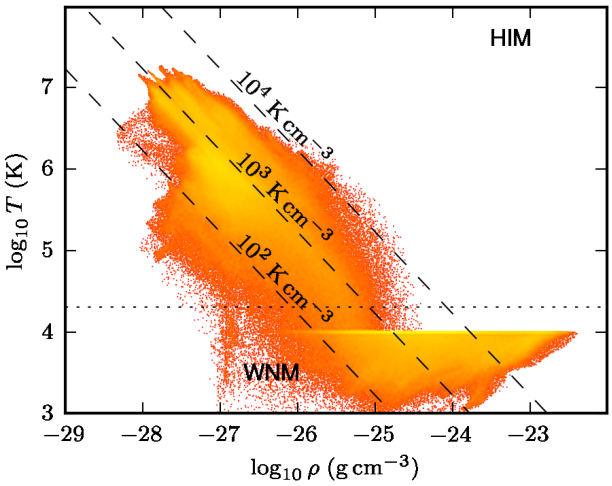

Figure 3.3: Density-temperature histogram for the fiducial model at L3 resolution. Each pixel is coloured by the fraction of cells at given $\rho - T$. *Dashed black lines* indicate lines of constant pressure, $p/k_{\rm B} = 10^2, 10^3, 10^4$ K cm^{-3} as indicated in the panel. We see the simulation volume is in approximate pressure equilibrium, with a bimodality in the gas phases into an HIM and WNM that we have segregated approximately with the *dotted black line*, a temperature cut at $20,000$ K. Above 10^4K and $\rho > 10^{-24}$g cm^{-3} the cooling time of the gas is very short and the gas quickly cools to 10^4K. Some gas reaches lower than this temperature due to adiabatic expansion.

intermediate temperatures suggests they have very short cooling times, which is consistent with a pressure equilibrium view. The hot tail of the distribution suggests the hottest gas either mixes with cooler gas or escapes from the simulation volume.

Figure 3.3 is the density-temperature phase diagram for the fiducial model at L3 resolution (3 pc cells), which is broadly described by two regions. In the lower right, lying horizontally at a nearly constant temperature of order $T_0 = 10^4$ K (the base of the cooling curve) is the WNM, which contains most of the mass. The HIM is in the upper left. On examination of time dependent movie of this simulation we see the structure in the HIM is due to multiple supernovae, each supernova blast forms a 'finger' roughly along an isobar, and as these shocked regions evolve and expand these lines descend to lower temperatures forming the mixture in the lower right region. As one looks to lower temperatures the fingers start to merge and become indistinct. We see that instantaneously we have near pressure equilibrium within approximately one order of magnitude, and that a significant fraction of the volume is in the HIM.

The characteristic temperature of the HIM

It is interesting to consider where the characteristic temperature of the hot phase in Fig. 3.2 may appear from. We recall that the cooling function used in these simulations was intentionally chosen to be independent of temperature for $T \geq T_0 = 10^4$ K, and as such cannot by itself introduce a characteristic temperature scale, yet in Fig. 3.2 the hot gas quite clearly has a well defined peak temperature $\sim 10^6$ K. This is much higher than the escape temperature for the simulation volume ($\sim 10^5$ K, derived from Eq. 3.24), and as our SNe are injected just as thermal energy, there is no characteristic temperature for this gas. Since all of the hot gas in our simulations has been produced by the action of SNe it is reasonable to suppose that the temperature of this phase may be determined by the transition from the adiabatic to the momentum driven phases, as described by Cox (1972); Chevalier (1974) and Larson (1974).

In this explanation, the supernovae would rapidly expand in the adiabatic phase until the action of cooling relative to expansion causes the growth of the remnant to decelerate, and the edge to form a cold dense shell. This shell still expands, but at a considerably reduced rate, driven primarily by the momentum of the shell. We expect the adiabatic phase to remain approximately spherical due to the short sound crossing time within the hot volume, however when the blast enters the momentum driven phase, the cooling shell is unstable and the remnant can become quite asymmetric. If the edge of the remnant reaches other sparse material the hot interior of the remnant can leak out (i.e. a 'chimney' such as those seen in Ceverino and Klypin, 2009), otherwise the hot material will gradually be consumed into the dense shell as it radiates away its pressure support.

The post shock temperature, T_s, of the hot remnant at which the 'sag' occurs (when cooling dominates over adiabatic expansion) was calculated in Cox (1972) as

$$T_s \approx 2.0 \times 10^6 \left(\frac{n}{1\ \mathrm{cm}^{-3}}\right)^{4/11} \left(\frac{E_{\mathrm{SN}}}{10^{51}\ \mathrm{erg}}\right)^{2/11} \times \left(\frac{\Lambda}{10^{-22}\mathrm{erg\,cm^3\,s^{-1}}}\right)^{6/11} \mathrm{K}\,. \tag{3.29}$$

The obstacle which radiates away the energy of the SN is the warm disk gas of Fig. 3.1. Taking a mean density of these from Fig. 3.2

$$n = 3\ \mathrm{cm}^{-3}\,, \tag{3.30}$$

($\rho = 5 \times 10^{-24}$ g cm^{-3}) we expect a characteristic temperature of the remnants to be $T_{\mathrm{hot}} \approx 3 \times 10^6$ K, very close to our HIM temperature of $\sim 10^6$ K.

Another interesting application of Eq. (3.29) is to estimate the mass heated by a single supernova before it ends the adiabatic phase. By finding the amount of mass required to absorb the

thermal energy of a supernova we derive

$$\begin{aligned} M_{\rm hot} &= \frac{2}{3}\frac{m_{\rm p}E_{\rm SN}}{k_{\rm B}T_s} \\ &= 1350\,{\rm M}_\odot \left(\frac{T_s}{3\times10^6{\rm K}}\right)^{-1} \frac{E_{\rm SN}}{10^{51}{\rm erg}}\,, \end{aligned} \tag{3.31}$$

where we have neglected the initial thermal energy of the heated gas, the SN ejecta themselves (see also Kahn, 1975), and assumed that none of the SN energy has yet been lost radiatively. For comparison, in the model of Efstathiou (2000), a supernova evaporates a similar mass $M_{\rm ev} \sim 540\,{\rm M}_\odot$ of cold clouds. If all this hot gas were to escape from the simulation without entraining any other material we would derive a mass loading of

$$\begin{aligned} \beta &= \frac{M_{\rm hot}\varepsilon_{100}}{100\ {\rm M}_\odot} \\ &\approx 13\varepsilon_{100}\left(\frac{n}{3\ {\rm cm}^{-3}}\right)^{-4/11}\left(\frac{E_{\rm SN}}{10^{51}\ {\rm erg}}\right)^{9/11}\times \\ &\quad \left(\frac{\Lambda}{10^{-22}{\rm erg\,cm^3\,s^{-1}}}\right)^{-6/11} \end{aligned} \tag{3.32}$$

$$\begin{aligned} &\approx 13\varepsilon_{100}\left(\frac{\Sigma_{\rm g}}{10\,{\rm M}_\odot\,{\rm pc}^{-2}}\right)^{-8/11}\left(\frac{f_{\rm g}}{0.1}\right)^{4/11}\times \\ &\quad \left(\frac{E_{\rm SN}}{10^{51}\ {\rm erg}}\right)^{9/11}\left(\frac{\Lambda}{10^{-22}{\rm erg\,cm^3\,s^{-1}}}\right)^{-6/11}\,, \end{aligned} \tag{3.33}$$

where in Eq. (3.32) we have used the warm cloud density $n = 3\ {\rm cm}^{-3}$ from Eq. (3.30), and in Eq. (3.33) we have used the hydrostatic mid-plane density from Eq. (3.21). The mass loading is higher at lower surface densities (and also volume densities), at higher gas fractions, and for gas that cools more slowly, and increases with the SN energy injected. If all the gas escapes at $T = T_s$ then this is an upper bound for the mass loss, since some energy will be converted to other forms such as radiation and turbulent motion, and for this simulation we do find the measured β is significantly below this (see section 3.5).

In this section we have described a snapshot of a simulation of a patch of the ISM with similar parameters to that of the solar neighbourhood. We have reproduced a warm and hot phase in approximate pressure equilibrium, with a value similar to that estimated for the local volume. We have explored the relation between the temperature of the hot phase and related this to the density of the warm phase via the energy of each SN and the cooling time of the gas.

3.4.2 Time dependence

We now turn our attention to the time dependence within our simulation. We have seen in Fig. 3.1 that our idealised disk is disrupted by the energy injection from supernovae, and we are interested

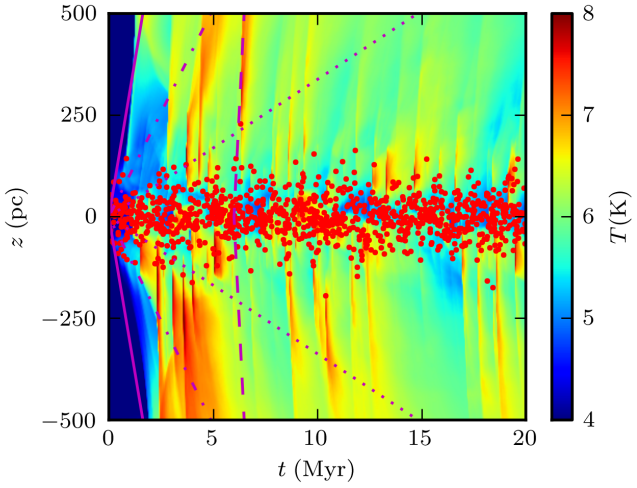

Figure 3.4: Volume weighted mean temperature as a function of height and time, for the fiducial disk parameters yet in a wider box of $800 \times 800 \times 1000$pc. At each height we have taken the average over a horizontal slice. Superimposed are *red dots* indicating the locations and times of the SN events. As the simulation progresses the activity of many SNe shock heat gas and drive a vertical wind from the disk at around $300\mathrm{km\,s^{-1}}$. *Dotted, dot-dashed, solid* and *dashed* magenta lines denote outflows of 33, 100, 300 and 1000 $\mathrm{km\,s^{-1}}$ respectively. Subsequent and around each supernovae can be seen a pulse (in orange) in the temperature. After a short ($t < 1$ Myr) flurry of supernova activity within the disk ($z = \pm 53\mathrm{pc}$), the shocked regions begin to combine and rise out of the disk and the simulation volume. Occasionally, individual supernovae high above the disk (where the gas density is low) make a significant individual contribution to the wind. The 1000 $\mathrm{km\,s^{-1}}$ line has been offset to start at 6 Myr to be compared with the propagation of one of such temperature pulses.

in the evolution that results from this. The injected energy can be converted into a number of forms, heating of the warm phase, the thermal energy of the hot phase, the mechanical energy of turbulence and the wind, the gravitational potential of the gas as it is lifted out of the disk, and the photons lost through radiative cooling. It is worth recalling that cooling is one of two ways in which energy can leave the simulation volume, the second being the advection of mass across the vertical boundaries of the simulation, taking with it the thermal, mechanical and gravitational potential energy of the gas.

Fig. 3.4 is a 'space-time' plot of the onset of the outflow: time is along the horizontal axis,

and the projected mean temperature, $\bar{T}$, as a function of height is colour coded and shown on the vertical axis, red dots correspond to the times and location of individual SN injection events. The initially hydrostatic gas at temperature $T = T_0$ seen at the far left of the figure is quickly replaced by gas at a range of temperatures. The dark blue coloured band, corresponding to $\bar{T} \approx T_0$, episodically widens as a function of time, as the disk puffs up. Gas with a mean temperature $\bar{T} \sim 10^6$ K is seen to stream out of the disk at a range of velocities. From Fig. 3.2 we recall that there is actually very little gas by mass at 10^6 K: this gas is a mixture of HIM with entrained WNM, and the mean temperature value is seen due to projection. Around each supernova a plume of hot gas can be seen (cyan against the colder dark blue gas). At late times these plumes combine and drive the galactic wind.

Comparing with the velocity lines we can see the evolution of the outflow velocity with time, with many structures with velocities in the range of 30-300 $\mathrm{km\,s^{-1}}$. Superposed, however, are some extremely steep (w.r.t. time, i.e. high velocity) discontinuities where much of the simulation volume rapidly experiences an increase in temperature. These appear to propagate from individual SNe, and race away from the disk with velocities in excess of $1000\ \mathrm{km\,s^{-1}}$, consistent with a sudden pressurisation of the hot phase of the ISM[3]. This increased pressure causes stripping from the warm material as shocks drive in to the warm clouds, adding to the mass of the hot phase.

To analyse our simulations we reduced our data set down to the following parameters, listed below. These are chosen to give us a broad overview of the evolution of the star forming disk, rather than information on the individual cells and clouds. For these parameters there is some freedom of definition, e.g. when one attempts to measure the pressure one could take the mid-plane pressure, the pressure within the star forming scale height b, the mean pressure within the simulation volume, or the mean pressure within a volume adjusted by some measure of the current disk scale height. In all cases we have attempted to choose a definition which strikes the balance between reducing stochasticity (some candidate measures show considerably more noise than others) and ease of physical intuition.

1. Mass ejection, $\Sigma_{\mathrm{ej}}(t)$, is the amount of gas ejected from the disk per unit area. This is calculated from the mass advected through the boundary at $z = \pm 500\mathrm{pc}$, divided by the surface area of the simulated column. This quantity is used in the calculation of the cosmologically important quantity $\beta = \dot{\Sigma}_{\mathrm{ej}}/\dot{\Sigma}_\star$ where we have identified the mass ejected from the idealised disk with the mass ejected from the galaxy. To achieve the nearest correspondence we try to maximise the volume we are measuring the loss from, i.e. the entire simulation

[3]For reference, the temperature that correspond to a given sound speed c is $T = 7.3 \times 10^7\ \mathrm{K}\ (c/1000\ \mathrm{km\ s^{-1}})^2$.

volume. The corresponding normalised quantity is the fraction of gas remaining in the disk, $f_\Sigma \equiv 1 - \Sigma_{\rm ej}/\Sigma_{\rm g}$.

2. Cold gas/Hot gas surface density is the remaining cold/hot gas surface densities in the simulation volume, and in combination with the mass ejected, sum to the initial gas surface density $\Sigma_{\rm g}$.

3. Cold volume fraction, $f_{\rm cold}$, is the volume fraction of cold gas, sometimes quoted in terms of the porosity

$$P = -\log f_{\rm cold}\,, \tag{3.34}$$

(Silk, 2001). We distinguish between cold and hot phases at a cut-off of $2T_0$ (i.e. twice the lower limit of our cooling function). Though the choice of $2T_0$ may seem arbitrary, it is apparent from Fig. 3.2 that the bi-modality of the warm and hot phases is quite strong, so the dependence of our results on the choice of temperature cut-off is rather low. Since the effectiveness of SNe in driving feedback is highly suppressed in dense (and cold) regions, the volume filling factor largely determines the probability that an individual supernova will explode in the hot phase. The volume we study is $z \in [-250, 250]$ pc, as we are not interested in the hot gas far from the plane of the disk (where SNe do not occur).

4. Pressure, p, is the mean pressure in the entire simulation volume. Hot material from the disk is ejected by a mean pressure gradient to the edge of the simulation volume, however the stochastic nature of supernova events creates a significant variation over small time scales and large spatial scales[4] and thus it is desirable to smooth the pressure estimate over as large a volume as possible.

5. Outflow velocity, $v_{\rm edge}$, is the mean mass-weighted outflow velocity at the edge of the simulation volume,

$$v_{\rm edge} = \frac{1}{2}(\langle v_z \rangle_{500{\rm pc}} - \langle v_z \rangle_{-500{\rm pc}})\,. \tag{3.35}$$

These choices are made to allow the combination of this term with the mass ejection rate to make one component of the energy conservation equation, the vertical kinetic energy imparted in the wind $\dot{E}_{\rm wind,z} \equiv \frac{1}{2}\dot{\Sigma}_{\rm ej} v_{\rm edge}^2$. This quantity fluctuates with the considerable amount of turbulence within the simulation.

[4]The pressure equilibrium predicted by Spitzer (1956) holds over smaller spatial scales where the supersonic turbulence decays over the sound crossing time.

6. Half-mass height, $\lambda_{1/2}$, is defined as the height where $z \in [-\lambda_{1/2}, \lambda_{1/2}]$ contains half the original gas mass of the disk,

$$\lambda_{1/2} = \min \left\{ z' : \int_{-z'}^{z'} \langle \rho \rangle_z \, \mathrm{dz} > \frac{1}{2} \Sigma_\mathrm{g} \right\} . \tag{3.36}$$

At the start of the simulation this is related to the scale height by our choice of isothermal density profile, at $\lambda_{1/2} = \frac{1}{2} b \log 3$. Large outflows will 'puff-up' the disk to greater scale heights, at late times this would become inconsistent with our star formation profile.

7. Effective cooling rate, η_eff, is the total radiative cooling rate in the simulation volume divided by the mean SNe energy injection rate,

$$\eta_\mathrm{eff} = \frac{\int_V \Lambda n^2 \mathrm{dV}}{\int_\mathrm{area} E_\mathrm{SN} \epsilon_{100} (\dot{\Sigma}_\star / 100 \mathrm{M}_\odot) \mathrm{dA}} . \tag{3.37}$$

Conservation of energy implies that all of the energy not released as radiation must end up either in the wind or as gravitational potential energy. Due to the discrete nature of time sampling with snapshots (i.e. for many of the quantities such as cooling and we have instantaneous measurements of their time derivatives and not measurements of the integrated quantities themselves) there is some error on our estimate of the integrated quantities. Most susceptible is the estimate of the cooling rate: the tail of high-density gas seen in the density probability distribution function of Fig. 3.2, cools very rapidly, and our time sampling means its contribution to cooling is under-estimated. We will inevitably miss some cooling that would have occurred outside the simulation volume (although much of this gas is tenuous and will have a long cooling time, little gas remains dense in the outflowing material). Nevertheless our high snapshot frequency run gives us energy conservation to $\sim 1\%$ and confidence that we can accurately measure the outflowing components from the low frequency runs (energy conservation in the simulation itself is of course much better than this.)

In Figure 3.5 we inspect these parameters for our fiducial run. For the first 1 Myr, the most notable feature is the rapid rate of cooling (cyan curve) as all the supernova blast waves propagate into the disk and radiate away a significant fraction of their energy as they thermalise. The fraction that is radiated suddenly drops corresponding to a growth in the volume of hot gas (the porosity). The height of the disk remains approximately constant. As the simulation evolves, the remaining gas fraction declines (black curve) as gas leaves the simulation volume (blue curve). The mass lost from the simulation appears to be a nearly linear function of time at this stage, suggesting a constant outflow rate, which we investigate further in section 3.5.

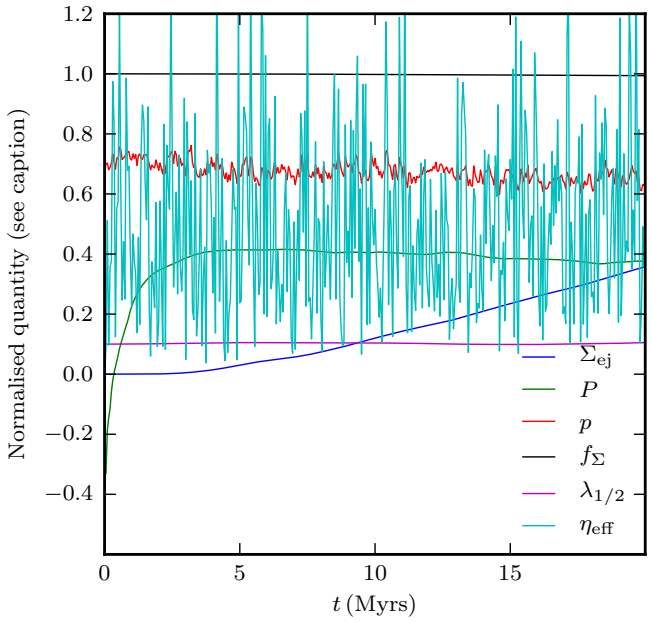

Figure 3.5: Generation of an outflow in the run in Fig. 3.4 as characterised by the evolution of normalised quantities described in (1)-(7) in the text. After a transient initial stage of ~ 5 Myr, gas starts to be ejected at a nearly constant rate of $\sim 0.01\,\mathrm{M}_\odot\,\mathrm{Myr}^{-1}\,\mathrm{pc}^{-2}$. The *dark blue line* is the cumulative mass ejected per unit area, in units of $0.2\mathrm{M}_\odot\,\mathrm{pc}^{-2}$. The porosity $P = -\log(f_{\rm cold})$ of hot gas builds very quickly, *green line* is $0.5 + 0.2P$, implying a filling factor of the HIM of approximately 50%. The *red line* is the mean pressure, $\log_{10}\left(p/10^3\mathrm{K\,cm}^{-3}\right)$, disturbed from its initial value of 0.7×10^3 K cm^{-3} in the base of the disk by action of the SNe. *Black line* is the fraction of gas remaining in the simulation. The *magenta line* is the evolution of the scale height, Eq. (3.36), in terms of $0.1\lambda_{1/2}(t)/\lambda_{1/2}(0)$. The *cyan line* is $\eta_{\rm eff}$, the instantaneous cooling rate as a fraction of the mean SNe energy injection rate. During the first ~ 2 Myr the porosity in the simulation rapidly increases, after which the material begins to be ejected from the simulation in a relatively linear fashion. There are periods where the cooling rate increases dramatically by a factor ~ 10, which are closely related to SN energy injection events. Energy injection has not significantly puffed up the disk.

3.4.3 Outflow as a rarefaction zone

A characteristic feature of both simulated and observed outflows (Steidel et al., 2010) is that the wind speed *increases* with height z above the disk, and it has been suggested that radiation driving is the cause of this (Murray et al., 2005). Since radiation driving is not included in our modelling yet the outflow does accelerate, we suggest the following physical model. The combined effects of several supernova explosions cause the ISM pressure to increase substantially above the hydrostatic equilibrium value. If gravity is not dominant, this will lead to the higher pressure ISM expanding into the lower pressure regions above the disk. In the launch region of such an outflow, 1D (plane-parallel) symmetry is a reasonable description of the geometry, in which case the behaviour of the outflow is a rarefaction wave, for which the similarity solution is

$$\begin{aligned} v(\eta) &= \frac{2}{\gamma+1} c_0 \, (1+\eta) \\ \rho(\eta) &= \rho_0 \left(\frac{2}{\gamma+1} - \frac{\gamma-1}{\gamma+1}\,\eta \right)^{2/(\gamma-1)} \\ \eta &\equiv \frac{z}{c_0 t}\,, \end{aligned} \tag{3.38}$$

valid for

$$\eta \in \left[-1, \frac{2}{\gamma-1} \right] . \tag{3.39}$$

In such a flow, speed increases with height z and density decreases. This is distinct from the flow due to a single blast wave, since in the Sedov-Taylor phase density *increases* with distance from the blast, which is not the case for the disk outflow (Fig. 3.1).

In a rarefaction wave, the acceleration is due to the pressure gradient in the outflow, and results in thermal energy being converted to kinetic energy, and the asymptotic flow speed is $v_{\max} = 3c_0$ for $\gamma = 5/3$. The outflowing gas above the disk is mainly warm ISM gas that is entrained by the hot SN bubbles that power the rarefaction wave. Figure 3.6 shows the behaviour of the simulation to be consistent with this model: velocity increases with height z, but decreases with time at a given height in way predicted by the similarity solution. The stochastic nature of the SN events complicates a full description of the model, and in reality the flow is built-up from a series of rarefaction waves. Note also that this cannot be a steady state solution, as the disk will eventually run out of gas. The spherically symmetric version of this model, involving continuous injection of energy mimicking a stellar wind, is described by for example Castor et al. (1975a); Weaver et al. (1977); McCray and Kafatos (1987).

3.4.4 Absorption features of galactic winds

Steidel et al. (2010) proposes that the CII absorption line data is also well fit with velocities

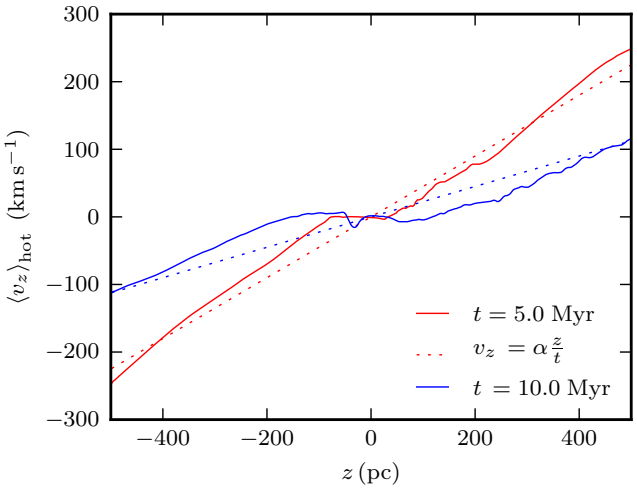

Figure 3.6: *Solid line* shows the mean vertical velocity as a function of height for two times in the $\Sigma_{\rm g} = 2.5$ M$_\odot$ pc^{-2}, $f_{\rm g} = 0.01$ simulation showing only the hot gas (where we have defined hot gas to be that above 2×10^4 K). *Red dotted line* is a linear fit ($\alpha = 2.6$) to the earlier snapshot ($t = 5$ Myr) which is then extrapolated to the later snapshot (*blue dotted line*). This shows the profile is evolving in an approximately self-similar fashion with the hot material accelerating away from the disk primarily due to its thermal energy being converted to kinetic energy.

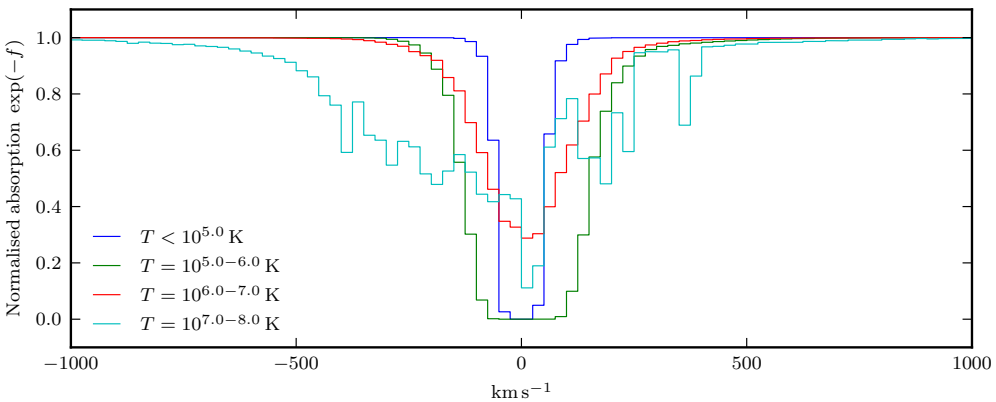

Figure 3.7: Normalised column density as a function of velocity, for gas with different different temperature (*coloured lines*). For low temperature absorbers ($\lesssim 10^6$ K) we to see a single peaked profile centred around the rest frame velocity of the disk. For higher temperatures absorbers, we see absorption at higher velocities relative to the disk, with velocity increasing with temperature. Only the $\gtrsim 10^7$ K distribution appears to show any significant asymmetry.

increasing with distance from the disk (in particular the lower panel of Fig. 24 of Steidel et al., 2010). The rarefaction explanation provides a physical mechanism for those measured features. This is without the radiation and dust driven mechanisms invoked by Murray et al. (2005); Martin (2005); Sharma et al. (2011).

We pointed-out in Fig. 3.1 the multi-phase nature of the outflow, as well as the fact that outflow speed depends on temperature. This is made more vivid in Fig. 3.7 in which we show mock 'absorption lines' of gas selected in narrow temperature bins. These mock line profiles are simply the fraction of gas in a given temperature range, that is moving with a given velocity, as a function of velocity, v. For the temperatures $T < 10^7$ K, the lines have their highest optical depths at $v \sim 0$ km s^{-1}, and shapes which vary little with temperature, T, and are almost symmetric in velocity. The line shapes broaden as the temperature increases, and for the hottest gas at $T > 10^6$ K the line becomes asymmetric and the absorption centre is now $\sim -100\ \mathrm{km\,s^{-1}}$. It is tempting to compare these to absorption line studies in outflows such as Martin (2005) in NaI and Weiner et al. (2009) in MgII, however more work would be required to calculate corrections for the geometry and ionisation.

Fig. 3.1 also shows colder clouds entrained inside the much hotter flow, with cometary-like tails where the cloud is being ablated by the hot gas rushing past. Absorption lines might arise from mass loading this hot flow either through conductive evaporation (see for example Boehringer and Hartquist, 1987; Gnat et al., 2010) and/or through ablation (e.g. Hartquist et al., 1986). Fujita et al. (2009) investigated these warm clouds in axisymmetric 2-dimensional simulations, where the clouds appear as Rayleigh-Taylor unstable cool shells and fragments that can explain the high velocity Na I absorption lines. We note that the metallicity of the gas phases is likely to be quite distinct, as the supernovae are both the origin of the heating and of the metals, and we intend to explore this in a subsequent paper.

3.5 The dependence of outflows on disk properties

In the previous section we have discussed in detail the features of a simulation of a supernova-driven wind using a set of fiducial parameters for the disk and supernova rate, the processes which drive it and the statistics that can be used to examine it. In this section we explore how the outflow properties vary and scale with the parameters. We will use such scalings in the next section to integrate over a full galactic disk.

In Fig. 3.8 we plot a velocity slice through the simulations we have performed varying $\Sigma_{\rm g}$ and $f_{\rm g}$. There appears to be a strong trend in wind velocity, with wind speed increasing with

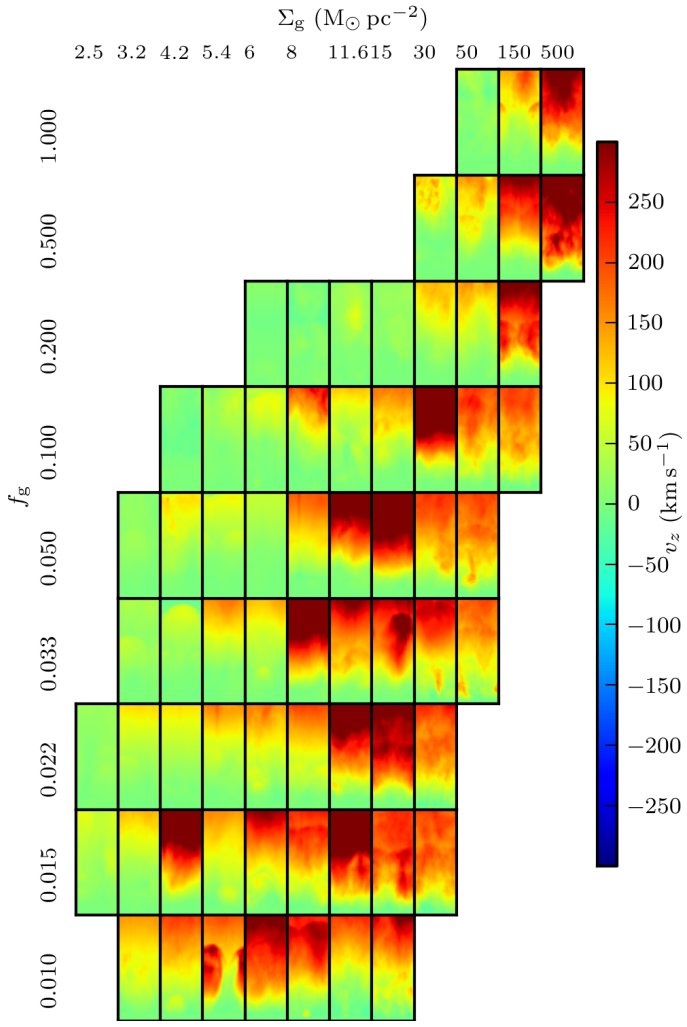

Figure 3.8: Matrix view of simulations varying gas surface density (Σ_g) and gas fraction (f_g), each panel showing a time averaged vertical velocity for the upper half plane of each simulation (i.e. the disk is at the base of each panel. Gas surface density increases from left to right, gas fraction increases from bottom to top. There appears to be a strong trend in wind velocity towards the lower right panels, i.e. a disk with low gas fraction but high gas surface density tends to generate a faster wind.

increasing gas surface density, but decreasing gas fraction. There are no simulations in the upper left as these would have a scale height larger than half the box size, or in the lower right as these would have a scale height less than 3 pc, comparable to the cell size and the SN injection radius.

3.5.1 Mass outflow

Inspecting the ratio of mass outflow rate to star formation rate gives us an analogous property to that of Eq. (3.1), i.e. for a specific area on the disk

$$\beta = \frac{\dot{\Sigma}_{\rm ej}}{\dot{\Sigma}_\star}\,, \tag{3.40}$$

which we use in our subsequent analysis. In theory every snapshot from our simulations contains an estimate of this β, as the mass outflow rate at a specific height, however this is rather stochastic, and as an alternative we calculate β as a fit to several measurements of the integrated outflow

$$y_i = \frac{\int_0^{t_i} \dot{\Sigma}_{\rm ej} {\rm d}t}{\int_0^{t_i} \dot{\Sigma}_\star {\rm d}t}\,, \tag{3.41}$$

which are easily obtained from each simulation snapshot. We fit the data samples $\{(t_i, y_i)\}_{i=1}^n$ with the ramp function,

$$f(t) = \begin{cases} 0, & t < t_0 \\ \beta t, & t \geq t_0\,, \end{cases} \tag{3.42}$$

where the parameters t_0 and β are free variables. The motivation for choosing such a fit is that, whilst the ejection rate is nearly linear in most cases, there is a time (t_0) required for the system to reach a quasi steady state. This will not be a true steady state, in that the wind will eventually exhaust the supply of cold gas, however this occurs over a sufficiently long time-scale that the fit is a reasonable description for our simulations.

The square error of this function can be analytically solved by finding linear regressions for the subsets s_k of $\{(t_i, y_i)\}_{i=1}^n$ defined by $\{(t_i, y_i)\}_{i=k}^n$ and choosing the minimum k such that the linear regression t-intercept $< t_k$. If we define $g(s_k)$ as the t-intercept of the linear regression for s_k, then

$$t_0 = \min\left\{t_k : g\left(s_k\right) < t_k, s_k \equiv \{(t_i, y_i)\}_{i=k}^n\right\}\,, \tag{3.43}$$

and β is the slope of this linear regression.

Plots of the gas fraction remaining in the simulation volumes can be seen in Fig. 3.5 for the fiducial model, and for the set of simulations of varying $\Sigma_{\rm g}$ and $f_{\rm g}$ in Fig. B.9 in Appendix B where we also show the fits given by Eq. (3.42).

In Fig. 3.9 we plot the mass loading β as a function of gas surface density $\Sigma_{\rm g}$. Each point represents a fit of $\beta(\Sigma_{\rm g})$ for the simulations varying $\Sigma_{\rm g}$ and $f_{\rm g}$. The first point to note is that our

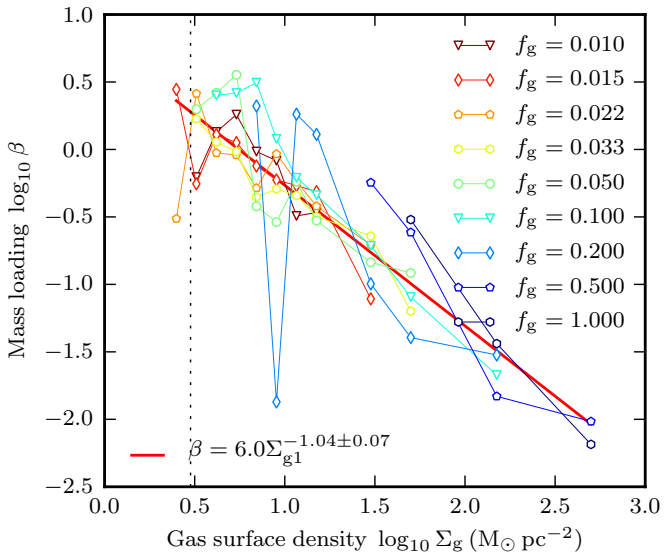

Figure 3.9: The mass loading β (mass ejection rate vs. rate of star formation) as a function of gas surface density Σ_g. Each point represents a fit of β (section 3.5) to a star formation simulation, varying Σ_g and f_g. *Red line* denotes a power law fit with jack-knife errors, *coloured symbols* (red-blue) correspond to the simulations with gas fraction $f_g = 0.01$ - 1.0 respectively. *Vertical grey dashed line* indicates the 3 $M_\odot$ pc^{-2} threshold for star formation from Schaye (2004). We see a significant negative dependency of $\beta \sim \left(\Sigma_g/1\ M_\odot\ \mathrm{pc}^{-2}\right)^{-1.04\pm0.07}$ on the gas surface density, which may be due to the larger gravitational potential or the higher rate of cooling (incurred by higher gas densities) or some combination of both. We also note that the scatter seems partially a function of f_g, with higher gas fractions showing larger β's than the lower (e.g. *blue* vs. *green*).

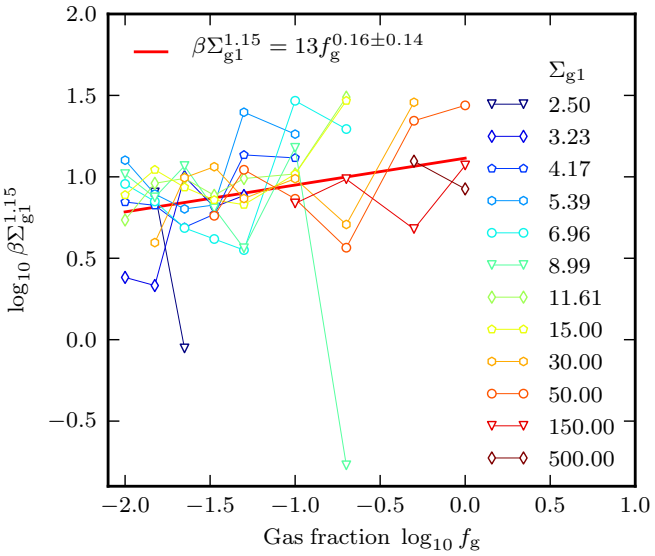

Figure 3.10: Joint dependence of the mass loading β on gas surface density, Σ_g, and gas fraction f_g. Differently coloured curves correspond to simulations with different values of $\Sigma_{g1} \equiv \Sigma_g / M_\odot\,pc^{-2}$, the *thick red line* is our best fit of the simulation points. We see a dependence of $\beta\Sigma_g^{1.15}$ on gas fraction, with a power law dependency of 0.16 ± 0.15. Higher gas fractions for a given gas surface density imply a shallower potential well, explaining why the outflow efficiency increases with f_g.

β values all lie below 4, and a large range has $\beta \ll 1$, i.e. our domain of parameter space switches from effective feedback (more gas ejected than stars formed) to ineffective, where the amount of gas released is much smaller than that converted into stars.

Based on jack-knife errors, our power law fit shows a significant negative dependency, $\beta \approx 6\Sigma_g^{-1.04\pm0.07}$, implying that at high gas surface densities the feedback is less efficient. This could be due to a number of effects. Since a higher gas surface density will correspond to a deeper potential well, the escape velocity of the gas is higher. Secondly, the higher gaseous surface densities correspond to higher gas volume densities (Eq. (3.21)), resulting in shorter cooling times.

Another notable dependency is that on the gas fraction. Some of the scatter seen in Fig. 3.9 actually depends systematically on the gas fraction, f_g, with higher gas fractions showing consistently larger β's than the lower values. We explore this in Figure 3.10, where we have performed a simultaneous fit of β to both the gas surface density and the gas fraction,

$$\beta = \beta_0 \Sigma_{g1}^{-\mu} f_g^{\nu}\,, \tag{3.44}$$

where we find the values

$$\beta_0 = 13 \pm 10 \quad (3.45)$$

$$\mu = 1.15 \pm 0.12 \quad (3.46)$$

$$\nu = 0.16 \pm 0.14\,, \quad (3.47)$$

By construction the joint fit now no longer shows a systematic dependence on either $\Sigma_{\rm g}$ or $f_{\rm g}$.

Accounting for this shows a positive dependency of $f_{\rm g}^{0.16\pm0.14}$, i.e. by holding the gas surface density constant but increasing the gas fraction (which reduces the gravitational strength, thus increasing the dynamical time and reducing the star formation rate) increases the mass loading. As with the dependence on gas surface density, we are effectively seeing a sub-linear dependence on star formation rate, as we decrease the star formation (increase the gas fraction), we see a less than proportionate drop in the outflow rate. Again, the mechanism causing this should be a combination of the processes for the $\Sigma_{\rm g}$ dependence, derived above.

In Fig. 3.10 there is considerable scatter, especially at high gas fraction where a number of simulations have mass ejection rates considerably above the trend. This is most likely due to heavy disruption of the disk out of the plane where the wind from subsequent supernovae can eject it from the simulation volume. With such stochasticity the description of all the simulations with a simple power law becomes inadequate.

Our measured value for the exponents $\mu = 1.15$ and $\nu = 0.16$ that relate mass loading to gas surface density and gas fraction, $\beta \propto \Sigma_{\rm g}^{-\mu} f_{\rm g}^{\nu}$, can be compared with the values from the model described in Section 3.4.1, which predicts scalings of $\mu = 8/11 = 0.72$ and $\nu = 4/11 = 0.37$. That model does not include gravity, and we suggest this is why the measured and predicted values differ. To verify this we have performed a series of simulations with significantly higher star formation rate, described in Appendix B. In these runs, the energy injection rate is much higher, the volume filling factor of the hot phase much larger, and the outflow rates are correspondingly larger as well. Consequently the effect of gravity of the disk is much reduced. Fitting $\beta \propto \Sigma_{\rm g}^{-\mu} f_{\rm g}^{\nu}$ to these runs yields $\mu = 0.82$ and $\nu = 0.48$, in much better agreement with the predictions of the simple model.

It would be interesting to extend the model to account for the gravity of the disk, along the lines followed by Stringer et al. (2011). Assume that the β of the hot gas in Eq. (3.33) is modified by an escape fraction $f_{\rm esc}$, which is equal to the fraction of material that has a temperature above the escape temperature of the simulation volume. Assuming the outflow has a range of temperatures, characterised by a Maxwell-Boltzmann distribution, and that only gas with $T > T_{\rm esc}$

escapes, the fraction is

$$f_{\rm esc} = \int_{T_{\rm esc}} f(T){\rm d}T \tag{3.48}$$

$$\approx 1 - \frac{4}{3\sqrt{\pi}}\left(\frac{T_{\rm esc}}{T_{\rm s}}\right)^{3/2} . \tag{3.49}$$

We have assumed that $T_{\rm esc} \ll T_{\rm s}$, i.e. the low energy tail of the distribution fails to escape. The net outflow will thus drop faster at high $\Sigma_{\rm g} \propto T_{\rm esc}$, making the dependence of the mass-loading on $\Sigma_{\rm g}$ stronger, which is consistent with the higher $\mu \approx 1.15$ we see in the lower SFR simulations.

3.5.2 Radiative efficiency and energy partition in the ISM

Whilst the mass loading of the galactic wind is one of the most cosmologically significant parameters to study, we would also like to evaluate the energy budgets and structure of the winds in our simulations. The energy injected by the SNe is absorbed into the gravitational binding energy, distributed into thermal and mechanical energy (both in the bulk motion of the wind and in turbulence throughout the simulation volume) and released as radiation (via cooling).

The energy partition also enables us to evaluate a wind velocity for the galaxy, which is commonly used to characterise feedback models for galaxy formation (e.g. Bower et al., 2011). The fraction of the energy that is incorporated into the wind, in combination with the mass loading, determines the overall wind speed for a galaxy. This is an important parameter in determining whether the wind can leave the galaxy and hence provide efficient quenching of star formation.

By examining our simulations we can determine the fractions of energy that has been converted in to the different modes. In our fiducial simulation, we discover that a fraction of 87% was radiated, 4.5% was advected out of the computational volume as thermal energy, 5% as mechanical energy (with over half of this in the form of turbulent energy), 1% went into heating the simulation volume[5], 1% went into turbulence in the simulation volume and a rather low 0.5% went into puffing-up the disk. The parameters here are averaged in a similar manner to the mass ejection rate, by taking the mean over snapshots after t_0 (Eq. 3.43), i.e. in the quasi-steady regime.

Summation of these quantities allows us to estimate η_T (Eq. 3.5), the fraction of power that is thermalised in to the outflow

$$\eta_T = \eta_{\rm therm} + \eta_{\rm mech} , \tag{3.50}$$

i.e. the sum of the thermal and mechanical (bulk and turbulent) contributions, (the remainder going almost entirely in to cooling). This allows us to calculate an effective velocity $v_{\rm eff}$ for the

[5]Note that in a true steady state this fraction should be compensated by cooling.

wind,

$$v_{\rm eff} = \sqrt{\frac{2\eta_T}{\beta}\left(\frac{E_{\rm SN}\varepsilon_{100}}{100{\rm M}_\odot}\right)}, \tag{3.51}$$

where we have combined the equation for mass loading, $\beta \equiv \dot{M}_{\rm wind}/\dot{M}_\star$, and the thermalisation of supernova energy into the kinetic energy of the wind (η_T), to find the specific energy in the wind (i.e an inversion of Eq. (3.5)). Notably this will be significantly higher than the wind velocities we see at the edge of our simulation volume because it includes the energy of the thermal and turbulent components. At larger distances from the galaxy, however, we expect this to be a more realistic estimate, as the thermal energy accelerates the wind and is converted in to the mechanical energy of the bulk flow. This is a consequence of our simulations focusing on the launch region of the galactic wind, and hence the wind has not yet reached its terminal velocity. Note that ram pressure from infalling gas may be an important obstacle in slowing down, or even preventing the outflowing gas from escaping (e.g. Theuns et al., 2002).

In Figure 3.11 we explore the dependence of the mass loading β, the fraction of power in the outflow, η_T, and the effective wind velocity, $v_{\rm eff}$, as a function of the total surface density of the disk, $\Sigma = \Sigma_{\rm g}/f_{\rm g}$. In terms of the mass loading we see a negative dependence on surface density, for comparison we have also included the power law fit from Eqs. (3.45-3.47).

The fraction of power released in to the wind, η_T, appears to be correlated almost entirely with gas fraction $f_{\rm g}$, at high gas fractions much of the energy of star formation is simply radiated away, which is intuitive since the higher gas fractions will have shorter cooling times. For comparison we also show values of $\eta_T = 0.1$ and 0.4, the former being the equivalent to the widely quoted 10% efficiency in Larson, 1974): we find star formation in disks to lie close to this value, except at very low gas fractions.

The fall in outflow power in Fig. 3.11 at low surface densities can also be seen as a fall in the effective wind velocity. Here we have converted our sample values of $\eta_T = 0.1,\ 0.4$ into effective wind velocities using the power law fit for β in Eqs. (3.45-3.47). Each gas fraction appears to follow a line of approximately constant η_T, although there is some suggestion of a change in slope below $\Sigma = 10^2\ {\rm M}_\odot\,{\rm pc}^{-2}$.

3.6 Conclusions

In this chapter we have constructed numerically well converged simulations of a simplified two-phase interstellar medium model, in which an initially isothermal and hydrostatic disk gets disrupted and heated by individual supernovae. By not simulating the cold phase of the ISM we

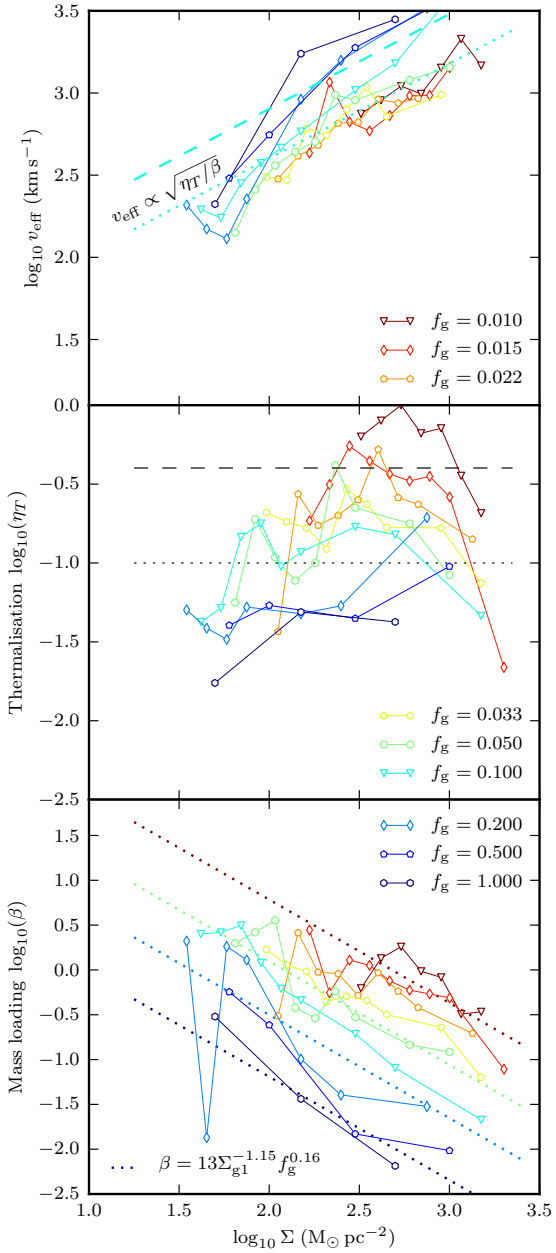

Figure 3.11: Effective wind speed (*upper panel*), outflow efficiency (*middle panel*) and mass loading (*lower panel*) as a function of total surface density $\Sigma = \Sigma_{\rm g}/f_{\rm g}$. Coloured lines with symbols are the simulations from figures (3.9-3.10), with values of the gas fraction $f_{\rm g}$ as indicated. *Dotted lines* in the lower panel are the scalings from equations (3.45-3.47), plotted for $f_{\rm g} = 0.01, 0.015, 0.2, 1.0$ in the corresponding colours. Lines of constant efficiency, $\eta_T = 0.1$ and 0.4 are shown in the middle panel (*black dotted* and *dashed*, respectively). Curves for the corresponding scaling of the effective wind speed for $f_{\rm g} = 0.1$ are shown in the upper panel. The outflow efficiency increases with surface density, as does the effective wind speed.

avoided the need to introduce significantly more physical ingredients which require heavy algorithmic approximations and/or fragile recipes. By restricting our simulation volume to only a small section of a disk, we achieve sub-parsec resolution, and are able to investigate the dependence of the outflow on the parameters of the disk. We have self-consistently included gravity, star formation that follows the Kennicutt-Schmidt relation, hydrodynamics and a cosmological cooling function. On scales outside the volume, the host disk galaxy for this toy model is reduced to the parameters of gas surface density, gas fraction and star formation efficiency normalised by the Kennicutt-Schmidt relation.

Our simulations demonstrate the ability of supernovae to drive a galactic wind vertically from a disk. The supernovae create a turbulent ISM with very distinct hot and warm phases, due to the strong transition of the cooling function at 10^4 K. These phases exist in approximate pressure equilibrium, with the warm material squeezed in to dense lumps, and the excess thermal energy of the hot material causing it to accelerate away from the disk. In section 3.4.3 we describe this as a rarefaction-like process, with the hot ISM escaping to an IGM which is comparatively sparse and pressure-free. Such a model naturally leads an outflow with speed increasing with height above the disk but density decreasing.

The hot outflow entrains colder ISM gas from the disk, that may have relatively high metallicity. The hot gas rushes past these clouds producing characteristic tails. Such interfaces may be the cites where lower ionisation lines are produced. In section 3.4.4 we explore this further by calculating the normalised cross section of different temperature phases in our simulations, where we see the velocity distribution of the cooler gas is significantly beneath that of the escaping material.

As the precise features of our simulations vary greatly due to turbulence and the stochastic nature of supernovae, we examine several global properties which are less sensitive, such as the disk pressure, cooling rate as a fraction of the mean energy injection rate, disk scale height and mass ejection. These reveal a disk that rapidly evolves to higher porosity before reaching a state with an approximately constant mass ejection rate. This evolution of porosity is broadly reminiscent of the model by Silk (2001).

We perform a range of simulations to investigate the dependence of the mass loading on gas surface density, gas fraction, and star formation efficiency, and fit the resulting trends with power laws. Our mass loadings lie in the range 0-4, suggesting a switch from a low to a high feedback regime. We find little dependence on the normalisation of the star formation relation but a significant dependence on the gas fraction and surface density. The latter two can be combined to explain the bulk of the trends as depending on the total surface density of the disk. At high surface densities we find low mass loading and a high effective wind speed. At low surface

densities the reverse is true, and there is an additional contribution due to an increase of the fraction of energy radiated by cooling gas. In Section 3.4.1 we present a simple model where SNe blasts stall as they run into clouds swept-up by previous explosions that are so dense that they cool very efficiently predicts that mass loading depends on gas surface density and gas fraction as $\beta = \dot{\Sigma}_{\rm wind}/\dot{\Sigma}_\star \propto \Sigma_{\rm g}^{-8/11}\, f_{\rm g}^{4/11}$. These scalings are very close to those we find from simulations with high star formation rate, $\beta \propto \Sigma_{\rm g}^{-0.82}\, f_{\rm g}^{0.48}$ and weaker (in terms of surface density) than that for the pure Kennicutt relation, $\beta \propto \Sigma_{\rm g}^{-1.15}\, f_{\rm g}^{0.16}$. Our prediction for the mass loading in the solar neighbourhood is that each supernova results in an ejection of around $50\ {\rm M}_\odot$ of gas, or a $\beta \sim 0.5$, slightly above 0.3, our average for the MW as a whole.

The relationship between the wind velocity and thermalisation efficiency exhibits a more complex relationship to the disk properties than that of the mass loading. The thermalisation efficiency appears to show a dependency on both the surface density and the gas fraction, and correspondingly the wind velocity does not show a straightforward power law implied from a constant efficiency model. For high surface densities and low gas fractions, an approximate 40% of the injected energy is converted into the outflow's thermal, turbulent and kinetic energy components.

Chapter 4 | *Galactic winds*

4.1 Introduction

In this chapter we apply our results from the previous chapter to the mass outflow from disk galaxies of different masses. In the previous chapter we studied a model of the evolution of a patch of a galactic disk, with various combinations of gas surface density and gas fraction. In this chapter we extend these models to entire galaxies by applying some of the theoretical and observational understanding of the statistics of galactic disks.

We begin with a discussion of an exponential surface density profile for galactic disks and their use in the successful Mo et al. (1998) formalism. We discuss the use of this in combination with our fits for outflow efficiency as a function of surface density from Chapter 3 to deduce an overall feedback efficiency. In order to address some of the limitations of this model, we also construct a model constrained by observations, centred around the Tully-Fisher relation (Tully and Fisher, 1977). We discuss the discrepancies between these two models before comparing them to phenomenological/semi-analytic models such as GALFORM, both in terms of the stellar mass function, and the constraints deduced from the MW.

4.2 Impact of outflows on galaxy evolution

4.2.1 Dependence on circular velocity from theoretical arguments

In this section we take our measured dependencies of the mass loading parameter (which are derived for a patch of the ISM) and apply them to an entire disk galaxy by integrating over the surface of the disk. This will allow us to compare with feedback schemes considered in Cole et al. (2000); Bower et al. (2006) etc., which introduce a relation between circular velocity, mass loading, and effective wind speed.

Our first step is to assume a model for a disk galaxy inside a dark matter halo where we follow Mo et al. (1998). The circular velocity of a spherical isothermal dark halo of mass M_{200} is given

by

$$V_{200}^3 = 10GM_{200}H(z)\,, \tag{4.1}$$

(Mo et al., 1998) where $H(z)$ is the Hubble parameter as a function of redshift, z. Since the baryonic component can release energy via cooling, it can collapse further to become a rotationally supported disk. Observed bulge-less disks have a near exponential profile in luminous mass of the form

$$\Sigma(r) = \Sigma_0 \exp\left(-r/R_{\rm d}\right)\,, \tag{4.2}$$

with normalisation Σ_0 and scale length $R_{\rm d}$. The mass of the disk is thus given by

$$M_{\rm d} = \int_0^\infty 2\pi\Sigma(r) r {\rm d}r = 2\pi\Sigma_0 R_{\rm d}^2\,. \tag{4.3}$$

The scale length $R_{\rm d}$ is controlled by the specific angular momentum of the material forming the disk (e.g. Fall and Efstathiou, 1980). An exponential disk with constant rotation velocity $V_{\rm d}$ has angular momentum

$$J_{\rm d} = 4\pi\Sigma_0 V_{\rm d} R_{\rm d}^3\,, \tag{4.4}$$

and if we parameterise in terms of the disk mass as a fraction of the halo mass, $m_{\rm d} \equiv M_{\rm d}/M_{200}$, the circular velocity of the disk as a fraction of the halo's, $v_{\rm d} \equiv V_{\rm d}/V_{200}$, and the angular momentum as a fraction of the halo $j_{\rm d} \equiv J_{\rm d}/J_{200}$ then we can infer the surface density normalisation to be

$$\begin{aligned}\Sigma_0 &= \frac{2}{\pi}\frac{M_{\rm d}^3 V_{\rm d}^2}{J_{\rm d}^2} \\ &= \frac{10H(z)}{\pi G}\lambda^{-2}\left(\frac{j_{\rm d}}{m_{\rm d}}\right)^{-2} m_{\rm d} v_{\rm d}^2 V_{200}\,,\end{aligned} \tag{4.5}$$

where the combination $j_{\rm d}/m_{\rm d}$ is the specific angular momentum fraction of the disk and λ is the spin parameter of the isothermal halo in Eq. (4.1). Notably if we set $v_{\rm d} = 1$ we recover the Mo et al. (1998) surface density equation, yet for real disks $v_{\rm d} > 1$ as the contribution of baryons to the rotation velocities is not insignificant.

We can now compute a mean mass loading $\hat{\beta}$ for such a galaxy, by evaluating

$$\hat{\beta} \equiv \frac{\dot{M}_{\rm wind}}{\dot{M}_\star} = \frac{\int 2\pi\beta\dot{\Sigma}_\star r {\rm d}r}{\int 2\pi\dot{\Sigma}_\star r {\rm d}r}\,, \tag{4.6}$$

where we will assume the surface density in star formation, $\dot{\Sigma}_\star$, follows the Kennicutt-Schmidt relation (Schmidt, 1959; Kennicutt, 1989),

$$\dot{\Sigma}_\star = A\Sigma_{\rm g}^n\,. \tag{4.7}$$

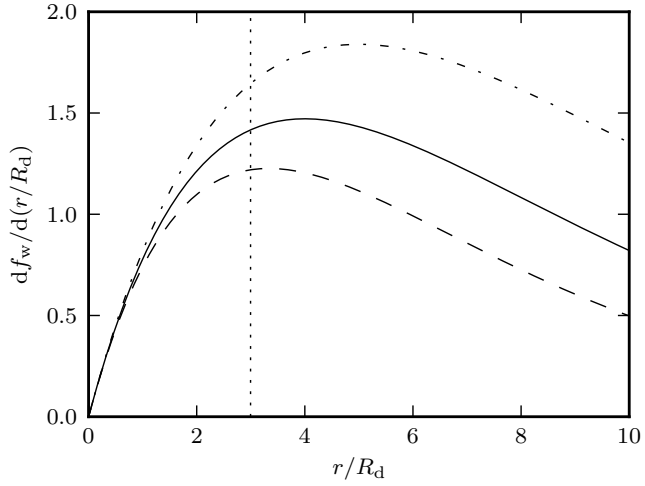

Figure 4.1: Fraction of the wind launched at each radii in the disk (Eq. 4.9), for a Kennicutt-Schmidt relation $\dot{\Sigma}_\star \propto \Sigma_\mathrm{g}^n$, with $n = 1.4$, and assuming mass loading scales with gas surface density as $\beta \propto \Sigma_\mathrm{g}^{-\mu}$, with $\mu = 1.15$ (Eq. 3.46). *Dotted line* indicates the characteristic wind radius $R_\mathrm{w}/R_\mathrm{d}$ for the galaxy, where the the local mass loading equals the net mass loading for the galaxy as a whole, $\hat{\beta} = \dot{M}_\mathrm{wind}/\dot{M}_\star$. The *dashed* and *dot-dashed* indicate the fractions of wind launched for $\mu = 1.1$ and $\mu = 1.2$.

Taking the dependence of mass loading on surface density found from our fits to the simulations, Eq. (3.44), then Eq. (4.6) can be integrated analytically. We re-write Eq. (3.44) in terms of the total surface density, Σ, and the gas fraction, f_g, and obtain

$$\beta(\Sigma, f_\mathrm{g}) = \beta_0 \left(\frac{\Sigma}{1\,\mathrm{M}_\odot\,\mathrm{pc}^{-2}} \right)^{-\mu} f_\mathrm{g}^{\nu-\mu}\,, \tag{4.8}$$

giving a dependence on the gas fraction, $\propto f_\mathrm{g}^{-0.99}$, using $\mu = 1.15$ and $\nu = 0.16$ from Chapter 3. The fraction of the wind launched as a function of radius is given by,

$$\begin{aligned} \frac{\mathrm{d}f_\mathrm{w}}{\mathrm{d}(r/R_\mathrm{d})} &= \frac{2\pi R_\mathrm{d} \beta(r) \dot{\Sigma}_\star(r)}{\dot{M}_\mathrm{wind}} \\ &= (n-\mu)^2 \left(\frac{r}{R_\mathrm{d}} \right) \exp\left[-(n-\mu) r/R_\mathrm{d}\right]\,, \end{aligned} \tag{4.9}$$

which gives the differential rate of production of the star-formation driven wind, normalised by the total wind. This function is plotted in Fig. 4.1. At large radii the star formation is most effective at driving a wind, but the net contribution to the galaxy outflow is limited by the low rate of star formation there. Conversely at small radii the wind is limited by the small area of the disk, and so it is at intermediate radii where the local mass loading equals that of the galaxy as a whole.

We can characterise this further by defining a wind radius $R_{\rm w}$ by

$$\hat{\beta} = \beta\left(\Sigma(R_{\rm w}), f_{\rm g}\right) \,, \tag{4.10}$$

that is, $R_{\rm w}$ is that radius in the galaxy where the local mass loading, $\beta = \dot{\Sigma}_{\rm ej}/\dot{\Sigma}_{\star}$, equals the total mass loading of the entire galaxy, $\hat{\beta} = \dot{M}_{\rm wind}/\dot{M}_{\star}$. The wind radius for the galaxy is then given by,

$$\begin{aligned} R_{\rm w} &= \frac{2}{\mu}\ln\left(\frac{n}{n-\mu}\right) R_{\rm d} & (4.11)\\ &\approx 3.0 R_{\rm d} \,, & (4.12)\end{aligned}$$

where we have substituted in $n = 1.4$ for the exponent in the KS relation, and used the value for μ from Eq. (3.46). Notably this is quite a strong function of μ, as indicated by the additional lines in the figure for $\mu = 1.1$ and $\mu = 1.2$. For the Milky Way, a disk scale length of $R_{\rm d} = 2.5\,{\rm kpc}$ gives a wind radius of $R_{\rm w} = 7.5\,{\rm kpc}$, inside the solar radius but outside the galactic bulge. We have neglected the fact that there will not be any star formation far out in the disk if the gas surface density drops too low, as well as the presence of a bulge, where there may be little gas and hence also little star formation. This will lead us to overestimate the wind in the tails of Fig. 4.1.

To parameterise feedback in terms of the circular velocity, V_{200}, we apply Eq. (4.5) and use our fiducial values of β_0, μ, ν and $f_{\rm g}$, to find

$$\begin{aligned} \hat{\beta} &= \beta_0 \left(\frac{n}{n-\mu}\right)^2 \left(\frac{\Sigma_0}{1\,{\rm M}_\odot\,{\rm pc}^{-2}}\right)^{-\mu} f_{\rm g}^{\nu-\mu} & (4.13)\\ &\approx 10\left(\frac{\beta_0}{13}\right)\left(\frac{f_{\rm g}}{0.2}\right)^{\nu-\mu}\left(\frac{j_{\rm d}}{m_{\rm d}v_{\rm d}}\right)^{2\mu}\times \\ &\quad \left[\left(\frac{\lambda}{0.05}\right)^{-2}\left(\frac{V_{200}}{155\,{\rm km\,s^{-1}}}\right)\left(\frac{m_{\rm d}}{0.03}\right)\frac{H(z)}{H_0}\right]^{-\mu} \,, & (4.14)\end{aligned}$$

where we also assumed $H_0 = 71\ {\rm km\,s^{-1}\,Mpc^{-1}}$ (Freedman et al., 2001).

To convert to disk properties we can eliminate the spin parameter with

$$R_{\rm d} = \frac{\lambda V_{200}}{\sqrt{200}H(z)}\left(\frac{j_{\rm d}}{m_{\rm d}v_{\rm d}}\right) \,. \tag{4.15}$$

Setting $j_{\rm d}/m_{\rm d}$ and $v_{\rm d}$ as unity, however, yields a MW with a rather low circular velocity (155 km s^{-1}) and scale length considerably higher than estimated for the MW disk.

The formation of the baryonic disk can increase the rotation velocities from V_{200} both directly and indirectly. The baryons make their own contribution to the gravitational potential, and can also induce changes in the profile of the dark matter, for example due to adiabatic contraction (e.g. Mo et al., 2010). Even without baryons, there will be some adjustment to $v_{\rm d}$ due to the

non-isothermal nature of halos (Navarro et al., 1997), i.e. a dependence on the concentration parameter. Here we will take $v_{\rm d} = 1.29$ to give a circular speed of $V_{\rm d} = v_{\rm d} V_{200} = 200\ {\rm km\,s^{-1}}$, similar to the value of the MW (Dehnen and Binney, 1998; Flynn et al., 2006, but see also Reid et al., 2009 that has the speed closer to $250\ {\rm km\,s^{-1}}$).

Having set the circular speed, the disk scale length is implied by the specific angular momentum fraction in Eq. (4.15). For the 2.5 kpc disk of Flynn et al. (2006) we set $j_{\rm d}/m_{\rm d} = 0.42$, i.e. the disk is preferentially formed of the low angular momentum baryons. A possible reason for the lower specific angular momentum is the delayed collapse of baryons in the disk due to photo-heating (since disks grow in an inside-out manner, with the low angular momentum material accreted first), Navarro and Steinmetz (1997).

Finally we should mention that the spin parameter of the MW may differ from 0.05, and indeed recent simulations that remove transient objects from halos have suggested halos have a smaller λ (e.g. Bett et al., 2007), however we have made no account for this as it is outside the scope of this model.

This tweaking of parameters ($v_{\rm d} = 1.29$, $j_{\rm d}/m_{\rm d} = 0.42$) is a feature of the Mo et al. (1998) model. With these new parameters, the MW disk has a more realistic higher surface density, and Eq. (4.14) becomes

$$\hat{\beta} \approx 0.31 \left(\frac{\beta_0}{13}\right) \left(\frac{f_{\rm g}}{0.2}\right)^{\nu-\mu} \times \left[\left(\frac{V_{\rm d}}{200\,{\rm km\,s^{-1}}}\right)^{3} \left(\frac{R_{\rm d}}{2.5\ {\rm kpc}}\right)^{-2} \left(\frac{m_{\rm d}}{0.03}\right) \frac{H_0}{H(z)}\right]^{-\mu}. \quad (4.16)$$

The normalisation and scaling with $V_{\rm d}$ we find are somewhat below our expectations for supernova feedback. For a Milky-Way like halo, the star formation would remove less than one solar mass of gas for every solar mass of stars formed ($\hat{\beta} \sim 0.31$). Nevertheless, halos with smaller circular velocities with the same disk radius and disk mass fraction show increasingly effective feedback, $\hat{\beta} \propto V_{\rm d}^{-3.4}$, a similar scaling to energy conserving winds (e.g. Stringer et al., 2011). Note that the power-law dependence on $V_{\rm d}$ is somewhat stronger than the value of -1 found by Hopkins et al. (2012a). Those authors also found an exponent of -0.5 for the dependence of mass loading on surface density, which is weaker than our exponent in Eq. (4.16) of $\hat{\beta} \propto \Sigma^{-1.15}$. Whilst the agreement between these simulations is not particularly good, this is perhaps not surprising given that they are performed with some different physics, at different resolutions and using different hydrodynamical schemes.

Despite the appeal of the above framework in supplying us with predictions for the mass loading in terms of redshift and the disk properties, there is a caveat here in our adjustment of

$j_{\rm d}/m_{\rm d}$ and $v_{\rm d}$ to match the observed MW. Although we can derive this from observations for the MW, and the mechanism for this appears to be understood, it would be erroneous to suggest we have a consistent model for this, and current numerical simulations such as those of Scannapieco et al. (2011) have yet to converge on the properties of a disk for a single halo. Most concerning is that these quantities almost certainly have some implicit dependence on halo mass and thus there should be a corresponding adjustment to the scaling relation in Eq. (4.16).

4.2.2 Dependence from observed data

Given the approximate ingredients required to construct the formalism of the previous section, it is interesting to ask whether we can parameterise our fit to the mass-loading, Eq. (4.13), with purely observational estimates, i.e. to compute the disk surface density from observed disk properties, side-stepping the models of Mo et al. (1998).

One particularly attractive method is to invert Eq. (4.3) to write the surface density in terms of the disk radius $R_{\rm d}$ and mass $M_{\rm d}$, where the latter can be estimated from the circular velocity of the disk with the Tully-Fisher relation (Tully and Fisher, 1977). A recent calibration of the baryonic Tully-Fisher relations gives $M_{\rm d} = 8 \times 10^{10}\,{\rm M}_{\odot}(V_{\rm max}/200\ {\rm km\ s^{-1}})^4$ (Trachternach et al., 2009), application of which gives

$$\begin{aligned}\hat{\beta}_{\rm TF} &= 0.31\left(\frac{\beta_0}{13}\right)\left(\frac{f_{\rm g}}{0.2}\right)^{\nu-\mu}\times \\ &\qquad \left[\left(\frac{V_{\rm d}}{200\,{\rm km\,s^{-1}}}\right)^4\left(\frac{R_{\rm d}}{2.5\ {\rm kpc}}\right)^{-2}\right]^{-\mu}, \end{aligned} \tag{4.17}$$

which is very close to the relation in Eq. (4.16), including normalisation and the $R_{\rm d}$ scaling. The difference is in the exponent of $V_{\rm d}$, and the dependence of Eq. (4.16) on $m_{\rm d}$, which implicitly depends upon $V_{\rm d}$ as well.

In principle it is possible to calculate the mass fraction in the disk from the stellar mass to halo mass function using an abundance matching approach, which would relate $m_{\rm d}$ to V_{200}. A single power law, $m_{\rm d} \propto M \propto V_{200}^3$ is a good fit, although from Eq. (3.4) we see there is a dependence on the faint end slope of the stellar mass function (and at higher masses a broken power law may be more appropriate, e.g. Yang et al., 2003; Moster et al., 2010; Guo et al., 2010). Substituting this relation for $m_{\rm d}$ in Eq. (4.17) then yields $\hat{\beta} \propto V_{200}^{-6.9}R_{\rm d}^{2.3}$ versus $\hat{\beta}_{\rm TF} \propto V_{\rm d}^{-4.6}R_{\rm d}^{2.3}$ from Eq. (4.17) (taking $\mu = 1.15$ for both). Finally we can try to eliminate the dependence on R_d, assuming $R_{\rm d} \propto M_{\rm d}^{0.15}$, as inferred by Shen et al. (2003). This yields a scaling of $\hat{\beta} \propto V_{\rm d}^{-4.8}$ versus $\hat{\beta}_{\rm TF} \propto V_{\rm d}^{-2.5}$. The difference between these scalings is due to the discrepancies between the modelled and observed slope for the Tully-Fisher relation and the uncertainty in modelling

the disk mass fraction.

Although both our scalings are strongly dependent on $V_{\rm d}$, our β values were all in the range $0.01 - 4$, so the change in feedback acts more like a switch. At low disk circular velocities $V_{\rm d} \lesssim 140\ {\rm km\,s^{-1}}$ the feedback is high ($1 < \beta < 4$) and at the higher disk velocities the feedback shuts off, all over a relatively small range in $V_{\rm d}$.

To summarise, we have developed two approaches to analyse the mass loading for a galaxy based upon our estimates for the mass loading in our ISM patches. In Section 4.2.1 we take an analytic approximation to the properties of disk in their host halos which allows us to trace the feedback with redshift. This does, however, require us to make assumptions about the scaling of the gravitational contribution of the baryonic disks and the preferential accretion of low angular momentum baryons, neither of which are fully understood. Section 4.2.2 has bypassed these model concerns by parameterising the galaxies using the observed disk mass-velocity relation to directly apply the mass loadings. One price for this is the loss of the dependence on redshift and the cosmological parameters.

Although these two approaches lead to different scalings, they do give a consistent normalisation for the feedback in the MW at redshift zero. In principle, one way to test this formalism is to apply it in phenomenological models such as GALFORM, where such parameters as $j_{\rm d}, v_{\rm d}$ and $m_{\rm d}$ are followed. We discuss this comparison further in the next section.

4.2.3 Comparison to cosmological models

We are now in a position to compare the outflow rate we measured in our high resolution simulations with values assumed in semi-analytic models such as GALFORM (Cole et al., 2000). The feedback prescription for the original GALFORM was

$$\beta = \left(\frac{V_{\rm d}}{V_{\rm hot}}\right)^{-\alpha_{\rm hot}}, \tag{4.18}$$

with values in the reference model of $V_{\rm hot} = 200\ {\rm km\,s^{-1}}$ and $\alpha_{\rm hot} = 2.0$. These models give a slope to the faint end of the galaxy luminosity function, $\alpha \approx -1.5$. More recent models such as Bower et al. (2006) have used $\alpha_{\rm hot} = 3.2$ for a good match to the $b_{\rm J}$ and K-band galaxy luminosity functions. These can be compared with our exponents from the previous paragraph, $\alpha_{\rm hot} = 4.8$ and $\alpha_{\rm hot,TF} = 2.5$, which bracket the value used by Bower et al. (2006). For the normalisation, Cole et al. (2000) parameters yield $\beta_{200} = 1.0$ (β for a disk of $V_{\rm d} = 200$ km s^{-1}), whilst the Bower et al. (2006) parameters give $\beta_{200} \approx 17$ (although this drops to 12 using updated cosmological parameters, see Bower et al., 2011) as compared with our value of $\hat{\beta}_{200} = 0.31$. The net mass loading for MW like galaxies obtained from our simulations is less than that assumed by

(Cole et al., 2000) by about a factor 2, and considerably less than assumed by Bower et al. (2006).

It is also interesting to consider whether the values of β should rise in starburst galaxies, where the star formation rate may be significantly above the normalisation of the Kennicutt-Schmidt relation. Although our higher star formation rate simulations (discussed in Appendix B) did show higher values of β, this is only by a factor of 2, with β still falling at high gas surface densities. This suggests that the mechanism for galaxies to stay at high mass loadings is to remain in a state with relatively low surface densities (e.g. Read et al., 2006).

An alternative formulation of feedback in semi-analytics, suggested by Bower et al. (2011), is to attempt to match only the observable portion of the stellar mass function rather than trying to match a slope that goes to arbitrarily faint galaxies. For example, a model with a constant wind speed (from the disk) ultimately produces a faint end slope that is identical to that of the halo mass function. In an intermediate mass range, however, the effects of the gravitational potential causes material to be recycled back into the galaxy, producing a characteristic flat portion to the galaxy stellar mass function. By tuning the value of the wind speed, a nearly flat stellar mass function can be achieved over a restricted range. Although this mechanism cannot be extended to arbitrarily faint galaxies (which may be suppressed by other mechanisms, for example by re-ionization), it does provide a good fit to the observations with a constant $\beta \approx 8$ over this portion of the mass function.

In contrast to some of the predictions of semi-analytic models are the smaller estimates for the normalisation for mass loading found by hydrodynamic simulations. Oppenheimer et al. (2010) use a $\beta = 2$ and a $v_{\rm wind} = 680\ {\rm km\,s^{-1}}$ to recreate the $z = 0$ mass function. These simulations are at low resolution with the wind particles partially decoupled from the surrounding gas, making them more comparable to semi-analytic models. Fully hydrodynamical simulations where the wind is coupled to the surrounding ISM are much harder to interpret. Resolution of these issues is beyond the scope of this thesis, but better understanding of the differences between semi-analytic models and hydro simulations is clearly required.

In terms of the observed MW, Wakker et al. (2008) estimates the mass accretion rate to be $0.4\ {\rm M_\odot\,yr^{-1}}$ from infalling high velocity clouds. If this is combined in a steady state model of a MW with star formation rate of $1\ {\rm M_\odot\,yr^{-1}}$ (e.g. Chomiuk and Povich, 2011) suggests a $\beta_{200} \approx 0.6$, so there is some tension between the observed star formation of the MW and the semi-analytic models that would reduce its baryon fraction, and our simulations lie nearer the observed estimates.

One option is that the semi-analytic models consistently over-estimate the β_{200} required. In particular, there are significant degeneracies between β_{200} and the exponent. Moreover, many

models assume that the wind scaling has a fixed energy efficiency (η_T) and do not correctly account for the recapture of gas ejected from low mass galaxies (see Bower et al., 2011 for further discussion). It is entirely plausible that a careful search of parameter space may reveal strongly mass dependent solutions much closer to those found here.

On the hydrodynamical side, there are a number of physical processes that we neglected that may nevertheless be important. In terms of the gas phases we have included, the inhomogeneous metallicity will make an adjustment to the cooling, and larger scale effects such as a full 3-dimensional galactic potential along with shear and features such as bars and spiral arms will also play a role in shaping the ISM. However, it is not apparent why either of these effects will change the overall mass leaving the disk. In terms of the stellar populations we could explore the star formation distribution in terms of the correlation with molecular clouds and also the clustering of stars, which may allow the explosions to strip more material, but this is unlikely because SNe are delayed sufficiently to diffuse out of their parent clouds. The large scale radiation field may provide an additional mechanism to accelerate the wind (Murray et al., 2005; Hopkins et al., 2012a), however in our simulations the rarefaction from the disk already provides sufficient velocities to escape the halo.

Potentially the largest discrepancy we have identified is the inconsistency of the distribution of SNe with the gas evolution, i.e. matching the scale height of star formation with the new scale height of the disk. It may even be possible to make the simulations completely self consistent by matching the star formation rate to the turbulent structure of the ISM, in a manner such as that envisaged by Krumholz and McKee (2005).

Future simulations could also include the cold phase of the ISM by including radiative cooling below 10^4 K. On its own this would tend to reduce β, since a cold phase removes material from the warm phase it would not directly increase the mass loading, however the physics of this brings in other processes such as self gravity, magnetic fields, and cosmic rays (which may be dominant at these scales). Magnetic fields in particular seem a candidate for entraining more material into the wind, although simulations such as Hill et al. (2012) do not find it to play a significant role.

Overall, whilst we will include the above physical processes in future work, we suspect that these processes will not radically alter the mass-loading or significantly change the scalings we have found.

4.3 Conclusions

In this chapter we have employed the scaling relation obtained from the simulations in Chapter 3 to calculate the net mass loading, $\hat{\beta} = \dot{M}_{\rm wind}/\dot{M}_{\star}$, of an exponential disk galaxy with constant gas fraction. Using the Mo et al. (1998) scaling relation between disk and halo, we obtain a scaling with circular velocity of $\hat{\beta} \propto V_{\rm d}^{-4.8}$, stronger than either energy or momentum-driven winds. Using the observed Tully-Fisher relation we find a weaker dependence, $\hat{\beta} \propto V_{\rm d}^{-2.5}$. This compares well with recent semi-analytic models which assume $\alpha_{\rm hot} \in [2.0, 3.2]$.

The normalisation of our net mass loading at redshift $z = 0$ for a Milky-Way like galaxy is significantly lower than assumed in recent phenomenological models, although these models appear to have some degeneracy between the exponent and the normalisation, which we will explore in future work. Notably the mass loading only increases weakly with star formation rate but decreases strongly with surface density, so for starburst galaxies the feedback may be less efficient. Interestingly, our estimated normalisation is comparable with inferred values of outflow for the MW based upon the observed accretion and star formation. If indeed there is a higher mass loading, it will require supernovae to heat a larger mass of material to a lower temperature, or for the hot outflow to entrain a larger fraction of the warm ISM gas.

The scaling we find sets the investigation of galaxy winds on a new footing, providing a physically motivated sub-grid description of winds that can be implemented in cosmological simulations and semi-analytic models.

Chapter 5

The Metallicity of Galactic Winds

5.1 Introduction

Supernovae are a key ingredient in modern galaxy formation models. They are believed to eject large fractions of the baryons from small galaxies (Rees and Ostriker, 1977; White and Rees, 1978a), control the turbulence in the interstellar medium (ISM) (McKee and Ostriker, 1977; Elmegreen and Scalo, 2004) and be almost exclusively responsible for the nucleosynthesis of the heavy elements observed in the sky. The challenge of hydrodynamical simulations today is to confirm or deny whether the physics we have ascribed to these SNe correctly imply the multitude of observed galaxy properties they are believed to be responsible for.

One of the components in galaxy formation that is gradually becoming observable is that of the distribution of metals, i.e. those elements with atomic number greater than 2. Outside of our galaxy, metals can be observed in stellar absorption lines (Worthey, 1994), nebular lines of other galaxies (Tremonti et al., 2004), in galactic winds (Heckman et al., 1990, 2000; Pettini et al., 2001) and in the intergalactic medium (IGM) (Cowie et al., 1995; Schaye et al., 2003). Whilst we are far from having a complete inventory of the cosmic metals (e.g. Fukugita et al., 1998) due to the selection bias of the tracers and some unobserved sinks such as coronal gas, molecular clouds and low mass stars, we are starting to build constraints on the hydrodynamic processes that transfer metals between the different phases (Finlator and Davé, 2008; Peeples and Shankar, 2011; Davé et al., 2012).

Metals are also interesting in their ability to enhance the cooling of gas with their additional energy transitions, particularly in the range from $10^5 - 10^7$ K. This can adjust the equilibrium between the gas phases. The accumulation of galactic metals allows a form of 'archeology', where we can infer the history of star formation activity from the metal content of a galaxy. Type II SNe produce r-process elements, polluting the ISM of a galaxy, with some additional help (especially for iron) from type Ia SNe and asymptotic giant branch stars (see e.g. Burbidge et al.,

1957). By combining hydrodynamic models of the accretion and outflow of gas from galaxies it should be possible to track the evolution of metals in some detail, e.g. in Pilkington et al. (2012) where cosmological simulations had individual galaxies re-simulated (zoom simulations) to track the metal distribution in dwarfs.

Many of the uncertainties regarding star formation and the ISM cannot be resolved in cosmological simulations, however, as the balance between the phases of the ISM and the star formation rate are not simulated directly. It is therefore desirable to have simulations of the mixing in this multi-phase ISM and the rate of ejection of metals. In a recent paper (Creasey et al., submitted, hereafter CTB12) we focused on one prominent relation, that of the galaxy mass function, showing how hydrodynamical simulations of SNe entraining the ISM into a wind can be used to infer the total baryon loss and slope of the low mass end of the stellar mass function. In this chapter we extend these simulations to follow the highly enriched SN ejecta, allowing us to track the metal enrichment of the different phases and the subsequent loss of metals into the galactic wind.

5.2 Methodology

In this section we describe the set of simulations that we use to analyse the metal ejection from galactic disks. As these are an extension of the simulations in CTB12 (Chapter 3) we begin with a brief overview of that simulation set up in Section 5.2.1 before describing the addition of SN ejecta in Section 5.2.2 and their metal composition in 5.2.3.

5.2.1 Supernovae modelling

In this work we largely follow the methodology of CTB12 unless otherwise stated. Briefly, CTB12 constructed long boxes ($200 \times 200 \times 1000$ pc) through a column of an idealised warm galactic disk that is initially in hydrostatic equilibrium at $T = T_0 \equiv 10^4$ K. The boundary conditions are periodic in the short horizontal directions (x, y) and outflowing in the vertical (z), allowing material to escape from the idealised disk.

The processes included in these simulations were gravity, cooling (for $T > T_0$) and the injection of thermal energy from SNe (the rate of which was controlled by the Kennicutt-Schmidt relation). The resolution was high enough to resolve the effect of individual SNe on the ISM resulting in the launch of a wind and the development of a two phase medium of hot and warm material. The gravitational potential is static and the gravitational mass is assumed to exceed the gas mass by a fraction $1/f_{\rm g}$.

5.2.2 Supernova ejecta

The deviation from the model of CTB12 is the inclusion of SNe ejecta. In the model of CTB12 we include only the thermal energy of SNe, injected in a Gaussian profile of

$$\Delta p(\mathbf{x}) = (\gamma - 1) E_{\rm SN} \left(2\pi r_s\right)^{-3/2} \exp\left(-\frac{1}{2}\frac{r^2}{r_s^2}\right) , \tag{5.1}$$

which has been normalised by $E_{\rm SN} = 10^{51}$ erg, the energy released by a single SN, where r is the distance from the centre of the SN and $r_s = 2{\rm pc}$ is the scale radius of the thermal injection, optimised to give us good resolution (i.e. not smearing the supernova over a large volume) but also to allow for the limitations of the hydrodynamics solver (by not placing the energy in only 1 cell). In this work we extend this to include an additional fluid, that of the ejecta, i.e. $\rho = \rho_p + \rho_e$, where ρ_p is the pristine gas and ρ_e is the gas injected by SNe. Initially ρ_e is set to zero everywhere and is increased by each SN by

$$\Delta \rho_e(\mathbf{x}) = M_{\rm SN} \left(2\pi r_s\right)^{-3/2} \exp\left(-\frac{1}{2}\frac{r^2}{r_s^2}\right) , \tag{5.2}$$

where $M_{\rm SN} = 10\ {\rm M}_\odot$ is the total mass added (a progenitor stellar mass of $\approx 12\ {\rm M}_\odot$, see Woosley and Weaver, 1995), chosen to be representative of a Chabrier IMF where core collapse occurs for stars in the range $[6, 100]\ {\rm M}_\odot$.

Notably this sets a specific energy for the remnant which was absent from the simulations of CTB12. In those simulations the SNe could explode in arbitrarily sparse environments, and there would be a (very small) tail of gas at $T > 10^9$ K. In these simulations the SNe energy inject gas at a temperature of

$$\begin{aligned} T_e &\equiv \frac{\mu \Delta p}{k_{\rm B} \Delta \rho_e} && (5.3) \\ &= (\gamma - 1) \frac{\mu E_{\rm SN}}{k_{\rm B} M_{\rm SN}} \\ &\approx 9.1 \times 10^8\ {\rm K}\,. && (5.4) \end{aligned}$$

5.2.3 Cooling and the metal composition of ejecta

The specific choice of $10\ {\rm M}_\odot$ for the mass of the SN ejecta may at first appear crucial to the subsequent metallicity evolution of the ISM, as this sets the quantity of metals that are introduced. The hydrodynamics of our simulations, however, are only weakly dependent on this mass (the evolution of the remnant is primarily driven by the energy of the SN), via the temperature in Eq. (5.3), so to reduce the number of simulations we keep our ejecta mass fixed and simply assume that the metallicity of this varies with the yield, i.e.

$$Z_{\rm ej} \equiv \frac{M_{Z,\rm SN}}{M_{\rm SN}} = y\left(\frac{100\epsilon_{100}\rm M_{\odot}}{M_{\rm SN}}\right), \quad (5.5)$$

where to be consistent with CTB12 we use $\epsilon_{100} = 1$ SN per 100 $\rm M_{\odot}$ of stars formed, and the yield y refers to the mass of oxygen released into the ISM per 1 $\rm M_{\odot}$ of star formation. This analysis could be repeated for other elements. However, for other elements (particularly iron) the departure from instantaneous recycling due to the importance of long lived stars on the returned fraction will make the approximations progressively poorer (e.g. Schmidt, 1963 and Tinsley, 1980).

The actual value of the metal yield $y \approx 0.02$, which we take as our fiducial value, but is known only to a factor of ~ 2 (Woosley and Weaver, 1995; Finlator and Davé, 2008, hereafter FD08). Where possible we quote in fractions of y to reduce this degeneracy. In order to retain the scale-free nature of the calculation this means that we must also choose a cooling function that is independent of metallicity. To this end we use the cooling function of CTB12. Had we included these metallicity terms the rate of cooling would be enhanced, particularly around 10^6 K (see e.g. Wiersma et al., 2009a). We also note that we do not run these simulations for longer than 20 Myr, and so the unpolluted disk gas at the beginning of our simulations would already contain a significant quantity of metals, and thus a cooling correction should also be applied to this gas.

The specific value of the solar metallicity $Z_{\odot}$ is only of interest for reference purposes in our calculations. When it is used we take the value of $Z_{\odot} = 0.0165$ (Asplund et al., 2005). Given the values in the previous paragraphs this is around 8% of the ejecta metallicity (i.e. the Sun has formed from diluted material). We are also making the assumption of well mixed ejecta, in reality different progenitor stars will have different abundance patterns.

5.2.4 Stellar winds

We run a number of simulations that include the winds from massive stars. We consider these to occur at the same sites as the SNe, and act uniformly over a time of 10 Myr. They can thus be considered either to issue from the progenitor stars of the SNe or of the OB associations in which the SNe occur.

The prescription for the stellar winds is the introduction of thermal and kinetic energy, in a similar way to the instantaneous energy injection for the SNe. The evolution of the fluid variables

due to these (for each SN) are

$$\dot{\rho}|_{\rm OB} = \dot{M}_{\rm OB} \left(2\pi r_s^2\right)^{-3/2} \exp\left(-\frac{1}{2}\frac{r^2}{r_s^2}\right) \quad (5.6)$$

$$\dot{p}|_{\rm OB} = (\gamma-1)\dot{E}_{\rm OB} \left(2\pi r_s^2\right)^{-3/2} \exp\left(-\frac{1}{2}\frac{r^2}{r_s^2}\right) \quad (5.7)$$

$$\left.\frac{\partial}{\partial t}(\rho \mathbf{v})\right|_{\rm OB} = \frac{\mathbf{r}}{r_s}\frac{\dot{P}_{\rm OB}}{8\pi r_s^3} \exp\left(-\frac{1}{2}\frac{r^2}{r_s^2}\right), \quad (5.8)$$

where we have normalised such that the rate of mass injection is $\dot{M}_{\rm OB}$, the rate of thermal energy injection to $\dot{E}_{\rm th,OB}$, and the rate of (absolute) momentum injection is $\dot{P}_{\rm OB}$. Our fiducial values for these rates are

$$\dot{M}_{\rm OB} = 0.1\ {\rm M}_\odot\,{\rm Myr}^{-1} \quad (5.9)$$

$$\dot{E}_{\rm OB} = 10^{50}\ {\rm erg\,Myr}^{-1} \quad (5.10)$$

$$\dot{P}_{\rm OB} = 920\ {\rm km\,s}^{-1}\,{\rm M}_\odot\,{\rm Myr}^{-1}, \quad (5.11)$$

where the momentum injection corresponds to a kinetic energy injection rate of approximately $\dot{P}_{\rm OB}^2/2\dot{M}_{\rm OB} \approx 8.5\times10^{49}\ {\rm erg\,Myr}^{-1}$ (close to that of Castor et al., 1975b), though this will to some extent depend on the local environment. Over the 10 Myr lifetime of the star we will have released an additional $E_{\rm SN}$ in thermal energy and almost the same again in mechanical energy. We have intentionally not chosen conservative values for the energy injection rates in order to make the effects of these winds more apparent in our simulations. The high implied wind velocity ($\dot{P}_{\rm OB}/\dot{M}_{\rm OB}$) is partly due to this but mostly to account for the momentum injection due to the radiation driving of the winds (see also Murray et al., 2005), i.e. the massive stars release a large fraction of energy as radiation which couples to more than just the mass in the wind (e.g. Hopkins et al., 2011).

5.3 Results

In this section we describe the evolution of metallicity in our simulations. We present the distribution of metallicity within the ISM in terms of the different phases and discuss the effects of our parameter choices. We then move on to looking at the outflowing metals that escape from the galactic disk and the dependency of this on the disk properties. Finally, we discuss the origin of the correlation between thermalisation and metal mass loading from the disk.

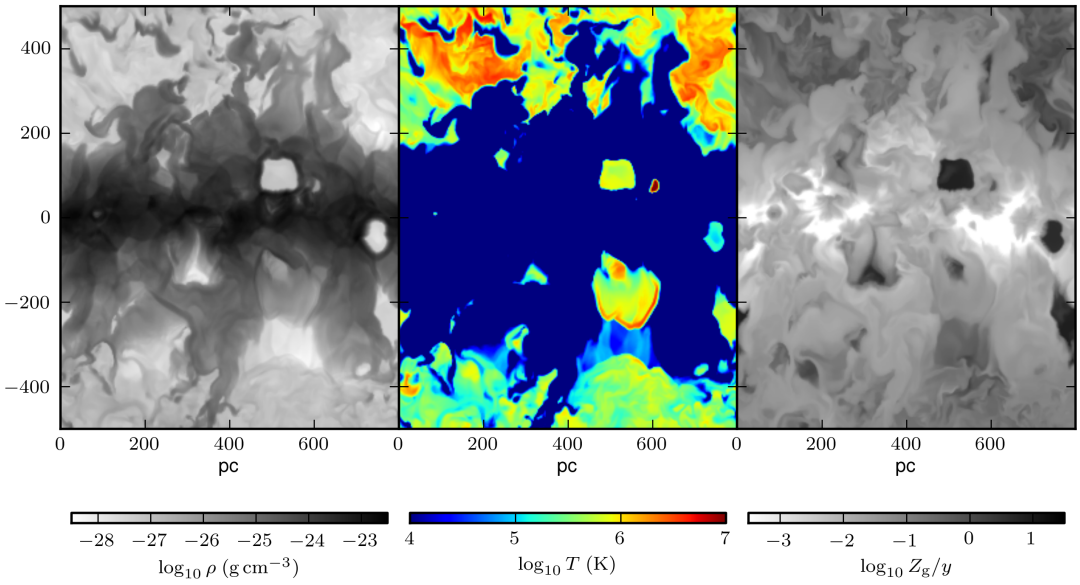

Figure 5.1: Slice through the simulation volume at 15 Myr. From left to right, density of gas, temperature of gas and metallicity of gas. We see the disrupted horizontal feature of the disk with cavities of hot, metal rich gas due to individual SNe. The outflow (above and below the disk) consists of metal enriched gas at a range of temperatures undergoing turbulent mixing.

5.3.1 The metallicity of the ISM

We begin with an illustrative slice of a simulation volume at 15 Myr for a $\Sigma_{\rm g} = 11.6\ {\rm M}_\odot\ {\rm pc}^{-2}$ and gas fraction $f_{\rm g} = 0.1$ in a box of width 800pc shown in Fig. 5.1. At $z = 0$ we see the disrupted disk, where the initially pristine gas has been polluted (in metallicity) by several generations of SNe.

In a few regions individual recent SN remnants are discernable, where they stand out as noticeably hot and sparse high metallicity bubbles. Above and below the disk is the hot wind of Chapter 3, which, although quite turbulent, appears to have a higher mean metallicity than the disk. Indeed, there appears to be a correlation between temperature and metallicity, and an anti-correlation between density and metallicity as we discuss further in Section 5.3.3.

In Fig. 5.2 we take a closer look at the ISM by studying the phase space in metallicity vs. density and temperature at a snapshot of the fiducial simulation at 10 Myr. We see that the hot, sparse phase has a significantly higher metallicity than the warm dense phase. Interestingly, however, in terms of total mass in metals, the warm phase still dominates due to its much greater mass. Our reference value of 8% for solar metallicity as a fraction of the ejecta metallicity lies

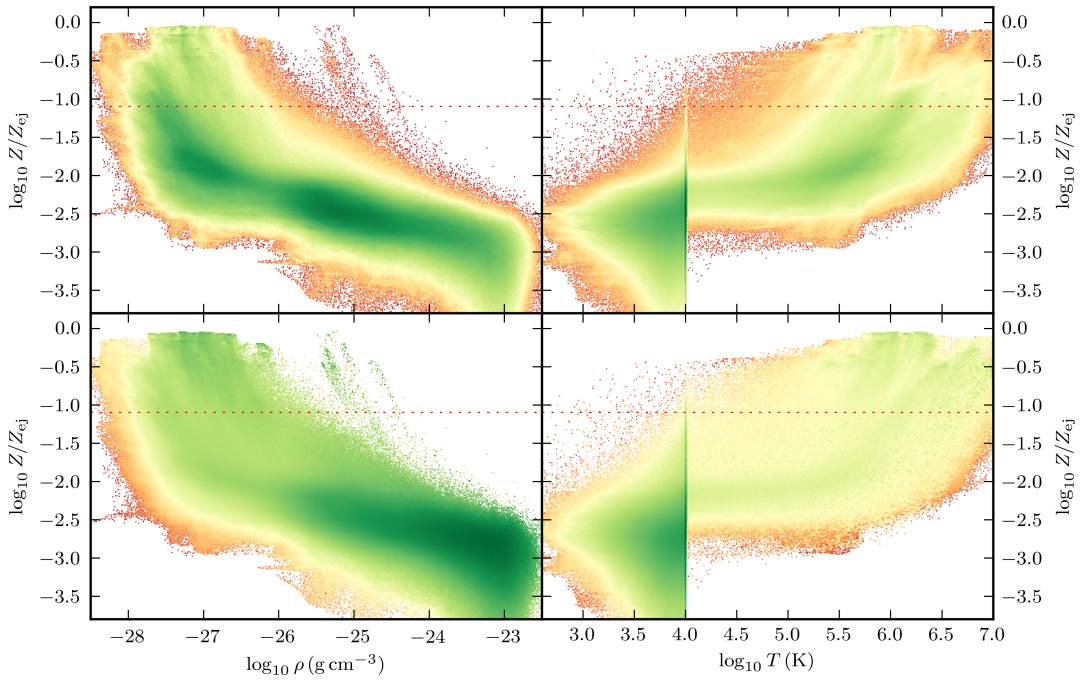

Figure 5.2: Density vs. metallicity and temperature vs. metallicity phase space diagrams. *Left panels* show the density vs. metallicity, *right panels* show the temperature vs. metallicity. *Upper panels* are shaded by volume in each phase (from *red*, low, to *green*, high), whilst the *lower panels* are shaded by the fraction of metals in each phase. The vertical feature at 10^4 K is the base of the cooling function. *Red dashed line* indicates solar metallicity, where we have assumed a yield $y = 0.02$ (see Eq. 5.5 for details). Most of the metals lie in the warm, dense phase, although the hot phase has a higher average metallicity. The semblance of a reflection symmetry between the *left* and *right panels* is due to the (approximate) pressure equilibrium of the ISM, i.e. density is the inverse of temperature.

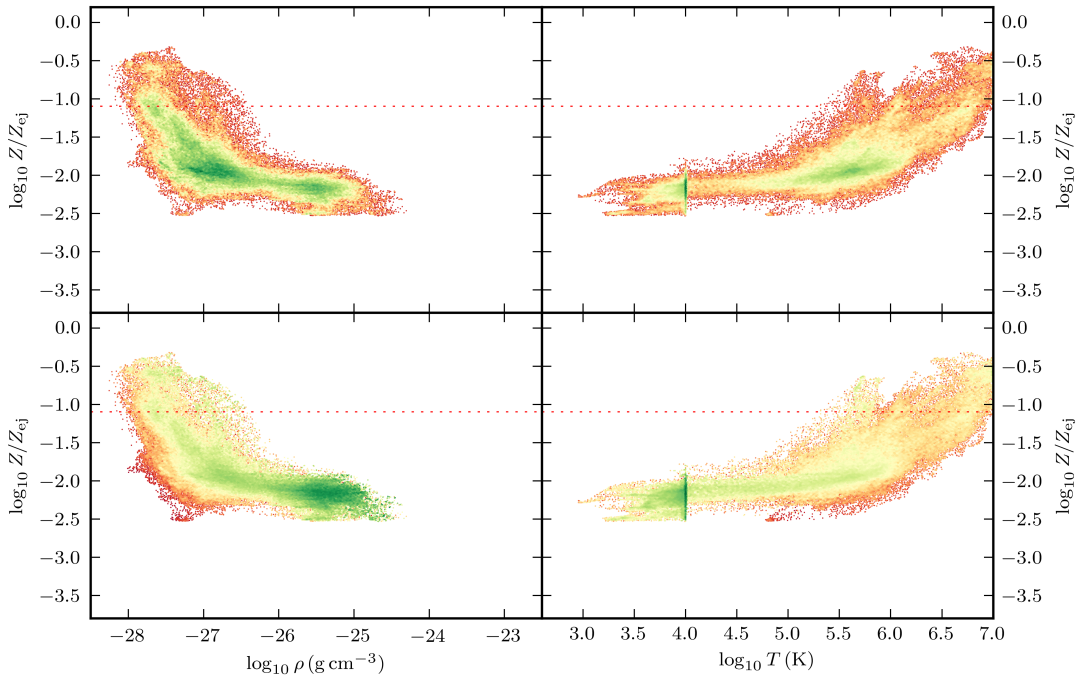

Figure 5.3: As for Fig. 5.2 but only for the material being ejected from the disk. *Upper panels* are shaded by volume fraction, *lower panels* by metal fraction. The fraction in the warm (10^4K) dense ($\sim 10^{-23}\,\mathrm{g\,cm^{-3}}$) phase is markedly reduced.

at the lower range of metallicities for the hot phase and higher than the metallicities of the warm phase. The metallicity of the warm phase is not static, however, as it is being steadily enriched by successive generations of SN, and after several Gyr we would expect the cooler material to be sufficiently enriched to form higher metallicity stars. Notably there is a considerable amount of scatter in the metallicities of the hot phase. The gas below 10^4 K is due to adiabatic expansion, in the turbulent ISM the compression and expansion combined with cooling in the compressed phase allows the gas to scatter below 10^4 K.

In contrast, the metallicity of the unbound hot phase is in approximate equilibrium, as the injected metals can escape from the disk. In Fig. 5.3 we restrict our attention to the outflowing material from the disk (in the same manner as Chapter 3). We see that this is dominated by the hot, low density, high metallicity phase, indeed there is no gas with density above 10^{-24} $\mathrm{g\,cm^{-3}}$ or relative metallicity below $10^{-2.5}$ $Z_{\rm ej}$. The nature of our enrichment mechanism entails that the outflowing gas from galactic disks will be of significantly higher metallicity than the average gas phase metallicities of the ISM. Unfortunately, as this gas is rather hot and of low column density it is hard to observe directly, and it may be easier to derive constraints from the X-ray coronae of

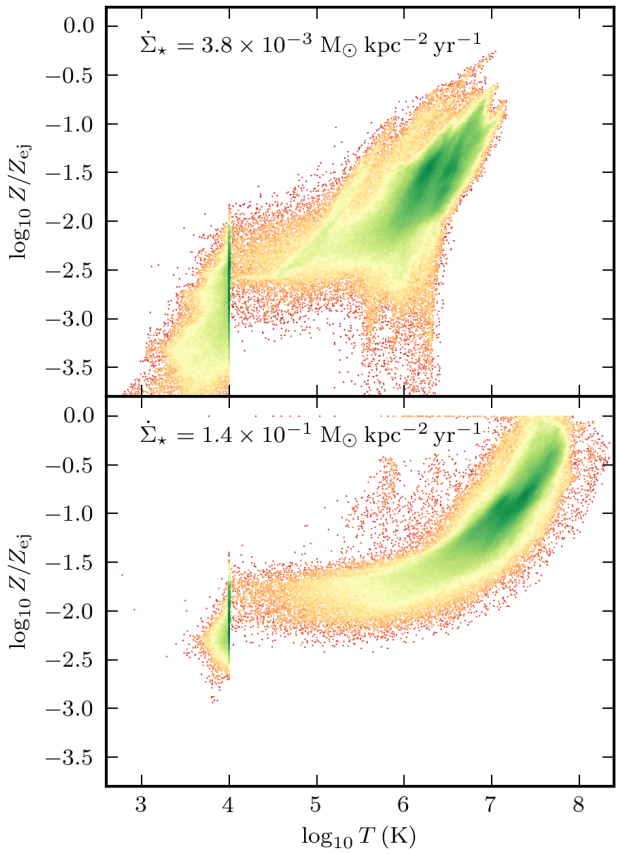

Figure 5.4: Comparison of ISM temperature-metallicity phases for disks with different star formation rates. *Lower panel* has a high star formation rate of $\dot{\Sigma}_\star = 1.4 \times 10^{-1}\ \mathrm{M}_\odot\ \mathrm{kpc}^{-2}\,\mathrm{yr}^{-1}$ whilst the *upper panel* has a lower SFR of $\dot{\Sigma}_\star = 3.8 \times 10^{-3}\ \mathrm{M}_\odot\ \mathrm{kpc}^{-2}\,\mathrm{yr}^{-1}$.

halos (e.g. Crain et al., 2010). There is also the complication that this gas will quickly mix with material in the circum-galactic medium to form a lower metallicity blend.

In Chapter 3 we saw how higher gas surface density disks (with higher star formation rates) would in general have a higher temperature hot phase (and consequently lower mass loadings). We expect this to carry through to these simulations that include the ejecta, and also that there will be a corresponding trend in metallicity, where the outflows in simulations with higher surface densities entrain less gas and are both hotter and more metal rich. In Fig. 5.4 we probe this by comparing the ISM at a single time for two different surface densities. We can indeed see that the peak of the distribution of the hot phase for the higher surface density simulation lies at a temperature and metallicity nearly an order of magnitude higher than that for the low surface density ISM.

We now turn our attention to the time evolution of the ISM. In Chapter 3 we saw how the

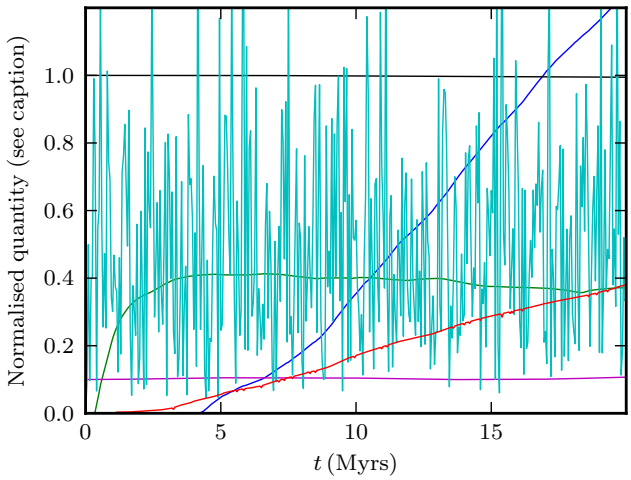

Figure 5.5: The time evolution of the metal ejection simulation shown in Fig. 5.1. *Cyan line* is the cooling rate of the simulation volume as a fraction of the mean SN heating rate, *black line* is the fraction of gas remaining in the simulation volume, *green line* is the porosity normalised as $0.2P+0.5$. *Dark blue line* is the surface density of gas ejected from the disk in units of $0.05\ \mathrm{M}_\odot\,\mathrm{pc}^{-2}$, *red line* is the ejected surface density of metals divided by yield, in units of $0.03\ \mathrm{M}_\odot\,\mathrm{pc}^{-2}$.

stochastic mass ejection from the disks could be averaged over a large number of events to estimate a mean outflow rate for a given idealised disk. We attempted to measure this by combining the net mass loss from several snapshots in time and performing a linear fit with some delay time, such that the slope of the mass loss would indicate the outflow rate. In Section 5.3.2 we will attempt the corresponding analysis, but in terms of the metal ejection rate, and for this reason we investigate the time evolution for a single simulation.

In Fig. 5.5 we show the evolution of disk mass, scale height, porosity, cooling rate, mass loss and metal loss as a function of time, for the same simulation as Fig. 5.1 (the larger disk area considered makes the statistics less stochastic). We see that after a period of ≈ 4 Myr the porosity of the ISM has converged and the mass and metal losses are proceeding approximately linearly. Over the simulation time the total mass of gas and the scale height of the disk have not adjusted significantly.

In Fig. 5.6 we study the effects of including stellar winds from OB associations. The overall effect is an increase in the outflow of $\approx 7\%$, approximately in proportion to their mass as a fraction of the SN ejecta, but far less than their energy input, as the amount of energy we have injected of the 10 Myr duration of the stellar winds is of the same order as E_{SN}. This will in part

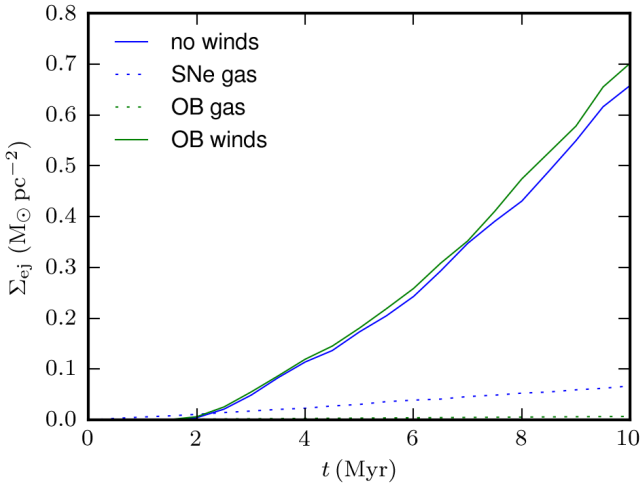

Figure 5.6: Gas ejection due to stellar winds. *Blue solid line* indicates the ejected surface density from a simulation with star formation rate $\dot{\Sigma}_\star = 6.7 \times 10^{-2}\ \mathrm{M_\odot\,kpc^{-2}\,yr^{-1}}$, with SN ejecta but no thermal or kinetic feedback from OB associations, and *dotted blue* indicates SN ejecta mass released. *Green line* indicates the outflow from the same simulation, but with the addition of stellar winds (see text for description). The total mass released by these winds is indicated in the *dotted green line*. The gas ejected from SNe and in winds has coupled to a much larger mass in gas, entraining it in a wind from the disk. The effect of stellar winds is small.

be due to our lack of resolution for this process, but our energy injection rate is rather high and the site of the injection (exactly at the position of the SN rather than with a large dispersion) will count against this, so we infer from this that SN are still the dominant process for gas ejection.

It is interesting to compare this to other simulations where radiation and dust driving mechanisms (Murray et al., 2005; Martin, 2005; Sharma et al., 2011) have been included, such as the scheme of Hopkins et al. (2011) applied in Hopkins et al. (2012b). The latter concludes that although radiation and winds are important for unbinding GMCs, SN are still the dominant mechanism for driving galactic winds, which is consistent with the results in Fig. 5.6. Our simulations are less reliant on the stellar winds to destroy the dense star forming regions since our SN distribution is pre-computed according to the Kennicutt-Schmidt relation and not tied to the gas distribution in which they explode. If anything we see even less effect of stellar winds on the outflow, which may be due to their use of multiple photon scatterings to drive a stronger wind.

Fig. 5.6 also provides an alternative aspect from which to imply the mass loading of the winds. Since the gas ejection rate from SNe is related to the star formation rate via the ejecta mass and

the proportion of SNe in the IMF, i.e. $\dot{\Sigma}_{\rm SN}/\dot{\Sigma}_\star = (M_{\rm SN}/100\,{\rm M}_\odot)\epsilon_{100}^{-1} \approx 0.1$ for this model, then the mass loading can be deduced as the product of this and the ratio of ejected surface density to SN ejecta. This can be read from Fig. 5.6 as $\dot{\Sigma}_{\rm w}/\dot{\Sigma}_{\rm SN} \approx 10$, implying $\beta \equiv \dot{\Sigma}_{\rm w}/\dot{\Sigma}_\star \approx 1$ for this simulation.

5.3.2 Outflow dependencies

We now turn our attention to the rate at which metals are ejected from the disk. In order to make comparisons with cosmological properties, we define the quantity $\beta_{\rm Z}$ as the ratio of the mass of metals ejected to the mass of stars formed,

$$\beta_{\rm Z} \equiv \frac{\dot{M}_{\rm w,Z}}{\dot{M}_\star}\,, \tag{5.12}$$

as measured from the slopes of the delayed linear fits for the time evolution (i.e. Fig. 5.5) for each simulation.

In Fig. 5.7 we explore how the outflow depends on total surface density $\Sigma = \Sigma_{\rm g}/f_{\rm g}$. We show the mass ejected per unit star formation (β, see also Chapter 3), the fraction of metals ejected, and the ratio of these two, i.e. a measure of the metallicity of the wind. The mass loading shows the same trend as Chapter 3, with higher surface densities and higher gas fractions resulting in lower mass ejection rates (the dependence on gas fraction inverts when parameterised on $\Sigma_{\rm g}$ and $f_{\rm g}$ rather than Σ and $f_{\rm g}$). To a large extent the disk surface density can be used as a proxy for galaxy mass, and so we expect high mass galaxies to have more 'mass loaded' winds.

The same trend is significant (although less strong) for the metal ejection fraction, i.e. at high disk surface densities and gas fractions the disks are less efficient at ejecting their metals. It should be noted that we are only examining the disk here, and so these metals may not escape the halo (and indeed may be recycled back in to the disk), an effect which again will be more prominent for more massive galaxies with deeper potentials.

The ratio of these two estimates the fraction of metals ejected per unit mass ejected gives a measure of the average metallicity of the wind. The scatter is reduced in this data, i.e. the SN distributions that are more effective at ejecting metals are also more effective at driving the winds. As discussed in Chapter 3 the latter effect seems a result of a greater fraction of SN occurring near to the edge of the disk and is probably the cause of the former too, entailing the correlation. Since the negative trend with surface density is less strong for the metal fraction, the metallicity becomes an increasing function of surface density, i.e. although high density disks are less effective at ejecting metals, they are even less effective at driving a wind and as a result the metallicity of the wind is higher.

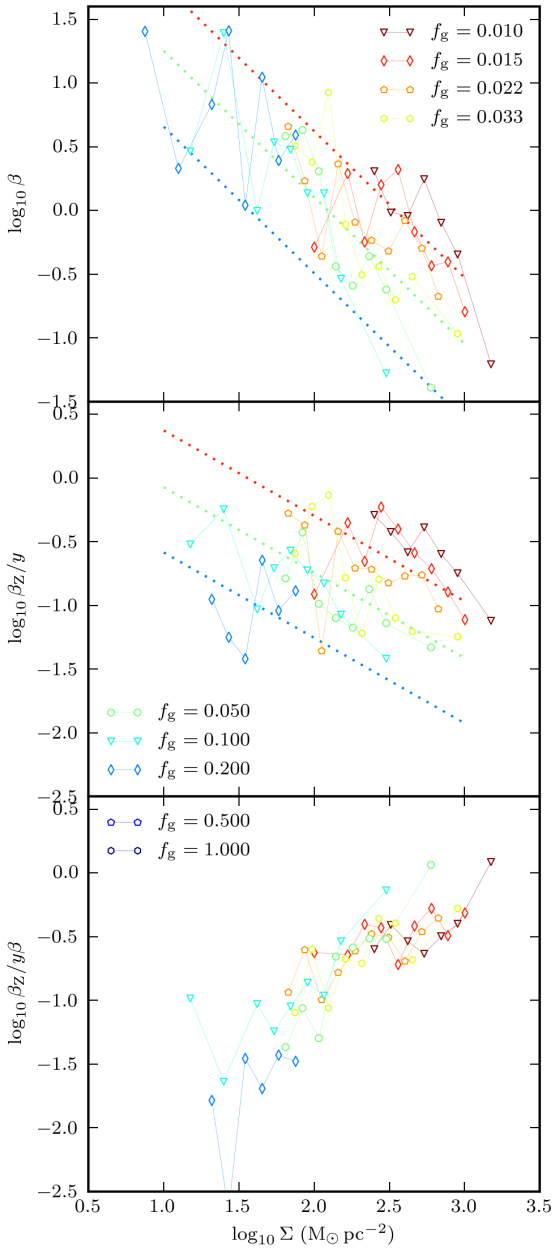

Figure 5.7: The dependence of the mass loading ($\beta \equiv \dot{M}_w/\dot{M}_\star$) and the metal mass loading ($\beta_Z \equiv \dot{M}_{w,Z}/\dot{M}_\star$ plotted as a fraction of the yield, y) as a function of total surface density $\Sigma = \Sigma_g/f_g$ (stars and gas). *Coloured symbols* indicate the different gas fractions (f_g), *red*, *green* and blue dashed lines show the best power law fit to the surface density evaluated for the gas fractions $f_g = 0.015$, 0.05 and 0.2 (colours matched to symbol colours). There is a large amount of scatter in the upper panels, both due to the stochasticity of the star formation but also the residual dependence on f_g. This is reduced somewhat in the lowest panel, suggesting that the stochastic locations which induce higher mass ejections also induce higher metal ejections.

The best fit regression for the metal ejection fraction is

$$\beta_{\rm Z}/y = [0.10 \pm 0.01] \left(\frac{\Sigma_{\rm g}}{10 \, {\rm M}_\odot \, {\rm pc}^{-2}} \right)^{-0.67 \pm 0.14} \left(\frac{f_{\rm g}}{0.1} \right)^{-0.18 \pm 0.10} , \quad (5.13)$$

where we give jackknife errors. We see that the metal mass loading has a negative dependence on gas surface density and a weak dependence on gas fraction. A leading coefficient of < 0.5 indicates that the most of the metals distributed by the SNe are retained by the ISM. We find a best fit dependence of the mass loading (β, the mass ejection per unit star formation) from the simulations in Chapter 3 of

$$\begin{aligned} \beta &\equiv \frac{\dot{M}_{\rm w}}{\dot{M}_\star} \\ &\approx [0.6 \pm 0.5] \left(\frac{\Sigma_{\rm g}}{10 \, {\rm M}_\odot \, {\rm pc}^{-2}} \right)^{-1.15 \pm 0.12} \left(\frac{f_{\rm g}}{0.1} \right)^{0.16 \pm 0.14} , \end{aligned} \quad (5.14)$$

(the fit for the mass loading from these simulations is consistent with that from Chapter 3, but we use the latter as it has smaller error estimates due to the lower scatter). The mass loading has a stronger negative dependence on surface density and the dependence on gas fraction is also quite weak. This implies that when we take the ratio of these to find the metallicity, $\beta_{\rm Z}/\beta$, this will be an increasing function, i.e. at higher surface densities the winds become more metal rich.

It is interesting to contrast with the limits imposed by our simulation. If all the ejecta were to escape, but entrain none of the ISM gas, we would have an ejecta metallicity of the yield $\beta_{\rm Z}/y = 1$ and a mass loading of $\beta = (M_{\rm SN}/100 \, {\rm M}_\odot)\epsilon_{100}^{-1} = 0.1$, and the ISM would remain un-enriched as all the metals are propelled out of the simulation volume. We see, however, that in our simulations a large amount of gas is entrained into the wind, $\beta \gg 0.1$, and most of the ejecta is recaptured by the disk, $\beta_{\rm Z}/y \ll 1$. Nevertheless, the metallicity of the wind still lies between that of the ISM and the ejecta, i.e. $Z_{\rm ISM} < Z_{\rm w} < Z_{\rm ej}$ (see Figures 5.2 and 5.3), indeed it would be extremely difficult to alter the order of these metallicities, a point we discuss in the following section.

5.3.3 Hydrodynamic considerations

In an idealised gas, the diffusivity of heat and mass are almost equal to the kinematic viscosity ν due to their molecular origins, and as such, turbulent mixing processes diffuse these quantities at similar rates. This observation is of particular relevance for SN feedback as the SNe are the source of both the metals and the thermal energy for feedback.

There are of course other ways to transfer thermal energy in the ISM (in particular radiation, which we will discuss later), allowing thermal energy to 'escape' from the metals, but the idea of thermal energy tracking metals and vice versa is still a useful concept.

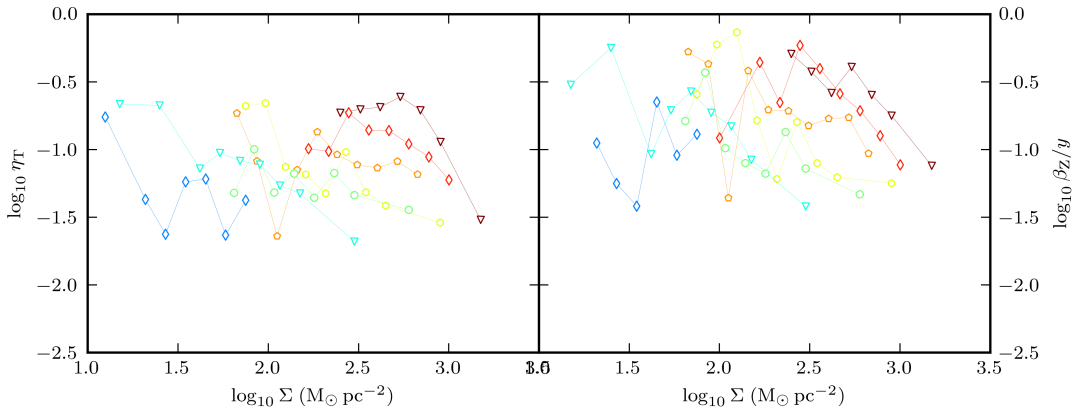

Figure 5.8: *Left panel*, the thermalisation efficiency as a function of total surface density Σ. *Right panel*, the fraction of metals entrained in the wind, β_Z/y. Gas fractions are coloured as for Fig. 5.7.

One of the first implications of such a model is that the ISM phases may exhibit a correlation between temperature and metallicity. As SNe inject both metals and thermal energy into the ISM, these cascade down into the hot, warm and cold phases, with the metallicity following the specific energy (i.e. the temperature). The cooler phases mop up less of the SNe energy and metals. A model where this correlation were completely eliminated would require that all the SNe explode initially, creating a homogeneous hot phase, and warm and cold phases appear only by a cooling instability and thus retain the same metallicity as the ejecta. No accretion could be allowed either, as this would also preferentially introduce low metallicity cooler gas.

This picture could be slightly adjusted by the stronger cooling rates in metal enriched gas (i.e. driving high metallicity gas to lower temperatures faster), but this will be diluted by the diffusion of metals and is unlikely to exceed the effects of accretion and SN feedback.

This preferential distribution of metals in the hot phase also appears to be found in observations, with Ferrara et al. (2005) finding that only 5%-9% of metals lie in the cool (10^4 K) phase of the ISM, whereas the rest go into an unbound hot phase. We explore this correspondence in Figures 5.8 & 5.9.

In CTB12 we constructed a model, based upon the snowplough models of Cox (1972) and Chevalier (1974), of a shock expanding until the thermal energy losses due to cooling became comparable to the thermal energy dilution due to shock heating. In this very simple model, a mass $M_{\rm hot}$ of gas was heated by each SN, which escaped to form the galactic wind. Since the blast wave contains all the energy and mass of the SN, we would expect a complete escape of this bubble to also carry 100% of the metals. However, if we weaken this slightly by the inclusion of radiation, then we only expect a fraction $\eta_{\rm T}$ of the SN energy to be thermalised into the wind,

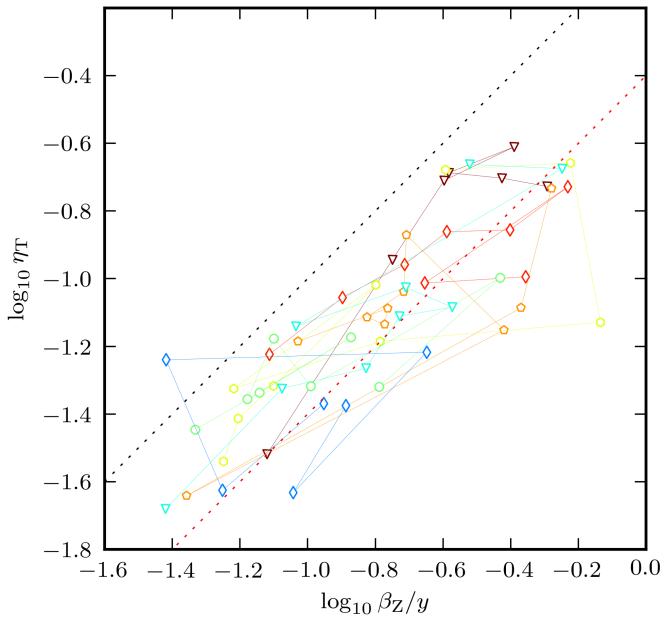

Figure 5.9: The thermalisation efficiency η_T and fraction of metals entrained β_Z/y. Gas fractions are coloured as for Fig. 5.7. *Dotted black line* indicates where the points would lie if $\eta_T = \beta_Z/y$, i.e. the same fraction of metals and thermal energy escape. *Dotted red line* indicates the relation $\eta_T = 0.4\beta_Z/y$, i.e. if the fraction of energy escaping in the outflow is 40% of the fraction of metals ejected.

and this would also correspond to a fraction $\beta_{\rm Z}$ of the metals escaping. As such $\eta_T = \beta_Z/y$ is ostensibly an upper limit, as the thermal energy and metals are completely mixed in the ejecta of our SN.

We have indicated both of these scenarios in Fig. 5.9, where we see an illustrative model with the escaping metals carrying 40% of their fraction of the SN energy (i.e. $\eta_{\rm T} = 0.4\beta_{\rm Z}/y$), representing quite a good fit to the data. In a steady-state disk model, one would expect the metals that remain in the disk to radiate all their thermal energy, so this result suggests that, in addition, the ejecta that escapes radiates away 60% of its energy as it mixes with the ISM gas. $\log_{10}\eta_{\rm T} = 0$ and $\log_{10}\beta_{\rm Z}/y$ can both be considered upper limits, i.e. the far right and above the top of the figure. It is interesting to compare the thermalisation efficiency to the commonly quoted 10% of Larson (1974). Our simulations suggest that this fraction depends upon the metal ejection and is not universal.

5.4 Application: The Mass Metallicity relation

In this section our aim is to use the simulation results to understand the evolution of the mean gas phase metallicity $\langle Z_{\rm g} \rangle$ of a galaxy, and the mass-metallicity relation of galaxies ($Z_{\rm g}(M_\star)$). We construct a simple model of metallicity distributions from the gas and stellar evolution of galaxies along with the metal ejection rates. We demonstrate that these assumptions are consistent with the metallicity distribution of faint stars (G-Dwarfs) and that it is straightforward to match the observed mass-metallicity relation of galaxies with reasonable values for the metal ejection rates. We discuss the origin of the turnover in the mass metallicity relation in our model and compare to other analytic models. Finally, we compare the metallicity ejection rates with those found in the hydrodynamical simulations of Section 5.3.

5.4.1 Inferring ISM metallicities

The gas reservoir of a galaxy evolves with the following sources and sinks

$$\dot{M}_{\rm g} = \dot{M}_{\rm a} - (1 - f_r)\dot{M}_\star - \dot{M}_{\rm w} \,, \tag{5.15}$$

where $\dot{M}_{\rm a}$ is the cold gas accretion rate, $\dot{M}_\star$ is the star formation rate $\dot{M}_{\rm w}$ is the wind loss rate and f_r is the fraction of gas released back in to the ISM via short lived stars and stellar winds (we assume instantaneous recycling[1]). The total metal mass of this gas reservoir, $M_{\rm Z}$, evolves as

$$\begin{aligned} \dot{M}_{\rm Z} &\equiv \frac{\rm d}{{\rm d}t}\left[Z_{\rm g} M_{\rm g}\right] & (5.16) \\ &= (y + f_r Z_{\rm g})\dot{M}_\star + Z_{\rm a}\dot{M}_{\rm a} - Z_{\rm w}\dot{M}_{\rm w} - Z_{\rm g}\dot{M}_\star \,, & (5.17) \end{aligned}$$

where y is the yield and $Z_{\rm a}$, $Z_{\rm w}$ and $Z_{\rm g}$ are the metallicities of the accreting, wind and ISM gas respectively. The terms on the right then refer to metals released by short lived stars, metals accreted from inflowing gas, metals lost in the wind and metals locked away by star formation.

Our first approximation is that $Z_{\rm a} = 0$, as the metallicity of the inflowing gas is very low. We note that this may be violated for high mass galaxies that are recycling metals through their halos and we return to this in Section 5.4.4. We also write the outflowing metals in terms of the star formation rate, $Z_{\rm w}\dot{M}_{\rm w} \equiv \beta_{\rm Z}(t, M_\star)\dot{M}_\star$, transforming Eq. (5.17) to

$$\dot{Z}_{\rm g} M_{\rm g} + Z_{\rm g}\dot{M}_{\rm g} = \left[y - \beta_{\rm Z}(M_\star, t) - Z_{\rm g}(1 - f_r)\right]\dot{M}_\star \,. \tag{5.18}$$

[1]Note that in our convention $M_\star$ refers to the total amount of stellar mass created, not just the fraction $(1 - f_r)M_\star$ that is in long-lived stars.

If we then make the assumption that there is no extra dependence on time (or equivalently redshift), other than that implied in the stellar mass, i.e.

$$M_{\rm g}(M_\star, t) = M_{\rm g}(M_\star) \tag{5.19}$$

$$Z_{\rm g}(M_\star, t) = Z_{\rm g}(M_\star) \tag{5.20}$$

$$\beta_{\rm Z}(M_\star, t) = \beta_{\rm Z}(M_\star) \tag{5.21}$$

then we can write Eq. (5.18) parameterised in terms of $M_\star$ rather than time as

$$\frac{\rm d}{{\rm d}M_\star}\left[Z_{\rm g}M_{\rm g}\right] = -(1-f_r)Z_{\rm g} + y - \beta_{\rm Z}(M_\star)\,. \tag{5.22}$$

In order to proceed further we need some estimate of $M_{\rm g}(M_\star)$, i.e. the gas mass at each stellar mass (note we have already neglected redshift dependence, so we are assuming galaxies just move along the redshift zero relations, parameterised only by their stellar mass). In general this precludes growth in stellar (and gas) mass due to mergers, which would disrupt this relation. We assume a power law of the form

$$M_{\rm g} = A_{\rm g}\left(\frac{M_\star}{10^{10}\,{\rm M}_\odot}\right)^{\alpha_{\rm g}} 10^{10}\,{\rm M}_\odot\,, \tag{5.23}$$

(we discuss the observational $M_{\rm g} - M_\star$ relation later in this section), where $A_{\rm g}$ and $\alpha_{\rm g}$ are dimensionless constants. This allows us to solve Eq. (5.22) in integral form as

$$\begin{aligned} Z_{\rm g}(M_\star) &= \frac{1}{M_{\rm g}(M_\star)}\int_0^{M_\star} {\rm d}m\,(y - \beta_{\rm Z}(m)) \\ &\quad \exp\left[-\left(\frac{1-f_r}{1-\alpha_{\rm g}}\right)\left(\frac{M_\star}{M_{\rm g}(M_\star)} - \frac{m}{M_{\rm g}(m)}\right)\right]\,. \end{aligned} \tag{5.24}$$

Special cases

Equation (5.24) has two special cases that are of particular interest when approximating the mass-metallicity relation, that of $M_\star \gg M_{\rm g}$ and $M_\star \ll M_{\rm g}$, corresponding to high and low stellar mass galaxies. In the former, low gas reservoir limit, we find

$$\begin{aligned} Z_{\rm g}(M_\star) &= \lim_{M_{\rm g}/M_\star \to 0} \frac{1}{M_{\rm g}(M_\star)}\int_0^{M_\star} {\rm d}m\,(y - \beta_{\rm Z}(m)) \\ &\quad \exp\left[-\left(\frac{1-f_r}{1-\alpha_{\rm g}}\right)\left(\frac{M_\star}{M_{\rm g}(M_\star)} - \frac{m}{M_{\rm g}(m)}\right)\right] \\ &= \lim_{A_{\rm g}\to 0}\left(\frac{M_\star}{10^{10}\,{\rm M}_\odot}\right)^{1-\alpha_{\rm g}}\int_0^1 {\rm d}x\,(y - \beta_{\rm Z}(M_\star - M_\star x)) \\ &\quad \exp\left[-\frac{1}{A_{\rm g}}\left(\frac{1-f_r}{1-\alpha_{\rm g}}\right)\left(\left(\frac{M_\star}{10^{10}\,{\rm M}_\odot}\right)^{1-\alpha_{\rm g}} - \left(\frac{M_\star - M_\star x}{10^{10}\,{\rm M}_\odot}\right)^{1-\alpha_{\rm g}}\right)\right] \\ &= \frac{y - \beta_{\rm Z}(M_\star)}{1-f_r}\,, \end{aligned} \tag{5.25}$$

i.e. instantaneous response of the metallicity to the star formation. The gas reservoir is so small that it no longer has any 'memory' of the star formation history, and the metallicity is set purely by the yields and the current metal ejection rate. Eq. (5.25) is also the limit when star formation is *slow*, i.e. Eq. (5.18) is allowed to evolve to a point where $\dot{Z}_{\rm g} = \dot{M}_{\rm g} = 0$ (which will be violated for small galaxies since the total stellar mass is increasing fast).

In the latter case, when we are in the low stellar mass, gas dominated case $M_\star \ll M_{\rm g}$, we have

$$Z_{\rm g}(M_\star) \approx \frac{M_\star}{M_{\rm g}} \left(y - \beta_{\rm Z}(M_\star)\right) , \tag{5.26}$$

to first order in $y - \beta_{\rm Z}(M_\star)$. Here we see the mass-metallicity relation will be strongly driven by the evolution of gas and stellar mass. The metallicity is not set by an equilibrium, but rather by the yield of the total mass in stars that have been formed up to that time.

It is notable that these relations do not depend directly upon the gas accretion rate $\dot{M}_{\rm a}$ or the mass loading of the wind, $\beta = \dot{M}_{\rm w}/\dot{M}_\star$. The metallicities derived from Eq. (5.24) depend only upon the difference of these quantities (the evolution of the gas mass) which is implied by the $M_\star$-$M_{\rm g}$ relation in Eq. (5.23).

One final case that is of interest is when we assume ISM gas and metal masses have reached an equilibrium, i.e. Eq. (5.17) with the LHS set to zero, and that the metallicity of the outflow $Z_{\rm w} = Z_{\rm g}$, the mean ISM metallicity. This corresponds to a well mixed outflow, with equilibrium metallicity of

$$Z_{\rm g} = \frac{y}{1 + \beta - f_r} , \tag{5.27}$$

as assumed in FD08 and Davé et al. (2011), with $f_r = 0$.

Stellar mass to Gas mass

In order to apply this formalism to follow the evolution of metallicity, we require knowledge of the stellar mass to ISM gas mass relation. Stellar masses are usually inferred from the K-band luminosity (e.g. Bell and de Jong, 2001); however, inferring the gas mass is more subtle. McGaugh (2005) and West et al. (2009) give stellar mass to HI (21cm) gas masses, but for high mass galaxies there may also be a large H_2 component. Leroy et al. (2008) estimate the HI+H_2 mass using CO measurements (discussed in Chapter 1). For our purposes some of the HI may not be important for the ISM, as the HI disk is considerably more extended than the stellar disk (Walter et al., 2008). These data sets are also primarily focused on star forming galaxies, which bias their normalisations to higher gas masses (Catinella et al., 2010).

A more indirect method of measuring the total gas mass is via the star formation rate (inferred from the H-α luminosity), e.g. as used by Tremonti et al., 2004. Some radial profile for the gas surface density is assumed and then a normalisation deduced by inverting the Kennicutt-Schmidt relation on the star formation rate.

The use of the above methods to construct a stellar mass to gas mass relation is discussed in some detail in Peeples and Shankar (2011), where the gas mass seems to be well fit by a power law in stellar mass. Gas mass increases with stellar mass, but in a less than proportionate way, so the gas fraction is a decreasing function of stellar mass. Ignoring the considerable scatter, a good fit to the relation appears to be

$$M_{\rm g} = 10^{10} \left(\frac{M_\star}{10^{10}\,{\rm M}_\odot} \right)^{1/2} {\rm M}_\odot \,, \tag{5.28}$$

from the HI and H_2 data. The gas masses found from inverting the Kennicutt-Schmidt relation would prefer a higher exponent, nearer to 0.8, probably partially due to the differing stellar and HI sizes with luminosity.

5.4.2 Comparison with closed box models

One of the simplest ways to test the metal enrichment scenario described above is to estimate the number of old faint stars of a given metallicity. For sufficiently faint stars, their lifetimes will exceed the age of the universe and thus they become a tracer of the evolution of star formation. The relative absence of low metallicity faint stars (van den Bergh, 1962 and Schmidt, 1963) compared to a closed box model has become colloquially known as the G-Dwarf problem.

The simplest closed box model of star formation assumes that there are just 2 types of stars with low and high masses. The high mass stars explode immediately and return the (enriched) gas to the ISM, whilst the low mass stars lock away their progenitor ISM metallicity indefinitely (the ISM is also assumed to be completely homogeneous in metallicity). Assuming an ISM gas reservoir of mass $M_{\rm g}(t)$ that is converted into stars, the metallicity of this gas reservoir will be

$$Z_{\rm g} = -y \ln \mu \,, \tag{5.29}$$

where $\mu = M_{\rm g}/(M_\star + M_{\rm g})$ is the gas to total mass fraction which gradually becomes more polluted (metal rich) as the remaining gas reservoir depletes, i.e. the gas metallicity is a monotonically decreasing function of μ.

Not only this, however, but the distribution function of stars of different metallicities will be a monotonically decreasing function of metallicity (Schmidt, 1963; Pagel and Patchett, 1975; Edmunds, 1990) and the cumulative distribution (defined as the somewhat awkward inverse cumu-

lative distribution function of metallicity fraction as a function of stellar fraction, due to Schmidt, 1963) will be a convex function with a large tail of low metallicity faint stars, i.e.

$$\frac{S(<Z)}{S(<Z_1)} = \frac{1-\mu_1^{Z/Z_1}}{1-\mu_1}\,, \tag{5.30}$$

where $S(<Z)$ denotes the number of stars of metallicity $<Z$, and Z_1, μ_1 are the maximum (minimum) metallicity (gas fraction) in the closed box model, related by Eq. (5.29). The observations (e.g. Bond, 1970), however, do not find these low metallicity stars and suggest that the distribution will be largely concave[2].

In order to produce a peak in the distribution function it is necessary that the accelerating rise of metallicity of the ISM be stalled at some stage. This is usually understood to require inflow (e.g. Edmunds, 1990), as a model with outflow, although removing metals, cannot reduce the *mean* metallicity of a homogeneous ISM, which would need some low metallicity inflow to dilute. As we have seen, however, the outflows in our simulations are of higher metallicity than the average of the ISM. They preferentially remove high metallicity gas and so deplete the average metallicity of the ISM.

With this in mind we applied the corresponding approximations to calculate the metallicity of stars using the formalism of the previous section. In Fig. 5.10 we show the metallicity distributions of faint stars as predicted by the closed box model, where the fraction of gas to total mass (μ_1) is 0.2, and observational points found by Schmidt (1963) and Bond (1970). We also show the result of integrating Eq. (5.22) to find the metallicity distribution of stars for a $M_\star = 3\times10^{10}\ \mathrm{M}_\odot$ galaxy with gas evolution given by Eq. (5.28). More recent data exists which we will discuss shortly, here we are simply contrasting the models.

The small population of stars at low metallicities is clearly missing from the data, which was initially solved by Schmidt (1963) by introducing a time dependent initial mass function to produce more massive stars at early times in the galaxy's evolution. The model from Eq. (5.22) does a very good job of keeping the number of low metallicity stars small, but seems to have a normalisation problem against the Schmidt data. This, however, is the result of taking the fraction of the maximum metallicity. Eq. (5.22) has a sharp cut-off at a maximum metallicity of $Z_\mathrm{g}(M_\star)$ which carries through to the cumulative distribution. A more realistic model would have the faint stars forming with some scatter about the mean metallicity of the ISM, producing a tail at higher metallicity which would lower the normalisation in Fig. 5.10 to closer agreement with the data, and we have illustrated the effect of this by showing the same model with ±0.06 dex of scatter.

[2]If the distribution function looks even close to Gaussian then the inverse cumulative distribution will always be concave at low fractions and convex at high ones, so they are unlikely to be described as entirely concave or convex.

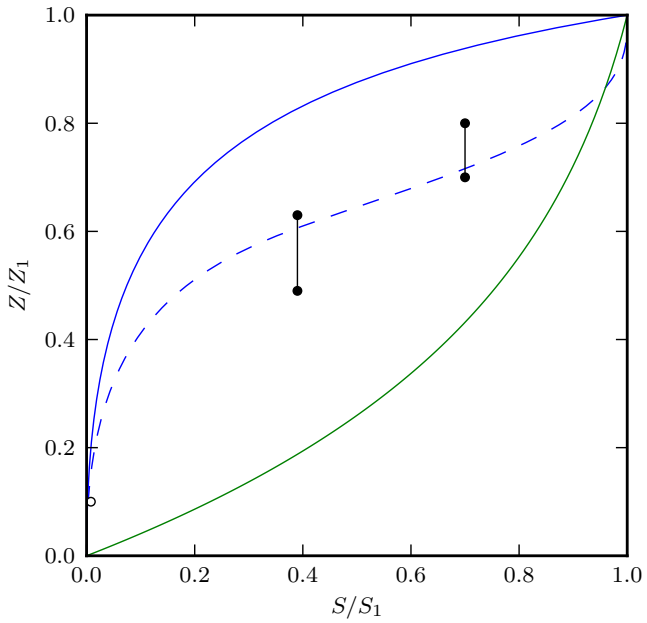

Figure 5.10: Cumulative normalised metallicity distribution of faint stars, the horizontal axis indicating the proportion of stars below the metallicity indicated on the vertical axis. *Green line* is the closed box model with $\mu_1 = 0.2$, *blue line* is the simple metallicity evolution described in the text, *blue dashed line* is the same model but assuming the faint stars form with a scatter in metallicity of 0.06 dex. *Solid black circles* are the data from Schmidt (1963) and the *empty circle* is the data point from Bond (1970).

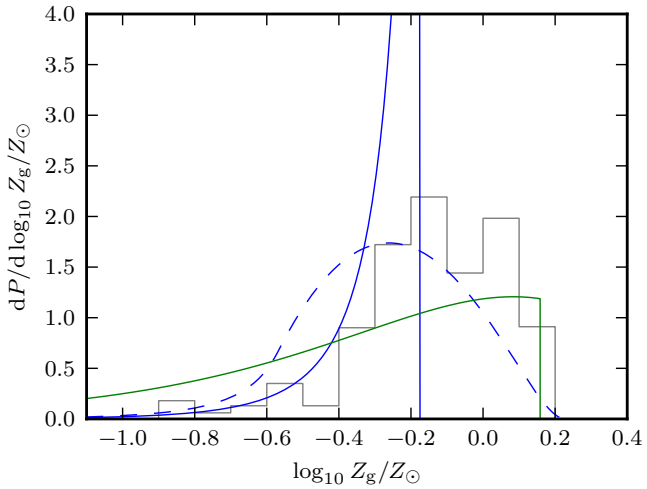

Figure 5.11: Probability density function of faint stars. *Grey histogram* is the data from Jørgensen (2000). *Solid blue line* is the metallicity evolution model described in the text, *dotted blue line* is the same model but with ± 0.18 dex in scatter, *green line* is the equivalent closed box model.

To avoid the problems of normalisation due to a tail in high metallicity stars, a more robust method is to calculate the PDF of stellar metallicities. In Fig. 5.11 we also compare to the data of Jørgensen (2000) for stars in the range $0.7 < \mathrm{M}/\mathrm{M}_\odot < 1.0$. More extensive Hipparcos data was analysed in Nordström et al. (2004), with very similar distribution. After the addition of 0.18 dex scatter in metallicity the model shows a good agreement in profile to the data, but with an offset in metallicity where the data is approximately 0.2 dex higher. One way to achieve this would be to slightly increase the yield or the retained metal fractions by this factor. For reference we also show the closed box model for the same galaxy, which reaches higher metallicity (since it does not lose metals) and has the unobserved low metallicity population.

5.4.3 Predicting the Mass-Metallicity relation

In this section we apply the results from our simulations in addition to the analysis of section 5.4.1 in order to deduce the mass metallicity relation of galaxies. This allows direct comparison between simulated metallicities and those from observations.

In this section we will use the Kewley and Ellison (2008) fits to the $M_\star$-Z_g data of Tremonti et al. (2004) and Denicoló et al. (2002),

$$\begin{aligned} 12 + \log_{10}(\mathrm{O/H})_{\mathrm{T04}} &= -0.759210 + 1.30177x \\ &\quad +0.003261x^2 - 0.00364112x^3\,, \qquad (5.31) \\ 12 + \log_{10}(\mathrm{O/H})_{\mathrm{D02}} &= -8.91951 + 4.18231x \\ &\quad -0.323383x^2 + 0.00818179x^3\,, \qquad (5.32) \end{aligned}$$

(see also Peeples and Shankar, 2011) where $x \equiv \log_{10}\mathrm{M}_\star/\mathrm{M}_\odot$ and T04 and D02 refer to Tremonti et al. (2004) and Denicoló et al. (2002) respectively. The large variation in the values of the coefficients is a result of this definition of x (i.e. $x = 10$ for a $10^{10}\,\mathrm{M}_\odot$ galaxy) and the number of significant figures is probably somewhat optimistic. In general there is a scatter in the metallicity data of a factor ~ 2.5 in the mass range $10^9 - 10^{11}\ \mathrm{M}_\odot$ (Kewley and Ellison, 2008), where the T04 relation has a relatively steep slope compared to other fits. D02 has a mid-range slope but is slightly low in normalisation, by a factor ~ 1.5, in comparison to the distribution of fits displayed in (Kewley and Ellison, 2008).

These are converted to metal mass fractions using

$$\log_{10} Z_\mathrm{g} = \log_{10}\mathrm{O/H} + 0.9560\,, \qquad (5.33)$$

implied by a 75% H, 25% He mix by mass.

We now turn our attention to the $M_\star$-Z_g relation predicted by our analytic model. By combining the metallicity integral in Eq. (5.24) with the gas mass to stellar mass relation from Eq. (5.28), the only remaining component is the dependency of the metals lost in the wind, β_Z, upon the stellar mass. This quantity was calculated for small patches of a disk in Section 5.3.2, and we will explore this correspondence in Section 5.4.4. We begin, however, by exploring some simple models for the dependence on stellar mass that illustrate how we can compare to the observed $M_\star$-Z_g relations.

We choose three power law relations for the retained metal fraction. Recall that β_Z is defined as the mass of metals ejected from the disk (not necessarily the halo) per unit mass of star formation, so $1 - \beta_\mathrm{Z}/y$ is the fraction of metals retained,

$$1 - \frac{\beta_{\mathrm{Z},1}}{y} = 0.6\,, \tag{5.34}$$

$$1 - \frac{\beta_{\mathrm{Z},2}}{y} = 0.47 M_{\star 9}^{-0.1}, \tag{5.35}$$

$$1 - \frac{\beta_{\mathrm{Z},3}}{y} = 0.45 M_{\star 9}^{-0.2}, \tag{5.36}$$

where $M_{\star 9} \equiv M_\star / 10^9\ \mathrm{M}_\odot$ and we also clamp the values to be in the range $[0, 1]$. The first two have been chosen to be close fits to the Tremonti et al. (2004) and Denicoló et al. (2002) relations using the adjustments in Peeples and Shankar (2011), whilst the third has been chosen to be indicative of the effect of changing the exponent of $M_\star$ and to compare later with the simulation data in Section 5.4.4.

In Fig. 5.12 we show the effects of these retained fractions against the observed mass metallicity relations. We can immediately see that we have achieved good normalisations without invoking extreme retained fractions. The normalisation is degenerate between changing the yield, y, and normalisation of the retained fraction, but a value of $\approx 50\%$ for the fraction of metals ejected is quite reasonable (and consistent with, say, the IGM calculations of Ferrara et al., 2000 or the QSO absorption studies in Meiring et al., 2012).

In addition to the normalisation, the transition from large to small (or even zero) slope also seems to fit well. As the exponent of $M_\star$ in the retained fraction falls, e.g. to the most in extreme value in Eq. (5.36), the slope of the $M_\star$-Z_g falls correspondingly at high masses. This can be understood in terms of the special cases described in Section 5.4.1, which we discuss now.

At low stellar masses, we will be in a gas dominated phase, $M_\star \ll M_\mathrm{g}$, and hence from Eq.

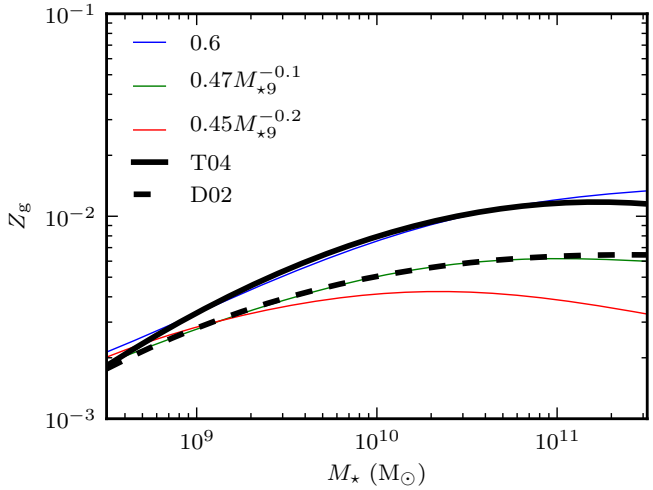

Figure 5.12: Derived mass-metallicity relations for the different models of metal outflows. *Heavy black solid* and *dashed* lines are the Tremonti et al. (2004) and Denicoló et al. (2002) $M_\star$-$Z_{\rm g}$ relations respectively. *Blue, green* and *red* lines are the simple models found using retained metal fractions from Equations (5.34)-(5.36) respectively.

(5.24)

$$\begin{aligned} Z_{\rm g} &\approx \frac{M_\star}{M_{\rm g}}\left(y - \beta_{\rm Z}(M_\star)\right) \\ &\approx \left(\frac{M_\star}{10^{10}\,\mathrm{M}_\odot}\right)^{1/2}\left(y - \beta_{\rm Z}(M_\star)\right)\,, \end{aligned} \tag{5.37}$$

whilst at the high stellar masses the gas reservoir is small, $M_{\rm g} \ll M_\star$, and we have the limit given by Eq. (5.25),

$$Z_{\rm g} \approx \frac{y - \beta_{\rm Z}(M_\star)}{1 - f_r}\,. \tag{5.38}$$

In the former case, unless the metal outflow is large, the slope will be driven almost entirely by the gas mass to stellar mass relation, in our case with a slope of 0.5. At high stellar masses the metallicity simply follows the retained fraction slope which is more gentle. We note that this gentle slope requires that the retained fraction must be a weak function of stellar mass, with exponents of -0.1 and 0 for the relations shown. This explains the turnover in the slope of both the observed and model mass-metallicity relations in figure 5.12, which gradually transitions as the stellar mass exceeds the gas mass. In Tremonti et al. (2004) this turnover is argued to be due to metal loss via galactic winds, which is less quantitative although not inconsistent with our explanation.

The argument of FD08 is that the transition is driven by the changes in mass loading from high ($\beta \gg 1$) to low ($\beta \ll 1$), and that the metallicity is approximately given by Eq. (5.27)

in both cases. Their assumptions are distinct from ours, but the model has similar aspects and hence is worth contrasting. In the FD08 model it is assumed that the galaxies are in instantaneous equilibrium, with inflow balancing star formation and outflow, which allows the deduction of the dilution of metals and hence the gas phase metallicity (in equilibrium). In our model we assume a relation between the gas mass and the stellar mass and hence at all stellar masses we can calculate the dilution. Since our galaxies are growing in gas mass whilst the FD08 gas reservoir is constant, the metallicities will be distinct, although for the high mass galaxies the growth rates will be small and the predictions close. Even for low mass galaxies, however, if the outflow rate ($\dot{M}_{\rm w}$) is an approximately constant fraction of the inflow rate ($\dot{M}_{\rm a}$), then for power-law inflow rates (in $M_\star$) the ratio of the gas mass to the stellar mass compared to the mass loading will only differ by a factor, making the models very similar in form and normalisation.

In terms of retained fraction of metals, the FD08 model assumes a well-mixed ISM, i.e. the wind metallicity is the same as the ISM metallicity, in contrast to our model where the wind can preferentially carry away metals. This allows our models slightly more freedom to adjust the slope of of the $M_\star$-$Z_{\rm g}$ relation at high stellar masses, where the mass loading $\beta \ll 1$, i.e. Eq. (5.27) implies the metallicities will converge to the effective yield, whereas the introduction of $\beta_{\rm Z}(M_\star)$ in Eq. (5.25) releases us from this constraint.

5.4.4 Comparison with simulations

We are now in a position to discuss perhaps the most interesting aspect of all, the use of hydrodynamical simulations which in principle allow us to predict the retained metal fraction and compare it to observations. We should bear in mind, however, that the observed mass-metallicity relation suggests a rather weak dependency of retained metal fraction as a function of stellar mass with an exponent of perhaps -0.1, i.e. $1 - \beta_{\rm Z}/y \sim M_\star^{-0.1}$.

The simulations performed in Section 5.3 were parameterised in terms of gas surface density $\Sigma_{\rm g}$ and gas fraction $f_{\rm g}$, so to put these on the mass metallicity relation we must transform these into stellar masses. We performed a similar analysis in Chapter 4 to estimate dependencies on circular velocity from those on surface density, and our method will be analogous here. We begin by assuming the disks to be exponential, giving a total mass of

$$M_{\rm d} = 2\pi\Sigma_{\rm g0}R_{\rm d}^2 f_{\rm g}^{-1}\,, \tag{5.39}$$

where $R_{\rm d}$ is the disk scale length. Shen et al. (2003) estimates the sizes of disks to scale weakly as $R_{\rm d} \propto M_\star^{0.15}$, and so we normalise to a MW with a stellar mass of 5×10^{10} $\mathrm{M}_\odot$ and scale radius 2.5 kpc, to find the gas surface density.

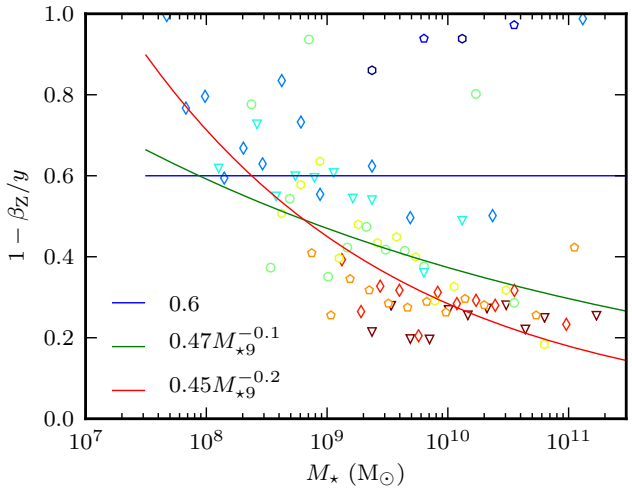

Figure 5.13: Estimates for the retained metal fraction, $1-\beta_Z/y$ as a function of stellar mass, $M_{\star 9} \equiv M_\star/10^9$ $M_\odot$. *Blue, green* and *red* lines are the simple models from Figure 5.12 and Equations (5.34)-(5.36) respectively. *Coloured symbols* are the estimates from the hydrodynamical simulations converted to a stellar mass dependency using Eq. (5.39), with colours and symbols from Fig. 5.7 (low gas fraction in *red*, to high gas fraction in *blue*).

We show these dependencies in Fig. 5.13. We see that there is a large amount of scatter in the estimates of retained metal fractions from the simulations, which is due to the stochastic nature of the energy injection by SNe (in time and in position in the disk), and hence it is difficult to constrain the dependence on stellar mass. At high stellar masses this is particularly noticeable, with only the low gas fraction points exhibiting convergence to a single retained fraction. The re-parameterisation into M_d displays a strong residual correlation of the retained metal fraction with the gas fraction f_g, with more gas rich disks retaining a larger fraction of metals.

Although it is unwarranted to place a great deal of attention to the exact normalisation (due to both the outliers and uncertainties in the yield and the Z_g-$M_\star$ relation etc.), it does appear reasonable, both between the curves and the data and compared to IGM estimates (e.g. Ferrara et al., 2000; Meiring et al., 2012). The data is also suggestive of a weak negative dependency on stellar mass that was implied by the observed mass-metallicity relation. Indeed, the closest simple model is the stronger dependency with stellar mass exponent of -0.2, given in Eq. (5.36) which actually implies a slight downturn in metallicity at $M_\star \approx 10^{11}$ $M_\odot$ (see also Fig. 5.12).

If the dependency on stellar mass is indeed this strong, one process which may reduce its effect is that of gravity. For massive halos the metals may escape the disk but not the halo, leading to significant recycling of the metals. This could be parameterised either as a lower ‘effective’

ejection fraction, or by re-introducing the metallicity $Z_{\rm a}$ of accreting gas in Eq. (5.17) which was assumed to be zero in the analysis of Section 5.4.1.

One other intriguing possibility from this type of simulation is to study models of the radial distribution of metals in galaxy disks and compare to observational constraints e.g. from Kewley et al. (2010). This is complicated by the radial transport of metals (e.g. Werk et al., 2011) and we leave this for future work.

5.5 Conclusions

In this chapter we have performed a series of hydrodynamical simulations that extend the work of Chapters 3 and 4 to trace the metal enrichment of the interstellar medium. We simulate patches of SN driven turbulence in a gravitationally bound disk, including cooling and metal enrichment via the SN ejecta.

In Section 5.3 we investigated the metallicity of the ISM and the mixing produced by successive generations of SNe, where we found a metallicity bi-modality between an ejecta-rich, metal-rich hot phase, and a slowly polluted warm phase. We discuss the fundamental hydrodynamical reasons for this in Section 5.3.3.

In Section 5.3.2 we parameterised the metal loss in the outflows as a function of gas surface density and gas fraction. We found a weak dependence of metal mass loss on surface density, such that the metallicity of the outflow (the ratio of the metal mass loss to the total mass loss) has a negative dependence on surface density. This implies that higher surface density disks with higher star formation will have more enriched outflows.

In Section 5.4 we constructed a simple model of the metallicity evolution, showing how the dependence of galaxy gas mass and metal ejection as a function of stellar mass can be used to infer the gas phase metallicities. We compare this to closed box models of the metallicity distribution of faint stars and demonstrate that this model captures enough detail to prevent large populations of low metallicity stars, without resorting to extreme yields and/or values of the metal retention factors.

Finally, we have provided some example models of the ejected metal fraction that produce mass-metallicity relations close to observed fits to the mass-metallicity relation, which are consistent in both normalisation and turnover. We have shown that this is largely a consequence of the transition to low gas fractions for high mass galaxies. Using the formalism developed in Chapter 4 we transform the metal ejection fractions dependent on surface density into a dependence on stellar mass, allowing comparison with our example models. Although the stochasticity due

to SNe limits the constraining power of this data set, we find a relatively good correspondence between metal ejection fractions from the simulations and those implied from the observed data, without invoking any additional physical mechanisms.

Several avenues exist for future work, such as the modelling of the recycling of metals in halos to improve the constraints at high stellar masses. It would also be very interesting to apply this dataset to study the radial evolution of metallicity in disk galaxies.

Chapter 6 | *Conclusions*

6.1 Discussion

This thesis has focused on the use of hydrodynamical simulations to study the evolution of gas in galaxies and halos in ΛCDM cosmologies. In Chapter 2 we investigated one of the most stringent resolution constraints in cosmological simulations, that of the fast cooling of high density baryons. We have applied our estimates to thermal feedback from AGN or supernovae blast waves, in the presence of radiative cooling. We have seen that the energy required to drive thermal feedback at a given mass scale, for current numerical results, is an order of magnitude higher than one would expect just from physical considerations. For cosmological simulations ($10^6 \mathrm{M}_\odot$ gas particles) of an $n_\mathrm{H} = 1.0\,\mathrm{cm}^{-3}$ interstellar medium we calculate that temperatures in excess of 10^7 K are required to effectively drive thermal feedback by avoiding spurious suppression of the feedback by numerical overcooling.

We have found a general analytical solution for 1d piecewise linear collisional cooling functions and compared it to numerical simulations of the same shock, performed with an SPH code (GADGET) and an AMR code (FLASH). These codes smear out the shock over several particles or cells, and such an artificial 'pre-shock' results in numerical overcooling which may prevent the formation of a hot post-shock region. We have estimated a general resolution criterion to avoid such overcooling, and applied it to the problems of virial shocks and the production of hot gaseous halos. We have found that to avoid numerical overcooling of accretion shocks onto halos that should develop a hot corona requires a particle or cell mass resolution of $10^6 \mathrm{M}_\odot$, which is within reach of current state-of-the-art simulations.

In Chapters 3 and 4 we have constructed numerically well converged simulations of a simplified two-phase interstellar medium model, in which an initially isothermal and hydrostatic disk gets disrupted and heated by individual supernovae. By not simulating the cold phase of the ISM we avoided the need to introduce significantly more physical ingredients which require heavy algorithmic approximations and/or fragile recipes. By restricting our simulation volume to only a small section of a disk, we achieved sub-parsec resolution, and were able to investigate the depen-

dence of the outflow on the parameters of the disk. We have self-consistently included gravity, star formation that follows the Kennicutt-Schmidt relation, hydrodynamics and a cosmological cooling function. On scales outside the volume, the host disk galaxy for this toy model is reduced to the parameters of gas surface density, gas fraction and star formation efficiency normalised by the Kennicutt-Schmidt relation.

Our simulations demonstrate the ability of supernovae to drive a galactic wind vertically from a disk. The supernovae create a turbulent ISM with very distinct hot and warm phases, due to the strong transition of the cooling function at 10^4 K. These phases exist in approximate pressure equilibrium, with the warm material squeezed into dense lumps, and the excess thermal energy of the hot material causing it to accelerate away from the disk. We describe this as a rarefaction-like process, with the hot ISM escaping to an IGM which is comparatively sparse and pressure-free. Such a model naturally leads to an outflow with speed increasing with height above the disk but density decreasing.

The hot outflow entrains colder ISM gas from the disk that may have relatively high metallicity. The hot gas rushes past these clouds producing characteristic tails. Such interfaces may be the sites where lower ionisation lines are produced. We explore this further by calculating the normalised cross section of different temperature phases in our simulations, where we see that the velocity distribution of the cooler gas is significantly beneath that of the escaping material.

As the precise features of our simulations vary greatly due to turbulence and the stochastic nature of supernovae, we examine several global properties which are less sensitive, such as the disk pressure, cooling rate as a fraction of the mean energy injection rate, disk scale height and mass ejection. These reveal a disk that rapidly evolves to higher porosity before reaching a state with an approximately constant mass ejection rate. This evolution of porosity is broadly reminiscent of the model by Silk (2001).

We perform a range of simulations to investigate the dependence of the mass loading on gas surface density, gas fraction, and star formation efficiency, and fit the resulting trends with power laws. Our mass loadings lie in the range $0.01 - 4$, suggesting a switch from a low to a high feedback regime. We find little dependence on the normalisation of the star formation relation, but a significant dependence on the gas fraction and surface density. The latter two can be combined to explain the bulk of the trends as depending on the total surface density of the disk. At high surface densities we find low mass loading and a high effective wind speed. At low surface densities the reverse is true, and there is an additional contribution due to an increase of the fraction of energy radiated by cooling gas. We present a simple model where SNe blasts stall as they run into clouds swept up by previous explosions that are so dense that they cool very

efficiently, which predicts that mass loading depends on gas surface density and gas fraction as $\beta = \dot{\Sigma}_{\rm wind}/\dot{\Sigma}_\star \propto \Sigma_{\rm g}^{-8/11} f_{\rm g}^{4/11}$. These scalings are very close to those we find from simulations with high star formation rate, $\beta \propto \Sigma_{\rm g}^{-0.82} f_{\rm g}^{0.48}$ and weaker (in terms of surface density) than that for the pure Kennicutt relation, $\beta \propto \Sigma_{\rm g}^{-1.15} f_{\rm g}^{0.16}$. Our prediction for the mass loading in the solar neighbourhood is that each supernova results in an ejection of around $50\ {\rm M}_\odot$ of gas, or a $\beta \sim 0.5$, slightly above 0.3, our average for the MW as a whole.

The relationship between the wind velocity and thermalisation efficiency (the fraction of the SN energy that is released into the wind) exhibits a more complex relationship to the disk properties than that of the mass loading. The thermalisation efficiency appears to show a dependency on both the surface density and the gas fraction, and correspondingly the wind velocity does not show a straightforward power law implied from a constant efficiency model. For high surface densities and low gas fractions, an approximate 40% of the injected energy is converted into the outflow's thermal, turbulent and kinetic energy components.

We employ the scaling relation obtained from the simulations to calculate the net mass loading, $\hat{\beta} = \dot{M}_{\rm wind}/\dot{M}_\star$, of an exponential disk galaxy with constant gas fraction. Using the Mo et al. (1998) scaling relation between disk and halo, we obtain a scaling with circular velocity of $\hat{\beta} \propto V_{\rm d}^{-4.8}$, stronger than either energy or momentum-driven winds. Using the observed Tully-Fisher relation we find a weaker dependence, $\hat{\beta} \propto V_{\rm d}^{-2.5}$. This compares well with recent semi-analytic models which assume $\alpha_{\rm hot} \in [2.0, 3.2]$.

The normalisation of our net mass loading at redshift $z = 0$ for a Milky Way-like galaxy is significantly lower than assumed in recent phenomenological models, although these models appear to have some degeneracy between the exponent and the normalisation, which we will exploit in future work. Notably the mass loading only increases weakly with star formation rate, but decreases strongly with surface density, so for starburst galaxies the feedback may be less efficient. Interestingly, our estimated normalisation is comparable with inferred values of outflow for the MW based upon the observed accretion and star formation. If indeed there is a higher mass loading, it will require supernovae to heat a larger mass of material to a lower temperature, or for the hot outflow to entrain a larger fraction of the warm ISM gas. The scaling we find sets the investigation of galaxy winds on a new footing, providing a physically motivated subgrid description of winds that can be implemented in cosmological simulations and semi-analytic models.

In Chapter 5 we have performed a series of hydrodynamical simulations that extend the work of Chapters 3 and 4 to trace the metal enrichment on the interstellar medium. We simulate patches of SN driven turbulence in a gravitationally bound disk, including cooling and metal enrichment

via the SN ejecta. We investigated the metallicity of the ISM and the mixing produced by successive generations of SNe, where we found a metallicity bi-modality between an ejecta-rich, metal-rich hot phase, and a slowly polluted warm phase. We discuss the fundamental hydrodynamical reasons for this in Section 5.3.3.

We parameterised the metal loss in the outflows as a function of gas surface density and gas fraction. We found a weak dependence of metal mass loss on surface density, such that the metallicity of the outflow (the ratio of the metal mass loss to the total mass loss) has a negative dependence on surface density. This implies that higher surface density disks with higher star formation will have more enriched outflows.

We constructed a simple model of the metallicity evolution, showing how the dependence of galaxy gas mass and metal ejection as a function of stellar mass can be used to infer the gas phase metallicities. We compare this to closed box models of the metallicity distribution of faint stars and demonstrate that this model captures enough detail to prevent large populations of low metallicity stars, without resorting to extreme yields and/or values of the metal retention factors.

Finally, we have provided some example models of the ejected metal fraction that produce mass-metallicity relations close to observed fits to the mass-metallicity relation, which are consistent in both normalisation and turnover. We have shown that this is largely a consequence of the transition to low gas fractions for high mass galaxies. Using the formalism developed in Chapter 4 we transform the metal ejection fractions dependent on surface density into a dependence on stellar mass, allowing comparison with our example models. Although the stochasticity due to SNe at present limits the constraining power of this data set, we find a good correspondence between metal ejection fractions from the simulations and those implied from the observed data, without invoking any additional physical mechanisms.

6.2 Future Work

This thesis opens up several avenues for future research in terms of both pure numerical modelling and in terms of exploring the role of astrophysical mechanisms of the ISM in cosmological simulations.

In Chapter 2 we saw that whilst all of the issues surrounding the determination of the evolution of cooling shocks could be rectified by increasing the resolution, the minimum thermal energy of injected feedback required to avoid artificial cooling scales weakly with decreasing particle mass, $\propto m_{\rm SPH}^{2/9}$. Consequently, a potentially fertile region of study may be that of cooling switches, *i.e.* a criterion for disabling cooling through a shock. Such a switch would allow a simulation

to resolve temperatures much closer to the physical temperatures of radiative shocks without requiring extreme resolutions. Unfortunately it is not a straightforward problem to have a criterion that will consistently suppress cooling in the presence of shocks yet does not affect cooling in regions where there are no shocks. Since we can never hope to completely remove resolution effects it seems sensible to have a more limited aim, perhaps to capture the temperatures of shocks up to some maximum cooling rate. As such one might wish to suppress cooling, when the cooling time is greater than some fraction of the shock heating time.

Further work could include the effects of shock-induced non-collisional ionizational equilibrium (CIE) or non-thermalised gas. Since the resolution can make such a significant modification to the thermal history of a gas, we expect a criterion due to non-CIE may be quite strict.

In Chapter 3 we constructed a model of SN driven outflows from idealised disks using a small subset of the physics of the ISM. We are almost at the stage where these physics could be applied to entire galaxies, and certainly it is possible to perform these simulations on dwarf galaxies at higher redshift.

The orthogonal direction is to include additional physics such as magnetic fields, molecular cooling, self gravity and radiative transfer. Some of these, such as molecular cooling and radiative transfer, are likely to be extremely computationally expensive, as not only will they introduce a high density phase, but this phase has a much stricter resolution requirement. Magnetic fields work in the opposite direction, supporting material against collapse, and we intend to demonstrate simulations with these in future work.

In Chapter 4 we discussed the implications of these simulations for semi-analytic models, in terms of the mass loading of winds controlling the efficiency of galaxy formation. Clearly there is more work to be done in understanding the evolution of the stellar mass function, both in hydrodynamical cosmological simulations and in semi-analytic models. Using our fits as a prescription could be performed in either type of simulation, although it would perhaps be more straightforward in semi-analytic models where the ejection model is more explicit, and the work of Bower et al. (2011) and Lagos et al. (2012) already seem to have experiments advancing in this direction.

In Chapter 5 we saw how these models could be used to trace the metals in the ISM and predict observables, such as the mass metallicity relation and the distribution of metallicities of faint stars. Whilst these are the lowest hanging fruit in terms of observables, these models could also be used to predict other metallicity gradients, such as the vertical and radial metallicity gradients in the Milky Way. It would also be possible to trace the outflows from different SNe, in particular distinguishing type Ia and II, which may tell us a great deal about the O/Fe distribution

and evolution.

Appendix A

Radiative shocks with piecewise linear cooling functions

A.1 Similarity solution for a 1d radiatively cooling shock

We start with an ideal gas with adiabatic index γ

$$p = (\gamma - 1)\rho u \,, \tag{A.1}$$

and a collisional radiative cooling function

$$\mathrm{d}u|_\Lambda = -\rho f(u)\mathrm{d}t \,. \tag{A.2}$$

These combine to give an evolution of

$$\mathrm{d}u = (\gamma - 1)\frac{u}{\rho}\mathrm{d}\rho - \rho f(u)\mathrm{d}t \,. \tag{A.3}$$

Stationary solutions of a post shock cooling region satisfy integrals of the mass and momentum equations, i.e.

$$\rho(v - u_s) = \rho_0(v_0 - u_s) \tag{A.4}$$

$$p + \rho(v - u_s)^2 = p_0 + \rho_0(v_0 - u_s)^2 \,, \tag{A.5}$$

where u_s is the shock velocity and ρ_0, p_0, v_0 denote the density, pressure and velocity at some arbitrary downstream point. Thus the density, velocity and thermal energy can be written in terms of a similarity variable λ

$$\rho/\rho_0 = \lambda \tag{A.6}$$

$$\frac{v - u_s}{v_0 - u_s} = \lambda^{-1} \tag{A.7}$$

$$u/u_0 = (a+1)\lambda^{-1} - a\lambda^{-2} \,, \tag{A.8}$$

with

$$a = \frac{\rho_0 (v_0 - u_s)^2}{p_0} \,. \tag{A.9}$$

Now we assume we have a piecewise linear cooling function, i.e. we can solve each segment separately with the linear cooling function

$$f(u) = A(u - u_c) \,, \tag{A.10}$$

where A is some constant and u_c denotes the 'cold' thermal energy where cooling vanishes. This gives an o.d.e for x of the form

$$\frac{\mathrm{d}x}{\mathrm{d}\lambda} = \frac{v_0 - u_s}{A\rho_0} \left(\frac{\gamma(a+1)\lambda^{-4} - (\gamma+1)a\lambda^{-5}}{(a+1)\lambda^{-1} - a\lambda^{-2} - u_c/u_0} \right) \,, \tag{A.11}$$

which can be solved generally, however in the case of $u_c = u_0$ we have the particularly simple case,

$$\begin{aligned} x - x_0 &= \frac{v_c - u_s}{A\rho_c} \left[\frac{\gamma - a}{a-1} \log(\lambda^{-1} - 1) + \right. \\ &\quad \frac{1 - a\gamma}{(a-1)a^2} \log(1 - a\lambda^{-1}) \\ &\quad \left. - \frac{a+1}{a}\lambda^{-1} - \frac{\gamma+1}{2}\lambda^{-2} \right] \\ \lambda &\in \left[\frac{a}{a+1}\frac{\gamma+1}{\gamma}, 1 \right] \,, \end{aligned}$$

the left hand limit for λ coming from entropy considerations. An example cooling shock of this form can be seen in Fig. 2.1.

A.2 Colliding gas

Assume two homogeneous flows collide from the left and right, with properties $\rho_0, p_0, \pm v_0$. With no cooling a hot, static region is created in the centre, with properties p_c, and ρ_c. The mass, momentum and energy equations are

$$(v_0 - u_s)\rho_0 = -\rho_c u_s \tag{A.12}$$

$$(v_0 - u_s)^2 \rho_0 + p_0 = \rho_c u_s^2 + p_c \tag{A.13}$$

$$\frac{p_0}{\rho_0} + \frac{1}{2}(\gamma - 1)v_0^2 = \frac{p_c}{\rho_c} \,, \tag{A.14}$$

where u_s is the velocity of the left moving shock in the rest frame. Eliminating p_c, ρ_c gives

$$u_s^2 + \frac{1}{2}(\gamma - 3)u_s v_0 = \frac{p_0}{\rho_0} + \frac{1}{2}(\gamma - 1)v_0^2 \,, \tag{A.15}$$

so

$$u_s = -\frac{1}{4}(\gamma - 3)v_0 - \frac{1}{4}\sqrt{v_0^2(\gamma+1)^2 + 16\frac{p_0}{\rho_0}}\,. \tag{A.16}$$

Assume now that there *is* cooling and that the gas in the centre cools to the temperature of the pre-shock gas (where cooling is assumed to vanish). In this case the mass, momentum and energy equations are

$$\begin{aligned}
(v_0 - u_s)\rho_0 &= -\rho_c u_s & \text{(A.17)}\\
(v_0 - u_s)^2\rho_0 + p_0 &= \rho_c u_s^2 + p_c & \text{(A.18)}\\
p_0/\rho_0 &= p_c/\rho_c\,, & \text{(A.19)}
\end{aligned}$$

where these equations are only dependent on the cooling function via the thermal state at which cooling vanishes, p_0/ρ_0. Eliminating p_c, ρ_c gives

$$u_s^2\rho_0 - u_s v_0 \rho_0 - p_0 = 0\,. \tag{A.20}$$

The solution for the shock velocity $u_s = v_0/2 - \sqrt{(v_0/2)^2 + p_0/\rho_0}$. p_c, ρ_c can be found by substitution.

The conditions immediately to the right of the shock (v_s, ρ_s, p_s) can be found from the usual Rankine-Hugoniot relations,

$$\begin{aligned}
(v_0 - u_s)\rho_0 &= (v_s - u_s)\rho_s & \text{(A.21)}\\
(v_0 - u_s)^2\rho_0 + p_0 &= (v_s - u_s)^2\rho_s + p_s & \text{(A.22)}\\
\frac{1}{2}(v_0 - u_s)^2 + \frac{\gamma}{\gamma-1}\frac{p_0}{\rho_0} &= \frac{1}{2}(v_s - u_s)^2 + \frac{\gamma}{\gamma-1}\frac{p_s}{\rho_s}\,. & \text{(A.23)}
\end{aligned}$$

Appendix B

Convergence and Parameter fits

In this appendix we investigate the convergence properties of our simulations, along with the dependence upon some of the numerical and physical parameters such as the box size, simulation end time, the star formation rate, the cooling function and the energy of each supernovae. We also include evolution graphs showing the fits to the mass loading which are central to this work.

We begin by describing a set of simulations where we run an alternative star formation rate, which is compared to the main set of simulations in Section 3.5. In this parameterisation, the surface density of star formation is

$$\dot{\Sigma}_\star = 0.1\Sigma_{\rm g}/t_{\rm dyn}\,, \tag{B.1}$$

(more commonly used in cosmological simulations), which is appropriate for a marginally Toomre stable disk (Toomre, 1964), i.e. the vertical dynamical time is close to the orbital time scale. Such prescriptions are discussed thoroughly in Schaye and Dalla Vecchia (2008), where they show that with self-regulating feedback this will recover an approximate Kennicutt-Schmidt relation of $\Sigma_{\rm g}^{3/2}$.

If we apply Eq.(B.1) to the warm disk of our initial conditions, however, we generally have a much higher star formation rate due to the short dynamical time, which is equivalent to saying the HI disk is not Toomre stable. If we substitute in the $t_{\rm dyn}$ from Eq. (3.22) we have a star formation rate of

$$\begin{aligned}\dot{\Sigma}_\star &= 2.6\times10^{-3}\left(\frac{f_{\rm g}}{0.1}\right)^{-1}\left(\frac{\Sigma_{\rm g}}{10\ {\rm M}_\odot\,{\rm pc}^{-2}}\right)^{\frac{1}{2}}\times \\ &\quad \Sigma_{\rm g1}^{1.5}\ {\rm M}_\odot\,{\rm kpc}^{-2}\,{\rm yr}^{-1}\,,\end{aligned} \tag{B.2}$$

which we can see from the leading coefficient is an order of magnitude higher than Eq. (3.13) (although there is some residual dependence on $f_{\rm g}$ and $\Sigma_{\rm g}$), and simulates the conditions more relevant to a starburst galaxy.

In Fig. B.1 we investigate the effect of altering the star formation law from Eq.(3.13) to Eq.(B.1), where the latter in general has much higher star formation rates due to the short vertical

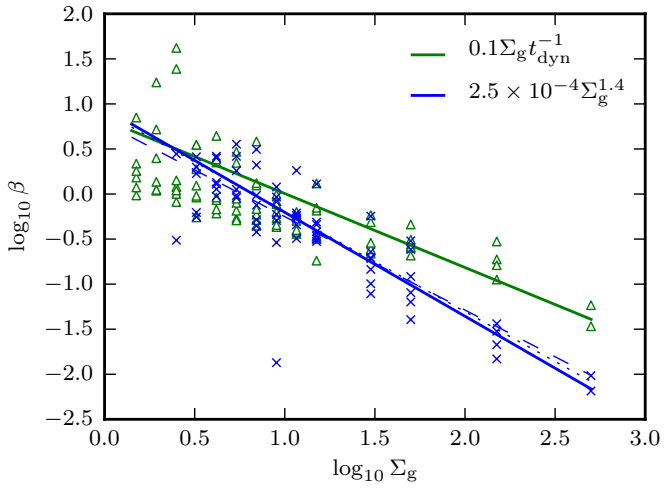

Figure B.1: Mass loading β as a function of Σ_g for the star formation laws in Eq. (3.13) (*blue crosses*) and Eq. (B.1) (*green triangles*). *Solid lines* indicate the best fit for $f_g = 0.1$ (see text for exact parameterisation). *Dashed* and *dotted blue* lines show the fit when varying the end time of the data used for the fit by ± 3 Myr.

dynamical time of the disk. At low gas surface densities more simulations were possible due to the higher star formation rates. The best fit to the former was given in the main text, whilst the best fit to the latter is

$$\beta \sim (20 \pm 8)\Sigma_{g1}^{-0.82\pm0.07} f_g^{0.48\pm0.08} . \tag{B.3}$$

The effect of increasing the star formation rate flattens the dependency on Σ_g and increases the dependency on f_g, very close to the values predicted in Eq. (3.33), which is to be expected as gravity is much less important in these simulations (see also the discussion in Section 3.5). The relative insensitivity of β to the order of magnitude change in $\dot{\Sigma}_\star$ can be explained by the fact that the outflows are normalised by the star formation rate, so although those simulations have much higher outflows, the outflow per supernova deviates by a much smaller amount. The higher star formation rate runs can also be seen to have less scatter, as they are less susceptable to the Poisson noise of individual SN events.

Fig. B.1 also illustrates the effect of the simulation end time on our estimate for the gas surface density dependency, by varying by ± 3 Myr the final snapshot which is used to construct the fits for β (for the normal star formation rates). This shows little effect, a result of the outflow rates being (on average) very close to linear in these simulations. We perform a corresponding fit for the fiducial parameters in Fig. B.2 where we simulate 100 Myr to check that the outflows we see are not a transient phenomena and continue after the 20 Myr of our simulations. The box

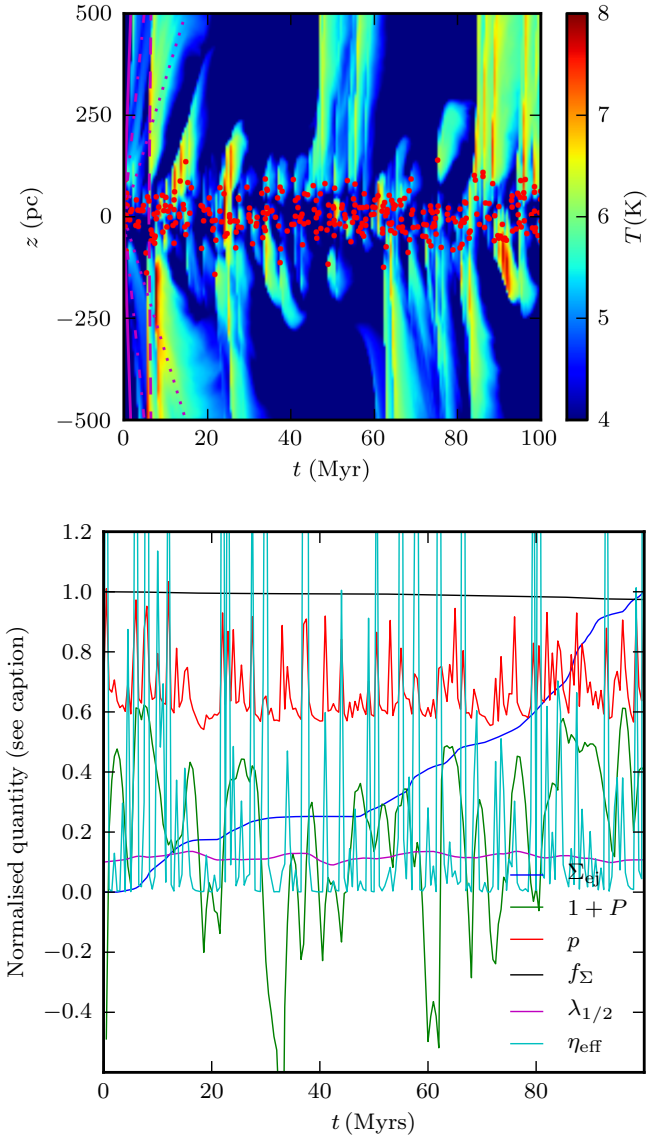

Figure B.2: As for figures B.3 (*lower panel*) and 3.4 (*upper panel*) but for a run of 100 Myr. In the lower panel the surface density ejected (*dark blue line*) has been scaled to 0.3 $\mathrm{M}_{\odot}\,\mathrm{pc}^{-2}$.

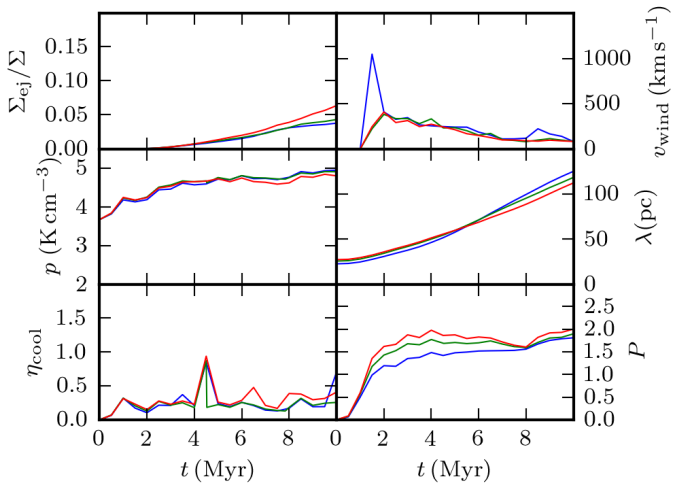

Figure B.3: Numerical convergence of a high star formation rate run at resolution of L2, L3, L4 (cell size of 6.3, 3.1 and 1.6 pc and shown in red, green and blue respectively). *Upper left panel* shows the fraction of gas that has left the simulation volume, *middle left* indicates the mean pressure in the simulation volume. *Lower left panel* shows the rate of cooling as a fraction of the mean supernovae energy injection rate, *upper right* shows the mean wind velocity, *middle right* shows the scale height of the disk and *lower right* shows the evolution of the porosity in the simulation. The red and green curves follow each-other closely, indicating good convergence.

width in this simulation was 200 pc, so we expect to see more stochasticity, and indeed we see fluctuations lasting many Myrs, such that the outflow estimated from a single 20 Myr window could show a deviation of a factor of a few. This is probably the main reason for the scatter in Fig. 3.9.

We also test how well our simulations are converged with respect to the resolution by taking one of the high star formation rate runs and re-simulating it at the three resolutions L2, L3 and L4 (corresponding to a cell size of 6.3, 3.1 and 1.6 pc, respectively). In Fig. B.3 we show six different parameters, the fraction of surface density ejected, the mean pressure in the simulation volume, rate of cooling (as a fraction of the supernova energy injection), the porosity and scale heights of the disk and the wind velocity for three different resolutions. All of these properties appear to be well converged with respect to resolution, with the possible exception of the porosity and the disk scale height at the lowest resolution. With respect to the scale height it is notable that there is some error even at the initial snapshot due to the coarseness of the grid in this case.

We explore the importance of cooling, both in broad terms about the dependence on the

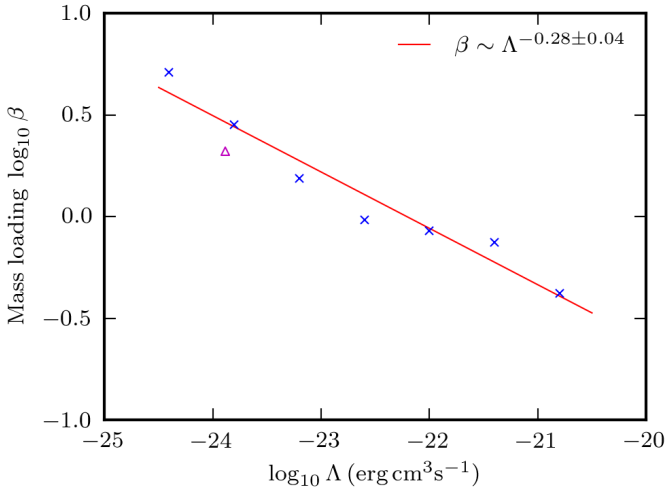

Figure B.4: Dependence of the mass loading parameter β on the cooling rate. *Blue crosses* show the estimated β for different values of Λ for Heaviside-shaped cooling function ($\Lambda = 10^{-22}\,\mathrm{erg\,cm^3\,s^{-1}}$ is the fiducial value). For comparison, the *maroon triangle* indicates the value of β calculated with the Sutherland and Dopita (1993) cooling function, at the minimum value of this function (Eq. (3.12)).

magnitude of the cooling, and also upon our specific choice of cooling function. In Fig. B.4 we look at the dependency of β for the previous simulation on the magnitude of the cooling function and for comparison we have included the Sutherland and Dopita (1993) cooling function for low metallicity plasma, Eq. (3.11). The linear regression does indeed show a relationship albeit a weak one, with an exponent of -0.28. For the Sutherland and Dopita (1993) cooling function we have taken the magnitude of cooling to be that at the minimum, Eq. (3.12). The fitted β calculated using this figure is a factor of $\sim 25\%$ lower than that using our Heaviside cooling function using the same normalisation. This is not quite as strong as the dependence suggested by Eq. (3.32), of $-6/11 \approx -0.54$.

In Fig. B.5 we make a further comparison between the Sutherland and Dopita (1993) cooling function and our flat cooling function. We chose the run with the nearest normalisation ($\Lambda = 1.5 \times 10^{-24}\,\mathrm{erg\,cm^3\,s^{-1}}$) to that of the minimum of the Sutherland and Dopita (1993) cooling function (Eq. 3.12). We see a very similar phase distribution of the ISM, suggesting that the detailed structure of the cooling function above $10^4\,\mathrm{K}$ does not play a large role in determining the features of the ISM.

In Fig. B.6 we have taken another high star formation rate simulation and adjusted the energy associated with a single supernova. Here, we keep the average rate of energy injected per unit

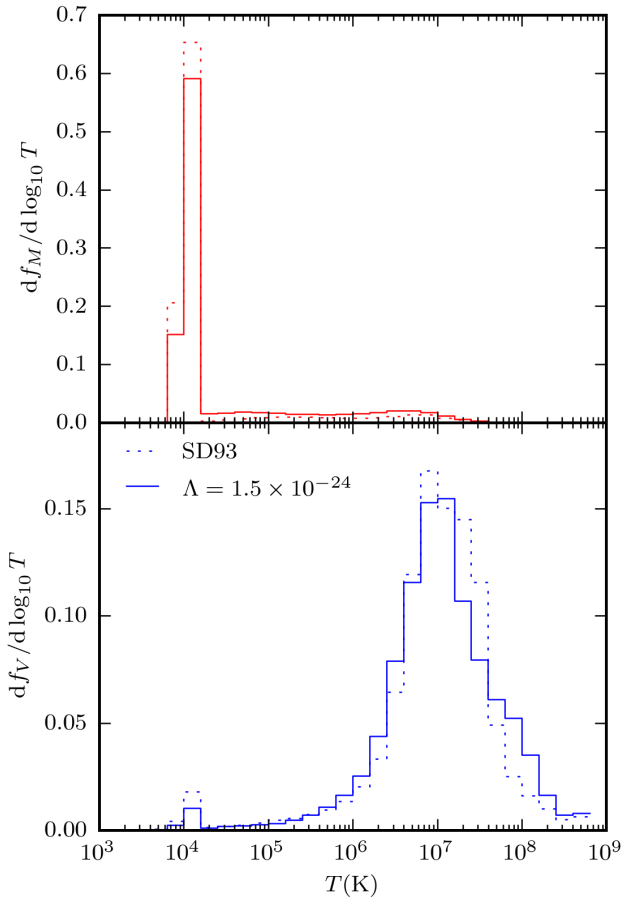

Figure B.5: *Upper panel*, mass fraction of the gas in different temperature phases, *solid, dashed lines* refer to the $\Lambda = 1.5 \times 10^{-24}$ erg cm^3 s^{-1} Heaviside cooling function, and the Sutherland and Dopita (1993) cooling functions respectively. *Lower panel* shows the corresponding volume fractions. The fraction in each phase appears very similar, with the SD93 cooling function showing a slightly narrower temperature distribution of the hot phase by volume.

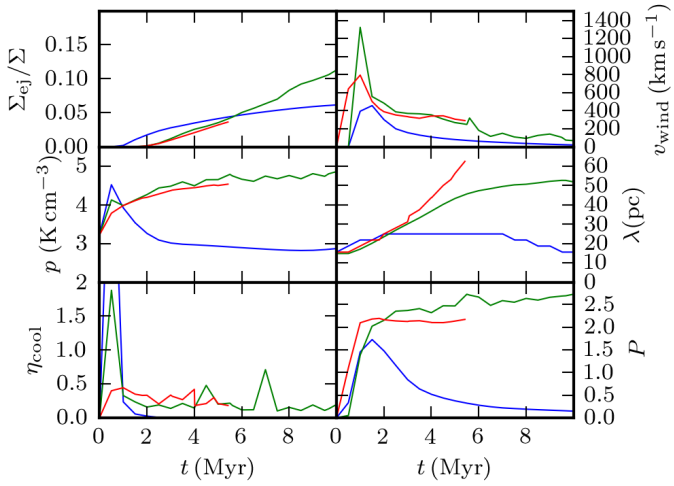

Figure B.6: Evolution of the simulations as a function of supernovae granularity. *Green line* shows a run with 10^{51} ergs per SN. *Red line* is the same simulation, but with $50\times$ the frequency of SNe, each releasing $1/50$th of the energy (2×10^{49} ergs). *Blue line* has SNe at $1/50$th of the frequency, with $50\times$ the energy (5×10^{52} ergs).

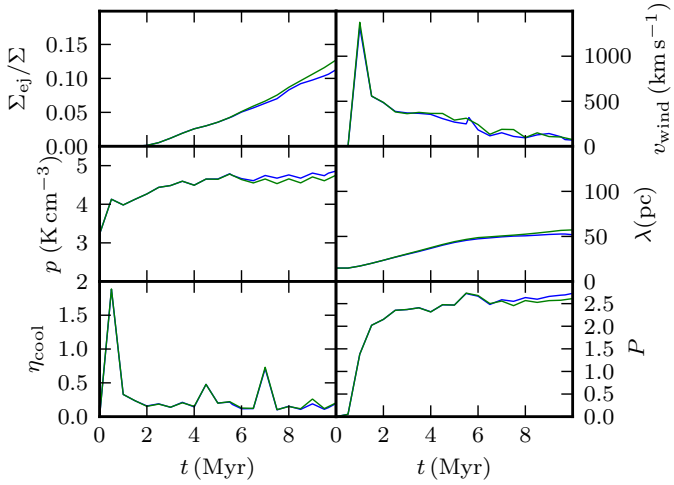

Figure B.7: As for Fig.B.3 but testing the effect of changing the vertical box size. *Blue line* is the outflow estimated for a simulation with the fiducial box height (500 pc), *green line* for 1 kpc.

time fixed, but inject the energy in more (less) frequent explosions with less (more) energy. The variation between these simulations is surprisingly large: the behaviour of the ISM is indeed quite sensitive to how smooth or stochastic the injected energy is.

In Figs. B.7-B.8 we investigate the dependence of the simulations on the size of the simulation volume. In Fig. B.7 we adjust the vertical size of the simulation volume, i.e. whether increasing

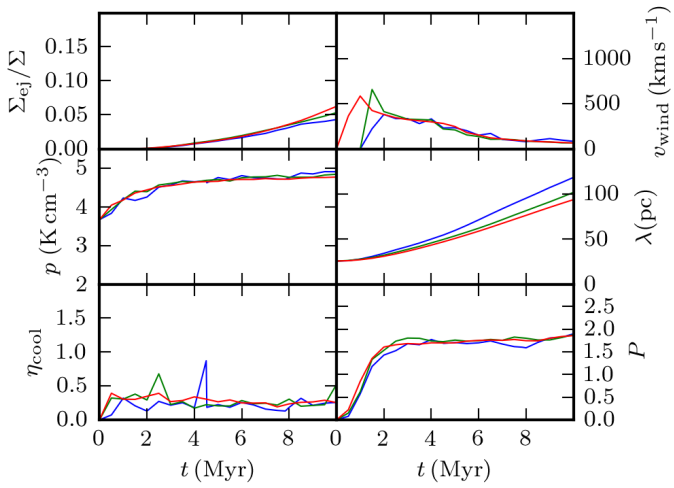

Figure B.8: As Fig. B.3, but for 3 different box sizes. *Blue line* indicates the run at the L3 resolution, *green line* with $2\times$ the box width and *red line* with $4\times$ the box width.

the volume to simulate more of the outflow adjusts the dynamics, for example by allowing some material to fall back to the disk. All parameters are still computed for the original volume ($\pm$500 pc), only the simulation volume has been expanded. All the parameters appear to be almost independent of this change. In Fig. B.8 we adjust the horizontal size of simulation volume, where we have multiplied the box width by a factors of 2 and 4 respectively. The parameters here also show extremely good convergence, with the larger volumes generally showing less variation in values due to the reduced Poisson noise. The larger volumes also appear to show a marginal reduction in the evolution of the disk scale height.

Finally, in Fig. B.9 we have constructed equivalent graphs to that of Fig. 3.5, but now showing all simulations varying $\Sigma_{\rm g}$ and $f_{\rm g}$ in Table 3.1. Each panel shows the time evolution of a single simulation, showing the surface density, porosity, instantaneous cooling rate, disk height, mass ejected and pressure, along with a ramp function fit, Eq. (3.42)), to the mass ejection rates. We can see a strong evolution of the feedback from top left to lower right, i.e. at high surface densities and low gas fractions the simulations develop much stronger mass ejection rates and pressures, and the disk is more heavily disrupted. Note that the mass ejection rate has not been normalised by the surface density, so much of the increase is due to the increased star formation in the higher surface density disks. In a couple of the high surface density panels the simulation has failed early although there are enough data points to perform a fit to the mass ejection. Although there is considerable stochasticity in the 2 parameter fits, they seem quite robust.

In conclusion, these studies demonstrate that our simulations are effective at modelling a SN

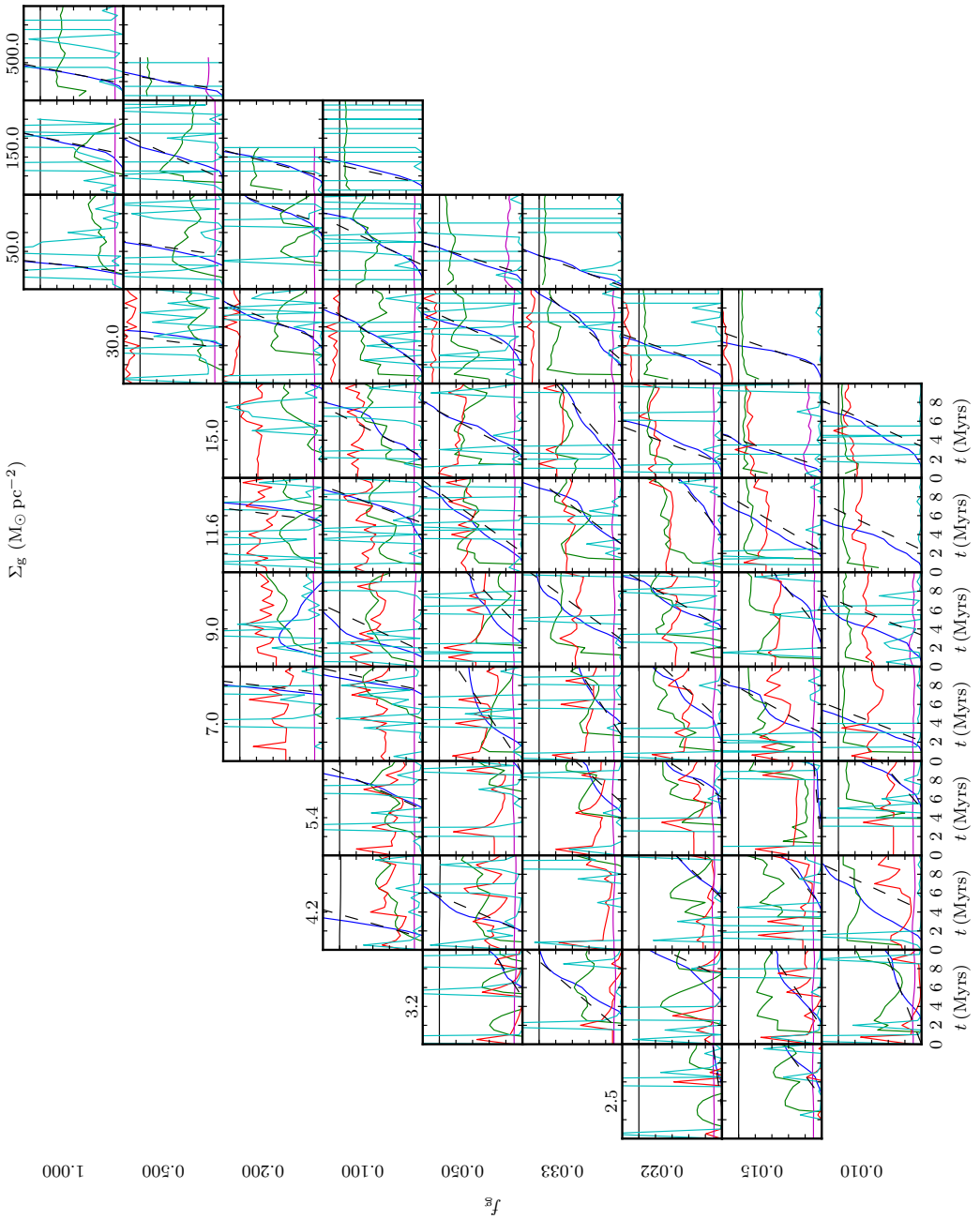

Figure B.9: Lines as for Fig. 3.5, but for all simulations varying Σ_g and f_g in Table 3.1. Additional *black dashed lines* have been added to show a fit to ejection (*solid blue lines*) given by Eq. (3.42). $\Sigma_{g1} \equiv \Sigma/1 M_\odot\,\mathrm{pc}^{-1}$ runs from 1.5 to 11.6 from left to right panels. f_g runs from 0.01 to 0.05 from lower to upper panels. *Blue line*, the amount of gas that has been ejected from the simulation, has now been scaled to units of $5\,\mathrm{M}_\odot\,\mathrm{pc}^{-2}$ for clarity.

driven ISM and resilient to changes in numerical parameters. The exact nature of the cooling function exhibits little effect on the disk evolution, in fact the limiting factor is largely the physical granularity of the discrete SNe and their locations in the disk. To this end reducing the scatter in our disk property dependencies could be acheived by taking a larger ensemble of runs or alternatively by simulating larger disk areas, either of which increases the total number of SNe introduced.

Bibliography

T. Abel. rpSPH: a novel smoothed particle hydrodynamics algorithm. MNRAS, 413:271–285, May 2011. doi: 10.1111/j.1365-2966.2010.18133.x.

T. Abel, P. Anninos, Y. Zhang, and M. L. Norman. Modeling primordial gas in numerical cosmology. *New Astronomy*, 2:181–207, August 1997. doi: 10.1016/S1384-1076(97)00010-9.

O. Agertz, B. Moore, J. Stadel, D. Potter, F. Miniati, J. Read, L. Mayer, A. Gawryszczak, A. Kravtsov, Å. Nordlund, F. Pearce, V. Quilis, D. Rudd, V. Springel, J. Stone, E. Tasker, R. Teyssier, J. Wadsley, and R. Walder. Fundamental differences between SPH and grid methods. MNRAS, 380:963–978, September 2007. doi: 10.1111/j.1365-2966.2007.12183.x.

A. Aguirre, L. Hernquist, J. Schaye, N. Katz, D. H. Weinberg, and J. Gardner. Metal Enrichment of the Intergalactic Medium in Cosmological Simulations. ApJ, 561:521–549, November 2001. doi: 10.1086/323370.

A. Aguirre, J. Schaye, T.-S. Kim, T. Theuns, M. Rauch, and W. L. W. Sargent. Metallicity of the Intergalactic Medium Using Pixel Statistics. III. Silicon. ApJ, 602:38–50, February 2004. doi: 10.1086/380961.

A. Aguirre, J. Schaye, L. Hernquist, S. Kay, V. Springel, and T. Theuns. Confronting Cosmological Simulations with Observations of Intergalactic Metals. ApJ, 620:L13–L17, February 2005. doi: 10.1086/428498.

M. Asplund, N. Grevesse, and A. J. Sauval. The Solar Chemical Composition. In T. G. Barnes III & F. N. Bash, editor, *Cosmic Abundances as Records of Stellar Evolution and Nucleosynthesis*, volume 336 of *Astronomical Society of the Pacific Conference Series*, page 25, September 2005.

J. N. Bahcall, C. Flynn, and A. Gould. Local dark matter from a carefully selected sample. ApJ, 389:234–250, April 1992. doi: 10.1086/171201.

I. K. Baldry, K. Glazebrook, T. Budavári, D. J. Eisenstein, J. Annis, N. A. Bahcall, M. R. Blanton, J. Brinkmann, I. Csabai, T. M. Heckman, H. Lin, J. Loveday, R. C. Nichol, and D. P. Schneider. The Sloan Digital Sky Survey u-band Galaxy Survey: luminosity functions and evolution. MNRAS, 358:441–456, April 2005. doi: 10.1111/j.1365-2966.2005.08799.x.

I. K. Baldry, S. P. Driver, J. Loveday, E. N. Taylor, L. S. Kelvin, J. Liske, P. Norberg, A. S. G. Robotham, S. Brough, A. M. Hopkins, S. P. Bamford, J. A. Peacock, J. Bland-Hawthorn, C. J. Conselice, S. M. Croom, D. H. Jones, H. R. Parkinson, C. C. Popescu, M. Prescott, R. G. Sharp, and R. J. Tuffs. Galaxy And Mass Assembly (GAMA): the galaxy stellar mass function at z ¡ 0.06. MNRAS, 421:621–634, March 2012. doi: 10.1111/j.1365-2966.2012.20340.x.

M. L. Balogh, F. R. Pearce, R. G. Bower, and S. T. Kay. Revisiting the cosmic cooling crisis. MNRAS, 326:1228–1234, October 2001. doi: 10.1046/j.1365-8711.2001.04667.x.

D. S. Balsara. von Neumann stability analysis of smooth particle hydrodynamics–suggestions for optimal algorithms. *Journal of Computational Physics*, 121:357–372, 1995. doi: 10.1016/S0021-9991(95)90221-X.

M. Bate. PhD thesis, PhD thesis, Univ. Cambridge, (1995), 1995.

E. F. Bell and R. S. de Jong. Stellar Mass-to-Light Ratios and the Tully-Fisher Relation. ApJ, 550:212–229, March 2001. doi: 10.1086/319728.

P. Bett, V. Eke, C. S. Frenk, A. Jenkins, J. Helly, and J. Navarro. The spin and shape of dark matter haloes in the Millennium simulation of a Λ cold dark matter universe. MNRAS, 376:215–232, March 2007. doi: 10.1111/j.1365-2966.2007.11432.x.

F. Bigiel, A. Leroy, F. Walter, E. Brinks, W. J. G. de Blok, B. Madore, and M. D. Thornley. The Star Formation Law in Nearby Galaxies on Sub-Kpc Scales. AJ, 136:2846–2871, December 2008. doi: 10.1088/0004-6256/136/6/2846.

Y. Birnboim and A. Dekel. Virial shocks in galactic haloes? MNRAS, 345:349–364, October 2003. doi: 10.1046/j.1365-8711.2003.06955.x.

M. R. Blanton, D. W. Hogg, N. A. Bahcall, J. Brinkmann, M. Britton, A. J. Connolly, I. Csabai, M. Fukugita, J. Loveday, A. Meiksin, J. A. Munn, R. C. Nichol, S. Okamura, T. Quinn, D. P. Schneider, K. Shimasaku, M. A. Strauss, M. Tegmark, M. S. Vogeley, and D. H. Weinberg. The Galaxy Luminosity Function and Luminosity Density at Redshift z = 0.1. ApJ, 592:819–838, August 2003. doi: 10.1086/375776.

M. R. Blanton, R. H. Lupton, D. J. Schlegel, M. A. Strauss, J. Brinkmann, M. Fukugita, and J. Loveday. The Properties and Luminosity Function of Extremely Low Luminosity Galaxies. ApJ, 631:208–230, September 2005. doi: 10.1086/431416.

H. Boehringer and T. W. Hartquist. Steady models of radiatively modified conductively driven evaporation from interstellar clouds. MNRAS, 228:915–931, October 1987.

H. E. Bond. A Search for Metal-Deficient Stars. ApJS, 22:117, September 1970. doi: 10.1086/190220.

J. R. Bond, S. Cole, G. Efstathiou, and N. Kaiser. Excursion set mass functions for hierarchical Gaussian fluctuations. ApJ, 379:440–460, October 1991. doi: 10.1086/170520.

C. M. Booth and J. Schaye. Cosmological simulations of the growth of supermassive black holes and feedback from active galactic nuclei: method and tests. MNRAS, 398:53–74, September 2009. doi: 10.1111/j.1365-2966.2009.15043.x.

C. M. Booth, T. Theuns, and T. Okamoto. Molecular cloud regulated star formation in galaxies. MNRAS, 376:1588–1610, April 2007. doi: 10.1111/j.1365-2966.2007.11570.x.

C. M. Booth, J. Schaye, J. D. Delgado, and C. Dalla Vecchia. The filling factor of intergalactic metals at redshift z= 3. MNRAS, 420:1053–1060, February 2012. doi: 10.1111/j.1365-2966.2011.20047.x.

N. Bouche, W. Hohensee, R. Vargas, G. G. Kacprzak, C. L. Martin, J. Cooke, and C. W. Churchill. Physical properties of galactic winds using background quasars. *ArXiv e-prints*, October 2011.

J. Bovy and S. Tremaine. On the local dark matter density. *ArXiv e-prints*, May 2012.

R. G. Bower, A. J. Benson, R. Malbon, J. C. Helly, C. S. Frenk, C. M. Baugh, S. Cole, and C. G. Lacey. Breaking the hierarchy of galaxy formation. MNRAS, 370:645–655, August 2006. doi: 10.1111/j.1365-2966.2006.10519.x.

R. G. Bower, A. J. Benson, and R. A. Crain. What Shapes the Galaxy Mass Function? Exploring the Roles of Supernova-Driven Winds and AGN. *ArXiv e-prints*, December 2011.

S. Bowyer, R. Lieu, S. D. Sidher, M. Lampton, and J. Knude. Evidence for a large thermal pressure imbalance in the local interstellar medium. Nature, 375:212–214, May 1995. doi: 10.1038/375212a0.

D. Breitschwerdt and M. A. de Avillez. Dynamical evolution of a supernova driven turbulent interstellar medium. In B. G. Elmegreen & J. Palous, editor, *IAU Symposium*, volume 237 of *IAU Symposium*, pages 57–64, 2007. doi: 10.1017/S1743921307001226.

G. L. Bryan and M. L. Norman. A Hybrid AMR Application for Cosmology and Astrophysics. *ArXiv Astrophysics e-prints*, October 1997.

E. M. Burbidge, G. R. Burbidge, W. A. Fowler, and F. Hoyle. Synthesis of the Elements in Stars. *Reviews of Modern Physics*, 29:547–650, 1957. doi: 10.1103/RevModPhys.29.547.

J. Castor, R. McCray, and R. Weaver. Interstellar bubbles. ApJ, 200:L107–L110, September 1975a. doi: 10.1086/181908.

J. I. Castor, D. C. Abbott, and R. I. Klein. Radiation-driven winds in Of stars. ApJ, 195:157–174, January 1975b. doi: 10.1086/153315.

B. Catinella, D. Schiminovich, G. Kauffmann, S. Fabello, J. Wang, C. Hummels, J. Lemonias, S. M. Moran, R. Wu, R. Giovanelli, M. P. Haynes, T. M. Heckman, A. R. Basu-Zych, M. R. Blanton, J. Brinchmann, T. Budavári, T. Gonçalves, B. D. Johnson, R. C. Kennicutt, B. F. Madore, C. D. Martin, M. R. Rich, L. J. Tacconi, D. A. Thilker, V. Wild, and T. K. Wyder. The GALEX Arecibo SDSS Survey - I. Gas fraction scaling relations of massive galaxies and first data release. MNRAS, 403:683–708, April 2010. doi: 10.1111/j.1365-2966.2009.16180.x.

R. Cen and J. P. Ostriker. Cosmic Chemical Evolution. ApJ, 519:L109–L113, July 1999. doi: 10.1086/312123.

D. Ceverino and A. Klypin. The Role of Stellar Feedback in the Formation of Galaxies. ApJ, 695:292–309, April 2009. doi: 10.1088/0004-637X/695/1/292.

G. Chabrier. Galactic Stellar and Substellar Initial Mass Function. PASP, 115:763–795, July 2003. doi: 10.1086/376392.

Y.-M. Chen, C. A. Tremonti, T. M. Heckman, G. Kauffmann, B. J. Weiner, J. Brinchmann, and J. Wang. Absorption-line Probes of the Prevalence and Properties of Outflows in Present-day Star-forming Galaxies. AJ, 140:445–461, August 2010. doi: 10.1088/0004-6256/140/2/445.

R. A. Chevalier. The Evolution of Supernova Remnants. Spherically Symmetric Models. ApJ, 188:501–516, March 1974. doi: 10.1086/152740.

R. A. Chevalier and J. N. Imamura. Linear analysis of an oscillatory instability of radiative shock waves. ApJ, 261:543–549, October 1982. doi: 10.1086/160364.

L. Chomiuk and M. S. Povich. Toward a Unification of Star Formation Rate Determinations in the Milky Way and Other Galaxies. AJ, 142:197, December 2011. doi: 10.1088/0004-6256/142/6/197.

S. Cole, C. G. Lacey, C. M. Baugh, and C. S. Frenk. Hierarchical galaxy formation. MNRAS, 319:168–204, November 2000. doi: 10.1046/j.1365-8711.2000.03879.x.

P. Colella and P. R. Woodward. The Piecewise Parabolic Method (PPM) for Gas-Dynamical Simulations. *Journal of Computational Physics*, 54:174–201, September 1984. doi: 10.1016/0021-9991(84)90143-8.

J. L. Cooper, G. V. Bicknell, R. S. Sutherland, and J. Bland-Hawthorn. Three-Dimensional Simulations of a Starburst-driven Galactic Wind. ApJ, 674:157–171, February 2008. doi: 10.1086/524918.

R. Courant, K. Friedrichs, and H. Lewy. Über die partiellen Differenzengleichungen der mathematischen Physik. *Mathematische Annalen*, 100:32–74, 1928. doi: 10.1007/BF01448839.

L. L. Cowie and C. F. McKee. The evaporation of spherical clouds in a hot gas. I - Classical and saturated mass loss rates. ApJ, 211:135–146, January 1977. doi: 10.1086/154911.

L. L. Cowie, A. Songaila, T.-S. Kim, and E. M. Hu. The metallicity and internal structure of the Lyman-alpha forest clouds. AJ, 109:1522–1530, April 1995. doi: 10.1086/117381.

D. P. Cox. Cooling and Evolution of a Supernova Remnant. ApJ, 178:159–168, November 1972. doi: 10.1086/151775.

R. A. Crain, T. Theuns, C. Dalla Vecchia, V. R. Eke, C. S. Frenk, A. Jenkins, S. T. Kay, J. A. Peacock, F. R. Pearce, J. Schaye, V. Springel, P. A. Thomas, S. D. M. White, and R. P. C. Wiersma. Galaxies-intergalactic medium interaction calculation - I. Galaxy formation as a function of large-scale environment. MNRAS, 399:1773–1794, November 2009. doi: 10.1111/j.1365-2966.2009.15402.x.

R. A. Crain, I. G. McCarthy, C. S. Frenk, T. Theuns, and J. Schaye. X-ray coronae in simulations of disc galaxy formation. MNRAS, 407:1403–1422, September 2010. doi: 10.1111/j.1365-2966.2010.16985.x.

P. Creasey, T. Theuns, R. G. Bower, and C. G. Lacey. Numerical overcooling in shocks. MNRAS, 415:3706–3720, August 2011. doi: 10.1111/j.1365-2966.2011.19001.x.

C. Dalla Vecchia and J. Schaye. Simulating galactic outflows with kinetic supernova feedback. MNRAS, 387:1431–1444, July 2008. doi: 10.1111/j.1365-2966.2008.13322.x.

R. Davé, K. Finlator, and B. D. Oppenheimer. Galaxy evolution in cosmological simulations with outflows - II. Metallicities and gas fractions. MNRAS, 416:1354–1376, September 2011. doi: 10.1111/j.1365-2966.2011.19132.x.

R. Davé, K. Finlator, and B. D. Oppenheimer. An analytic model for the evolution of the stellar, gas and metal content of galaxies. MNRAS, 421:98–107, March 2012. doi: 10.1111/j.1365-2966.2011.20148.x.

P. Dayal, A. Ferrara, and J. S. Dunlop. The physics of the fundamental metallicity relation. *ArXiv e-prints*, February 2012.

M. A. de Avillez and D. Breitschwerdt. Volume filling factors of the ISM phases in star forming galaxies. I. The role of the disk-halo interaction. A&A, 425:899–911, October 2004. doi: 10.1051/0004-6361:200400025.

M. A. de Avillez and D. Breitschwerdt. Global dynamical evolution of the ISM in star forming galaxies. I. High resolution 3D simulations: Effect of the magnetic field. A&A, 436:585–600, June 2005a. doi: 10.1051/0004-6361:20042146.

M. A. de Avillez and D. Breitschwerdt. Testing Global ISM Models: A Detailed Comparison of O VI Column Densities with FUSE and Copernicus Data. ApJ, 634:L65–L68, November 2005b. doi: 10.1086/498744.

T. de Jong, W. Boland, and A. Dalgarno. Hydrostatic models of molecular clouds. A&A, 91: 68–84, November 1980.

W. Dehnen and J. Binney. Mass models of the Milky Way. MNRAS, 294:429, March 1998. doi: 10.1046/j.1365-8711.1998.01282.x.

A. Dekel and J. Silk. The origin of dwarf galaxies, cold dark matter, and biased galaxy formation. ApJ, 303:39–55, April 1986. doi: 10.1086/164050.

G. Denicoló, R. Terlevich, and E. Terlevich. New light on the search for low-metallicity galaxies - I. The N2 calibrator. MNRAS, 330:69–74, February 2002. doi: 10.1046/j.1365-8711.2002.05041.x.

C. L. Dobbs. GMC formation by agglomeration and self gravity. MNRAS, 391:844–858, December 2008. doi: 10.1111/j.1365-2966.2008.13939.x.

Y. Dubois and R. Teyssier. On the onset of galactic winds in quiescent star forming galaxies. A&A, 477:79–94, January 2008. doi: 10.1051/0004-6361:20078326.

F. Durier and C. Dalla Vecchia. Implementation of feedback in smoothed particle hydrodynamics: towards concordance of methods. MNRAS, 419:465–478, January 2012. doi: 10.1111/j.1365-2966.2011.19712.x.

M. G. Edmunds. General Constraints on the Effect of Gas Flows in the Chemical Evolution of Galaxies. MNRAS, 246:678, October 1990.

G. Efstathiou. Suppressing the formation of dwarf galaxies via photoionization. MNRAS, 256: 43P–47P, May 1992.

G. Efstathiou. A model of supernova feedback in galaxy formation. MNRAS, 317:697–719, September 2000. doi: 10.1046/j.1365-8711.2000.03665.x.

G. Efstathiou, M. Davis, S. D. M. White, and C. S. Frenk. Numerical techniques for large cosmological N-body simulations. ApJS, 57:241–260, February 1985. doi: 10.1086/191003.

B. Einfeldt. On Godunov-Type Methods for Gas Dynamics. *SIAM Journal on Numerical Analysis*, 25:294–318, April 1988. doi: 10.1137/0725021.

V. R. Eke, S. Cole, and C. S. Frenk. Cluster evolution as a diagnostic for Omega. MNRAS, 282: 263–280, September 1996.

B. G. Elmegreen and J. Scalo. Interstellar Turbulence I: Observations and Processes. ARA&A, 42:211–273, September 2004. doi: 10.1146/annurev.astro.41.011802.094859.

S. M. Fall and G. Efstathiou. Formation and rotation of disc galaxies with haloes. MNRAS, 193: 189–206, October 1980.

A. Ferrara, M. Pettini, and Y. Shchekinov. Mixing metals in the early Universe. MNRAS, 319: 539–548, December 2000. doi: 10.1046/j.1365-8711.2000.03857.x.

A. Ferrara, E. Scannapieco, and J. Bergeron. Where Are the Missing Cosmic Metals? ApJ, 634: L37–L40, November 2005. doi: 10.1086/498845.

K. Finlator and R. Davé. The origin of the galaxy mass-metallicity relation and implications for galactic outflows. MNRAS, 385:2181–2204, April 2008. doi: 10.1111/j.1365-2966.2008.12991.x.

C. Flynn, J. Holmberg, L. Portinari, B. Fuchs, and H. Jahreiß. On the mass-to-light ratio of the local Galactic disc and the optical luminosity of the Galaxy. MNRAS, 372:1149–1160, November 2006. doi: 10.1111/j.1365-2966.2006.10911.x.

W. L. Freedman, B. F. Madore, B. K. Gibson, L. Ferrarese, D. D. Kelson, S. Sakai, J. R. Mould, R. C. Kennicutt, Jr., H. C. Ford, J. A. Graham, J. P. Huchra, S. M. G. Hughes, G. D. Illingworth, L. M. Macri, and P. B. Stetson. Final Results from the Hubble Space Telescope Key Project to Measure the Hubble Constant. ApJ, 553:47–72, May 2001. doi: 10.1086/320638.

K. O. Friedrichs and P. D. Lax. Systems of Conservation Equations with a Convex Extension. *Proceedings of the National Academy of Science*, 68:1686–1688, August 1971. doi: 10.1073/pnas.68.8.1686.

B. Fryxell, K. Olson, P. Ricker, F. X. Timmes, M. Zingale, D. Q. Lamb, P. MacNeice, R. Rosner, J. W. Truran, and H. Tufo. FLASH: An Adaptive Mesh Hydrodynamics Code for Modeling Astrophysical Thermonuclear Flashes. ApJS, 131:273–334, November 2000. doi: 10.1086/317361.

A. Fujita, M.-M. Mac Low, A. Ferrara, and A. Meiksin. Cosmological Feedback from High-Redshift Dwarf Galaxies. ApJ, 613:159–179, September 2004. doi: 10.1086/422861.

A. Fujita, C. L. Martin, M.-M. Mac Low, K. C. B. New, and R. Weaver. The Origin and Kinematics of Cold Gas in Galactic Winds: Insight from Numerical Simulations. ApJ, 698:693–714, June 2009. doi: 10.1088/0004-637X/698/1/693.

M. Fukugita, C. J. Hogan, and P. J. E. Peebles. The Cosmic Baryon Budget. ApJ, 503:518, August 1998. doi: 10.1086/306025.

F. A. Gent, A. Shukurov, A. Fletcher, G. R. Sarson, and M. J. Mantere. The supernova-regulated ISM. I. The multi-phase structure. *ArXiv e-prints*, April 2012.

J. P. E. Gerritsen. PhD thesis, , Groningen University, the Netherlands, (1997), 1997.

R. A. Gingold and J. J. Monaghan. Smoothed particle hydrodynamics - Theory and application to non-spherical stars. MNRAS, 181:375–389, November 1977.

O. Gnat, A. Sternberg, and C. F. McKee. Metal-ion Absorption in Conductively Evaporating Clouds. ApJ, 718:1315–1331, August 2010. doi: 10.1088/0004-637X/718/2/1315.

N. Y. Gnedin and T. Abel. Multi-dimensional cosmological radiative transfer with a Variable Eddington Tensor formalism. *N/A*, 6:437–455, October 2001. doi: 10.1016/S1384-1076(01)00068-9.

S. K. Godunov and V. S. Ryabenki. *Theory of difference schemes - an introduction*. 1964.

Q. Guo, S. White, C. Li, and M. Boylan-Kolchin. How do galaxies populate dark matter haloes? MNRAS, 404:1111–1120, May 2010. doi: 10.1111/j.1365-2966.2010.16341.x.

Amiram Harten, Peter D. Lax, and Bram van Leer. On upstream differencing and godunov-type schemes for hyperbolic conservation laws. *SIAM Review*, 25(1):35–61, 1983. doi: 10.1137/1025002. URL `http://link.aip.org/link/?SIR/25/35/1`.

T. W. Hartquist, J. E. Dyson, M. Pettini, and L. J. Smith. Mass-loaded astronomical flows. I - General principles and their application to RCW 58. MNRAS, 221:715–726, August 1986.

T. M. Heckman, L. Armus, and G. K. Miley. On the nature and implications of starburst-driven galactic superwinds. ApJS, 74:833–868, December 1990. doi: 10.1086/191522.

T. M. Heckman, M. D. Lehnert, D. K. Strickland, and L. Armus. Absorption-Line Probes of Gas and Dust in Galactic Superwinds. ApJS, 129:493–516, August 2000. doi: 10.1086/313421.

A. S. Hill, M. R. Joung, M.-M. Mac Low, R. A. Benjamin, L. M. Haffner, C. Klingenberg, and K. Waagan. Vertical structure of a supernova-driven turbulent magnetized ISM. *ArXiv e-prints*, February 2012.

R. W. Hockney and J. W. Eastwood. *Computer simulation using particles*. 1988.

R. W. Hockney, S. P. Goel, and J. W. Eastwood. A 10000 particle molecular dynamics model with long range forces. *Chemical Physics Letters*, 21:589–591, September 1973. doi: 10.1016/0009-2614(73)80315-X.

P. F. Hopkins, E. Quataert, and N. Murray. Self-regulated star formation in galaxies via momentum input from massive stars. MNRAS, 417:950–973, October 2011. doi: 10.1111/j.1365-2966.2011.19306.x.

P. F. Hopkins, E. Quataert, and N. Murray. Stellar feedback in galaxies and the origin of galaxy-scale winds. MNRAS, 421:3522–3537, April 2012a. doi: 10.1111/j.1365-2966.2012.20593.x.

P. F. Hopkins, E. Quataert, and N. Murray. The structure of the interstellar medium of star-forming galaxies. MNRAS, 421:3488–3521, April 2012b. doi: 10.1111/j.1365-2966.2012.20578.x.

L. Hui and N. Y. Gnedin. Equation of state of the photoionized intergalactic medium. MNRAS, 292:27–+, November 1997.

R. M. Hutchings and P. A. Thomas. In-shock cooling in numerical simulations. MNRAS, 319: 721–727, December 2000. doi: 10.1046/j.1365-8711.2000.03723.x.

S. Inutsuka. Godunov-type SPH. Mem. Soc. Astron. Italiana, 65:1027–+, 1994.

B. R. Jørgensen. The G dwarf problem. Analysis of a new data set. A&A, 363:947–957, November 2000.

M. K. R. Joung and M.-M. Mac Low. Turbulent Structure of a Stratified Supernova-driven Interstellar Medium. ApJ, 653:1266–1279, December 2006. doi: 10.1086/508795.

M. R. Joung, M.-M. Mac Low, and G. L. Bryan. Dependence of Interstellar Turbulent Pressure on Supernova Rate. ApJ, 704:137–149, October 2009. doi: 10.1088/0004-637X/704/1/137.

M. Jubelgas, V. Springel, T. Enßlin, and C. Pfrommer. Cosmic ray feedback in hydrodynamical simulations of galaxy formation. A&A, 481:33–63, April 2008. doi: 10.1051/0004-6361: 20065295.

F. D. Kahn. Supernova Remnants. In *International Cosmic Ray Conference*, volume 11 of *International Cosmic Ray Conference*, page 3566, 1975.

S. T. Kay, F. R. Pearce, C. S. Frenk, and A. Jenkins. Including star formation and supernova feedback within cosmological simulations of galaxy formation. MNRAS, 330:113–128, February 2002. doi: 10.1046/j.1365-8711.2002.05070.x.

R. C. Kennicutt, Jr. The star formation law in galactic disks. ApJ, 344:685–703, September 1989. doi: 10.1086/167834.

R. C. Kennicutt, Jr. The Global Schmidt Law in Star-forming Galaxies. ApJ, 498:541–+, May 1998. doi: 10.1086/305588.

F. J. Kerr and D. Lynden-Bell. Review of galactic constants. MNRAS, 221:1023–1038, August 1986.

L. J. Kewley and S. L. Ellison. Metallicity Calibrations and the Mass-Metallicity Relation for Star-forming Galaxies. ApJ, 681:1183–1204, July 2008. doi: 10.1086/587500.

L. J. Kewley, D. Rupke, H. J. Zahid, M. J. Geller, and E. J. Barton. Metallicity Gradients and Gas Flows in Galaxy Pairs. ApJ, 721:L48–L52, September 2010. doi: 10.1088/2041-8205/721/1/L48.

A. Kolmogorov. The Local Structure of Turbulence in Incompressible Viscous Fluid for Very Large Reynolds' Numbers. *Akademiia Nauk SSSR Doklady*, 30:301–305, 1941.

M. R. Krumholz and C. F. McKee. A General Theory of Turbulence-regulated Star Formation, from Spirals to Ultraluminous Infrared Galaxies. ApJ, 630:250–268, September 2005. doi: 10.1086/431734.

S. R. Kulkarni and C. Heiles. The atomic component. In D. J. Hollenbach and H. A. Thronson, Jr., editors, *Interstellar Processes*, volume 134 of *Astrophysics and Space Science Library*, pages 87–122, 1987.

K. Kulpa-Dybeł, K. Otmianowska-Mazur, B. Kulesza-Żydzik, M. Hanasz, G. Kowal, D. Wóltański, and K. Kowalik. Global Simulations of the Magnetic Field Evolution in Barred Galaxies Under the Influence of the Cosmic-ray-driven Dynamo. ApJ, 733:L18, June 2011. doi: 10.1088/2041-8205/733/2/L18.

C. D. P. Lagos, C. G. Lacey, and C. M. Baugh, 2012. in preparation.

R. B. Larson. Effects of supernovae on the early evolution of galaxies. MNRAS, 169:229–246, November 1974.

A. K. Leroy, F. Walter, E. Brinks, F. Bigiel, W. J. G. de Blok, B. Madore, and M. D. Thornley. The Star Formation Efficiency in Nearby Galaxies: Measuring Where Gas Forms Stars Effectively. AJ, 136:2782–2845, December 2008. doi: 10.1088/0004-6256/136/6/2782.

C. Li and S. D. M. White. The distribution of stellar mass in the low-redshift Universe. MNRAS, 398:2177–2187, October 2009. doi: 10.1111/j.1365-2966.2009.15268.x.

F. J. Lockman. The H I halo in the inner galaxy. ApJ, 283:90–97, August 1984. doi: 10.1086/162277.

C. Longair. High Energy Astrophysics. Vol.1. Particles, Photons and their Detection. *Astronomische Nachrichten*, 317:156, February 1996.

L. A. Lopez, M. R. Krumholz, A. D. Bolatto, J. X. Prochaska, and E. Ramirez-Ruiz. What Drives the Expansion of Giant H II Regions?: A Study of Stellar Feedback in 30 Doradus. ApJ, 731:91, April 2011. doi: 10.1088/0004-637X/731/2/91.

L. B. Lucy. A numerical approach to the testing of the fission hypothesis. AJ, 82:1013–1024, December 1977.

M.-M. Mac Low and A. Ferrara. Starburst-driven Mass Loss from Dwarf Galaxies: Efficiency and Metal Ejection. ApJ, 513:142–155, March 1999. doi: 10.1086/306832.

M.-M. Mac Low and R. S. Klessen. Control of star formation by supersonic turbulence. *Reviews of Modern Physics*, 76:125–194, January 2004. doi: 10.1103/RevModPhys.76.125.

C. L. Martin. Mapping Large-Scale Gaseous Outflows in Ultraluminous Galaxies with Keck II ESI Spectra: Variations in Outflow Velocity with Galactic Mass. ApJ, 621:227–245, March 2005. doi: 10.1086/427277.

C. L. Martin and R. C. Kennicutt, Jr. Star Formation Thresholds in Galactic Disks. ApJ, 555: 301–321, July 2001. doi: 10.1086/321452.

C. L. Martin, H. A. Kobulnicky, and T. M. Heckman. The Metal Content of Dwarf Starburst Winds: Results from Chandra Observations of NGC 1569. ApJ, 574:663–692, August 2002. doi: 10.1086/341092.

P. G. Martin, D. H. Schwarz, and M. E. Mandy. Master Equation Studies of the Collisional Excitation and Dissociation of H_2 Molecules by H Atoms. ApJ, 461:265, April 1996. doi: 10.1086/177053.

C. D. Matzner. On the Role of Massive Stars in the Support and Destruction of Giant Molecular Clouds. ApJ, 566:302–314, February 2002. doi: 10.1086/338030.

I. G. McCarthy, J. Schaye, A. S. Font, T. Theuns, C. S. Frenk, R. A. Crain, and C. Dalla Vecchia. Rotation rates, sizes, and star formation efficiencies of a representative population of simulated disc galaxies. *ArXiv e-prints*, April 2012.

R. McCray and M. Kafatos. Supershells and propagating star formation. ApJ, 317:190–196, June 1987. doi: 10.1086/165267.

S. S. McGaugh. The Baryonic Tully-Fisher Relation of Galaxies with Extended Rotation Curves and the Stellar Mass of Rotating Galaxies. ApJ, 632:859–871, October 2005. doi: 10.1086/432968.

C. F. McKee and J. P. Ostriker. A theory of the interstellar medium - Three components regulated by supernova explosions in an inhomogeneous substrate. ApJ, 218:148–169, November 1977. doi: 10.1086/155667.

J. D. Meiring, T. M. Tripp, J. K. Werk, C. Howk, E. B. Jenkins, J. X. Prochaska, N. Lehner, and K. R. Sembach. QSO absorption systems detected in Ne VIII: Evidence for high-metallicity, multiphase gas far from galaxies. *ArXiv e-prints*, January 2012.

H. Mo, F. C. van den Bosch, and S. White. *Galaxy Formation and Evolution*. 2010.

H. J. Mo, S. Mao, and S. D. M. White. The formation of galactic discs. MNRAS, 295:319–336, April 1998. doi: 10.1046/j.1365-8711.1998.01227.x.

J. J. Monaghan. SPH and Riemann Solvers. *Journal of Computational Physics*, 136:298–307, September 1997. doi: 10.1006/jcph.1997.5732.

J. J. Monaghan. Smoothed particle hydrodynamics. *Reports on Progress in Physics*, 68:1703–1759, August 2005. doi: 10.1088/0034-4885/68/8/R01.

M. Mori, A. Ferrara, and P. Madau. Early Metal Enrichment by Pregalactic Outflows. II. Three-dimensional Simulations of Blow-Away. ApJ, 571:40–55, May 2002. doi: 10.1086/339913.

B. P. Moster, R. S. Somerville, C. Maulbetsch, F. C. van den Bosch, A. V. Macciò, T. Naab, and L. Oser. Constraints on the Relationship between Stellar Mass and Halo Mass at Low and High Redshift. ApJ, 710:903–923, February 2010. doi: 10.1088/0004-637X/710/2/903.

N. Murray, E. Quataert, and T. A. Thompson. On the Maximum Luminosity of Galaxies and Their Central Black Holes: Feedback from Momentum-driven Winds. ApJ, 618:569–585, January 2005. doi: 10.1086/426067.

J. F. Navarro and M. Steinmetz. The Effects of a Photoionizing Ultraviolet Background on the Formation of Disk Galaxies. ApJ, 478:13, March 1997. doi: 10.1086/303763.

J. F. Navarro and S. D. M. White. Simulations of Dissipative Galaxy Formation in Hierarchically Clustering Universes - Part One - Tests of the Code. MNRAS, 265:271–+, November 1993.

J. F. Navarro, C. S. Frenk, and S. D. M. White. A Universal Density Profile from Hierarchical Clustering. ApJ, 490:493, December 1997. doi: 10.1086/304888.

B. Nordström, M. Mayor, J. Andersen, J. Holmberg, F. Pont, B. R. Jørgensen, E. H. Olsen, S. Udry, and N. Mowlavi. The Geneva-Copenhagen survey of the Solar neighbourhood. Ages, metallicities, and kinematic properties of ∼14 000 F and G dwarfs. A&A, 418:989–1019, May 2004. doi: 10.1051/0004-6361:20035959.

T. Okamoto, L. Gao, and T. Theuns. Mass loss of galaxies due to an ultraviolet background. MNRAS, 390:920–928, November 2008a. doi: 10.1111/j.1365-2966.2008.13830.x.

T. Okamoto, L. Gao, and T. Theuns. Mass loss of galaxies due to an ultraviolet background. MNRAS, 390:920–928, November 2008b. doi: 10.1111/j.1365-2966.2008.13830.x.

B. D. Oppenheimer and R. Davé. Cosmological simulations of intergalactic medium enrichment from galactic outflows. MNRAS, 373:1265–1292, December 2006. doi: 10.1111/j.1365-2966.2006.10989.x.

B. D. Oppenheimer and R. Davé. Mass, metal, and energy feedback in cosmological simulations. MNRAS, 387:577–600, June 2008. doi: 10.1111/j.1365-2966.2008.13280.x.

B. D. Oppenheimer, R. Davé, D. Kereš, M. Fardal, N. Katz, J. A. Kollmeier, and D. H. Weinberg. Feedback and recycled wind accretion: assembling the z = 0 galaxy mass function. MNRAS, 406:2325–2338, August 2010. doi: 10.1111/j.1365-2966.2010.16872.x.

B. E. J. Pagel and B. E. Patchett. Metal abundances in nearby stars and the chemical history of the solar neighborhood. MNRAS, 172:13–40, July 1975.

J. A. Peacock. *Cosmological Physics*. January 1999.

P. J. E. Peebles. *Principles of Physical Cosmology*. 1993.

M. S. Peeples and F. Shankar. Constraints on star formation driven galaxy winds from the mass-metallicity relation at z= 0. MNRAS, 417:2962–2981, November 2011. doi: 10.1111/j.1365-2966.2011.19456.x.

M. Pettini, A. E. Shapley, C. C. Steidel, J.-G. Cuby, M. Dickinson, A. F. M. Moorwood, K. L. Adelberger, and M. Giavalisco. The Rest-Frame Optical Spectra of Lyman Break Galaxies: Star Formation, Extinction, Abundances, and Kinematics. ApJ, 554:981–1000, June 2001. doi: 10.1086/321403.

C. Pfrommer, T. A. Enßlin, V. Springel, M. Jubelgas, and K. Dolag. Simulating cosmic rays in clusters of galaxies - I. Effects on the Sunyaev-Zel'dovich effect and the X-ray emission. MNRAS, 378:385–408, June 2007. doi: 10.1111/j.1365-2966.2007.11732.x.

K. Pilkington, B. K. Gibson, C. B. Brook, F. Calura, G. S. Stinson, R. J. Thacker, L. Michel-Dansac, J. Bailin, H. M. P. Couchman, J. Wadsley, T. R. Quinn, and A. Maccio. The distribution of metals in cosmological hydrodynamical simulations of dwarf disc galaxies. MNRAS, page 3484, August 2012. doi: 10.1111/j.1365-2966.2012.21353.x.

L. Portinari, C. Chiosi, and A. Bressan. Galactic chemical enrichment with new metallicity dependent stellar yields. A&A, 334:505–539, June 1998.

L. C. Powell, A. Slyz, and J. Devriendt. The impact of supernova-driven winds on stream-fed protogalaxies. MNRAS, 414:3671–3689, July 2011. doi: 10.1111/j.1365-2966.2011.18668.x.

W. H. Press and P. Schechter. Formation of Galaxies and Clusters of Galaxies by Self-Similar Gravitational Condensation. ApJ, 187:425–438, February 1974. doi: 10.1086/152650.

D. J. Price. Modelling discontinuities and Kelvin Helmholtz instabilities in SPH. *Journal of Computational Physics*, 227:10040–10057, December 2008. doi: 10.1016/j.jcp.2008.08.011.

D. J. Price and J. J. Monaghan. Smoothed Particle Magnetohydrodynamics - III. Multidimensional tests and the ∇.B= 0 constraint. MNRAS, 364:384–406, December 2005. doi: 10.1111/j.1365-2966.2005.09576.x.

J. I. Read, A. P. Pontzen, and M. Viel. On the formation of dwarf galaxies and stellar haloes. MNRAS, 371:885–897, September 2006. doi: 10.1111/j.1365-2966.2006.10720.x.

J. I. Read, G. Lake, O. Agertz, and V. P. Debattista. Thin, thick and dark discs in ΛCDM. MNRAS, 389:1041–1057, September 2008. doi: 10.1111/j.1365-2966.2008.13643.x.

J. I. Read, T. Hayfield, and O. Agertz. Resolving mixing in smoothed particle hydrodynamics. MNRAS, 405:1513–1530, July 2010. doi: 10.1111/j.1365-2966.2010.16577.x.

D. S. Reed, R. Bower, C. S. Frenk, A. Jenkins, and T. Theuns. The halo mass function from the dark ages through the present day. MNRAS, 374:2–15, January 2007. doi: 10.1111/j.1365-2966.2006.11204.x.

M. J. Rees and J. P. Ostriker. Cooling, dynamics and fragmentation of massive gas clouds - Clues to the masses and radii of galaxies and clusters. MNRAS, 179:541–559, June 1977.

M. J. Reid, K. M. Menten, X. W. Zheng, A. Brunthaler, L. Moscadelli, Y. Xu, B. Zhang, M. Sato, M. Honma, T. Hirota, K. Hachisuka, Y. K. Choi, G. A. Moellenbrock, and A. Bartkiewicz. Trigonometric Parallaxes of Massive Star-Forming Regions. VI. Galactic Structure, Fundamental Parameters, and Noncircular Motions. ApJ, 700:137–148, July 2009. doi: 10.1088/0004-637X/700/1/137.

D. S. Rupke, S. Veilleux, and D. B. Sanders. Outflows in Infrared-Luminous Starbursts at z ¡ 0.5. II. Analysis and Discussion. ApJS, 160:115–148, September 2005. doi: 10.1086/432889.

T. R. Saitoh and J. Makino. A Necessary Condition for Individual Time Steps in SPH Simulations. ApJ, 697:L99–L102, June 2009. doi: 10.1088/0004-637X/697/2/L99.

C. Scannapieco, M. Wadepuhl, O. H. Parry, J. F. Navarro, A. Jenkins, V. Springel, R. Teyssier, E. Carlson, H. M. P. Couchman, R. A. Crain, C. Dalla Vecchia, C. S. Frenk, C. Kobayashi, P. Monaco, G. Murante, T. Okamoto, T. Quinn, J. Schaye, G. S. Stinson, T. Theuns, J. Wadsley, S. D. M. White, and R. Woods. The Aquila comparison Project: The Effects of Feedback and Numerical Methods on Simulations of Galaxy Formation. *ArXiv e-prints*, December 2011.

E. Scannapieco and M. Brüggen. Simulating supersonic turbulence in galaxy outflows. MNRAS, 405:1634–1653, July 2010. doi: 10.1111/j.1365-2966.2010.16599.x.

J. Schaye. Star Formation Thresholds and Galaxy Edges: Why and Where. ApJ, 609:667–682, July 2004. doi: 10.1086/421232.

J. Schaye and C. Dalla Vecchia. On the relation between the Schmidt and Kennicutt-Schmidt star formation laws and its implications for numerical simulations. MNRAS, 383:1210–1222, January 2008. doi: 10.1111/j.1365-2966.2007.12639.x.

J. Schaye, A. Aguirre, T.-S. Kim, T. Theuns, M. Rauch, and W. L. W. Sargent. Metallicity of the Intergalactic Medium Using Pixel Statistics. II. The Distribution of Metals as Traced by C IV. ApJ, 596:768–796, October 2003. doi: 10.1086/378044.

J. Schaye, C. Dalla Vecchia, C. M. Booth, R. P. C. Wiersma, T. Theuns, M. R. Haas, S. Bertone, A. R. Duffy, I. G. McCarthy, and F. van de Voort. The physics driving the cosmic star formation history. MNRAS, 402:1536–1560, March 2010a. doi: 10.1111/j.1365-2966.2009.16029.x.

J. Schaye, C. Dalla Vecchia, C. M. Booth, R. P. C. Wiersma, T. Theuns, M. R. Haas, S. Bertone, A. R. Duffy, I. G. McCarthy, and F. van de Voort. The physics driving the cosmic star formation history. MNRAS, 402:1536–1560, March 2010b. doi: 10.1111/j.1365-2966.2009.16029.x.

M. Schmidt. The Rate of Star Formation. ApJ, 129:243, March 1959. doi: 10.1086/146614.

M. Schmidt. The Rate of Star Formation. II. The Rate of Formation of Stars of Different Mass. ApJ, 137:758, April 1963. doi: 10.1086/147553.

N. Z. Scoville and D. B. Sanders. H2 in the Galaxy. In D. J. Hollenbach and H. A. Thronson, Jr., editors, *Interstellar Processes*, volume 134 of *Astrophysics and Space Science Library*, pages 21–50, 1987.

L. I. Sedov. *Similarity and Dimensional Methods in Mechanics*. 1959.

M. Sharma, B. B. Nath, and Y. Shchekinov. Dust-driven Wind from Disk Galaxies. ApJ, 736: L27, August 2011. doi: 10.1088/2041-8205/736/2/L27.

S. Shen, H. J. Mo, S. D. M. White, M. R. Blanton, G. Kauffmann, W. Voges, J. Brinkmann, and I. Csabai. The size distribution of galaxies in the Sloan Digital Sky Survey. MNRAS, 343: 978–994, August 2003. doi: 10.1046/j.1365-8711.2003.06740.x.

S. Shen, J. Wadsley, and G. Stinson. The enrichment of the intergalactic medium with adiabatic feedback - I. Metal cooling and metal diffusion. MNRAS, 407:1581–1596, September 2010. doi: 10.1111/j.1365-2966.2010.17047.x.

J. Silk. The formation of galaxy discs. MNRAS, 324:313–318, June 2001. doi: 10.1046/j.1365-8711.2001.04197.x.

S. J. Smartt. Progenitors of Core-Collapse Supernovae. ARA&A, 47:63–106, September 2009. doi: 10.1146/annurev-astro-082708-101737.

L. Spitzer, Jr. On a Possible Interstellar Galactic Corona. ApJ, 124:20–+, July 1956. doi: 10.1086/146200.

V. Springel. The cosmological simulation code GADGET-2. MNRAS, 364:1105–1134, December 2005. doi: 10.1111/j.1365-2966.2005.09655.x.

V. Springel. E pur si muove: Galilean-invariant cosmological hydrodynamical simulations on a moving mesh. MNRAS, 401:791–851, January 2010. doi: 10.1111/j.1365-2966.2009.15715.x.

V. Springel and L. Hernquist. Cosmological smoothed particle hydrodynamics simulations: the entropy equation. MNRAS, 333:649–664, July 2002. doi: 10.1046/j.1365-8711.2002.05445.x.

V. Springel and L. Hernquist. Cosmological smoothed particle hydrodynamics simulations: a hybrid multiphase model for star formation. MNRAS, 339:289–311, February 2003. doi: 10.1046/j.1365-8711.2003.06206.x.

V. Springel, S. D. M. White, A. Jenkins, C. S. Frenk, N. Yoshida, L. Gao, J. Navarro, R. Thacker, D. Croton, J. Helly, J. A. Peacock, S. Cole, P. Thomas, H. Couchman, A. Evrard, J. Colberg, and F. Pearce. Simulations of the formation, evolution and clustering of galaxies and quasars. Nature, 435:629–636, June 2005. doi: 10.1038/nature03597.

C. C. Steidel, D. K. Erb, A. E. Shapley, M. Pettini, N. Reddy, M. Bogosavljević, G. C. Rudie, and O. Rakic. The Structure and Kinematics of the Circumgalactic Medium from Far-ultraviolet Spectra of z ˜= 2-3 Galaxies. ApJ, 717:289–322, July 2010. doi: 10.1088/0004-637X/717/1/289.

G. Strang. On the Construction and Comparison of Difference Schemes. *SIAM Journal on Numerical Analysis*, 5:506–517, September 1968. doi: 10.1137/0705041.

D. K. Strickland and T. M. Heckman. Supernova Feedback Efficiency and Mass Loading in the Starburst and Galactic Superwind Exemplar M82. ApJ, 697:2030–2056, June 2009. doi: 10.1088/0004-637X/697/2/2030.

D. K. Strickland and I. R. Stevens. Starburst-driven galactic winds - I. Energetics and intrinsic X-ray emission. MNRAS, 314:511–545, May 2000. doi: 10.1046/j.1365-8711.2000.03391.x.

M. J. Stringer, R. G. Bower, S. Cole, C. S. Frenk, and T. Theuns. Principles of supernova-driven winds. *ArXiv e-prints*, November 2011.

A. A. Suchkov, V. G. Berman, T. M. Heckman, and D. S. Balsara. Mass Loading and Collimation of Galactic Superwinds. ApJ, 463:528–534, June 1996. doi: 10.1086/177267.

R. S. Sutherland and M. A. Dopita. Cooling functions for low-density astrophysical plasmas. ApJS, 88:253–327, September 1993. doi: 10.1086/191823.

A. M. Swinbank, T. M. Webb, J. Richard, R. G. Bower, R. S. Ellis, G. Illingworth, T. Jones, M. Kriek, I. Smail, D. P. Stark, and P. van Dokkum. A spatially resolved map of the kinematics, star formation and stellar mass assembly in a star-forming galaxy at z = 4.9. MNRAS, 400:1121–1131, December 2009. doi: 10.1111/j.1365-2966.2009.15617.x.

E. J. Tasker and J. C. Tan. Star Formation in Disk Galaxies. I. Formation and Evolution of Giant Molecular Clouds via Gravitational Instability and Cloud Collisions. ApJ, 700:358–375, July 2009. doi: 10.1088/0004-637X/700/1/358.

G. Taylor. The Formation of a Blast Wave by a Very Intense Explosion. I. Theoretical Discussion. *Royal Society of London Proceedings Series A*, 201:159–174, March 1950. doi: 10.1098/rspa.1950.0049.

E. Tescari, M. Viel, V. D'Odorico, S. Cristiani, F. Calura, S. Borgani, and L. Tornatore. Cosmic evolution of the C IV in high-resolution hydrodynamic simulations. MNRAS, 411:826–848, February 2011. doi: 10.1111/j.1365-2966.2010.17761.x.

R. Teyssier. Cosmological hydrodynamics with adaptive mesh refinement. A new high resolution code called RAMSES. A&A, 385:337–364, April 2002. doi: 10.1051/0004-6361:20011817.

T. Theuns, A. Leonard, G. Efstathiou, F. R. Pearce, and P. A. Thomas. P^3M-SPH simulations of the Lyalpha forest. MNRAS, 301:478–502, December 1998. doi: 10.1046/j.1365-8711.1998.02040.x.

T. Theuns, M. Viel, S. Kay, J. Schaye, R. F. Carswell, and P. Tzanavaris. Galactic Winds in the Intergalactic Medium. ApJ, 578:L5–L8, October 2002. doi: 10.1086/344521.

K. Thornton, M. Gaudlitz, H.-T. Janka, and M. Steinmetz. Energy Input and Mass Redistribution by Supernovae in the Interstellar Medium. ApJ, 500:95, June 1998. doi: 10.1086/305704.

B. M. Tinsley. Evolution of the Stars and Gas in Galaxies. Fund. Cosmic Phys., 5:287–388, 1980.

A. Toomre. On the gravitational stability of a disk of stars. ApJ, 139:1217–1238, May 1964. doi: 10.1086/147861.

E. F. Toro, M. Spruce, and W. Speares. Restoration of the contact surface in the HLL-Riemann solver. *Shock Waves*, 4:25–34, July 1994. doi: 10.1007/BF01414629.

C. Trachternach, W. J. G. de Blok, S. S. McGaugh, J. M. van der Hulst, and R.-J. Dettmar. The baryonic Tully-Fisher relation and its implication for dark matter halos. A&A, 505:577–587, October 2009. doi: 10.1051/0004-6361/200811136.

C. A. Tremonti, T. M. Heckman, G. Kauffmann, J. Brinchmann, S. Charlot, S. D. M. White, M. Seibert, E. W. Peng, D. J. Schlegel, A. Uomoto, M. Fukugita, and J. Brinkmann. The Origin of the Mass-Metallicity Relation: Insights from 53,000 Star-forming Galaxies in the Sloan Digital Sky Survey. ApJ, 613:898–913, October 2004. doi: 10.1086/423264.

J. K. Truelove and C. F. McKee. Evolution of Nonradiative Supernova Remnants. ApJS, 120:299–326, February 1999. doi: 10.1086/313176.

R. B. Tully and J. R. Fisher. A new method of determining distances to galaxies. A&A, 54:661–673, February 1977.

S. van den Bergh. The frequency of stars with different metal abundances. AJ, 67:486–490, October 1962. doi: 10.1086/108757.

B. van Leer. Towards the ultimate conservative difference scheme. V - A second-order sequel to Godunov's method. *Journal of Computational Physics*, 32:101–136, July 1979. doi: 10.1016/0021-9991(79)90145-1.

S. Veilleux, G. Cecil, and J. Bland-Hawthorn. Galactic Winds. ARA&A, 43:769–826, September 2005. doi: 10.1146/annurev.astro.43.072103.150610.

J. von Neumann and R. D. Richtmyer. A Method for the Numerical Calculation of Hydrodynamic Shocks. *Journal of Applied Physics*, 21:232–237, March 1950. doi: 10.1063/1.1699639.

B. P. Wakker, D. G. York, R. Wilhelm, J. C. Barentine, P. Richter, T. C. Beers, Ž. Ivezić, and J. C. Howk. Distances to Galactic High-Velocity Clouds. I. Cohen Stream, Complex GCP, Cloud g1. ApJ, 672:298–319, January 2008. doi: 10.1086/523845.

F. Walter, E. Brinks, W. J. G. de Blok, F. Bigiel, R. C. Kennicutt, Jr., M. D. Thornley, and A. Leroy. THINGS: The H I Nearby Galaxy Survey. AJ, 136:2563, December 2008. doi: 10.1088/0004-6256/136/6/2563.

R. Weaver, R. McCray, J. Castor, P. Shapiro, and R. Moore. Interstellar bubbles. II - Structure and evolution. ApJ, 218:377–395, December 1977. doi: 10.1086/155692.

B. J. Weiner, A. L. Coil, J. X. Prochaska, J. A. Newman, M. C. Cooper, K. Bundy, C. J. Conselice, A. A. Dutton, S. M. Faber, D. C. Koo, J. M. Lotz, G. H. Rieke, and K. H. R. Rubin. Ubiquitous Outflows in DEEP2 Spectra of Star-Forming Galaxies at z = 1.4. ApJ, 692:187–211, February 2009. doi: 10.1088/0004-637X/692/1/187.

J. K. Werk, M. E. Putman, G. R. Meurer, and N. Santiago-Figueroa. Metal Transport to the Gaseous Outskirts of Galaxies. ApJ, 735:71, July 2011. doi: 10.1088/0004-637X/735/2/71.

A. A. West, D. A. Garcia-Appadoo, J. J. Dalcanton, M. J. Disney, C. M. Rockosi, and Ž. Ivezić. H I-Selected Galaxies in the Sloan Digital Sky Survey. II. The Colors of Gas-Rich Galaxies. AJ, 138:796–807, September 2009. doi: 10.1088/0004-6256/138/3/796.

S. D. M. White. Formation and Evolution of Galaxies: Les Houches Lectures. *ArXiv Astrophysics e-prints astro-ph/9410043*, October 1994.

S. D. M. White and C. S. Frenk. Galaxy formation through hierarchical clustering. ApJ, 379: 52–79, September 1991. doi: 10.1086/170483.

S. D. M. White and M. J. Rees. Core condensation in heavy halos - A two-stage theory for galaxy formation and clustering. MNRAS, 183:341–358, May 1978a.

S. D. M. White and M. J. Rees. Core condensation in heavy halos - A two-stage theory for galaxy formation and clustering. MNRAS, 183:341–358, May 1978b.

R. P. C. Wiersma, J. Schaye, and B. D. Smith. The effect of photoionization on the cooling rates of enriched, astrophysical plasmas. MNRAS, pages 20–+, January 2009a. doi: 10.1111/j.1365-2966.2008.14191.x.

R. P. C. Wiersma, J. Schaye, T. Theuns, C. Dalla Vecchia, and L. Tornatore. Chemical enrichment in cosmological, smoothed particle hydrodynamics simulations. MNRAS, 399:574–600, October 2009b. doi: 10.1111/j.1365-2966.2009.15331.x.

R. P. C. Wiersma, J. Schaye, C. Dalla Vecchia, C. M. Booth, T. Theuns, and A. Aguirre. The enrichment history of cosmic metals. MNRAS, 409:132–144, November 2010. doi: 10.1111/j.1365-2966.2010.17299.x.

R. J. Wilman, J. Gerssen, R. G. Bower, S. L. Morris, R. Bacon, P. T. de Zeeuw, and R. L. Davies. The discovery of a galaxy-wide superwind from a young massive galaxy at redshift z ˜ 3. Nature, 436:227–229, July 2005. doi: 10.1038/nature03718.

J. H. Wise and T. Abel. Resolving the Formation of Protogalaxies. III. Feedback from the First Stars. ApJ, 685:40–56, September 2008. doi: 10.1086/590417.

M. G. Wolfire, D. Hollenbach, C. F. McKee, A. G. G. M. Tielens, and E. L. O. Bakes. The neutral atomic phases of the interstellar medium. ApJ, 443:152–168, April 1995. doi: 10.1086/175510.

T. Wong and L. Blitz. The Relationship between Gas Content and Star Formation in Molecule-rich Spiral Galaxies. ApJ, 569:157–183, April 2002. doi: 10.1086/339287.

S. E. Woosley and T. A. Weaver. The Evolution and Explosion of Massive Stars. II. Explosive Hydrodynamics and Nucleosynthesis. ApJS, 101:181, November 1995. doi: 10.1086/192237.

G. Worthey. Comprehensive stellar population models and the disentanglement of age and metallicity effects. ApJS, 95:107–149, November 1994. doi: 10.1086/192096.

X. Yang, H. J. Mo, and F. C. van den Bosch. Constraining galaxy formation and cosmology with the conditional luminosity function of galaxies. MNRAS, 339:1057–1080, March 2003. doi: 10.1046/j.1365-8711.2003.06254.x.

Y. B. Zel'Dovich and Y. P. Raizer. *Physics of shock waves and high-temperature hydrodynamic phenomena*. 1967.